

Background studies for LUX and LZ: activation, gammas from rock and krypton removal



The
University
Of
Sheffield.

Andrew Samuel Naylor

Department of Physics and Astronomy
University of Sheffield

A dissertation submitted for the degree of
Doctor of Philosophy

September 2022

To my loving family

Abstract

Although there is considerable evidence for the existence of dark matter, which makes up the majority of matter in the Universe, a fundamental question still remains unanswered; what is dark matter made of? A new theorised elementary particle called Weakly Interacting Massive Particle (WIMP) is a promising candidate for dark matter. Dual-phase xenon time projection chamber (TPC) technology can search for low energy scattering signals produced by WIMP interactions with atomic nuclei.

Utilising this technology the Large Underground Xenon (LUX) experiment, located at the Sanford Underground Research Facility (South Dakota, USA), provided stringent limits on the spin-independent WIMP-nucleon cross-section. Its successor the LUX-ZEPLIN (LZ) experiment, a multi-tonne dual-phase xenon TPC, aims at considerably increasing the sensitivity to WIMP dark matter. In order to achieve high sensitivity in any rare event search experiment, characterising and suppressing backgrounds is fundamental.

This work characterises a number of important backgrounds and explores their mitigation strategies for the LUX and LZ experiments. The LZ gas charcoal chromatography system removes problematic noble radioactive impurities (primarily ^{85}Kr) in the xenon. An overview of this system along with xenon impurity measurements, taken with the LZ sampling system, is presented. The cavern walls surrounding the detector emit high energy gamma rays from the naturally occurring radiation in the rock. High statistics event biasing simulations have been performed to determine the background contribution in the LUX and LZ detectors, which are located in a large water tank to provide shielding. LZ commissioning data is also analysed to evaluate the current cavern wall gamma ray shielding. In addition, simulations of the activation of xenon and surroundings in LZ caused by neutron calibration sources, have been carried out to determine the background due to the delayed decay of radioactive isotopes.

Declaration

I declare that the contents of this dissertation is original and my own work, except where explicit reference is made to the work of others. This dissertation contains nothing which is the outcome of work done in collaboration with others, except as specified in the text. This dissertation has not been submitted in whole or in part for consideration for any other degree or qualification in this, or any other university.

Andrew Samuel Naylor
September 2022

Acknowledgements

On my PhD journey there have been numerous wonderful people who have supported and encouraged me for which I am eternally grateful. Although there has been many challenges along the way it has been an amazing experience. Firstly, I want to thank my Lord Jesus Christ for his enduring faithfulness and love. His continuing grace and peace has enabled me to finish this degree.

I would also like to thank my supervisor Prof. Vitaly Kudryavtsev, who gave me this incredible opportunity to pursue my dream of completing a PhD. I am very thankful for his patience with me and crucial guidance throughout the PhD. It was a pleasure to work with him. The Sheffield LZ group (current and past members) have also supported me during this journey. With special thanks to Elena, David and Peter who showed me the ropes and provided invaluable support over the years.

I want to extend my sincere thanks to all members of the LUX and LZ collaborations who helped make this journey enjoyable and interesting. In particular it has been a pleasure to work with these people over the past few years: Albert, Ibles, Austin, Dylan, Amy, Ewan, Luke, Ben, Micah, Scott K., Brais, Sally, Jordan, Rob, Vetri, Rafi (I'm sure I will have forget to mention someone). A special mention goes to Greg R. and Chris who made LZ conferences thoroughly enjoyable and have provided many laughs and support throughout the PhD. I also want to specifically thank Will and Andrew for the community and laughter they provided during lockdown. I am particularly grateful to Andrew for his friendship, it kept me sane during difficult times.

I have been incredibly fortunate to spend some of my PhD in the Bay Area. I would like to thank Quentin and Pauline for hosting me and showing me around San Francisco. I am very grateful to Wahid and all those at NERSC who helped make it such an incredible experience working at NERSC. I would also like extend a big thank you to Dan and Chantel who were such wonderful hosts during my placement at SLAC. Thank you to the SLAC krypton team (Eric, Christina, Drew, John) who helped make that placement an awesome experience. A special thank you goes to all the amazing people I met at Living Hope who welcomed me into their community with open arms.

Finally, I would like to express deep gratitude to my family. My parents continue to inspire me and have enabled me to follow my dreams. To my remarkable siblings I am grateful for your continual encouragement. This dissertation would not have been possible without your love and support.

Contents

List of Figures	vii
List of Tables	xix
Acronyms	xxi
Introduction	1
1 Dark matter in the Universe	2
1.1 Evidence for dark matter	2
1.1.1 Early history	2
1.1.2 Galaxy rotation curves	3
1.1.3 Gravitational lensing	3
1.1.4 Cosmic microwave background radiation	6
1.1.5 Big Bang nucleosynthesis	8
1.1.6 Large scale structure	9
1.2 Dark matter candidates	9
1.2.1 Dark matter properties	9
1.2.2 Weakly interacting massive particles	10
1.2.3 Axions	11
1.3 WIMP dark matter searches	12
1.3.1 Direct detection	13
1.3.2 Indirect detection	19
1.3.3 Collider searches	21
1.4 Summary	22
2 The LUX and LZ experiments	23
2.1 Particle interactions in liquid xenon	23
2.1.1 Xenon properties	23
2.1.2 Xenon microphysics	24
2.2 Dual-phase xenon time projection chambers	26

2.2.1	Concept	26
2.2.2	Light and charge yields	27
2.2.3	ER/NR discrimination	29
2.3	The LUX experiment	30
2.3.1	Overview	30
2.3.2	Background suppression methods	31
2.3.3	Results	31
2.4	The LZ experiment	31
2.4.1	Overview	31
2.4.2	Active veto detectors	32
2.4.3	Significant background sources	33
2.5	Simulating backgrounds	37
2.5.1	Geant4 based software	38
2.5.2	NEST	38
2.5.3	LZap	39
2.5.4	LZ Mock Data Challenges	40
2.6	Simulated background analysis cuts	41
3	Krypton removal from xenon	44
3.1	^{85}Kr concentration in xenon	44
3.2	LZ krypton removal system	46
3.2.1	Gas Charcoal Chromatography	46
3.2.2	Xenon recovery cold trap	49
3.2.3	Automated plotting of system information	50
3.3	Xenon Cold Trap Sampling System	55
3.3.1	Method	55
3.3.2	Sampling in LZ krypton removal system	57
4	Software	61
4.1	Introduction	61
4.2	PSquared	62
4.2.1	Overview of PSquared	62
4.2.2	Job submission interface	63
4.2.3	LZap	64
4.3	Hyper	67
4.4	LEOPARD	69

5	Cavern wall gamma rays	72
5.1	Motivation	72
5.2	Event biasing simulations	73
5.3	Analysis	75
5.4	Results	76
5.4.1	Attenuation of gamma rays in water	76
5.4.2	LUX results	79
5.4.3	LZ results	80
5.5	Gamma background from cavern walls for neutrinoless double beta decay	81
5.6	RockGammas BACCARAT generator	85
5.7	Conclusion	85
6	Xenon activation in the LZ detector	86
6.1	Activation processes	86
6.2	Activation from neutron calibration	87
6.2.1	Description of sources	87
6.2.2	Background analysis chain	90
6.2.3	DD neutron calibration simulation results	93
6.2.4	DD neutron simulation with uniform distribution of decays	96
6.2.5	AmLi neutron calibration simulation results	105
6.2.6	AmLi neutron simulation with uniform distribution of decays	107
6.3	$^{129\text{m}}\text{Xe}$ & $^{131\text{m}}\text{Xe}$	113
6.3.1	Validation	113
6.3.2	Method	117
6.3.3	Results	119
6.4	Conclusion	129
7	LZ commissioning data	130
7.1	Background acquisitions	130
7.2	Analysis	131
7.3	Results	133
7.4	Summary	137
8	Conclusion	138
A	Hyper example code	140
	Bibliography	141

List of Figures

1.1	NGC 6503 galaxy rotation curve observation (black dots) with dark-halo fit (solid curve). The individual components of the rotation curve are shown; dark halo (dash-dotted line), optical disk (dashed line) and gas (dotted line). Figure from Ref. [6].	4
1.2	An image of a horseshoe Einstein ring taken by the Hubble Space Telescope. The gravity of a luminous red galaxy (in the centre of the picture) has distorted the light from a distant blue galaxy resulting in the background galaxy's horseshoe shape appearance. Image courtesy of ESA/Hubble and NASA [8].	4
1.3	Colour image of the bullet cluster with reconstructed lensing signal (green contours), which is proportional to the mass in the system. The blue plus signs represent the centre of mass for the hot gas clouds. Figure from Ref. [12].	5
1.4	Bullet cluster X-ray image overlaid with reconstructed lensing signal (green contours), which is proportional to the mass in the system. This image of the two merging galaxy clusters reveals the gravitational centre is in a different position to the baryonic centre. Figure from Ref. [12].	6
1.5	The all-sky CMBR temperature map measured by the Planck satellite. It displays the coldest (blue) to the hottest (red) regions in the sky, from $-300 \mu\text{K}$ to $300 \mu\text{K}$. Figure from Ref. [15].	7
1.6	Temperature fluctuations in the CMBR at different angular scales on the sky detected by the Planck Satellite. The angular scales can be represented either with angular degrees (lower horizontal axis) or via multipole moment l (upper horizontal axis). The red dots are the Planck measurements with the green curve representing the ΛCDM model best fit to the data. Figure from Ref. [16].	8

- 1.7 Illustration of a thermal relic freeze out in the early universe. The cosmological abundance ($\Omega_\chi h^2$) evolves as a function of $x = m_\chi/T$ where m_χ is WIMP mass and T is universe temperature. The temperature is implicitly a function of time. The numbers specified above the lines are the WIMP annihilation cross-sections averaged over WIMP velocity distribution. The grey line labelled Planck is the observed dark matter density. Figure from Ref. [33]. 11
- 1.8 The SI NR rate (a) and SI nuclear form factor (b) as a function of NR energy for several target elements. The WIMP mass and WIMP-nucleon cross-section are assumed to be 100 GeV and 10^{-45} cm² respectively. Figures from Ref. [54]. 15
- 1.9 Illustrations of liquid noble gas direct detection experiments. The dark matter particle χ (represented by the red arrow) will scatter on a nucleus depositing energy. The single-phase detector (a) can only capture the primary scintillation signal, whereas the dual-phase detector (b) measures two signals as it can also capture the ionisation signal as the charges drift into the gas to produce a secondary scintillation signal. Figures from Ref. [56]. 17
- 1.10 Illustration of cryogenic solid-state direct detection experiments. Energy will be deposited as the dark matter particle χ (represented by the red arrow) scatters on a nucleus. The cryogenic crystal detector captures the heat signal via detecting phonons and either the ionisation signal or the scintillation signal. Figure from Ref. [56]. 18
- 1.11 Exclusion limits on the SI WIMP-nucleon cross-section as a function of WIMP mass as of the end of 2020. This figure contains the 90% CL limit from a number of experiments for SI WIMP-nucleon cross-sections for a range of WIMP masses . The neutrino floor is indicated by the light blue dashed line represents the region where coherent scattering of neutrinos becomes a significant background. Figure from Ref. [21]. 19
- 1.12 Exclusion limits and sensitives on the dark matter self-annihilation cross-section to neutrinos from indirect detection experiments. This figure contains 90% CL limits (solid line) and projected sensitives (dashed lines) up to masses of 10^8 GeV. Figure from Ref. [83]. 20
- 1.13 Comparing SI WIMP-nucleon cross-section constraints from direct detection experiments to the inferred limits from ATLAS results in the context of the vector leptophobic model. The limits shown are 95% CL for ATLAS and 90% CL for direct detection experiments and the shaded areas are excluded. Figure from Ref. [84]. 21

2.1	Diagram showing the different processes by which an energy deposition in LXe results in ionisation, scintillation and heat. ERs dissipate recoil energy mostly through ionisation whereas the heat process is dominant for NRs. Figure from Ref. [89].	25
2.2	Illustration of a particle interaction in a xenon dual-phase TPC. An example of the $S1$ and $S2$ signals detected by PMTs is on the right. Figure from Ref. [87].	27
2.3	$\log_{10}(S2/S1)$ vs $S1$ from LUX calibration data. The red and blue lines represent the ER and NR bands respectively. The median of the band is the solid line with the dashed line indicating 80% band width. Beta decays from a dispersed tritium source calibrate the LUX ER band shown in the top panel (a). Elastic neutron scattering from a deuterium-deuterium pulsed neutron source populates the LUX NR band displayed in the bottom panel (b). The grey lines are energy deposition contours and the dashed-dotted magenta lines display the location of the minimum $S2$ cut. Figure from Ref. [87].	29
2.4	3D rendering of the LUX TPC. On the left is a cutaway of the TPC and on the right is the TPC connected to the top flange of the ICV. Figure from Ref. [97].	30
2.5	3D rendering of major LZ detector subsystems. (1) LXe TPC, (2) acrylic vessels filled with liquid scintillator comprising the OD, (3) OD PMTs, (4) water tank, (5) high voltage cathode connection, (6) neutron calibration conduit. Inverted steel pyramid under water tank not shown. Figure from Ref. [101].	33
2.6	The predicted background energy spectra of ER (a) and NR (b) single scatter events within the 5.6 tonne fiducial region. Detector efficiencies and veto cuts have not been applied. Figures from Ref. [60].	35
2.7	^{238}U decay chain. Figure from Ref. [103].	36
2.8	Cutaway 3D visualisation of the LZ detector in BACCARAT. Inner part of the water tank shown in blue with the OD PMTs in light pink. The OD acrylic vessels containing liquid scintillator (yellow) surrounds the cryostat (light green) which houses the TPC (magenta). Figure from Ref. [110].	39
2.9	The simulation processing chains used to produce background data for the MDCs. Figure adapted from Ref. [110].	40
3.1	^{85}Kr beta decay energy spectrum in blue with Q-value 687 keV and the orange band is the WIMP ROI 1.5-6.5 keV _{ee} . Spectrum generated by BetaShape [115].	45
3.2	Separation of krypton from xenon via gas charcoal chromatography for the LUX experiment. A residual gas analyser (RGA) measures the gas concentrations in the mixture at the charcoal column exit. Figure from Ref. [98].	46

-
- 3.3 Picture of the LZ krypton removal system with key elements labelled. Photograph taken by Jacqueline Orrell/SLAC National Accelerator Laboratory in summer 2019. 47
- 3.4 Schematic overview diagram of the three main loops in the LZ gas charcoal chromatography system. Note in the diagram the cryogenic condenser is called freezer. Figure provided by Drew Ames (Stanford University, USA). . . 48
- 3.5 Simplified piping and valve diagram of the xenon recovery cold trap system. The arrows point to the gas flow direction through the system. The cold trap is a steel U-shaped pipe in liquid nitrogen filled dewar. It can be bypassed if needed and is connected to cylinders as a buffer volume. The system is connected to the 7BA, extra xenon storage, and a Universal Gas Analyser (UGA) can be connected either side of the trap. 49
- 3.6 Xenon recovery cold trap system. The control panel (left) is connected to the krypton removal system and the steel U-shaped pipe located in a dewar (right). Photograph taken by Andrew Naylor (University of Sheffield, UK). . . 51
- 3.7 The control panel for the xenon recovery cold trap system. Each valve on the panel has been labelled with the destination and gas flow direction. Photograph taken by Eric Miller (SLAC National Accelerator Laboratory, USA). . . 52
- 3.8 The frozen steel U-shaped trap connected to the xenon recovery cold trap system. Photograph taken by Dan Akerib (Stanford University, USA). 53
- 3.9 A figure produced by the plotting tool about the initial phase of run 22.8 when xenon is injected into the charcoal column. The solid lines are pressure readings from pressure transducers in the system and the dashed line is the xenon flow rate from a mass flow controller (MFC). The beginning of the xenon injection into the helium gas stream is indicated by the dotted line. . . 54
- 3.10 Run timestamp database Ignition page. System operators can view and edit run entries in the database. It also provides links to the local sensor data plots website and the status of the plotting daemon. 56
- 3.11 Simple diagram of the cold trap in xenon cold trap sampling. Gaseous xenon sample enters on the left and the bulk xenon freezes on the pipe walls. The xenon ice vapour enriched with impurities exits the trap on the right. Figure from Ref. [122]. 57
- 3.12 Sampling system control panel in the LZ krypton removal system. Photograph taken by Andrew Naylor (University of Sheffield, UK). 58

3.13	RGA partial pressure data from a high sensitivity krypton measurement. The black and red dotted lines indicate the background and signal phases of the measurement respectively. When the background phase ends the xenon sample starts to flow through the cold trap. This run 7.4 xenon sample contains 50 ± 28 ppq of krypton.	59
3.14	High sensitivity krypton measurement RGA partial pressure data. The black and red dotted lines indicate the background and signal phases of the measurement respectively. The 1000 ppq xenon calibration was measured to have 1015 ± 86 ppq of krypton.	60
4.1	Schematic diagram showing the different elements of the LZ job submission system at NERSC. Note PSquared can run large numbers of jobs on the NERSC supercomputers and up to 64 tasks in each job.	62
4.2	Illustration of the JSI running at NERSC interfacing with PSquared to execute simulations and analysis on the NERSC supercomputers where the red outline shows which parts are the JSI.	63
4.3	Screenshot of the JSI web interface running on Spin at NERSC. It is showing an example job request which has 1 task running and 2 other tasks submitted waiting to be executed on the NERSC Cori supercomputer nodes.	64
4.4	A screen capture of the new job request form on the JSI web interface at NERSC running on the Spin platform. Users fill in the form to create a job request to be approved by an administrator before the jobs are sent to PSquared and executed on the NERSC supercomputers.	65
4.5	Schematic diagram of Hyper framework overview.	68
4.6	Number of events processed per second in a simple analysis code written with Hyper and C++ frameworks.	69
4.7	A screenshot of the prototype LEOPARD Python website user input form. Users can input data catalogue requests with specified cuts and histograms for LEOPARD to execute and return the histograms.	70
4.8	Screen capture of plots produced by a user request on the prototype LEOPARD Python website. Users can browser the different plots generated by the request.	71
5.1	3D renderings of the LUX and LZ detectors in the water tank ($h \times d = 592.8$ cm \times 762 cm) in the Davis cavern. Inverted steel pyramid under water tank not shown. Figures (a) & (b) from Ref. [97] & [60] respectively.	73

5.2	Illustration of the event biasing method implemented into BACCARAT and LUXSim allowing effective simulation of large number of decays. The red-dashed lines represent the stage boundaries. Note there is a scintillator in the LZ detector only. Relative dimensions in the Figure not to scale. Figure published in Ref. [110].	74
5.3	γ -ray energy spectrum at the end of each simulation stage (except the final stage) produced in BACCARAT for LZ by ^{232}Th , ^{238}U and ^{40}K decay chains.	77
5.4	Z position (along the drift field) vs radius squared R^2 for ER energy depositions up to 100 keV from ^{232}Th BACCARAT simulations. The black dashed line represents the 5.6 tonne fiducial volume with the cathode located at $z = 0$ cm. No cuts were applied in (a). The standard background cuts (except for fiducial volume) have been applied in (b), highlighting the effectiveness of the single scatter, outer detector, xenon skin and WIMP ROI cut.	78
5.5	Energy spectra of simulated ERs from cavern wall gamma rays produced by LUXSim. These gamma rays are located within the TPC and no standard background cuts have been applied. The insert presents the energy spectra at low energies after standard cuts are applied.	79
5.6	The cavern wall gamma rays ER energy spectra produced by BACCARAT simulations. These gamma rays are located within the TPC and no standard background cuts have been applied. The insert presents the energy spectra at low energies after standard cuts are applied.	80
5.7	Z position (along the drift field) vs radius squared R^2 for ER energy depositions in the energy ROI, $Q_{\beta\beta} \pm 1\sigma$, from ^{232}Th BACCARAT simulations. The red dashed line represents the 967 kg fiducial volume with the cathode located at $z = 0$ cm. No cuts were applied in (a). $0\nu\beta\beta$ background analysis cuts (except for fiducial volume) were applied in (b), displaying the significant reduction to the $0\nu\beta\beta$ search background.	83
5.8	BACCARAT simulation energy spectra of ERs from the cavern wall gamma rays. These gamma rays are located within the inner 967 kg LXe fiducial volume. Around the $Q_{\beta\beta}$, dashed purple, is a grey band representing the energy ROI, $Q_{\beta\beta} \pm 1\sigma$, in (a). All $0\nu\beta\beta$ background cuts were in applied in (b).	84
6.1	Example xenon neutron cross-sections. Neutron radiative capture (blue line) and neutron inelastic (orange line) cross-sections on ^{132}Xe . Cross-section data taken from ENDF/B-VIII.0 evaluated nuclear reaction data library [144].	87

- 6.2 Drawing of the DD neutron generator (light green) positioned outside the water tank to fire neutrons into the LZ TPC located inside the water tank. The DD neutron generator is mounted on a lift which can be moved to emit a neutron beam either through the horizontal or angled conduit (light grey). The red line is an example neutron beam path that the DD neutron generator will use to fire neutrons into the LZ TPC. The acrylic tanks (dark green), part of the OD include cutouts for the two conduits to allow the neutron beam to travel through the tanks to the LZ TPC which is encased in a titanium cryostat. Figure not to scale. Figure from Ref. [148]. 88
- 6.3 Cutaway drawing of LZ detector in the water tank without the OD PMTs. The horizontal and angled conduits are used with the DD neutron generator for calibrations. Also labelled are the two visible calibration source deployment (CSD) tubes in which a radioactive source can be lowered into the space between the OCV and ICV for calibrations. Figure not to scale. Figure from Ref. [148]. 88
- 6.4 Measured neutron energy spectrum of a prototype AmLi source for the LZ experiment. Figure from Ref. [110]. 89
- 6.5 Drawing of the CSD system (top of the figure) inside the water tank. The CSD system will lower the AmLi neutron calibration source into the three tubes (highlighted by the red lines) located in between the outer and inner titanium cryostat vessels, OCV and ICV respectively. The OCV is surrounded by the acrylic tanks that make up the OD and the ICV houses the LZ TPC. Figure not to scale. Figure from Ref. [148]. 90
- 6.6 Initial particle momenta projections (direction cosines) (p_x , p_y & p_z) generated by the BACCARAT DD neutron generator. The particle momenta projections are without units and lie on the bottom surface of a rounded square pyramid. As the bottom face has a small curvature the value of p_x was expressed via colour; the lighter blue colour signifies larger p_x and the darker smaller p_x . The red dot is (0, 0, 0). Note the different axes scales with p_x from 0 to 1 and p_y & p_z from -0.03 to 0.03. 91
- 6.7 The number of radioactive nuclei produced in the DD neutron calibration simulations in the TPC, xenon skin and OD. The number of events has been normalised to 2 days of DD neutron calibrations. 93
- 6.8 Neutron radiative capture cross-sections of a few stable xenon isotopes multiplied by their natural abundance against neutron incident energy. Cross-section data from ENDF/B-VIII.0 evaluated nuclear reaction data library [144]. 94

- 6.9 Total simulated energy deposition in the DD neutron calibration simulations in active LXe for events taking place during a 60 day data run. The number of events has been normalised to 2 days of DD neutron calibrations. The blue histogram is all events which took place in the active LXe and the red histogram is only those events in the active LXe which passed the standard background cuts. Notable isotope decay lines have been labeled. 95
- 6.10 Z position (along the drift field) vs radius squared R^2 for events induced by the decays of activated isotopes from the DD neutron calibration simulations for events taking place during a 60 day data run in active LXe. The analysis assumed that the radioisotope decayed at the same position as they were produced. Events shown survived standard background cuts. The number of events has been normalised to 2 days of DD neutron calibrations. The black dotted line is the edge of the fiducial volume. 97
- 6.11 Decay chains of xenon isotopes which were simulated with the BACCARAT DecayChain generator. Half-life of the isotopes and their decay modes are given. Q values displayed are in keV. Decay chains taken from Ref. [151]. . . 98
- 6.12 Z position (along the drift field) vs radius squared R^2 for events from the DecayChain BACCARAT simulations for events in active LXe taking place during SR1. Events shown survived all background cuts. The number of events has been normalised to 2 days of DD neutron calibrations. The black dotted line is the edge of the fiducial volume. 99
- 6.13 Total simulated uniformly distributed energy depositions in the DecayChain simulations in active LXe for events taking place during 60 day data run. The number of events has been normalised to 2 days of DD neutron calibrations. The blue histogram includes all events that took place in the active LXe whereas the red histogram is only includes those events in the active LXe that passed all standard background cuts. 100
- 6.14 Total reconstructed energy deposition from generated S1 and S2 signals in the DecayChain simulations in active LXe for events taking place during 60 day data run. The number of events has been normalised to 2 days of DD neutron calibrations. All events which took place in the active LXe are included in the blue histogram and only those events in the active LXe which passed the standard background cuts are in the red histogram. 101

- 6.15 $\log_{10}(S2_c)$ vs $S1_c$ for events in active LXe during 60 days of data taking from the DecayChain simulations. The number of events plotted in the figures has been normalised to 2 days of DD neutron calibrations. The blue and red bands are the electron and nuclear recoil bands respectively (solid: mean; dashed: $\pm 1.28\sigma$ contours). The different shaded areas and corresponding dotted lines represent different ROI's; the green is the EFT ROI, the pink is the WIMP PLR ROI and the brown is the WIMP TDR ROI. 103
- 6.16 $\log_{10}(S2_c)$ vs $S1_c$ for events from the DecayChain simulations which were in active LXe during 60 days of data taking. In the figures the number of events plotted has been normalised to 2 days of DD neutron calibrations. Figure (a) shows all events which survived standard background cuts and Figure (b) displays the same events minus any events generated from ^{125}I decays. The different ROIs are represented by dotted lines in the figure; the green is the EFT ROI, the pink is the WIMP PLR ROI and the brown is the WIMP TDR ROI. The blue and red lines shows the boundary for the electron and nuclear recoil bands respectively (solid: mean; dashed: $\pm 1.28\sigma$ contours). 104
- 6.17 The number of radioactive nuclei produced in the TPC, xenon skin and OD in the AmLi neutron calibration simulations. The number of events has been normalised to 9 hours of AmLi neutron calibrations. 105
- 6.18 Total simulated energy deposition in the AmLi neutron calibration simulations for events taking place during a 60 day data run in active LXe. The number of events has been normalised to 9 hours of AmLi neutron calibrations. The blue histogram displays all events in the active LXe and the red histogram includes only events in the active LXe that passed the standard background cuts. Notable isotope decay lines have been labeled. 106
- 6.19 Z position (along the drift field) vs radius squared R^2 for events induced by the decays of the activated isotopes during a 60 day data run in active LXe from the AmLi neutron calibration simulations. The analysis assumed that the radioisotope decayed at the same position as they were produced. Events displayed passed all background cuts. The number of events has been normalised to 9 hours of AmLi neutron calibrations. The black dotted line is the edge of the fiducial volume. 107
- 6.20 Total simulated uniformly distributed energy deposition in the DecayChain simulations in active LXe for events taking place during 60 day data run. The number of events has been normalised to 9 hours of AmLi neutron calibrations. The blue histogram includes all events that took place in the active LXe whereas the red histogram is only includes those events in the active LXe that passed all standard background cuts. 108

- 6.21 Total reconstructed energy deposition from generated $S1$ and $S2$ signals in the DecayChain simulations in active LXe for events taking place during 60 days of data taking. The number of events has been normalised to 9 hours of AmLi neutron calibrations. All events which took place in the active LXe are included in the blue histogram and only those events in the active LXe which passed the standard background cuts are in the red histogram. 109
- 6.22 $\log_{10}(S2_c)$ vs $S1_c$ for events in active LXe during 60 days of data taking from the DecayChain simulations. The number of events plotted in the figures has been normalised to 9 hours of AmLi neutron calibrations. The blue and red bands are the electron and nuclear recoil bands respectively (solid: mean; dashed: $\pm 1.28\sigma$ contours). The different shaded areas and corresponding dotted lines represent different ROI's; the green is the EFT ROI, the pink is the WIMP PLR ROI and the brown is the WIMP TDR ROI. 111
- 6.23 $\log_{10}(S2_c)$ vs $S1_c$ for events from the DecayChain simulations which were in active LXe during 60 day data run. In the figures the number of events plotted has been normalised to 9 hours of AmLi neutron calibrations. Figure (a) shows all events which survived standard background cuts and Figure (b) displays the same events minus any events generated from ^{125}I decays. The different ROIs are represented by dotted lines in the figure; the green is the EFT ROI, the pink is the WIMP PLR ROI and the brown is the WIMP TDR ROI. The blue and red lines shows the boundary for the electron and nuclear recoil bands respectively (solid: mean; dashed: $\pm 1.28\sigma$ contours). . . 112
- 6.24 Metastable decay schemes taken from NuDat 2.8 [154]. The red text is the decay mode and branching ratio in percent. The green text is the half-life of that energy level and the blue text is the energy of the gamma in keV. 113
- 6.25 The sum of electron vs the sum of photon energies for $^{129\text{m}}\text{Xe}$ decays. The red line denotes the excitation energy for $^{129\text{m}}\text{Xe}$ (236.14 keV). 114
- 6.26 The sum of electron vs the sum of photon energies for $^{131\text{m}}\text{Xe}$ decays. The excitation energy for $^{131\text{m}}\text{Xe}$ (163.93 keV) is indicated by the red line. 114
- 6.27 The sum of electron vs the sum of photon energies for both part of $^{129\text{m}}\text{Xe}$ decay scheme. The red line indicates the energy difference between nuclear states, 196.6 keV and 39.6 keV for the first and second parts of the decay respectively. 115
- 6.28 The individual electron and photon energies for the simulated $^{131\text{m}}\text{Xe}$ decays as compared to a calculation with an accurate atomic model (red crosses) [155]. 116
- 6.29 Total reconstructed energy depositions from generated $S1$ and $S2$ signals where the red line is the minimum reconstructed energy associated with either $^{129\text{m}}\text{Xe}$ or $^{131\text{m}}\text{Xe}$ decays, 210 and 150 keV respectively. 119

- 6.30 Energy deposition in the $^{129\text{m}}\text{Xe}$ simulation for events taking place during a 60 day data run in active LXe. The number of events has been normalised to 2 days of DD neutron calibrations. The blue histogram is all events which took place in the active LXe and the red histogram is only those events in the active LXe which passed the standard background cuts. 122
- 6.31 $S2_c$ vs $S1_c$ for all events in the $^{129\text{m}}\text{Xe}$ simulation. The blue and red lines are the electron and nuclear recoil bands respectively (solid: mean; dashed: $\pm 1.28\sigma$ contours). Note linear scale on the y -axis for $S2_c$ 123
- 6.32 Z vs R for all $^{129\text{m}}\text{Xe}$ PED events after standard background cuts applied except for energy range cuts. 124
- 6.33 Z vs R for all $^{129\text{m}}\text{Xe}$ MSSSI events after standard background cuts applied except for energy range cuts. 124
- 6.34 $\log_{10}(S2_c)$ vs $S1_c$ for all $^{129\text{m}}\text{Xe}$ events in a 60 day data run, no cuts applied. The purple crosses are $^{129\text{m}}\text{Xe}$ MSSSI events with standard background cuts except for energy range cuts. The different ROIs are represented by the shaded areas and corresponding dotted lines in the figure; the brown is the WIMP ROI TDR, the pink is the WIMP ROI PLR and the green is the LUX-like EFT ROI. The blue and red bands are the electron and nuclear recoil bands respectively (solid: mean; dashed: $\pm 1.28\sigma$ contours). 125
- 6.35 Total Monte Carlo truth energy deposition in active LXe for $^{129\text{m}}\text{Xe}$ MSSSI events after standard background cuts applied except ROI. 125
- 6.36 Energy deposition in the $^{131\text{m}}\text{Xe}$ simulation for events taking place during a 60 day data run in active LXe. The number of events has been normalised to 2 days of DD neutron calibrations. The blue histogram is all events in the active LXe and the red histogram is only those events that passed all standard background cuts in the active LXe. 127
- 6.37 $\log_{10}(S2_c)$ vs $S1_c$ for all $^{131\text{m}}\text{Xe}$ events in a 60 day data run, no cuts applied. The purple cross is the only $^{131\text{m}}\text{Xe}$ MSSSI event which passed standard background cuts except energy range cuts. The different ROIs are represented by the shaded areas and corresponding dotted lines in the figure; the brown and the pink are the WIMP ROI TDR and PLR, respectively, and the green is the LUX-like EFT ROI. The blue and red lines show the boundary of the electron and nuclear recoil bands respectively (solid: mean; dashed: $\pm 1.28\sigma$ contours). 128
- 7.1 The combined biased PMT map for the top (Figure (a)) and bottom (Figure (b)) PMT arrays for all background acquisitions. The green and grey represent the biased and unbiased PMTs, respectively. The PMT $x - y$ positions are accurate but their size is not to scale. 132

-
- 7.2 The rate of post-trigger pulses versus pulse area in the BKG-1 (blue) and BKG-2 (orange) background acquisitions using the combined PMT map. The OD and water tank were empty during BKG-1 and filled by the BKG-2 acquisitions. 134
- 7.3 The rate of pulses versus pulse area in the BKG-1 (blue) background acquisitions compared to the BACCARAT background GXe simulations (orange). The simulations were processed with NEST using $g1 = 0.0665$ and $E = 1 \text{ V cm}^{-1}$ 136

List of Tables

2.1	Background estimates in the LZ detector over a 1000 day WIMP search from Monte Carlo simulations of notable sources within the 5.6 tonne fiducial volume. All standard background cuts (defined in Section 2.6) have been applied. A more extensive table can be found in Ref. [60].	34
4.1	Results of the LZap PSquared tests with a single NERSC Cori supercomputer node. KNL and HSW are the two Intel CPU architectures tested, Knights Landing and Haswell respectively. HT indicates that hyper-threading was enabled.	66
5.1	Results from LUXSim cavern wall γ -ray event biasing simulations. Calculations consider energy depositions up to 100 keV and use a 105.4 kg fiducial volume. No ER/NR discrimination cut applied. Errors quoted are standard error.	80
5.2	BACCARAT cavern wall γ -ray event biasing simulation results. Calculations apply no ER/NR discrimination and use a 5.6 tonne fiducial volume. Errors quoted are standard error.	81
6.1	The number of xenon isotope decays simulated in the active LXe with BACCARAT using the DecayChain generator.	97
6.2	For the DecayChain simulations the number of events after different cuts are applied normalised to 2 days of DD neutron calibrations. BKG cuts are the standard background cuts defined earlier in Section 6.2.2. No ER/NR discrimination cut applied. Numbers in brackets are determined using the MC truth energies instead of reconstructed energies. Errors quoted are 90% C.L. intervals (for large statistics standard error and for small statistics from Feldman-Cousins [152]).	102

6.3	For the DecayChain simulations the number of events after various cuts are applied. The numbers of events has been normalised to 9 hours of AmLi neutron calibrations. BKG cuts are the standard background cuts defined earlier in Section 6.2.2. No ER/NR discrimination cut applied. Numbers in brackets are determined using the MC truth energies instead of reconstructed energies. Errors quoted are 90% C.L. intervals (for large statistics standard error and for small statistics from Feldman-Cousins [152]).	110
6.4	The number of events in the $^{129\text{m}}\text{Xe}$ simulation after different cuts are applied. These numbers have been normalised to 2 days of DD neutron calibrations. BKG cuts are the standard background cuts defined earlier in Section 6.2.2. No ER/NR discrimination cut applied. Numbers in brackets are determined using the Monte Carlo truth energies instead of reconstructed energies. Errors quoted are 90% C.L. intervals (for large statistics standard error and for small statistics from Feldman-Cousins [152]).	120
6.5	The number of MSSI events in $^{129\text{m}}\text{Xe}$ simulations after various cuts have been applied. These numbers have been normalised to 2 days of DD neutron calibrations. BKG cuts are the standard background cuts defined earlier in Section 6.2.2. No ER/NR discrimination cut applied. Numbers in brackets are determined using the Monte Carlo truth energies instead of reconstructed energies. Errors quoted are 90% C.L. intervals (for large statistics standard error and for small statistics from Feldman-Cousins [152]).	121
6.6	The number of events in the $^{131\text{m}}\text{Xe}$ simulation after different cuts are applied. These numbers have been normalised to 2 days of DD neutron calibrations. BKG cuts are the standard background cuts defined earlier in Section 6.2.2. No ER/NR discrimination cut applied. Numbers in brackets are determined using the Monte Carlo truth energies instead of reconstructed energies. Errors quoted are 90% C.L. intervals (for large statistics standard error and for small statistics from Feldman-Cousins [152]).	126
7.1	Information about the background acquisition datasets. The DAQ runtime and live time is provided with the number of biased PMTs active during data taking. Also indicated is whether the OD and water tank were filled during those acquisition.	131
7.2	Post-trigger pulse rate for the BKG-1 and BKG-2 acquisitions using the combined PMT map. The OD and water tank were empty in during BKG-1 and filled by the BKG-2 acquisitions.	133
7.3	Pulse rate for the BKG-1 acquisitions and BACCARAT background GXe simulations.	135

Acronyms

API Application Programming Interface.

BAO Baryon Acoustic Oscillations.

BBN Big Bang Nucleosynthesis.

CL Confidence Level.

CLI Command Line Interface.

CMBR Cosmic Microwave Background Radiation.

CP Charge-Parity.

CSD Calibration Source Deployment.

DD Deuterium-Deuterium.

DER Detector Electronic Response.

EFT Effective Field Theory.

ER Electron Recoil.

GUI Graphical User Interface.

GXe Gaseous Xenon.

HSW Haswell.

ICV Inner Cryostat Vessel.

JSE Job Submission Engine.

JSI Job Submission Interface.

KNL Knights Landing.

LEOPARD Lz Exploring Online PAcKage Root Data.

LUX Large Underground Experiment.

LXe Liquid Xenon.

LZ LUX-ZEPLIN.

LZap LZ Analysis Package.

MACHO MAssive Compact Halo Objects.

MC Monte Carlo.

MDC Mock Data Challenge.

MFC Mass Flow Controller.

MOND Modified Newtonian Dynamics.

MSSI Multiple Scatter Single Ionisation.

nEDM Neutron Electric Dipole Moment.

NERSC National Energy Research Scientific Computing Centre.

NEST Noble Element Simulation Technique.

NR Nuclear Recoil.

OCV Outer Cryostat Vessel.

OD Outer Detector.

PBH Primordial Black Holes.

PED Partial Energy Deposition.

PMT Photomultiplier Tube.

PSD Pulse Shape Discrimination.

PTFE Polytetrafluoroethylene.

QCD Quantum Chromodynamics.

RGA Residual Gas Analyser.

ROI Region of Interest.

RQ Reduced Quantities.

SD Spin Dependent.

SI Spin Independent.

SLAC SLAC National Accelerator Laboratory.

SM Standard Model.

SURF Sanford Underground Research Facility.

SUSY Supersymmetry.

TDR Technical Design Report.

TPC Time Projection Chamber.

UGA Universal Gas Analyser.

VUV Vacuum Ultraviolet.

WIMP Weakly Interacting Massive Particle.

Introduction

There is a significant body of evidence on different astrophysical scales for the existence of a mysterious non-luminous substance, called dark matter. The make up of dark matter remains unknown despite the wealth of evidence accrued over many years for this incredibly abundant substance. A promising candidate for dark matter is the newly theorised elementary particle called Weakly Interactive Massive Particle (WIMP). This particle is extremely difficult to detect as it may only interact through the weak and gravitational forces. Direct dark matter experiments search for WIMP interactions with atomic nuclei via the low energy scattering signals produced.

At the Sanford Underground Research Facility (South Dakota, USA) the Large Underground Xenon (LUX) experiment and its successor the LUX-ZEPLIN (LZ) experiment are searching for these WIMP induced scattering signals utilising dual-phase xenon time projection chamber (TPC) technology. Due to the rarity and low energy signals from these WIMP interactions, high sensitivity to these interactions is crucial. In order to obtain the required detection sensitivity understanding and mitigating background events is vital.

The focus of this thesis is on the original work undertaken to characterise and explore a number of important backgrounds for the LUX and LZ experiments. The beginning of the thesis details the evidence for dark matter, potential dark matter particle candidates and numerous experiments searching for WIMP dark matter in Chapter 1. An overview of dual-phase xenon TPC technology along with descriptions of the LUX and LZ experiments follows in Chapter 2. Chapter 3 covers the LZ gas charcoal chromatography system, used to remove problematic noble radioactive impurities (predominantly ^{85}Kr) in xenon, and the sampling system. This is preceded by descriptions of software programs developed for LZ in Chapter 4. In Chapter 5 high statistics simulations of the cavern wall γ -ray background in the LUX and LZ experiments are presented. LZ simulations of activation from neutron calibration sources are outlined and analysed in Chapter 6. Finally, Chapter 7 explores LZ detector commissioning data.

Chapter 1

Dark matter in the Universe

Our understanding of the Universe was challenged in the 1930s when astronomers suggested the existence of a non-luminous matter within our own galaxy and elsewhere. Previously, astronomers had described this matter as “dark” as they thought the matter consisted of dim celestial objects which could not be detected by telescopes. Although at the time many were sceptical, subsequently significant discoveries were published corroborating the importance of this invisible matter, that makes up the majority of matter in our Universe.

As the evidence for dark matter has accumulated over the years the fundamental question still remains unanswered; what is dark matter made of? This chapter highlights the multitude of dark matter evidence, covers the leading particle candidates for dark matter and explores the different experimental search methods used to search for those dark matter particle candidates.

1.1 Evidence for dark matter

1.1.1 Early history

The first key piece of evidence was discovered by Swiss astronomer Fritz Zwicky in 1933. When studying the redshift of different galaxy clusters he noticed a large dispersion in the radial velocities of a number of galaxies within the Coma Cluster [1]. Applying the virial theorem in combination with an estimate for the mass and size of the cluster, Zwicky inferred that the velocity dispersion should be 80 km s^{-1} which was significantly smaller than the average observed velocity dispersion, approximately 1000 km s^{-1} . Given the notable disparity between the two velocities this showed that the Coma Cluster contained substantially more mass than estimated from the luminous matter observed. Zwicky suggested that if his work was correct then dark matter has a much greater density than luminous matter.

Zwicky was not the first to coin the term “dark matter”, his contemporaries (Kapteyn [2], Oort [3] and Jeans [4]) had previously suggested the existence of dark matter within our galaxy from their studies of star dynamics in the local Milky Way. Zwicky’s discovery was met with serious scepticism from the scientific community. It took many years and new astronomical observations to convince many astronomers of the existence and significance of dark matter.

1.1.2 Galaxy rotation curves

Observations by Rubin and Ford in the 1970s played a crucial role in persuading the scientific community that dark matter was a serious unsolved problem in astronomy. In 1970 they produced a groundbreaking paper detailing their Andromeda (M31) galaxy rotation curve observations [5]. They were tracking H II regions orbiting in M31 via the 21 cm emission line. Their observations revealed that at large radii the orbital velocity was constant, contradictory to the previously accepted Keplerian model of galaxy rotation. In the Keplerian model, formed from Newtonian dynamics, the orbital velocity beyond the galactic bulge is given as:

$$v(r) = \sqrt{\frac{GM(r)}{r}} \quad (1.1)$$

where v is the orbital velocity, r is the radius, G is the gravitational constant and $M(r)$ is the mass enclosed within that radius.

The constant orbital velocity could not be explained by the visible matter. It required considering a dark matter spherical halo to match the observations, as highlighted in Figure 1.1. The suggestion of a dark matter halo arose as luminous matter does not provide enough gravitational force required to hold the luminous galaxy together to withstand its high velocities.

An alternative suggestion to explain the constant orbital velocity anomaly was put forward by Mordehai Milgrom in 1983 [7]. Milgrom proposed modifying Newton’s second law in the limit of low acceleration. The idea, known as MOND (Modified Newtonian Dynamics), attempted to explain the flat galaxy rotation curves without the need for dark matter. Although some MOND-like theories have been successful in explaining galactic scale observations, they fall short in explaining galactic cluster scale anomalies such as the “bullet cluster” (discussed in Section 1.1.3). The consensus among the scientific community is that dark matter is the favoured explanation for the flat galaxy rotation curves.

1.1.3 Gravitational lensing

First detected in 1919, gravitational lensing discoveries provide compelling evidence for the existence of dark matter. Gravitational lensing occurs when an object in between a light

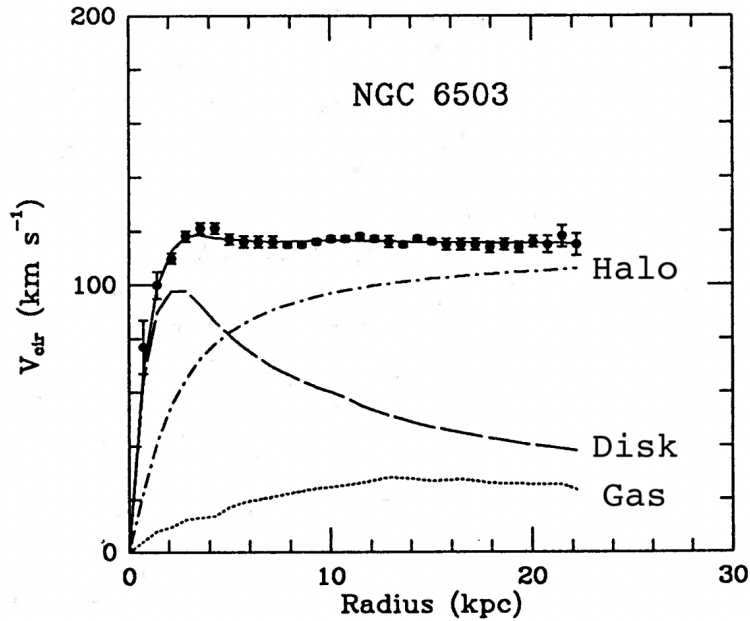


Figure 1.1: NGC 6503 galaxy rotation curve observation (black dots) with dark-halo fit (solid curve). The individual components of the rotation curve are shown; dark halo (dash-dotted line), optical disk (dashed line) and gas (dotted line). Figure from Ref. [6].

source and an observer bends spacetime, changing the path along which light travels as it follows the curvature of spacetime. This results in a distorted image seen by the observer, as seen in Figure 1.2.

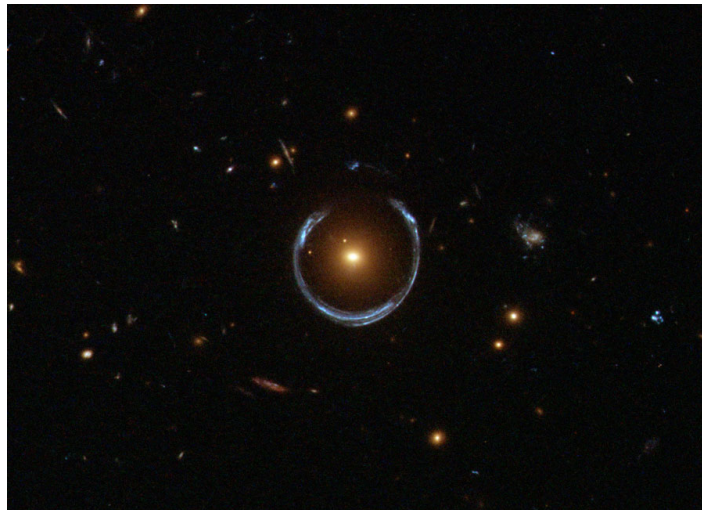


Figure 1.2: An image of a horseshoe Einstein ring taken by the Hubble Space Telescope. The gravity of a luminous red galaxy (in the centre of the picture) has distorted the light from a distant blue galaxy resulting in the background galaxy's horseshoe shape appearance. Image courtesy of ESA/Hubble and NASA [8].

Weymann *et al.* in 1979 provided the first confirmation of gravitational lensing on galactic scales [9]. They were studying what was thought to be twin quasars but the properties of the quasars were practically identical. They proposed it was a double image of the same quasar produced by gravitational lensing, a consequence of Einstein's general theory of relativity. Einstein himself in 1936 suggested that a massive celestial object could deflect the light from a distant source resulting in the appearance of a ring or multiple images [10].

Gravitational lensing can be used to measure the mass profile of the lensing matter, given the distortion of light is directly correlated to the mass of the lensing object [11]. This technique has been used to analyse mass distribution in galaxy clusters in conjunction with X-ray maps of those clusters. The mass profile of a number of galaxy clusters was found to contrast the distribution of baryonic matter observed from the X-ray maps. These discoveries indicate that these galaxy clusters contained significant amounts of dark matter.

This is clearly demonstrated by the famous "bullet cluster" where two galaxy clusters are merging, see Figure 1.3. In 2006, Clowe *et al.* were comparing the weak lensing observed to the X-ray emission from hot gas in the bullet cluster [12]. They noted that the gravitational potential did not trace the distribution of baryons concentrated mainly in the hot gas, observing a significant separation between the gravitational and baryonic centres, seen in Figure 1.4. The difference arises as the dark matter interacts differently than the intergalactic gas. The gas collides and interacts, slowing down the gas much more than the individual galaxies and dark matter. The result is a separation between the gas, which is the dominant baryonic mass component, and main source of the gravitational potential, dark matter.

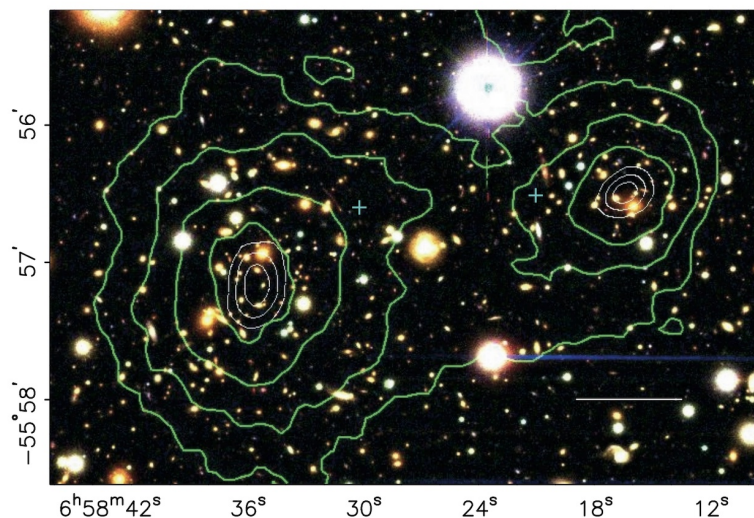


Figure 1.3: Colour image of the bullet cluster with reconstructed lensing signal (green contours), which is proportional to the mass in the system. The blue plus signs represent the centre of mass for the hot gas clouds. Figure from Ref. [12].

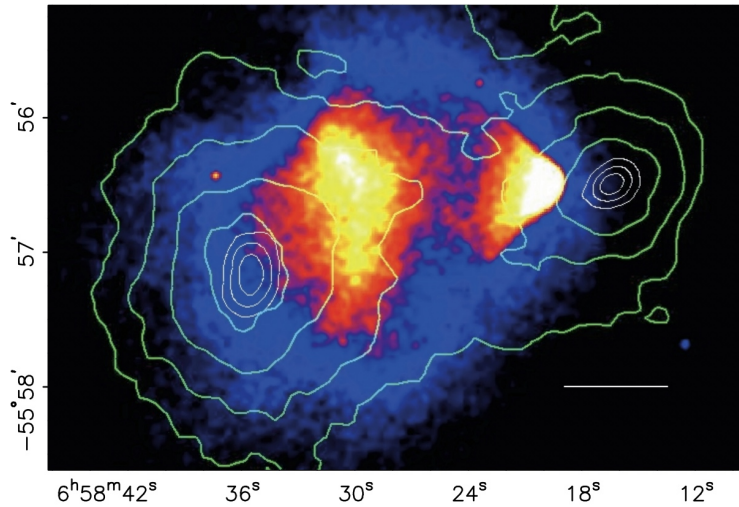


Figure 1.4: Bullet cluster X-ray image overlaid with reconstructed lensing signal (green contours), which is proportional to the mass in the system. This image of the two merging galaxy clusters reveals the gravitational centre is in a different position to the baryonic centre. Figure from Ref. [12].

The bullet cluster observations are difficult to explain with the MOND theory as the weak lensing data would be expected to follow the X-ray maps. It was thought that the substantial evidence for dark matter provided by the bullet cluster would bring an end to the MOND theory; however, MOND-like theories continue to attract attention [13].

1.1.4 Cosmic microwave background radiation

Discoveries and measurements in cosmology also substantiate the existence of dark matter. One of those discoveries came from analysing the cosmic microwave background radiation (CMBR). Predicted in the 1940s and accidentally discovered in 1965 by Penzias and Wilson [14], CMBR is remnant electromagnetic radiation from the early universe.

During the recombination epoch the Universe was expanding and the hot dense hydrogen plasma was cooling. Neutral hydrogen atoms began to form once the temperature had dropped enough and the Universe became transparent as photons were no longer scattered by free electrons. These photons which make up the CMBR fill the Universe today and their wavelengths have increased due to the expansion of space.

The CMBR is a near perfect blackbody spectra with a temperature of 2.7 K. As can be seen in Figure 1.5, the most recent CMBR map from the Planck satellite, the CMBR is very isotropic with fluctuations at one part in 100,000. These anisotropies are a consequence of matter density fluctuations in the early universe, due to conflict between the photon pressure and gravitational force in the photon-baryon plasma at the time.

In the recombination epoch there were oscillations in the density perturbations in the

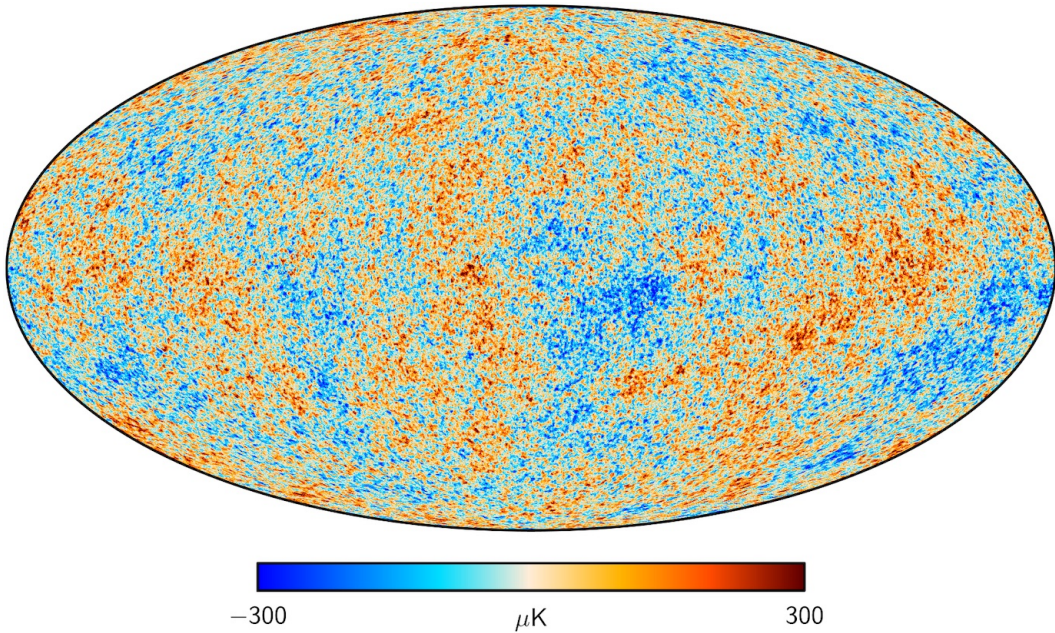


Figure 1.5: The all-sky CMBR temperature map measured by the Planck satellite. It displays the coldest (blue) to the hottest (red) regions in the sky, from $-300 \mu\text{K}$ to $300 \mu\text{K}$. Figure from Ref. [15].

photon-baryon plasma due to the counteracting gravitational attraction and photon pressure. These oscillations, known as baryon acoustic oscillations (BAO), remained active until photon decoupling when the CMBR was released.

Cosmological parameters can be constrained from the BAO peaks in the CMBR power spectrum (visible in Figure 1.6), which is created via arranging the CMBR temperatures anisotropies by their angular size. Parameters can also be constrained from a global fit to the power spectrum using the ΛCDM (lambda cold dark matter) model, the standard model of Big Bang cosmology. The CMBR power spectrum provides information on the flatness of the Universe and relative abundances of matter and energy. There is good agreement between the CMBR power spectrum and the ΛCDM model [16] which is constructed with dark energy and dark matter.

In cosmology it is standard to quantify densities with dimensionless ratios known as density parameters, Ω_x , where x can be various species:

$$\Omega_x = \frac{8\pi G\rho_x}{3H^2} = \frac{\rho_x}{\rho_c} \quad (1.2)$$

where G is the gravitational constant, ρ_x is the species density, H is the Hubble parameter and ρ_c is the critical density for which the spatial geometry of the universe is flat .

Using this formalism, results from the most recent Planck satellite data, combining BAO peaks and ΛCDM fitting, constrain the baryon density, $\Omega_b = 0.04897 \pm 0.00031$, and the

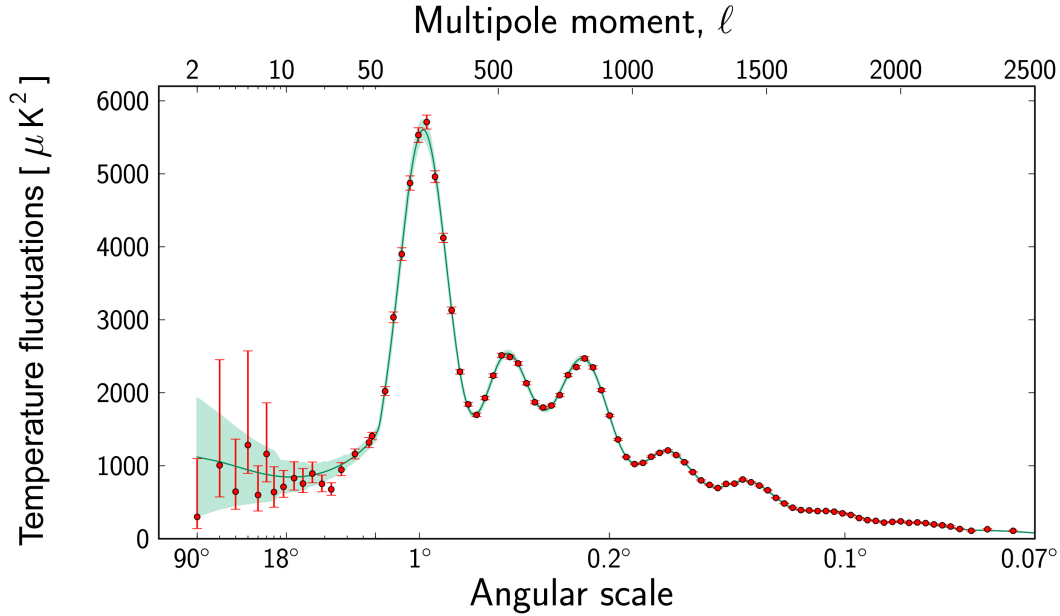


Figure 1.6: Temperature fluctuations in the CMBR at different angular scales on the sky detected by the Planck Satellite. The angular scales can be represented either with angular degrees (lower horizontal axis) or via multipole moment l (upper horizontal axis). The red dots are the Planck measurements with the green curve representing the Λ CDM model best fit to the data. Figure from Ref. [16].

matter density, $\Omega_m = 0.3111 \pm 0.0056$ (Hubble constant $H_0 = 67.66 \pm 0.42 \text{ km s}^{-1} \text{ Mpc}^{-1}$) [15]. The difference between the two densities reveals that there is “missing” matter which is non-baryonic (dark) matter and there is significantly more dark matter than baryonic matter in the Universe.

1.1.5 Big Bang nucleosynthesis

The baryon density can also be estimated from Big Bang nucleosynthesis (BBN), the production of light elements during the early universe. The relative abundance of light elements is sensitive to the baryon-to-photon ratio. Limits on the baryon density can be determined by observing the effect the baryon density has on light element relative abundances and comparing it to observations of the abundances now.

Using the deuterium to hydrogen ratio the baryon density has been constrained to $\Omega_b = 0.04946 \pm 0.00074$ (assuming $H_0 = 67.66 \text{ km s}^{-1} \text{ Mpc}^{-1}$) [17]. This results concurs with the CMBR baryon density limits, implying that only $\sim 5\%$ of the Universe is visible.

1.1.6 Large scale structure

Dark matter underpins cluster evolution, without it computer simulations cannot match the observed structure of the Universe. A number of research collaborations have run large cosmological N-body simulations of galaxy formation, approximating the motion of galaxy groups interacting gravitationally [18–20]. In these simulations they observe that fine structures, such as galaxies and galaxy clusters, are only produced in the presence of cold dark matter, which is non-relativistic and non-baryonic. These simulations support the validity of the Λ CDM model.

1.2 Dark matter candidates

Although there is a wealth of evidence for dark matter, the contents of that matter still remains mysterious. The properties of dark matter revealed from observations can be used to constrain potential dark matter candidates. This section will summarise the main properties of dark matter inferred from observations and discuss some of the favoured dark matter candidates.

1.2.1 Dark matter properties

From dark matter observations, potential dark matter candidates should be [21]:

- Non-baryonic.
- Neutral electric charge.
- Non-relativistic (at the time of decoupling from matter).
- Weakly interacting.
- Stable (or longer lifetime than the age of the Universe).

Astrophysical observations have shown that dark matter has particle like behaviour, therefore it seems plausible for dark matter to be composed of particles. Alternatively some have suggested dark matter is made up of celestial objects, such as primordial black holes (PBH) or massive compact halo objects (MACHO).

PBHs are a type of black hole which formed in the early universe with masses far below the stellar mass. Although originally PBHs were suggested to make up all dark matter, astrophysical observations have strongly challenged this notion placing stringent constraints on their abundance at different mass scales [22, 23]. The predicted abundance of MACHOs is also too small to make up a significant fraction of the total dark matter abundance [24].

Many years ago it was suggested that neutrinos could be a dark matter candidate, however, they were subsequently ruled out as they were relativistic at the time of decoupling and they are not massive or abundant enough [25]. Nonetheless, neutrino research did pave the way for another weakly interacting particle that became the leading candidate for dark matter, which is explored in the following subsection.

To solve problem of dark matter requires looking beyond the Standard Model (SM) of particle physics. Many of the well-motivated dark matter candidates proposed also resolve other problems in modern physics such as the sterile neutrino [26]. This potential candidate for dark matter is a newly theorised additional neutrino species which would only interact with matter gravitationally and can be produced from SM neutrino oscillations. If sterile neutrinos have masses $> \text{keV}$ they could account for all the dark matter in the Universe [27]. The neutrino oscillation experiment MicroBooNE [28] has not yet ruled out sterile neutrinos as the explanation for the excess electron-neutrino events observed in LSND [29] and MiniBooNE [30]. The parameter space of sterile neutrinos has been limited by null observations from X-ray telescopes [31].

1.2.2 Weakly interacting massive particles

The current leading dark matter candidate is the weakly interacting massive particle (WIMP), a new elementary particle. WIMPs satisfy the dark matter properties determined by astrophysical observations; they are non-baryonic, neutral, non-relativistic at the time of decoupling, interact via gravity and any other force that is as weak or weaker than the weak nuclear force and stable. Their mass is predicted in the GeV-TeV range [32].

In the hot and dense environment of the early universe all particles were in thermal equilibrium. Dark matter particles and antiparticles were annihilating into and forming from lighter particles, balancing each other out. As the Universe expanded the temperature and density dropped leading to WIMPs decoupling from the thermal plasma, freezing their abundance. This occurred when the density became too low for WIMP annihilation to proceed efficiently.

Altering the WIMP annihilation cross-section changes the evolution of the WIMP density as a function of the Universe temperature as shown in Figure 1.7. To match the WIMP relic density to the current observed dark matter density, Ω_{dm} , requires an annihilation cross-section of the order of magnitude that is expected for weak force interactions. Curiously enough new particles with these properties are predicted by supersymmetry (SUSY), an extension to the SM. This coincidence connecting particle physics and cosmology was so remarkable at the time it was coined the “WIMP miracle”.

SUSY theory postulates every particle in the SM has a “super-partner” with the same quantum numbers but different spin by a half. This leads to bosons having a fermion-like partner and fermions having a boson-like partner. As no supersymmetric particles

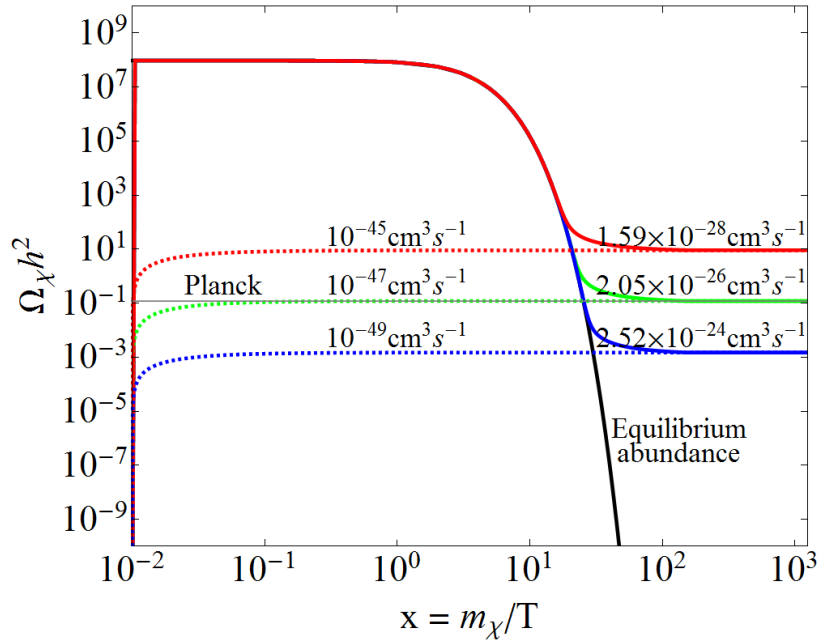


Figure 1.7: Illustration of a thermal relic freeze out in the early universe. The cosmological abundance ($\Omega_\chi h^2$) evolves as a function of $x = m_\chi/T$ where m_χ is WIMP mass and T is universe temperature. The temperature is implicitly a function of time. The numbers specified above the lines are the WIMP annihilation cross-sections averaged over WIMP velocity distribution. The grey line labelled Planck is the observed dark matter density. Figure from Ref. [33].

have ever been observed yet, the common assumption is that symmetry is broken and the predicted mass of the supersymmetric particles is significantly larger than SM particles. SUSY also solves the hierarchy problem in the SM and provides a mechanism for unifying the fundamental forces [34].

Unfortunately many SUSY models have been heavily constrained by the lack of evidence in direct searches underground and at collider experiments [35, 36]. However, other theories also predict valid WIMP dark matter candidates, such as Universal Extra Dimensions [37] and “WIMPzillas”, the massive non-thermal dark matter [38].

There are a number of different detection methods for this promising dark matter candidate; direct detection, indirect detection and collider experiments. Experiments searching for WIMP dark matter are explored in Section 1.3.

1.2.3 Axions

The axion is another strongly motivated dark matter candidate which is beyond the SM. It was originally proposed in 1977 by Peccei and Quinn to solve the strong charge-parity (CP) conservation anomaly in Quantum Chromodynamics (QCD) [39, 40].

It was previously thought that CP symmetry was always conserved, however, in 1964 research on neutral kaon decays revealed the first observations of CP violation [41]. CP violation plays an important role in the matter-antimatter asymmetry in the Universe. Without this violation after the Big Bang matter and antimatter would behave the same and total cancellation would occur resulting in a sea of radiation with no matter.

In theory CP violation is permitted within QCD, however it has not been observed. If CP violation occurs from QCD interactions this would induce a non-negligible electric dipole moment for the neutron (nEDM). Nevertheless, current experimental limits on nEDM are vanishingly small [42]. This suggests an abnormal conservation of CP symmetry within QCD, which is known as the “strong CP problem”.

The solution to this problem, proposed by Peccei and Quinn [43, 44], was to introduce a new global symmetry called “PQ symmetry” which cancels out the CP violating term in the QCD Lagrangian. The spontaneous symmetry breaking of this new scalar field gives rise to a new particle which was named the axion.

This new particle is a potential dark matter candidate, although, there were concerns about its predicted sub eV mass which suggests that axions are hot dark matter if they were produced as a thermal relic. Nevertheless, axions were never in thermal equilibrium with the rest of the Universe due to their extremely weak coupling so are cold dark matter candidates [45].

Through the inverse Primakoff effect, experiments can detect axions through their coupling to photons [46, 47]. In a strong magnetic field axions can convert to photons which creates the possibility for axion observations.

1.3 WIMP dark matter searches

There are a number of dark matter candidates and several ways to search for these candidates, this section will discuss three different types of WIMP dark matter searches:

- **Direct detection:** Aims to observe low-energy scattering signals caused by WIMP interactions with SM particles. To measure these signals necessitates ultra-low background detectors with high sensitivity located inside a mountain or deep underground.
- **Indirect detection:** Searches for the products of WIMP self-annihilation in outer space. The main targets are regions of high dark matter density such as the Galactic Centre, the core of the Sun and the centre of the Earth.
- **Collider searches:** Look for WIMP dark matter potentially produced by collisions in a collider. As WIMPs are expected to escape the collider undetected, this large amount of missing energy and momentum in the detector provides a signature.

Each approach has its own strengths and challenges, nonetheless, they are complementary to each other. Together they explore a greater range of the WIMP parameter space and provide a cross-check if WIMPs are discovered. The main focus of this section will be direct detection as this is the approach used in the LUX and LZ experiments.

1.3.1 Direct detection

1.3.1.1 WIMP-nucleus interactions

If the particle interpretation of dark matter is correct then a significant number of dark matter particles must be passing through the Earth each second ($\sim 10^5 \text{ cm}^{-2} \text{ s}^{-1}$ for WIMPs with 100 GeV mass). However, WIMP dark matter is extremely difficult to detect as it may only interact through the weak and gravitational force. Direct searches aim to measure the low-energy nuclear recoils (NR) produced by WIMP-nucleus collisions as WIMPs pass through the detector medium.

WIMPs typically scatter elastically off atomic nuclei. Although the NR energy from this collision is small it might be detectable. The differential event rate (R) as a function of NR energy (E_R) for a WIMP of mass m_χ scattering off a nucleus of mass m_A (typically expressed in units of events/kg/day/keV) takes the form [48]:

$$\frac{dR}{dE_R} = \frac{\rho_0}{m_A m_\chi} \int_{v_{min}}^{\infty} v f(v) \frac{d\sigma_A}{dE_R} dv \quad (1.3)$$

where ρ_0 is the local dark matter density, $f(v)$ is the WIMP velocity distribution and $\frac{d\sigma_A}{dE_R}$ is the differential cross-section for WIMP-nucleus elastic scattering. Formally the upper integration limit is infinite, however, the local escape velocity (v_{esc}) is the maximum velocity for WIMPs which are gravitationally bound to the Milky Way. The lower integration limit is the minimum WIMP velocity (v_{min}) that can induce a recoil of energy E_R , which is given by:

$$v_{min} = \sqrt{\frac{m_A E_R}{2\mu_A^2}} \quad (1.4)$$

where $\mu_A = m_\chi m_A / (m_\chi + m_A)$ is the WIMP-nucleus reduced mass.

The WIMP particles which induce these low-energy NRs are from the Milky Way's dark matter halo. The halo's density and velocity distribution governs the WIMP-nucleus scattering event rate, as seen in Eq. 1.3, thus these astrophysical parameters are of significant interest to the dark matter community. Canonical assumptions about these features are made by the dark matter community in order to simplify comparison between experimental results.

Although the estimations of the local dark matter density have fluctuated over the past 30 years and still have large uncertainties [49], it is assumed to be $\rho_0 = 0.3 \text{ GeV/cm}^3$ to

ensure experimental results can be compared. As the velocity distribution cannot be measured exactly, it is modelled from the astrophysical observations discussed in Section 1.1. The commonly used Standard Halo Model assumes an isotropic isothermal sphere of dark matter particles with a Gaussian velocity distribution (typically known as Maxwellian). The velocity distribution takes the form [48]:

$$f(\mathbf{v}) = \frac{1}{\sqrt{2\pi}\sigma} \exp\left(-\frac{|\mathbf{v}|^2}{2\sigma^2}\right) \quad (1.5)$$

where \mathbf{v} is WIMP velocity and the velocity dispersion σ is related to local circular velocity (v_0) by $\sigma = \sqrt{3/2}v_0$. For the local circular velocity (v_0) and local escape velocity (v_{esc}) the canonically assumed values are 220 km s^{-1} [50] and 544 km s^{-1} [51] respectively.

The differential cross-section for WIMP-nucleus elastic scattering in Eq. 1.3 ($\frac{d\sigma_A}{dE_R}$) can be expressed as a combination of spin-independent (SI) and spin-dependent (SD) contributions. In the SI interaction the WIMP couples to the mass of the nucleus, whereas for the SD interaction the WIMP couples to the spin of the nucleus [52]. To allow for comparison of different experimental results, direct detection dark matter experiments have generally focused on these two types of WIMP-nucleus interactions.

The WIMP-nucleus cross-section (σ_A^{SI}) for SI scatters is typically converted to a WIMP-nucleon cross-section (σ_n^{SI}) in order for comparison as experiments employ different target nuclei. If WIMP interactions with neutrons and protons are equivalent then the SI WIMP-nucleus cross-section is given by [52]:

$$\sigma_A^{SI} = \left(\frac{\mu_A}{\mu_n}\right)^2 A^2 \sigma_n^{SI} \quad (1.6)$$

where μ_n is the WIMP-nucleon reduced mass and A is the atomic mass of the target nucleus. As Eq. 1.6 reveals using a heavier target nuclei results in a higher event rate due to the A^2 factor. This is part of the motivation behind using heavy targets in direct searches to increase sensitivity to SI scattering.

Conversely, the SD WIMP-nucleus cross-section (σ_A^{SD}) does not contain this A^2 factor. For SD scatters the WIMP-nucleus cross-section is given by [52]:

$$\sigma_A^{SD} = \frac{3}{4} \lambda_s^2 J(J+1) \left(\frac{\mu_A}{\mu_n}\right)^2 \sigma_n^{SD} \quad (1.7)$$

where J is the total nuclear spin and λ_s is the spin constant unique to the target isotope. It is important to note that only isotopes with a net nuclear spin are sensitive to these interactions. To achieve the best sensitivity experiments use either odd-proton or odd-neutron nuclei, as nucleon pairs cancel out nuclear spin contributions. This thesis will focus on the SI contributions.

The nuclear form factor (F^2), which describes the dependence on momentum transfer (q), is also part of the differential cross-section, $\frac{d\sigma_A}{dE_R}$. In the SI case the Lewin-Smith [53] parameterisation of the Helm form factor is adopted, it is written as:

$$F_{SI}^2(E_R) = \left(\frac{3j_1(qR_1)}{qR_1} \right)^2 \exp(-q^2s^2) \quad (1.8)$$

where j_1 is the spherical Bessel function of the first kind, R_1 is an effective nuclear radius and s is the nuclear skin thickness. Figure 1.8b displays the SI nuclear form factor for a number of different target elements. There is a resonance that appears in the SI nuclear form factor spectra due to loss of scattering coherence, occurring when the de Broglie wavelength of the incoming WIMP is a similar size to the target nucleus.

As discussed previously using a heavier target substantially increase the event rate, as clearly displayed in Figure 1.8a. However, the trade-off is a lower event rate at higher NR energies than the lighter nuclei due to the rate suppression from the nuclear form factor. This can prove challenging for detector thresholds.

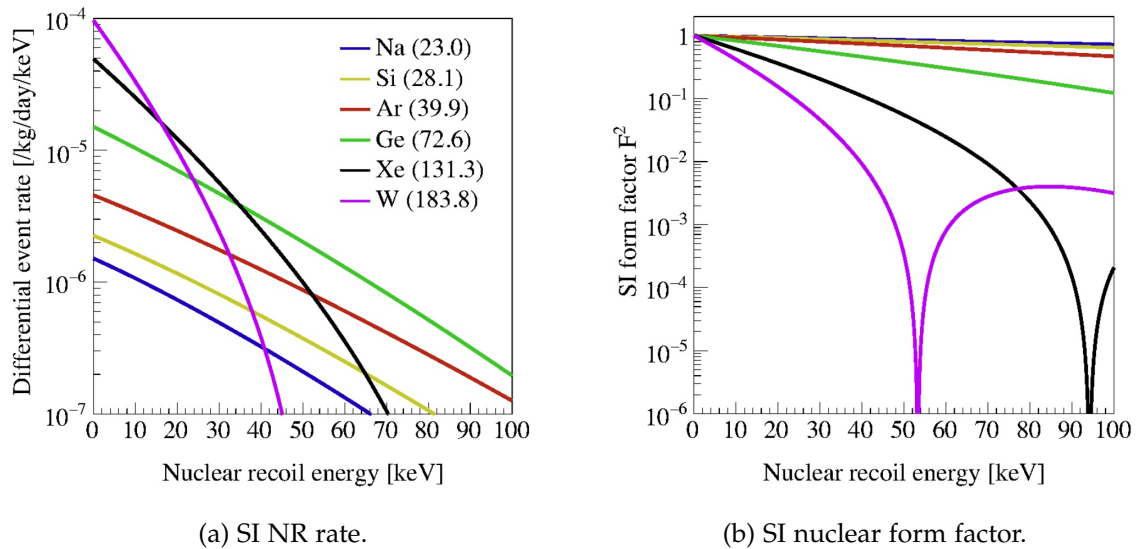


Figure 1.8: The SI NR rate (a) and SI nuclear form factor (b) as a function of NR energy for several target elements. The WIMP mass and WIMP-nucleon cross-section are assumed to be 100 GeV and 10^{-45} cm^2 respectively. Figures from Ref. [54].

1.3.1.2 Detection techniques

Although a high WIMP flux on Earth is predicted, the WIMP-nucleus scattering rate is very low. Experimental data has excluded SI WIMP-nucleon cross-sections of $\sigma_n \gtrsim 4 \times 10^{-47} \text{ cm}^2$ for $m_\chi \sim 30 \text{ GeV}$ which corresponds to less than 3 events/tonne/year [55]. As with any

rare event search optimising the signal to background ratio is of paramount importance to achieve the high sensitivity required.

To achieve the required sensitivity to the SI WIMP-nucleon cross-section direct search experiments tend to employ a detector medium with a large total mass and high atomic mass. However, experiments searching for sub-GeV WIMPs have to also consider the low energy detection threshold of a material.

The energy transferred to a target nucleus from particle interactions can manifest in three different channels: ionisation, excitation and heat. Direct detection experiments probe either one or a combination of these signals to determine the rate of WIMP-nucleus interactions. The choice of target medium consists of many factors such as cost, scalability and the ability to capture the different signal channels.

Taking into consideration how few WIMP-nucleus scatters are expected to occur in a detector, background mitigation plays a crucial role in direct detection. These backgrounds, covered in Chapter 2 in more detail, can come from cosmic rays, radioactivity and detector instrument noise. There are various ways in which direct searches suppress the different backgrounds, for example, experiments operate in ultra-low background environments (inside a mountain or deep underground with detector shielding) and select radio-pure materials to construct the detector.

A key background mitigation strategy arises from the different type of signals observed in the detector. A large proportion of the background events produce electron recoils (ER) in the detector. As ER and NR distribute their energy depositions differently between the three signal channels, direct searches exploit this property allowing them to discriminate between the background ERs and the expected NRs from WIMP-nucleus scatters.

Over the past decade the leading SI WIMP search technology was liquid xenon (LXe) time projection chambers (TPC), see Figure 1.9b for illustration. This technology captures the primary scintillation light from particle interactions and the ionisation signal from electroluminescence, induced by ionisation electrons extracted into the gas phase and accelerated there. Above a 10 GeV WIMP mass these experiments provide the best SI WIMP sensitivity. Further, they can also perform SD WIMP searches as xenon has a non negligible fraction of stable odd isotopes (^{129}Xe & ^{131}Xe) and axion searches are also possible.

Pioneered in 2006 by ZEPLIN-II [57] and then XENON10 [58], this technology has led the pursuit for WIMPs in direct searches. In 2013 the LUX experiment set world-leading limits for the SI WIMP-nucleon cross-section [59]. Currently a few collaborations (LZ [60], XENON [55] & PandaX [61]) employing this technology are racing to achieve greater WIMP sensitivity to potentially discover WIMPs. This thesis is focused on the LXe TPC technology used in the LUX and LZ experiments, explored in more detail in Chapter 2.

Argon can be used instead of xenon in a dual-phase TPC such as employed by the DarkSide-50 experiment [62]. A major advantage of using argon is that it is cheaper than

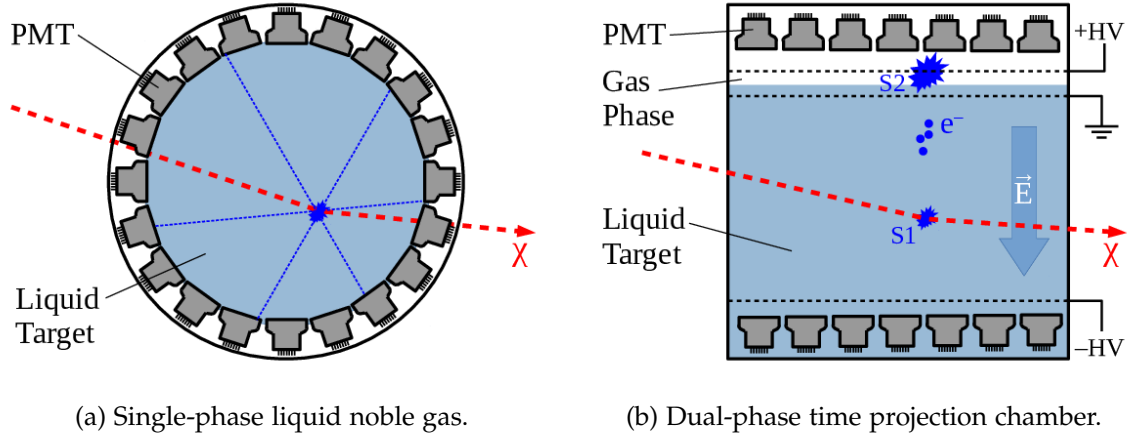


Figure 1.9: Illustrations of liquid noble gas direct detection experiments. The dark matter particle χ (represented by the red arrow) will scatter on a nucleus depositing energy. The single-phase detector (a) can only capture the primary scintillation signal, whereas the dual-phase detector (b) measures two signals as it can also capture the ionisation signal as the charges drift into the gas to produce a secondary scintillation signal. Figures from Ref. [56].

xenon, however, natural atmospheric argon contains a radioactive isotope, ^{39}Ar , that is a background for WIMP searches. ^{39}Ar can be difficult to mitigate, therefore, some argon dark matter experiments use low-radioactive underground argon as the detector medium but this is more expensive. Experiments also try to identify and remove ^{39}Ar events during data analysis [63].

There are single-phase liquid noble gas dark matter experiments (e.g. XMASS [64] & DEAP-3600 [65]), see Figure 1.9a for illustration. Unfortunately, their SI WIMP-nucleon cross-section sensitivities have been greatly exceeded by their experimental dual-phase contemporaries and as such single-phase detectors have broadly been phased out.

Leading the search for low mass WIMPs are solid-state cryogenic detectors, see Figure 1.10 for illustration. These experiments can probe WIMP masses down to $\sim 0.2\text{ GeV}$ as they have very low energy thresholds and light target nuclei [21]. They couple phonon sensors to a crystal target (e.g. Ge) to detect the heat signal produced by a particle interactions in the crystal. This is typically combined with either an ionisation or scintillation readout channel to provide ER/NR discrimination. However, some experiments forfeit ER/NR discrimination to probe lower WIMP masses via exploiting the Neganov-Trofimov-Luke effect [66, 67] which enhances the phonon signal at the cost of the ionisation signal.

The EDELWEISS [68] and SuperCDMS [69] collaborations operate experiments which use high purity Ge crystals with a charge readout channel to search for sub-GeV WIMPs, while the CRESST collaboration has taken a different approaching using CaWO_4 crystals with a scintillation readout channel [70]. Both approaches have pushed sub-GeV WIMP

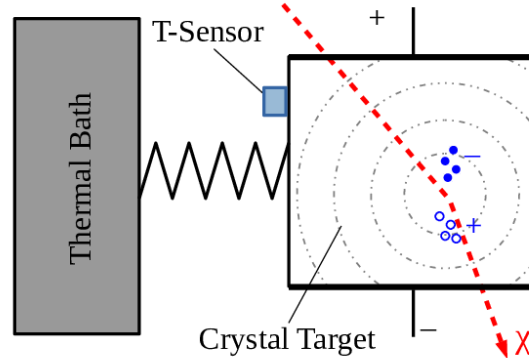


Figure 1.10: Illustration of cryogenic solid-state direct detection experiments. Energy will be deposited as the dark matter particle χ (represented by the red arrow) scatters on a nucleus. The cryogenic crystal detector captures the heat signal via detecting phonons and either the ionisation signal or the scintillation signal. Figure from Ref. [56].

direct detection searches to greater levels of sensitivity.

1.3.1.3 Status of the field

At time of writing, the most stringent limits on the SI WIMP-nucleon cross-section come from LXe TPC experiments. Different types of experiments are optimised for different WIMP mass ranges, as can be seen in the SI WIMP landscape in Figure 1.11. As expected at sub-GeV WIMP masses the solid-state cryogenic experiments produce the leading limits.

The only reported positive detection of dark matter has come from the DAMA experiment from observations of an annual modulating signal [71]. However, this results is incompatible with the many null observations from direct detection experiments. Additionally results from COSINE-100 [72] and ANAIS-112 [73], which search for an annually modulating signal with the same crystal scintillator technology as DAMA, are consistent with a null observation.

LXe TPCs from the LZ [60] and XENON [55] collaborations are currently operational and aiming to achieve SI WIMP-nucleon cross-section limits close to the coherent neutrino-nucleus scattering limit. Known as the “neutrino floor”, it is created by neutrino fluxes from the Sun and atmosphere and the uncertainties of these fluxes. These neutrinos produce low-energy NRs via coherent scattering that are indistinguishable from WIMPs signals. These neutrinos pose a significant challenge to the next generation of detectors, such as the DARWIN experiment [74] which aims to have the sensitivity to reach the neutrino floor. LXe TPCs are also applying novel ways to reach lower energy thresholds to improve sensitivity in the sub-GeV WIMP mass range.

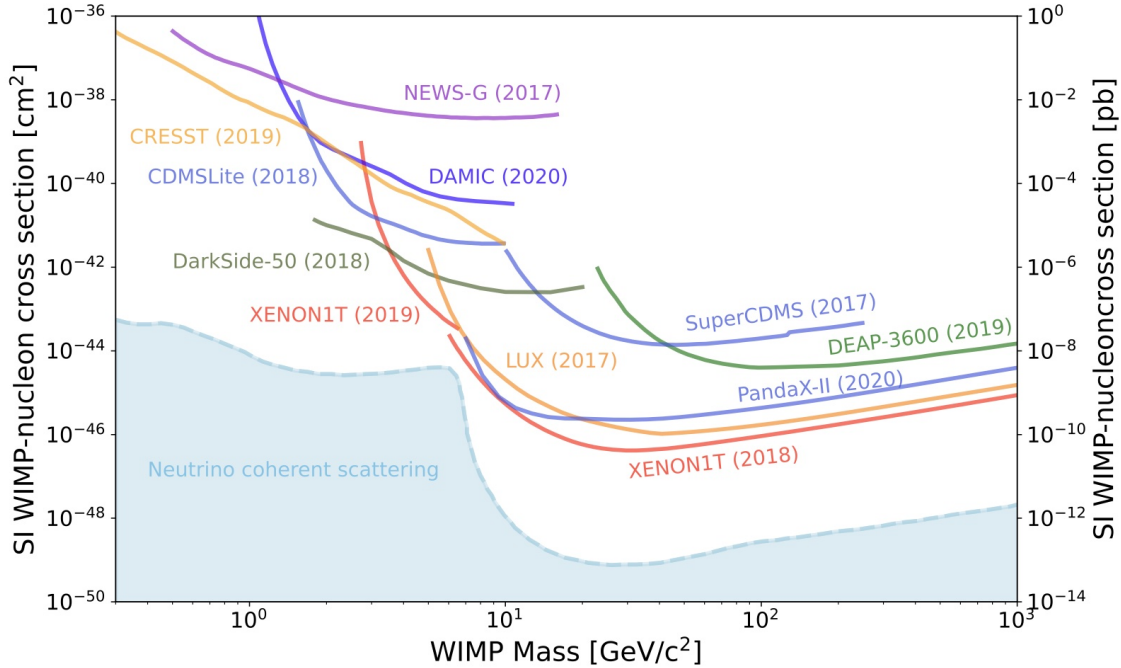


Figure 1.11: Exclusion limits on the SI WIMP-nucleon cross-section as a function of WIMP mass as of the end of 2020. This figure contains the 90% CL limit from a number of experiments for SI WIMP-nucleon cross-sections for a range of WIMP masses. The neutrino floor is indicated by the light blue dashed line represents the region where coherent scattering of neutrinos becomes a significant background. Figure from Ref. [21].

1.3.2 Indirect detection

Indirect dark matter detection is another way to search for WIMPs. This approach explores locations of high dark matter density for the products of WIMP self-annihilation. This is achieved by scanning for an excesses of particles and radiation created from these interactions.

As many of the astrophysical backgrounds in indirect searches are not well understood, these searches aim to optimise signal over background. As part of the optimisation indirect searches look for these excesses in places of high dark matter density such as the Galactic Centre, the core of the Sun and the centre of the Earth [75].

WIMP annihilations will produce a variety of different particles and radiation, however, only the gamma-rays, neutrinos, positrons and antiprotons can be discriminated from the large background of cosmic rays. There are both space and ground-based detectors searching for these gamma rays, as well as water/ice based experiments looking for neutrinos. Space-based detectors are also searching for positrons and antiprotons.

As the gamma rays from these WIMP annihilations interact in our atmosphere a cascade of secondary particle would be produced. This shower leads to Cherenkov radiation which

could be observed by ground-based Cherenkov telescopes (such as HESS [76]). In space, AMS-02 on the International Space Station [77] and satellites such as the Fermi Gamma-Ray Telescope (known as “Fermi”) search for gamma rays as well as positrons and antiprotons [78].

Although there has been a claim of gamma ray excess from the Galactic Centre the discussions are ongoing due to the large uncertainties in the astrophysical backgrounds [75]. Data from the satellite Fermi Telescope has provided one of the strongest limits on the WIMP annihilation cross-section, constraining the thermally-averaged annihilation cross-section $\langle\sigma_{ann}v\rangle < 3 \times 10^{-26} \text{ cm}^3 \text{ s}^{-1}$ for WIMPs below 100 GeV [79].

Neutrino experiments such as Super-Kamiokande [80], IceCube [81] and ANTARES [82] have been searching for an excess of high-energy neutrinos. These experiments instrument a large volume of water or ice to observe the Cherenkov radiation in the detector medium produced by the products of neutrino interactions. To date there has been no substantial neutrino excess observed, however, these experiments have provided constraints on the WIMP self-annihilation cross-section to neutrinos, see Figure 1.12.

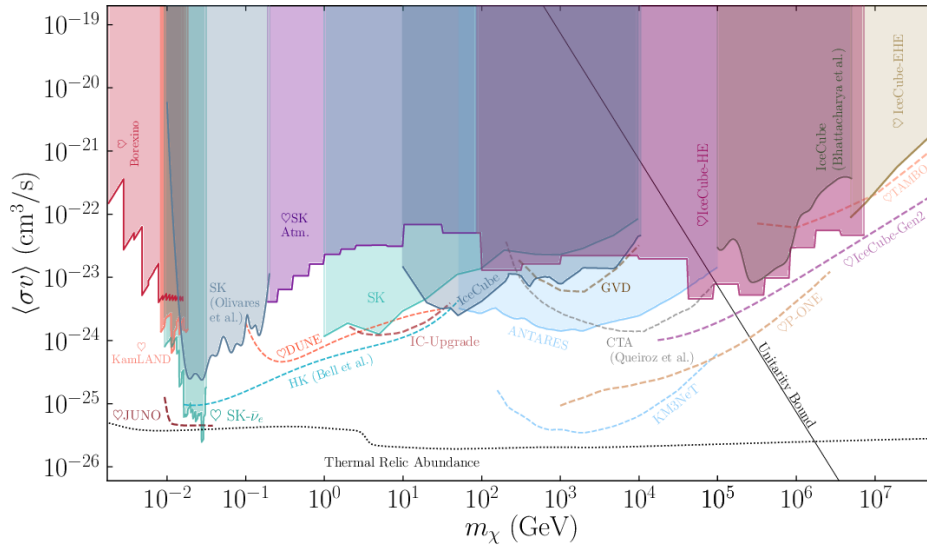


Figure 1.12: Exclusion limits and sensitivities on the dark matter self-annihilation cross-section to neutrinos from indirect detection experiments. This figure contains 90% CL limits (solid line) and projected sensitivities (dashed lines) up to masses of 10^8 GeV. Figure from Ref. [83].

Positrons and antiprotons are also probed to search for WIMP dark matter. Several experiments have detected an unexplained excess of high-energy positrons in the interstellar medium, the most recently AMS-02 [77]. If this excess is attributed to WIMP annihilation, this leads to a WIMP annihilation cross-section higher than previous constrained by other dark matter experiments. However, it is likely that the positron excess originated from a nearby pulsar [75].

1.3.3 Collider searches

In high energy collisions observed in colliders there is a possibility that WIMPs are produced, which escape without interacting, resulting in a significant amount of missing energy. Collider WIMP searches look for this missing transverse energy in collision events.

Both the ATLAS [84] and CMS [85] collaborations have carried out numerous searches for WIMP signatures with the Large Hadron Collider, the largest and highest-energy particle collider, operating proton-proton collisions at a centre of mass energy of 13 TeV. Currently no WIMP signal or evidence for SUSY has been observed [86]. Nonetheless, these searches have provided limits on masses, couplings and cross-sections, see Figure 1.13 for example ATLAS exclusion limits. It is not straightforward to compare constraints between collider and direct detection observations as collider limits are model-dependent. Although colliders alone cannot prove that a newly discovered particle is dark matter, they play an important role in the understanding WIMP-SM particle interactions.

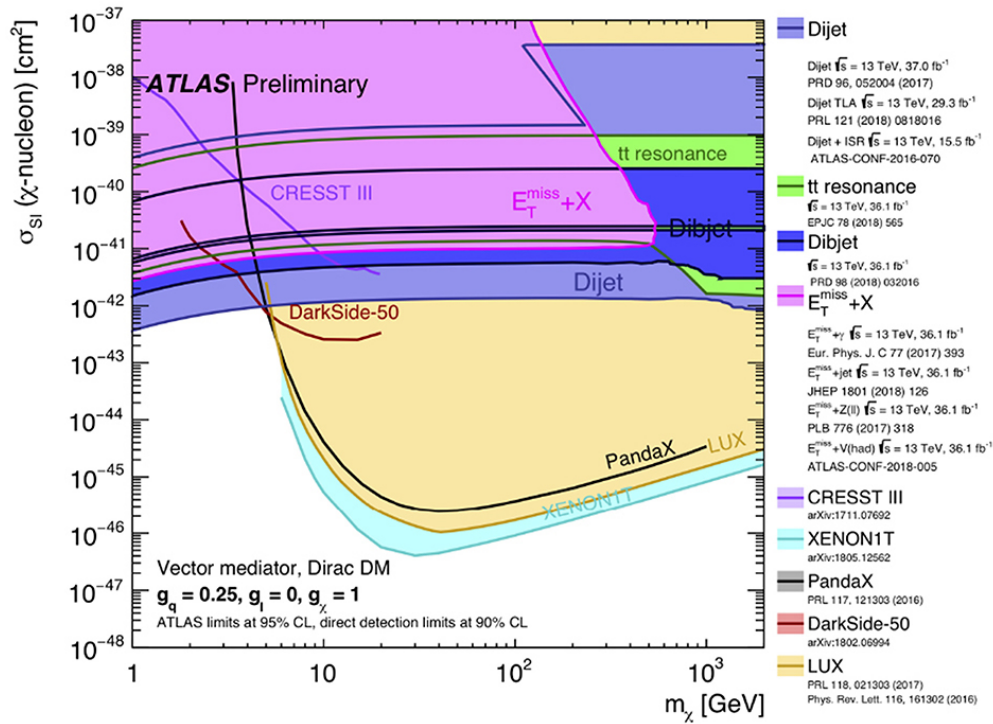


Figure 1.13: Comparing SI WIMP-nucleon cross-section constraints from direct detection experiments to the inferred limits from ATLAS results in the context of the vector leptophobic model. The limits shown are 95% CL for ATLAS and 90% CL for direct detection experiments and the shaded areas are excluded. Figure from Ref. [84].

1.4 Summary

As highlighted in this Chapter, there is a plethora of evidence for the existence of dark matter as well as a number of well motivated particle dark matter candidates. Many experiments are employing a variety of different techniques to search for these candidates hoping to provide strong evidence of a dark matter particle.

This thesis focuses on the LUX and LZ experiments, LXe TPC direct detection searches. An overview of these experiments will be covered in Chapter 2. The other chapters will concentrate on original work undertaken with the LUX and LZ experiments.

Chapter 2

The LUX and LZ experiments

For many years dual-phase xenon time projection chambers (TPC) have produced the most stringent limits for the SI WIMP-nucleon cross-section. The Large Underground Xenon (LUX) and LUX-ZEPLIN (LZ) experiments employ liquid xenon (LXe) TPC technology along with a variety of background suppression strategies to search for scattering signals produced by WIMP interactions with atomic nuclei. In this chapter the technology of dual-phase xenon TPCs is covered along with an overview of the LUX and LZ experiments.

2.1 Particle interactions in liquid xenon

2.1.1 Xenon properties

LXe possesses many strong qualities which make it a very good choice as the detector medium for WIMP direct searches. As mentioned in Chapter 1 using a heavier target nuclei greatly increases the sensitivity to SI WIMP-nucleon scattering as a result of the A^2 factor in the cross-section. A xenon target provides a high event rate at low nuclear recoil (NR) energies whilst maintaining a reasonable event rate at higher energies, see Figure 1.8a for SI scattering NR rate for numerous target elements. Moreover, xenon contains neutron-odd isotopes ^{129}Xe and ^{131}Xe with considerable natural isotopic abundance that are sensitive to SD WIMP interactions.

The self-shielding property of LXe provides a major advantage for rare event searches. Due to the high density of xenon in the liquid phase (2.88 g cm^{-3}) MeV neutrons and gamma rays can only travel a few centimetres before scattering multiple times, and subsequently be rejected, as their interaction lengths are much smaller than the LZ detector [87]. This high stopping power in combination with the ability to reconstruct interaction sites in three dimensions with high precision in data analysis provides an ultra low background shielded fiducial region in the centre of the active medium. Additionally scaling up the LXe medium can be incredibly beneficial as only a few centimetres of non-fiducial region

are required for self-shielding. There is a substantial increase in the percentage of fiducial mass between LUX and LZ, where the fiducial mass is $\sim 40\%$ and $\sim 80\%$ of the active mass within the TPC for LUX and LZ respectively [87].

As xenon is chemically inert, electronegative impurities can be easily removed and detector materials will not corrode. Xenon also contains no long-lived radioactive isotopes with problematic decays, and there should be no cosmogenic activation products remaining in the xenon after a few months of underground storage due to their short lifetimes.

In the liquid phase xenon, like other noble elements, has excellent scintillation and ionisation yields as well as being transparent to its own scintillation. Large detectors can be constructed with LXe whilst not degrading the scintillation and ionisation signals due to the large scintillation photon absorption length and high xenon purity.

2.1.2 Xenon microphysics

This section provides an overview of xenon microphysics, the process by which xenon atoms produce observable signals from scattering. For all noble elements this process is similar with only the lifetimes and energies differing. The discussion in this subsection largely follows Ref. [88].

Particles interacting in LXe can scatter off a nucleus or an atomic electron resulting in either NRs or electron recoils (ER) respectively. The large majority of background events produce ER whereas WIMPs are expected to scatter off the nucleus. The recoiling nucleus or electron interacts with other atoms nearby depositing its kinetic energy resulting in the production of scintillation photons, ionisation electrons and phonons. The fraction of recoil energy in each of the three processes is different for ER and NR. NRs dissipate a considerable fraction of the recoil energy via phonons due to atomic motion. In contrast, the energy lost through phonons in ERs is negligible with a large fraction lost through ionisation. The difference between the fraction of energy lost via ionisation and scintillation provides a unique signature for ERs and NRs enabling discrimination between the two.

LXe detectors only capture the scintillation and ionisation signals produced as a result of particle interaction energy depositions, an overview of the production of ionisation, scintillation and heat from energy depositions in LXe is shown in Figure 2.1. As phonons are not captured only the mechanisms for scintillation and ionisation will be explored.

Scintillation light can be produced as a result of both excited and ionised atoms. A ER or NR can directly excite a xenon atom producing an excitation (Xe^*). This excitation can bond with another xenon atom to form an excimer (Xe_2^{*v}), electronically and vibrationally excited xenon molecule. A vacuum-ultraviolet (VUV) photon (centered around 178 nm [90]) is emitted as the excimer relaxes vibrationally and dissociates into two xenon atoms.

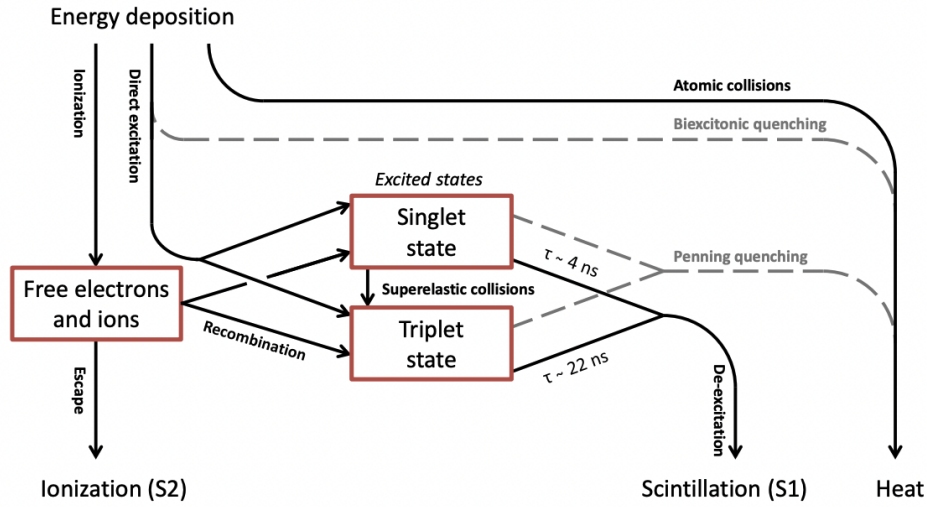
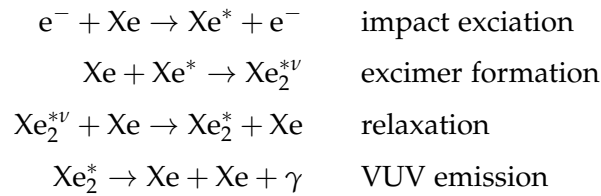
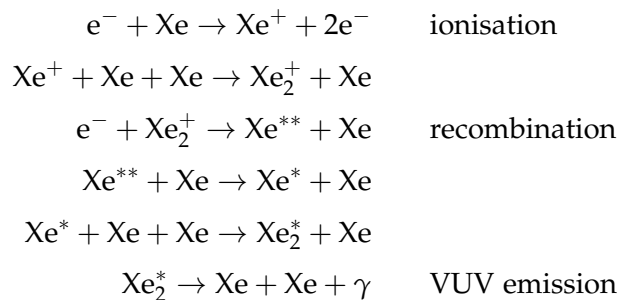


Figure 2.1: Diagram showing the different processes by which an energy deposition in LXe results in ionisation, scintillation and heat. ERs dissipate recoil energy mostly through ionisation whereas the heat process is dominant for NRs. Figure from Ref. [89].

This process follows the subsequent steps (shown here with an electron):



Similarly ionised xenon atoms can also produce VUV photons via recombination. Nearby xenon atoms combine with an ionised atom (Xe^+) to form a molecular ion (Xe_2^+). An electron recombines with the molecular ion to produce a doubly-excited xenon atom (Xe^{**}). This atom relaxes quickly to the ground state via Xe^* and emits a VUV photon. The presence of an electric field, the recoil energy and the interaction type determine the number of recombination events which take place. The recombination process follows these successive steps:



The excimer which produces the VUV photons has two decay times. There are two possible transitions to the ground state from the two lowest electronic excited states of the excimer: the singlet and triplet state. There is slight variation in decay time measurements for the singlet and triplet in LXe. A recent study measured the times to be 3.27 ns and 23.97 ns for the singlet and triplet states respectively [91]. As the populations of the singlet and triplet states are dependent on the type of interaction the VUV photon pulse shape differs for ERs and NRs. In LXe pulse shape discrimination (PSD) is challenging due to the small difference between decay times. However, in liquid argon PSD is widely used to provide ER/NR discrimination as there is a substantial difference ($\sim 1 \mu\text{s}$) in the excimer excited state decay times [92].

The ionisation signal produced during particle interactions in LXe can be captured via electroluminescence. The ionised electrons produced during these interactions can be drifted away with an electric field in order to avoid recombination. Electronegative impurities (such as water vapour and oxygen) in the LXe absorb the ionised electrons, which is why experiments constantly purify the LXe. These electrons are extracted from liquid into gas, however, a stronger electric field is required in the extraction region. Accelerated by the strong electric field the extracted electrons excite gaseous xenon atoms which ultimately produce VUV scintillation photons.

2.2 Dual-phase xenon time projection chambers

2.2.1 Concept

As already discussed LXe is a very good choice for WIMP direct searches as the detector medium. Dual-phase xenon TPCs search for WIMP interactions with xenon nuclei. The detector consists of a large volume of ultra-pure liquid xenon with a small xenon gas region above. The xenon volume is placed in a strong electric field and instrumented by photosensors (e.g. photomultiplier tubes (PMT)). Typically experiments use an array of PMTs above and below the active xenon region. An example of a particle interaction in a xenon dual-phase TPC is displayed in Figure 2.2.

Particle interactions in the LXe produce a prompt scintillation light (S_1) and ionised electrons. The ionised electrons drift towards the gas phase due to an electric field and when they reach the liquid-gas boundary a stronger electric field extracts them into the gas phase and accelerates them. Once in the gas phase the electrons produce secondary scintillation light (S_2) via electroluminescence. The photosensors detected these VUV scintillation photons.

As mentioned earlier ERs and NRs have a different ionisation-excitation ratio which enables them to be discriminated using these scintillation signals, explored more in Section 2.2.3. These signals are also used to reconstruct the recoil energy depositions in the LXe,

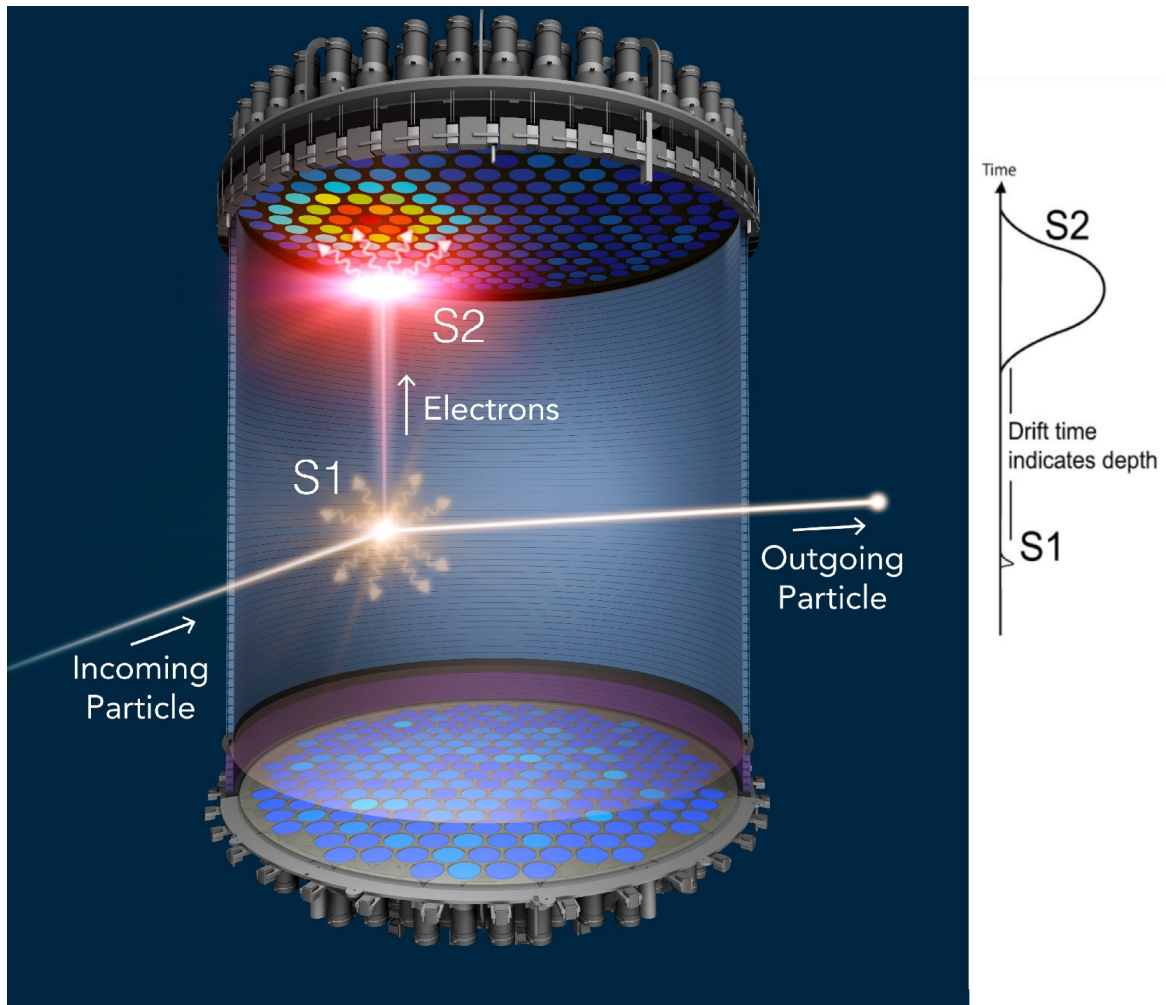


Figure 2.2: Illustration of a particle interaction in a xenon dual-phase TPC. An example of the S1 and S2 signals detected by PMTs is on the right. Figure from Ref. [87].

discussed in more detail in Section 2.2.2. Furthermore, this technology can identify and reject event with multiple scatters which cause more than one S2 signal.

Event positions can also be reconstructed with the information provided by the S1 and S2 signals. The time delay between the S1 and S2 signal provides the z (or vertical) position of an event, as can be seen in Figure 2.2. The photon hit pattern detected by the top array of photosensors is used to locate the xy (or horizontal) position of an event.

2.2.2 Light and charge yields

The number of extracted electrons (n_e) and VUV photons emitted (n_γ) produce by a particle interaction in LXe can be expressed as the initial number of excitations (N_{ex}) and ions (N_{ion})

prior to recombination:

$$\begin{aligned} n_\gamma &= N_{ex} + rN_{ion} \\ n_e &= (1 - r)N_{ion} \end{aligned} \quad (2.1)$$

Where r is the recombination probability. These observed quanta of light and charge are directly related to the energy deposited during the particle interaction. This total energy for an ER can be expressed as:

$$E_{ER} = W(n_e + n_\gamma) \quad (2.2)$$

where W is the average energy required to produce either an exciton or ion (determined experimentally to be 13.7 ± 0.02 eV in LXe [93]). The recoil energy expression for NRs is similar, however, it requires an additional factor due to the significant energy lost via atomic motion:

$$E_{NR} = \frac{W}{\mathcal{L}}(n_e + n_\gamma) \quad (2.3)$$

where \mathcal{L} is the energy dependent quenching factor. This factor originally theorised by Lindhard [94] represents the recoil energy fraction not transferred to atomic motion. In order to differentiate E_{ER} and E_{NR} they are typically expressed in units of keV_{ee} and keV_{nr} respectively. Unless stated otherwise keV references throughout the thesis refer to keV_{ee}.

As mentioned previously dual-phase xenon TPCs capture scintillation and ionisation via electroluminescence produced by particle interactions. The resulting S1 and S2 signals, measured in units of photons detected (phd), can be expressed in terms of the number of electrons and VUV photons:

$$\begin{aligned} S1 &= g_1 n_\gamma \\ S2 &= n_e g_2 \end{aligned} \quad (2.4)$$

where g_1 and g_2 are the gains from primary and secondary scintillation channels respectively. The g_1 gain represents the light collection efficiency in the liquid region and the g_2 gain is a combination of factors; light collection efficiency within the gas region, electroluminescence gain and electron extraction efficiency.

These scintillation pulse areas in conjunction with the detector gains can be used to reconstruct the recoil energy deposited by combining Eq. 2.4 with Eq. 2.2 for ER:

$$E_{ER} = W \left(\frac{S1}{g_1} + \frac{S2}{g_2} \right) \quad (2.5)$$

And similarly Eq. 2.3 for NR:

$$E_{NR} = \frac{W}{\mathcal{L}} \left(\frac{S1}{g_1} + \frac{S2}{g_2} \right) \quad (2.6)$$

2.2.3 ER/NR discrimination

As outlined earlier the ratio between ionisation and excitation differs for ER and NR providing a unique signature which enables discrimination. Discriminating between ER and NR is a key background strategy as a substantial proportion of background events produce ERs. Experimental measurements calculate the ratio N_{ex}/N_{ions} to be 0.06 and ~ 1 for ERs [95] and NRs [96] respectively. This contrast is observed in the ratio of $S2/S1$ signal sizes for the different interaction types. In $S2/S1$ vs $S1$ space two distinct bands form for ER and NR events, visible in Figure 2.3. Once these bands have been located for a detector, through calibrations, events within the ER band can be rejected.

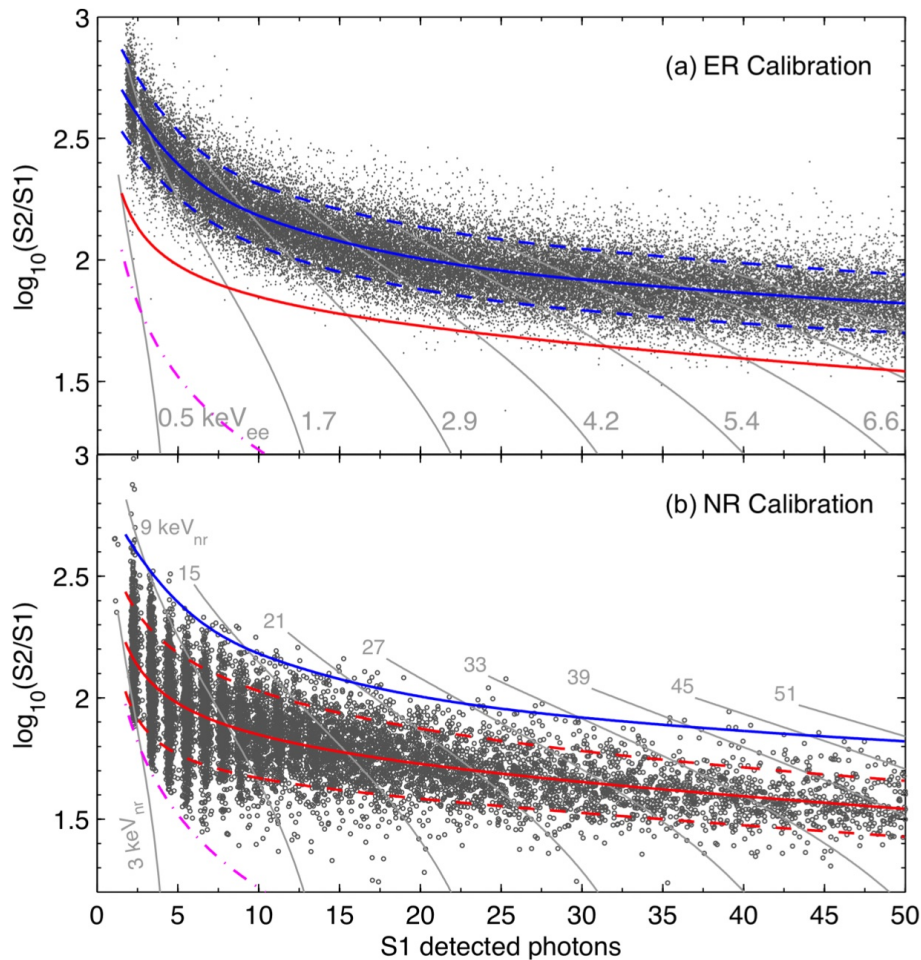


Figure 2.3: $\log_{10}(S2/S1)$ vs $S1$ from LUX calibration data. The red and blue lines represent the ER and NR bands respectively. The median of the band is the solid line with the dashed line indicating 80% band width. Beta decays from a dispersed tritium source calibrate the LUX ER band shown in the top panel (a). Elastic neutron scattering from a deuterium-deuterium pulsed neutron source populates the LUX NR band displayed in the bottom panel (b). The grey lines are energy deposition contours and the dashed-dotted magenta lines display the location of the minimum $S2$ cut. Figure from Ref. [87].

2.3 The LUX experiment

2.3.1 Overview

The LUX [97] experiment was a dual-phase xenon TPC operational between 2012 and 2016 with the main science goal of searching for WIMPs. The detector was located in the Davis cavern 4850 ft underground at the Sanford Underground Research Facility (SURF), South Dakota, USA.

The TPC (see Figure 2.4) is a dodecagonal prism with a diameter of 47 cm and a height of 48 cm (cathode-to-gate). The 250 kg of active LXe (~ 100 kg fiducial mass) within the TPC is instrumented with 122 low background Hamamatsu R8778 2" PMTs. These PMTs are divided evenly in two PMT arrays located above and below the active region in the gas and liquid respectively. In order to improve the VUV scintillation light collection efficiency the TPC walls were constructed with polytetrafluoroethylene (PTFE) panels. The TPC is housed within an inner cryostat vessel (ICV) that is situated inside an outer cryostat vessel (OCV), both vessels were assembled from low background titanium. The space between the ICV and OCV provided thermal insulation as it was held under vacuum. The cathode (anode) grid was positioned 5 cm above (below) the bottom (top) array PMT windows. The xenon liquid phase surface is located 5 mm above (below) the gate (anode) grid.

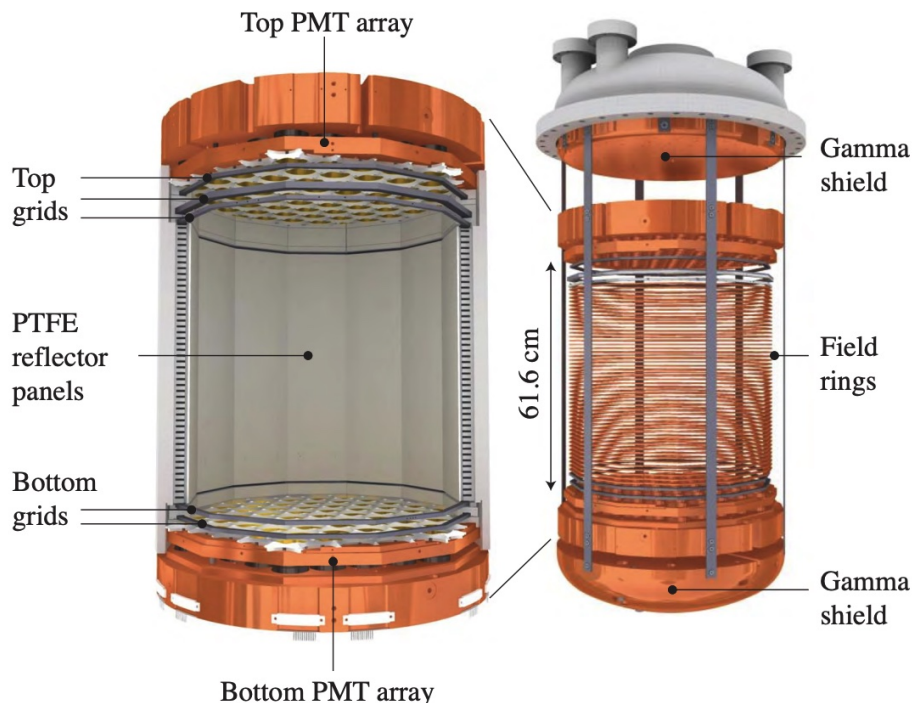


Figure 2.4: 3D rendering of the LUX TPC. On the left is a cutaway of the TPC and on the right is the TPC connected to the top flange of the ICV. Figure from Ref. [97].

2.3.2 Background suppression methods

To optimise the signal to background ratio the LUX experiment employed a variety of background reduction methods. One such strategy was to purify the LXe prior to filling the detector via gas charcoal chromatography in order to substantially reduced beta emitting noble radioactive impurities (^{85}Kr & ^{39}Ar) [98]. For more information on gas charcoal chromatography see Chapter 3.

Another background suppression strategy was to shield the detector from external gamma rays and neutrons. These are produced by radioactive decays and atmospheric muon interactions in the surrounding Davis cavern rock. The detector was placed inside a cylindrical water tank with a height of 592.8 cm and diameter of 762 cm to reduce the flux of gamma rays and neutrons inside the TPC. An inverted steel pyramid, constructed from 20 tonnes of low-radioactivity steel plates, was placed below the water tank to provide extra shielding. In addition, copper disks, shown in Figure 2.4, that were attached to the top and bottom of the ICV also contributed to the shielding of the external gamma rays. This strategy considerably reduced the external backgrounds in the TPC to a sub-dominant level for the WIMP search [99]. Chapter 5 contains more information about simulations undertaken to characterise the cavern wall γ -background in the LUX and LZ detectors.

Furthermore, operating the detector deep underground provided significant attenuation of the atmospheric muon flux ($\sim 3 \times 10^6$ reduction relative to the surface [87]). The water tank was also instrumented with 20 10" PMTs to detect Cherenkov radiation produced by atmospheric muons. This enabled muon events which produced a coincident signal in the TPC and water tank to be rejected.

2.3.3 Results

The LUX experiment undertook two extensive WIMP search data collection runs; Run3 (WS2013) lasting 95 days and Run4 (WS2014-2016) spanning 332 days. Although no evidence of WIMP NRs was detected LUX was able to set a world-leading exclusion limit for the SI WIMP-nucleon cross-section in 2016. By combining both WIMP search run data LUX determined the exclusion limit to be $1.1 \times 10^{-46} \text{ cm}^2$ for $m_\chi \sim 50 \text{ GeV}$.

2.4 The LZ experiment

2.4.1 Overview

The LZ [100] experiment formed from two previous collaborations, LUX and ZEPLIN which employed xenon dual-phase TPC technology, and other institutions searching for WIMPs. The aim of the LZ experiment was to significantly increase their sensitivity to WIMP dark matter by improving many aspects of the previous technology used. The LZ

detector is much larger than its predecessors and operates inside the LUX water tank above the inverted steel pyramid in the Davis cavern at SURF.

The design and operation of LZ is similar to LUX but incorporates a variety of upgrades to key detector subsystems [101]. The LZ TPC, shown in Figure 2.5, has a substantially large target mass than LUX; 7 tonnes of active LXe and 5.6 tonnes within the fiducial volume. The cylindrical TPC, constructed with PTFE panels, has a diameter of 145.6 cm and a height of 145.6 cm (cathode-to-gate). The active region is instrumented with 493 low background Hamamatsu R11410-22 3" PMTs split such that 241 PMTs are in the bottom PMT array and 253 in the top. Ultra-pure titanium has been used to manufacture the OCV and ICV which compose the vacuum insulated cryostat. This houses the TPC enabling the LXe inside to remain at 175 K. The LZ detector contains two active veto detectors (explained subsequently); xenon skin and outer detector (OD). These anti-coincidence systems enhance the background rejection within the TPC. LZ projects that a 1000 day WIMP search with the detector would exclude at 90% CL SI WIMP-nucleon cross-sections above $1.6 \times 10^{-48} \text{ cm}^2$ for $m_\chi \sim 40 \text{ GeV}$ [60].

2.4.2 Active veto detectors

The space between the ICV and the outer wall of the TPC, referred to as the xenon skin, is also filled with LXe. The region is optically isolated from the TPC and instrumented with PMTs (18 2" PMTs below the bottom PMT array and 113 1" PMTs looking at the sides). The xenon skin active veto system is able to reject gamma ray and neutron events within the TPC if a coincidence signal is also detected in this region.

The other LZ active veto detector is the OD, composed of acrylic vessels surrounding the OCV. These acrylic vessels are filled with gadolinium loaded liquid scintillator and monitored with 120 8" PMTs in the water tank. This system can tag problematic neutrons as they enter or exit the TPC. The liquid scintillator (linear alkylbenzene) in the OD can thermalise neutrons and is doped with gadolinium to increase the probability of neutron capture, as gadolinium has a very high neutron capture cross-section. Amongst stable nuclei ^{157}Gd ($\sim 15\%$ natural abundance) has the highest neutron capture cross-section at 240 kb [102]. The OD PMTs are also used to detect Cherenkov radiation in water to reject muon events.

The combination of the OD and xenon skin active veto detectors provides a powerful background rejection system. It is expected that WIMPs will only scatter once in the detector, therefore, any neutrons or gamma rays which interact in the TPC and any veto detector can be rejected as background.

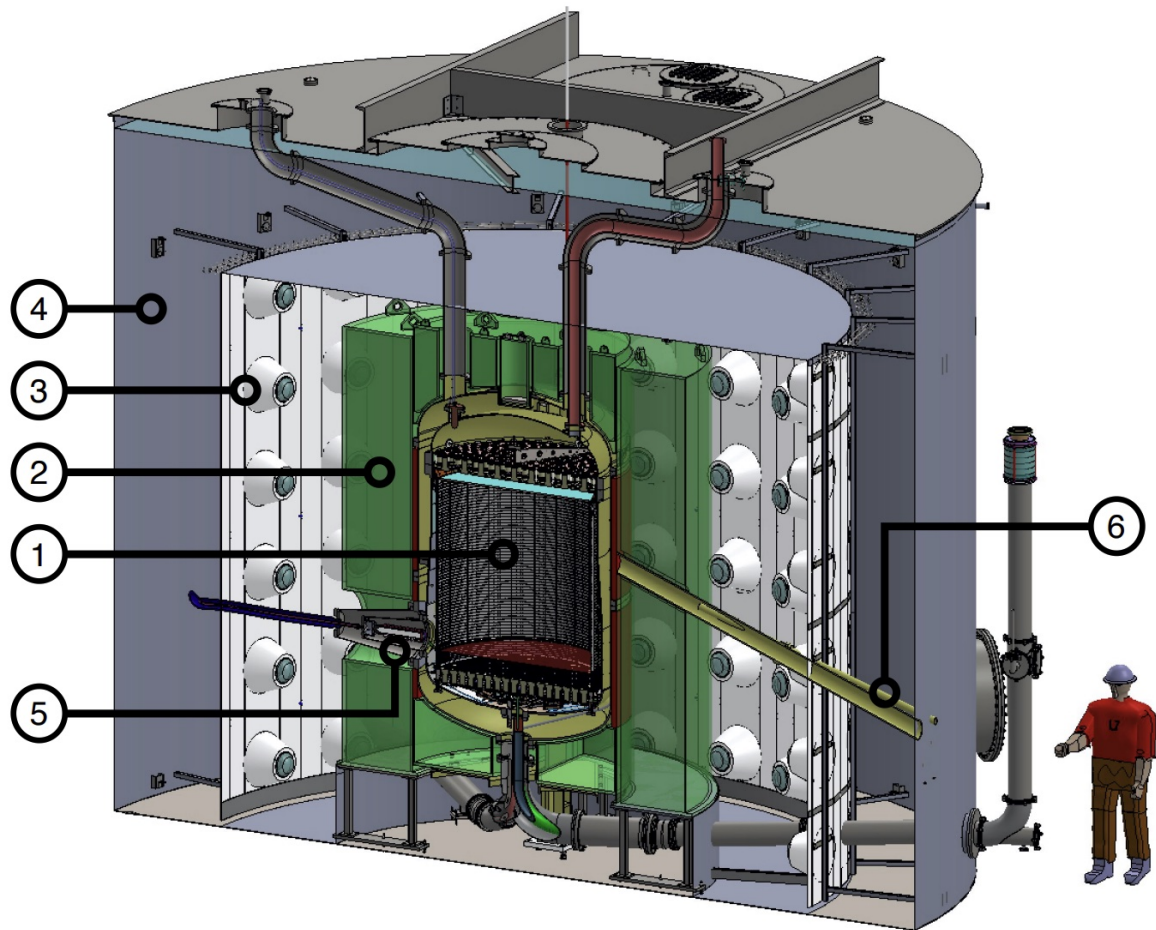


Figure 2.5: 3D rendering of major LZ detector subsystems. (1) LXe TPC, (2) acrylic vessels filled with liquid scintillator comprising the OD, (3) OD PMTs, (4) water tank, (5) high voltage cathode connection, (6) neutron calibration conduit. Inverted steel pyramid under water tank not shown. Figure from Ref. [101].

2.4.3 Significant background sources

2.4.3.1 Overview

For LZ to achieve the desired high sensitivity careful consideration of the detector backgrounds is required. A comprehensive effort has taken place to characterise and mitigate significant background sources [60]. The expected backgrounds in a 1000 day WIMP search from a variety of significant sources is summarised in Table 2.1. Figure 2.6 displays the predicted background energy spectra within the 5.6 tonne fiducial region. After applying all standard background cuts, ER discrimination (assumed to be 99.5% based on LUX measurements and extrapolation to LZ) and a 50% NR acceptance the total expected number of background events in a 1000 day WIMP search in the fiducial volume is 6.18 [60]. The LZ detector backgrounds can be separated into 5 categories; detector components, surface

contamination, xenon contaminants, laboratory & cosmogenics and physics. These will be explored in more detail subsequently.

Table 2.1: Background estimates in the LZ detector over a 1000 day WIMP search from Monte Carlo simulations of notable sources within the 5.6 tonne fiducial volume. All standard background cuts (defined in Section 2.6) have been applied. A more extensive table can be found in Ref. [60].

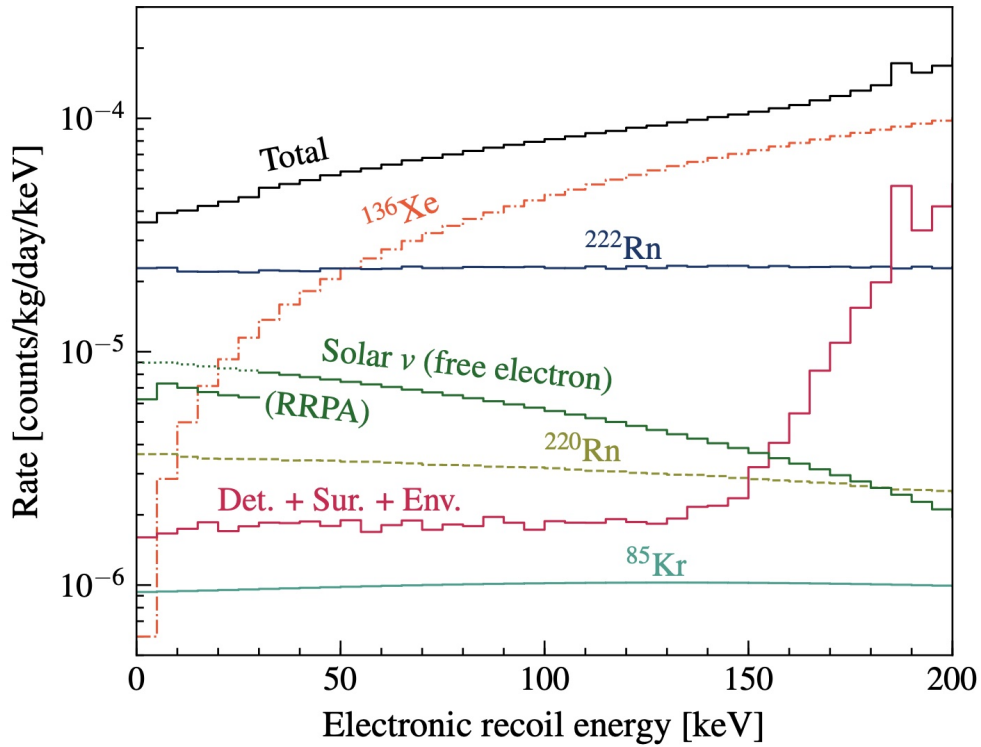
Background source categories	ER counts	NR counts
Detector components	9	0.07
Surface contamination	40	0.39
Xenon contaminants	819	0
Laboratory & cosmogenic	5	0.06
Physics	258	0.51
Total	1131	1.03
Total (with 99.5% ER discrimination & 50% NR efficiency)	5.66	0.52
Sum of ER & NR counts	6.18	

2.4.3.2 Detector components

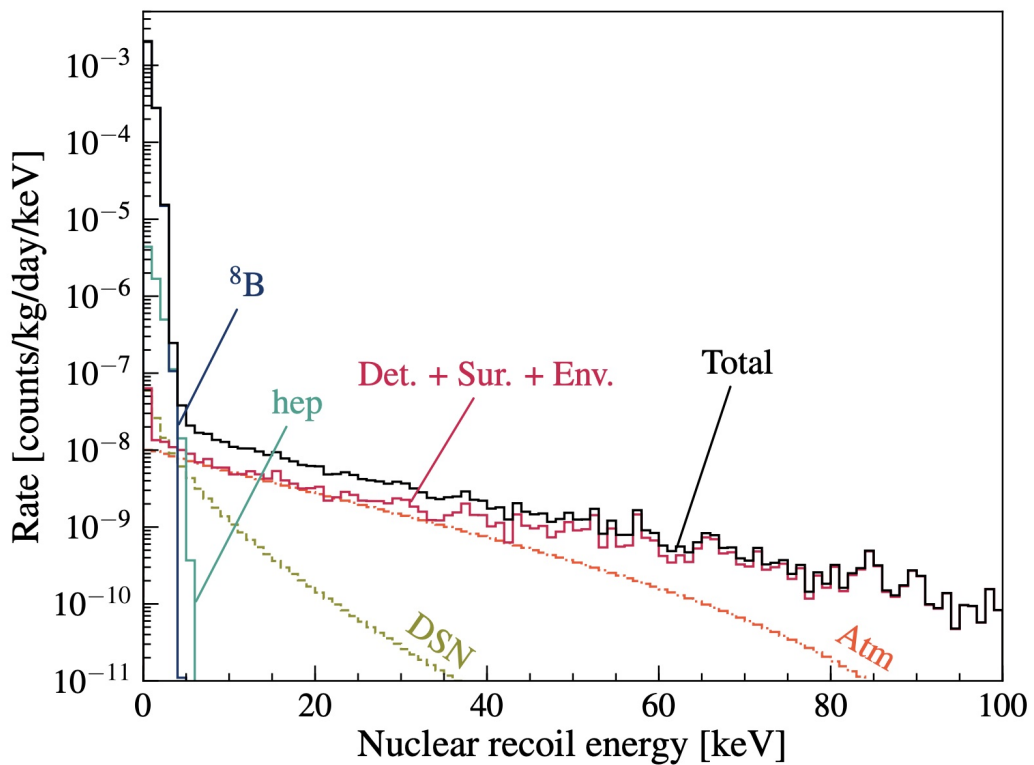
The materials used in detector construction contain naturally occurring radioisotopes which are potentially dangerous as some produce gamma rays: ^{40}K , ^{137}Cs , ^{60}Co , ^{238}U , ^{235}U , ^{232}Th and their daughters. Therefore, an extensive screening campaign, involving ~ 2000 radio assays, was carried out in order to choose only low radioactive materials. The uranium and thorium chains are also problematic as they emit neutrons from spontaneous fission and (α, n) reactions. The PMT arrays and LZ titanium cryostat are the dominant sources of background due to their large masses and proximity to active LXe region. However, the successful screening campaign in conjunction with the self-shielding property of LXe strongly limits the detector components background within the TPC [60], as can be seen in Table 2.1.

2.4.3.3 Surface contaminates

Exposing any detector components to airborne radon (particularly ^{222}Rn , decay chain shown in Figure 2.7) either during detector assembly, construction or installation can result in contamination with radon progeny. These progeny can deposit or become embedded on a material surface, referred to as plate-out. Most of the resulting gamma rays and beta particles produced are from short lived radon progeny (e.g. ^{218}Po $T_{1/2} = 3$ minutes). However, there is a long lived radon progeny ^{210}Pb ($T_{1/2} = 22$ years) which is problematic.



(a) ER background spectra.



(b) NR background spectra.

Figure 2.6: The predicted background energy spectra of ER (a) and NR (b) single scatter events within the 5.6 tonne fiducial region. Detector efficiencies and veto cuts have not been applied. Figures from Ref. [60].

The ^{210}Pb decay chain releases alpha particles which cause (α, n) reactions. The neutrons and alpha particles produced could mimic a WIMP signal. In addition dust on detector components also contains naturally occurring radioisotopes. To mitigate this background LZ has implemented a stringent set of cleanliness protocols for detector components and is constructing the detector in a reduced-radon cleanroom [101].

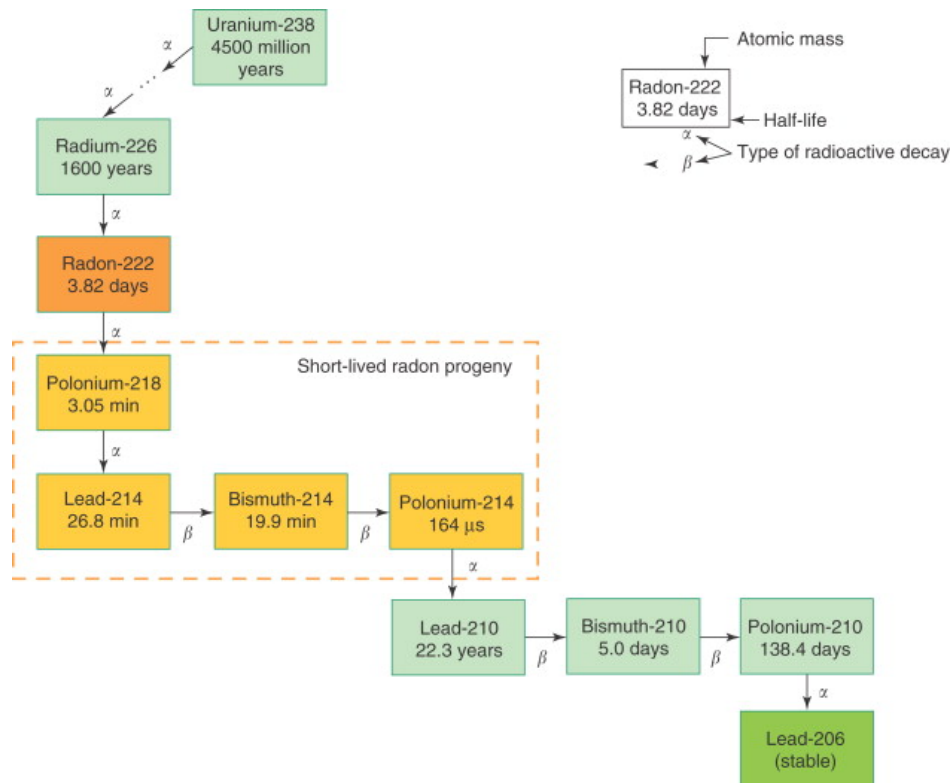


Figure 2.7: ^{238}U decay chain. Figure from Ref. [103].

2.4.3.4 Xenon contaminants

Another challenging background comes from dispersed radioactive isotopes within the xenon as they cannot be suppressed by LXe self-shielding. The LZ experiment will purify the xenon prior to installation to remove beta emitting noble radioactive impurities (^{85}Kr & ^{39}Ar) via a gas charcoal chromatography system [87], similar to LUX. ^{85}Kr and the LZ krypton removal system are explored more in Chapter 3. ^{222}Rn and ^{220}Rn emanating from dust and materials can become mobile in the LXe and are the largest contributors to the ER background in the TPC. The emission of a beta particle without a coincident gamma ray, referred to as “naked beta” decay, from ^{214}Pb and ^{212}Pb in the radon decay chains is challenging to reject in data analysis. In addition to the rigorous cleanliness protocols LZ has deployed a radon gas removal system which should reduce radon levels in problematic areas (e.g. cable conduits).

2.4.3.5 Laboratory & cosmogenics

As mentioned previously the surrounding Davis cavern walls emit gamma rays and neutrons which are produced by the naturally occurring radioisotopes and by atmospheric muon interactions in the rock. As with LUX, the detector is placed inside a water tank with an inverted steel pyramid located below to provide substantial shielding [104]. In addition the active veto detectors will reject some of the γ -ray events and a square steel plate has been added on top of the water tank to provide extra shielding for the neutrinoless double beta decay search. LUX and LZ simulations undertaken to characterise the cavern wall γ -ray background are explored in Chapter 5. Moreover, as the detector is located deep underground the atmospheric muon flux is considerably suppressed (reduced by $\sim 3 \times 10^6$ relative to the surface) [87]. The remaining muon events produce Cherenkov radiation in the water tank which is detected by the OD PMTs.

Additionally the cosmic rays at the surface (mainly neutrons) can activate the xenon and detector materials inducing radioactivity. The non-xenon isotopes produced by activation in the xenon can be removed via purification during operation, however, the remaining $^{131\text{m}}\text{Xe}$, $^{129\text{m}}\text{Xe}$ and ^{127}Xe could contribute to the WIMP search background. These isotopes will gradually decay and storing the xenon and detector components underground for ~ 6 months is sufficient to reduce this background to negligible levels within the LZ TPC [105].

Detector materials and xenon can also be activated by neutron calibrations undertaken during the detector commissioning phase to identify the LZ detector response. This background has been simulated and analysed in Chapter 6.

2.4.3.6 Physics

A number of natural physics processes, although very intriguing in their own right, are an irreducible background to the WIMP search. Solar neutrinos, predominantly from the pp chain, can scatter off atomic electrons producing an ER background in the TPC [106]. Furthermore, two-neutrino double beta decay ($2\nu\beta\beta$) from ^{136}Xe ($T_{1/2} \sim 10^{21}$ years & $\sim 9\%$ natural abundance) in the LXe will also contribute to the ER background. Due to coherent elastic neutrino-nucleus scattering, first observed by COHERENT [107], astrophysical neutrinos contribute significantly to the NR background in the TPC. Atmospheric neutrinos, ^8B and hep solar neutrinos, diffuse supernova neutrinos are all expected to produce NRs in the detector via this mechanism.

2.5 Simulating backgrounds

This section will cover the various software packages deployed within LUX and LZ to provide realistic simulations of particle interactions within the detector in order to charac-

terise the detector backgrounds. Monte Carlo (MC) simulations of particle production and transport are performed with GEANT4 [108] based software packages: LUXSim [109] and its successor BACCARAT [110], for the LUX and LZ experiments respectively. The NEST (Noble Element Simulation Technique) [111] package models the detector light and charge response to energy depositions. LZ has developed the LZ Analysis Package (LZap) to process PMT waveforms to reconstruct detector events. To prepare for incoming detector data LZ has performed a number of Mock Data Challenges (MDC) which utilise said software packages.

2.5.1 Geant4 based software

Originally released in 1998 GEANT4 has provided a critical toolkit for MC simulations of particle production and transport in matter to the nuclear and high-energy physics communities for many years. LUXSim was developed by LUX with the GEANT4 toolkit to meet the challenges of low-background experiments [109]. This gave LUX the ability to simulate radioactivity distributed throughout individual volumes in the detector geometry and record different levels of particle interaction information for various volumes. As LUXSim was not experiment agnostic, LZ developed BACCARAT from LUXSim [110]. The software packages operate in the same way, however, only BACCARAT is currently being updated and supported.

The LUX and LZ detectors have been replicated within the LUXSim and BACCARAT software geometries, see Figure 2.8 for LZ detector BACCARAT visualisation. LUXSim and BACCARAT are controlled with macro commands either entered at the command line or from a file. Users specify the individual volumes they would like to simulate with which custom particle generators and how much information to record in each volume (e.g. only energy depositions). A range of custom generators have been developed in order to allow users to simulate the wide variety of particle interactions expected in the detector with realistic timing and positioning (e.g. U/Th decay chains, $^{129\text{m}}\text{Xe}$ decay, $2\nu\beta\beta$, etc.).

2.5.2 NEST

The NEST software package [112] generates $S1$ and $S2$ signals from GEANT4 xenon energy deposition simulations. The model NEST uses to determine the scintillation and ionisation yield has been calibrated with a collection of different science and calibration data sets. The NEST simulation of the xenon microphysics considers a variety of factors; the type of particle and interaction, recoil energy, electric field, temperature and pressure of the xenon. NEST is very quick, however, it does not provide individual PMT level information and is dependent on averaged detector parameters. NEST models have been integrated into BACCARAT to provide the number of scintillation photons and ionisation from particle

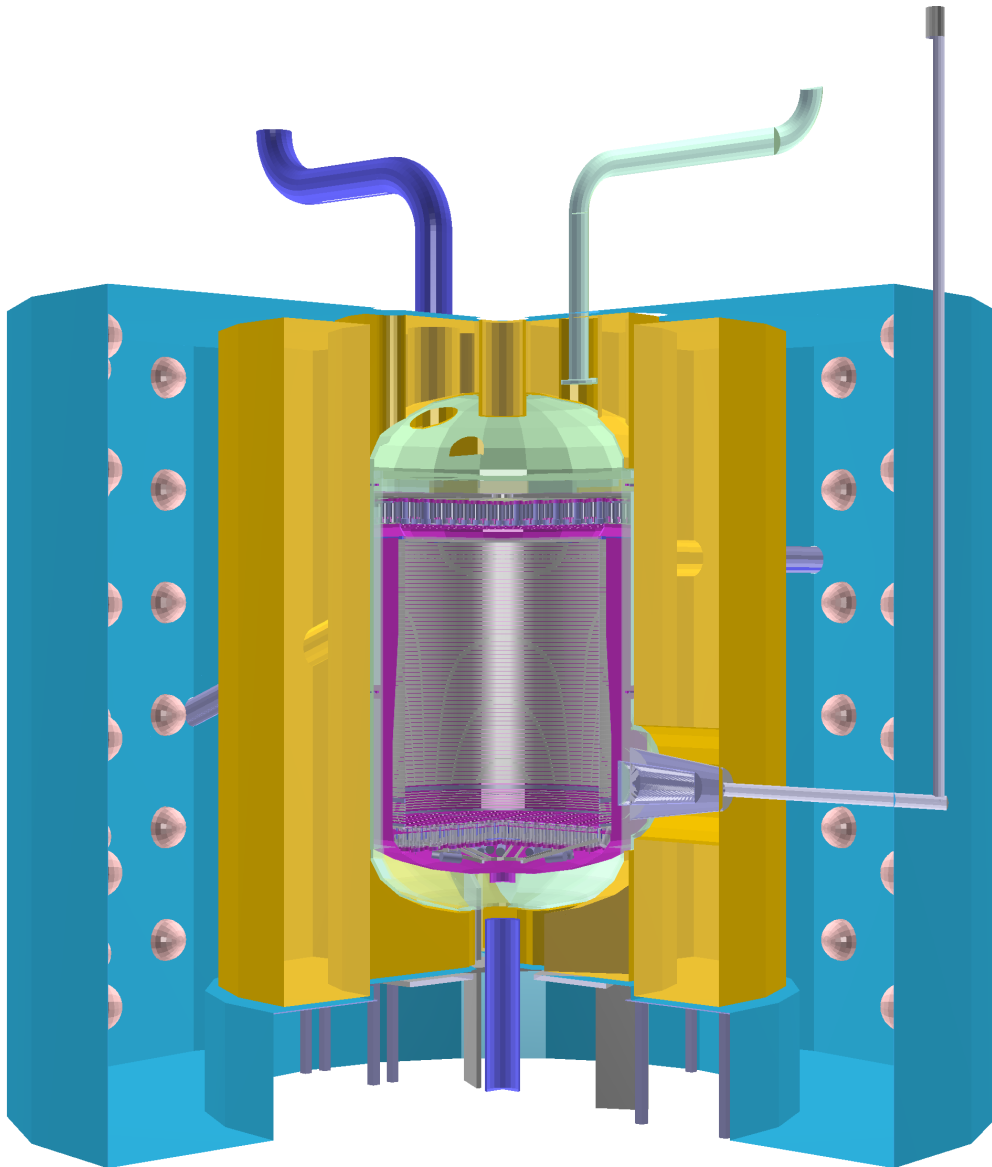


Figure 2.8: Cutaway 3D visualisation of the LZ detector in BACCARAT. Inner part of the water tank shown in blue with the OD PMTs in light pink. The OD acrylic vessels containing liquid scintillator (yellow) surrounds the cryostat (light green) which houses the TPC (magenta). Figure from Ref. [110].

interactions. The transport of these particles in the detector can be simulated, although this is computationally expensive for photons, resulting in PMT photon hits.

2.5.3 LZap

LZ has designed the LZap software package to reconstruct detector events from individual PMT channel waveforms into reduced quantities (RQ) ready for physics analysis. After

the LZ data acquisition system has been triggered the raw PMT waveforms are saved and then can be processed by LZap which applies a calibration to the individual waveforms due to the different PMT responses. LZap searches through the summed waveforms for each detector (TPC, xenon skin & OD) to locate and classify pulses (e.g. S_1 , S_2 , etc.). Once pulses have been classified LZap examines the sizes and number of S_1 and S_2 pulses to identify event type (e.g. single scatter, multiple scatter, etc.). Event reconstruction then takes place along with any relevant correction applied to RQs (e.g. detector light collection efficiency corrections). This same procedure for analysing real waveforms is also applied to waveforms generated from simulated events.

2.5.4 LZ Mock Data Challenges

LZ has undertaken a series of MDCs as part of the preparation to guarantee physics readiness prior to detector data collection. The MDCs have many useful functions; teaching users how to analyse LZ data, testing computing infrastructure, developing analysis and reconstruction tools.

The simulation chain implemented in the MDCs, shown in Figure 2.9, is comprised of three main LZ software packages. The chain aims to generate realistic commissioning and science run data from calibration and background simulations. At the beginning of the chain BACCARAT simulates particle production and transport within the detector. The physics models from the NEST package have been integrated into BACCARAT enabling it to convert energy depositions into PMT photon hits. The simulated PMT hits are then processed with the detector electronics response (DER) package to replicate the PMT response and the subsequent signal processing. The resulting simulated waveforms are passed to the LZap to reconstruct events for further data analysis.

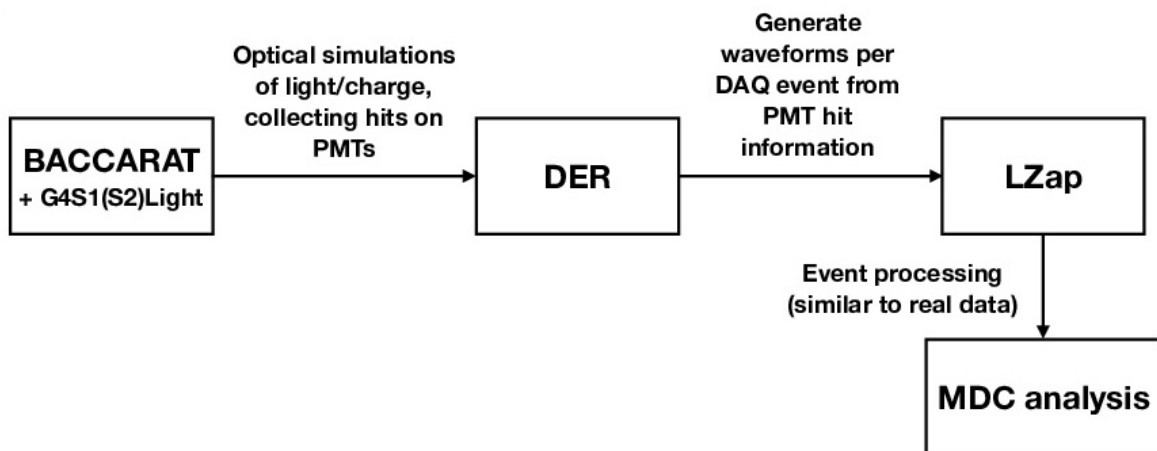


Figure 2.9: The simulation processing chains used to produce background data for the MDCs. Figure adapted from Ref. [110].

Three MDCs were undertaken, each one more complex than the previous. In 2017 MDC1 was carried out with a primary objective to generate full waveforms and test LZap processing. This was followed in 2018 by MDC2 which aimed to evaluate analysis tools created to produce exclusion limits or discovery results. MDC3 took place between 2019 and 2020 with the main goal of producing and analysing lifelike commissioning and science run data.

2.6 Simulated background analysis cuts

A key part of the background mitigation strategy for low-background experiments is the removal of background events with analysis cuts. As the LUX and LZ experiments are similar in detector technology and operation they employ comparable approaches to determine WIMP-like events from simulated data. This section discusses analysis cuts which have been used to evaluate detector sensitivity and determine the background contribution from particular sources when high statistics were required and no waveforms were generated. GEANT4 energy deposition simulations are processed with NEST to produce S1 and S2 signal information which can then be analysed.

It is expected that WIMPs will only scatter once within the detector due to the very small WIMP interaction cross-section, whereas gamma rays and neutrons typically scatter multiple times within the detector. Therefore, events are classified as multiple scatters if the energy-weighted position variance of the scatter is larger than the spatial resolution of the detector as WIMP interactions should appear as point like in the detector. The energy-weighted variance in position for the radial (σ_R) and vertical (σ_Z) directions is given by:

$$\sigma_R = \sqrt{\frac{\sum_i E_i (r_i - \langle R_E \rangle)^2 \times \sum_i E_i}{(\sum_i E_i)^2 - \sum_i (E_i^2)}}, \quad \sigma_Z = \sqrt{\frac{\sum_i E_i (z_i - \langle Z_E \rangle)^2 \times \sum_i E_i}{(\sum_i E_i)^2 - \sum_i (E_i^2)}} \quad (2.7)$$

where E_i is the energy deposition for each interaction vertex, r_i and z_i are the radial and z direction positions of the interaction vertex and $\langle R_E \rangle$ and $\langle Z_E \rangle$ are the energy weighted mean position define as:

$$\langle R_E \rangle = \frac{\sum_i (E_i r_i)}{\sum_i E_i}, \quad \langle Z_E \rangle = \frac{\sum_i (E_i z_i)}{\sum_i E_i} \quad (2.8)$$

For the LZ analysis single scatters were classified by $\sigma_Z < 0.2$ cm and $\sigma_R < 3.0$ cm, which has been determined by the PMT size and array layout [87]. In the LUX simulation background analysis a more conservative approach was taken classifying single scatter events by $\Delta Z_{MC} < 0.65$ cm, where ΔZ_{MC} is the MC vertical difference between the highest and lowest interaction vertex for an event.

Due to the self-shielding property of LXe a fiducial volume can be constructed within

the active LXe to minimise the impact of backgrounds. Defining a virtual cylindrical volume with boundaries a few centimetres in from the TPC walls enables the simple rejection of misreconstructed wall events near the edge of the TPC. The boundaries of the LZ fiducial volume, encompassing 5.6 tonnes of LXe, are defined as 1.5 cm above the cathode grid, 13.5 cm below the gate grid and 4 cm from the TPC walls [87]. The definition of these boundaries is primarily driven by the detector event position reconstruction accuracy, as it is crucial to remove misreconstructed wall events near the edge of the TPC. LUX defines the fiducial volume cut as a function of drift time (dt), which is a proxy for depth, and distance to the wall (d_{wall}). The events which do not satisfy $40 < dt < 300 \mu\text{s}$ and $d_{wall} > 3 \text{ cm}$ are outside of the 105.4 kg fiducial volume [113].

The LZ active veto detectors, xenon skin and OD, are a powerful background suppression system. As mentioned earlier WIMPs are expected to scatter once in the detector, therefore, LZ can reject TPC events which produce a time-coincident signal in either the xenon skin or OD detector. The xenon skin veto is triggered when it observes 3 or more phd within $800 \mu\text{s}$ before or after the S1 signal in the TPC. Likewise, the OD veto is activated when the total energy deposition in the OD is greater than 200 keV within $500 \mu\text{s}$ before or after the S1 [87].

Lastly, events with energy depositions outside of the WIMP energy region of interest (ROI) can be removed. In LUX simulated background analysis events with a total energy deposition in the active LXe larger than 100 keV are rejected. Both LUX and LZ require a minimum number of TPC PMTs to have observed the S1 signal (2 for LUX & 3 for LZ) and a larger enough raw S2 signal size for event position reconstruction (200 phd for LUX & 350 phd for LZ) [113][87]. LZ also requires WIMP-like events to have a corrected S1 signal of less than 20 phd. These limits approximately translate to ER (NR) energy depositions between 1.5-6.5 keV_{ee} (6-30 keV_{nr}) [87].

In summary the LUX experiment classifies WIMP-like events from simulated data by the following cuts:

- Single scatters ($\Delta Z_{MC} < 0.65 \text{ cm}$).
- Reconstructed position inside the 105.4 kg fiducial volume (above the cathode in the TPC).
- Total energy deposition in active LXe $< 100 \text{ keV}$.
- $S1 > 2 \text{ phd}$ & $S2 > 200 \text{ phd}$.

Similarly, the LZ experiment has a set of standard background cuts for selecting WIMP-like events from simulated data:

- Single scatters ($\sigma_Z < 0.2 \text{ cm}$ & $\sigma_R < 3 \text{ cm}$).

- Reconstructed position inside the 5.6 tonne fiducial volume (above the cathode in the TPC).
- Xenon skin (< 3 phd within $800 \mu\text{s}$).
- OD (< 200 keV within $500 \mu\text{s}$).
- WIMP ROI ($3 < S1_c < 20$ phd & $S2 > 350$ phd).

where $S1_c$ is the prompt scintillation light pulse area corrected for the variations in light collection efficiency throughout the detector.

Chapter 3

Krypton removal from xenon

3.1 ^{85}Kr concentration in xenon

Xenon is a by-product of separating air into oxygen and nitrogen. Through fractional distillation xenon can be recovered but it will contain noble radioactive impurities due to their similar boiling points. One such impurity, krypton, contains ^{85}Kr which is radioactive and may affect the sensitivity of an experiment to WIMPs.

The vast majority of ^{85}Kr in the atmosphere was produced by nuclear fuel reprocessing with small contributions from nuclear weapons testing and nuclear power plant disasters. Although ^{85}Kr can be produced naturally by cosmic ray interactions this only yields a small amount. It has an isotopic abundance of 2.5×10^{-11} ($^{85}\text{Kr}/^{nat}\text{Kr}$) in the atmosphere [114].

^{85}Kr has a half-life of 10.76 years and decays via beta decay with an electron spectrum extending up to 687 keV. This beta decay will produce electron recoil (ER) events in the LZ detector some of which will be low energy potentially located in the WIMP region of interest (ROI), see Figure 3.1. Despite the small absolute concentration of ^{85}Kr , nonetheless ^{85}Kr beta decays are particularly dangerous as they cannot be removed from liquid xenon (LXe) with commercial purification techniques and they will not be suppressed by LXe self-shielding.

^{39}Ar is another noble radioactive impurity present in xenon recovered from separating air. Like ^{85}Kr , ^{39}Ar decays via beta decay (endpoint electron energy 565 keV) which can create additional low energy background ER events in the LZ detector. However, as ^{39}Ar has a long half-life (269 years) and very small isotopic abundance (8×10^{-16} ($^{39}\text{Ar}/^{nat}\text{Ar}$)) [114] it produces significantly less background events than ^{85}Kr (1.5% of the ^{85}Kr background contribution) [87].

Commercially available xenon typically contains 100 parts per billion (ppb) of ^{nat}Kr resulting in a ^{85}Kr beta decay rate of 29 mBq/kg of xenon [87]. To achieve the ultra-low levels of krypton contamination in xenon for dark matter experiments that are acceptable, commercial xenon is processed via distillation or chromatographic separation. The LZ

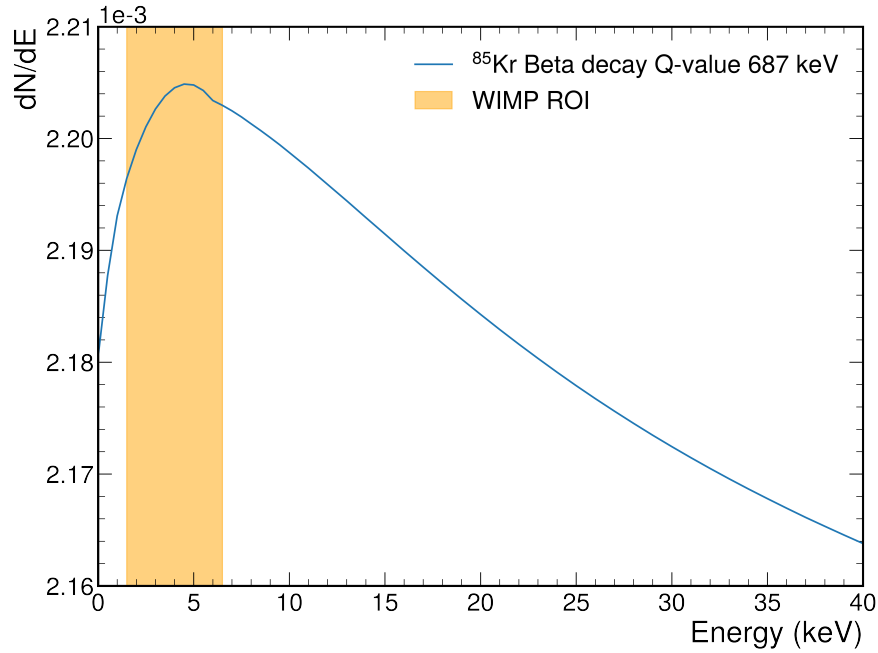


Figure 3.1: ^{85}Kr beta decay energy spectrum in blue with Q-value 687 keV and the orange band is the WIMP ROI 1.5-6.5 keV_{ee} . Spectrum generated by BetaShape [115].

experiment set a krypton concentration threshold limit of 300 parts per quadrillion (ppq) (g/g) ($^{nat}\text{Kr}/\text{Xe}$) expected to produce 480 background ER events during the 1000 day WIMP exposure [116]. Unless stated otherwise concentration references refer to mass ratios of ^{nat}Kr to ^{nat}Xe .

The techniques used to reduce krypton contamination also decrease argon concentration in xenon at the same time. The LZ experiment has constrained the argon concentration to be less than 0.45 ppb (g/g) ($^{nat}\text{Ar}/\text{Xe}$). This goal should be easily achieved as the argon concentration requirement is less challenging than the krypton and both concentration will be reduced at the same time.

The LZ krypton research group at SLAC National Accelerator Laboratory (SLAC) in the USA are responsible for purifying via gas charcoal chromatography LZ's 10 tonnes of xenon to 300 ppq krypton contamination. During the PhD I embarked upon a five month placement with the SLAC LZ krypton research group to learn and assist them with this challenging task.

This chapter covers gas charcoal chromatography and the implementation of this for the LZ experiment. Also covered in this chapter is the xenon recovery cold trap and plotting automation developed for the LZ krypton removal system. In addition this chapter will cover xenon cold trap sampling and the LZ krypton removal sampling system which measure impurities in xenon.

3.2 LZ krypton removal system

3.2.1 Gas Charcoal Chromatography

In industry adsorption-based chromatography is extensively used for gas separation. However, commercial purification techniques are not able to reduce krypton contamination in xenon to the required levels. As a result, in 2007 a new process was developed for the XENON-10 experiment to remove krypton from xenon via a charcoal adsorption system [117]. In two months this gas charcoal chromatography system processed 25 kg of xenon, lowering the krypton content to below 3 parts per trillion (ppt).

This was achieved by circulating helium carrier gas mixed with the krypton contaminated xenon through a charcoal column. The gases separate due to the differing transit times of the various gas species through the column. This difference in transit times occurs as krypton has weaker van der Waals attraction to charcoal than xenon; therefore, xenon travels slower than krypton through the column (see exit times of xenon and krypton through a charcoal column in Figure 3.2).

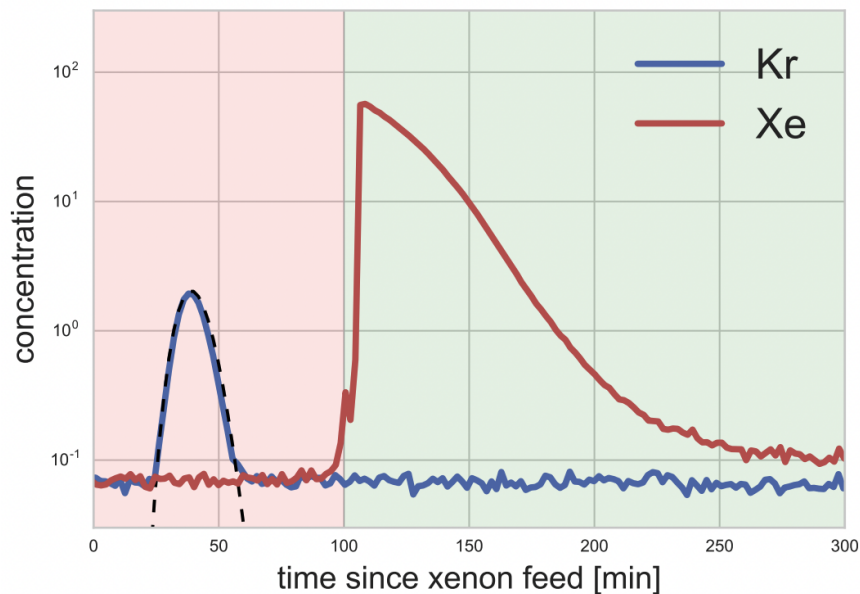


Figure 3.2: Separation of krypton from xenon via gas charcoal chromatography for the LUX experiment. A residual gas analyser (RGA) measures the gas concentrations in the mixture at the charcoal column exit. Figure from Ref. [98].

In 2017 the LUX experiment deployed a gas charcoal chromatography system, with activated charcoal, to process 400 kg of xenon. The average concentration of krypton in xenon was reduced from 130 ppb to 3.5 ppt in 4 months [98]. The LUX experiment also demonstrated that by processing the xenon twice they were able to reduce a krypton spiked

batch of 50 kg of xenon (krypton content approximately 0.01%) to a concentration of less than 0.2 ppt.

The researchers who developed this technique and proved it was successful are now at SLAC. They have constructed a new gas charcoal chromatography system, seen in Figure 3.3, for the LZ experiment which has higher mass-throughput and improved krypton reduction factor versus the LUX experiment system. The system consists of three separate main phases/loops; chromatography, recovery and storage (see Figure 3.4 for system diagram overview).

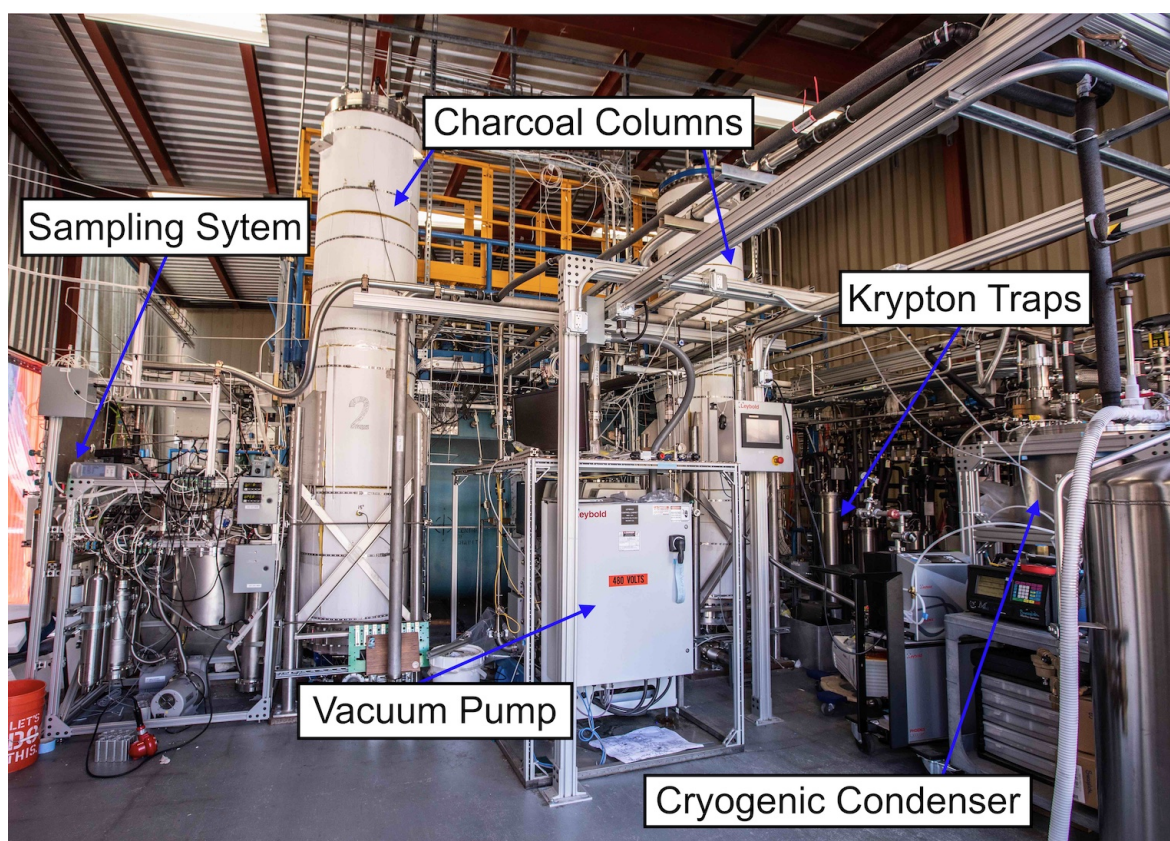


Figure 3.3: Picture of the LZ krypton removal system with key elements labelled. Photograph taken by Jacqueline Orrell/SLAC National Accelerator Laboratory in summer 2019.

In the chromatography phase trace amounts of krypton are being separated from xenon. Helium is continually circulated through the chromatography loop. 16 kg of xenon are injected into the helium gas stream. The flow-rate of the helium is tuned to optimise separation whilst minimising processing time. When the krypton leaves the charcoal column it is captured in a cold krypton trap allowing the purified helium to follow back into the column. The traps are stainless steel tubes filled with activated charcoal submerged in liquid nitrogen to retain the krypton longer than the processing cycle. Once xenon is detected in the column exit gas stream, via a binary gas analyser, the chromatography phase ends and

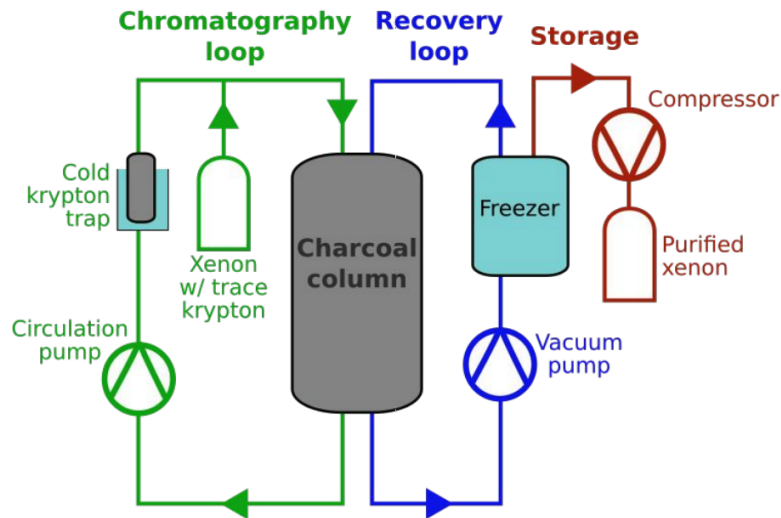


Figure 3.4: Schematic overview diagram of the three main loops in the LZ gas charcoal chromatography system. Note in the diagram the cryogenic condenser is called freezer. Figure provided by Drew Ames (Stanford University, USA).

the system switches to the recovery phase.

During the recovery phase the purified xenon is removed from the charcoal column. To accomplish this the vacuum pump reduces the column pressure down to ~ 10 mbar for maximum xenon removal efficiency. The xenon helium gas mixture leaving the column is redirected through the cryogenic condenser which is cooled to 77 K. The xenon is frozen out of the mixture leaving the helium to continue circulating. In addition, xenon samples are collected to be assayed for krypton and other impurities via the cold trap sampling system developed by University of Maryland, USA (discussed in Section 3.3).

Multiple chromatography and recovery phases occur in succession until the cryogenic condenser is full which can hold up to ~ 300 kg of xenon. Following this, the system enters the storage phase compressing the purified xenon into storage cylinders; ready to be transported to the Sanford Underground Research Facility (SURF) and stored underground. In this phase the cryogenic condenser is warmed and the resulting xenon gas is compressed to ~ 80 bar in the storage cylinders.

The LZ gas chromatography system has two 400 kg activated charcoal columns to process the xenon twice as fast; allowing one column to operate in the chromatography phase whilst the other column operates in the recovery phase. It takes ~ 3 -4 hours to complete one full chromatography then recovery cycle. The SLAC LZ krypton research group aimed to process the 10 tonnes of xenon in 60 days; reducing the average krypton concentration to below 300 ppq. Some of the xenon may require a second pass as it has high krypton concentration.

3.2.2 Xenon recovery cold trap

During the recovery phase of the krypton removal system not all the xenon can be extracted from the charcoal column in a timely manner, as xenon moves through the column slowly due to the strong xenon charcoal bonding. Instead of waiting a long time to recover all the xenon, it is more efficient to end the recovery cycle early and move onto the next chromatography cycle, leaving some xenon in the column. The SLAC LZ krypton research group estimated from initial recovery cycle testing that leaving 0.1% of the xenon in the charcoal column would reduce the recovery cycle time by 2 hours. Over time the small amounts of xenon left in the charcoal column accumulate in a krypton trap, however, the original LZ krypton removal system was not able to recover and reprocess that highly contaminated xenon.

A xenon recovery cold trap system (see Figure 3.5 for diagram) was designed, by the SLAC LZ krypton research group, to capture the contaminated xenon from the krypton trap during trap cleaning. Once the recovery cold trap was added to the LZ krypton removal system, the highly contaminated xenon in the krypton traps could be recovered and reprocessed.

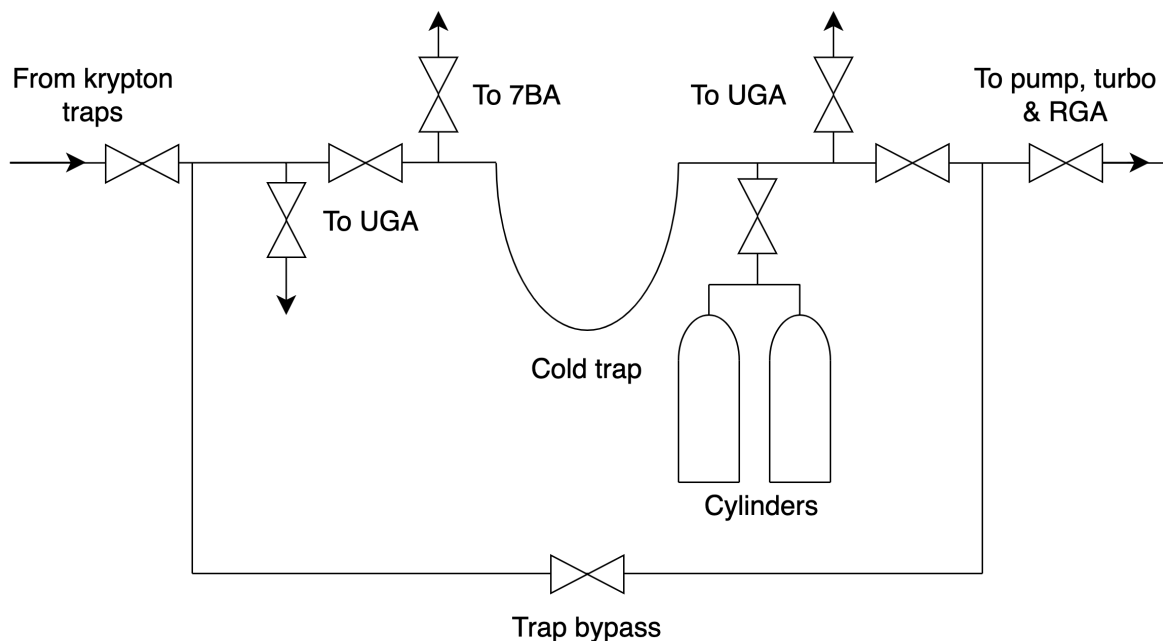


Figure 3.5: Simplified piping and valve diagram of the xenon recovery cold trap system. The arrows point to the gas flow direction through the system. The cold trap is a steel U-shaped pipe in liquid nitrogen filled dewar. It can be bypassed if needed and is connected to cylinders as a buffer volume. The system is connected to the 7BA, extra xenon storage, and a Universal Gas Analyser (UGA) can be connected either side of the trap.

The cold trap consists of a steel U-shaped pipe placed in a dewar which can be filled

manually with liquid nitrogen. If required the trap can be bypassed and is connected to cylinders as a buffer volume for warming xenon in the cold trap as xenon has a high liquid-to-gas expansion ratio. For mass spectrometry gas analysis a Universal Gas Analyser can be connected to either side of the cold trap. Xenon can also be transfer to the 7BA which is extra xenon storage.

I constructed and deployed the xenon recovery cold trap system (visible in Figure 3.6) with the assistance of Rafi Sazzad (University of Alabama, USA) and the SLAC LZ krypton research group. The valves were mounted to an aluminium panel and connected together with stainless steel piping and vacuum coupling radiation fittings. The aluminium control panel was fastened to the outer frame of the cryogenic condenser (displayed in Figure 3.7). Once installed the control panel was connected to the relevant external input and output pipes along with the steel U-shaped trap (seen in Figure 3.8). After all the connections were made the system underwent a helium leak test to detect and locate any small leaks into or out of the system.

When the krypton traps undergo cleaning the dewar containing the cold trap is filled with liquid nitrogen. Once the cold trap is frozen the path from the krypton traps is opened up and the incoming gases freeze in the trap. After the xenon has been recovered it is then pumped on by a vacuum pump to reduced some of the krypton content and can then be reprocessed later. The xenon recovery cold trap has been successfully used a number of times by the krypton removal system operators to recover xenon during the cleaning of krypton traps.

3.2.3 Automated plotting of system information

It is important that information about past chromatography and recovery cycles is easily accessible to system operators. This information helps operators understand previous runs, defined as a chromatography and then a subsequent recovery cycle, and aids them in tuning the LZ krypton removal system for future runs. As runs become more automated it is crucial that system operators are able to quickly analyse and compare runs using the relevant sensor data (e.g. pressure, temperature, flow rate, etc.).

System operators can access current and historic sensor data in the LZ krypton removal system via Ignition [118], a SCADA (supervisory control and data acquisition) software platform connected to the system. However, loading historical data from multiple sensors can be very slow and difficult through the Ignition user interface. As operators want to examine data from the same sensors for each run, it was suggested that this sensor information should be automatically plotted after each run and the plots catalogued online to provide easy access for the system operators.

Working in consultation with the SLAC LZ krypton research group, I automated and continued to develop a sensor data plotting tool created by Ibles Olcina (University of

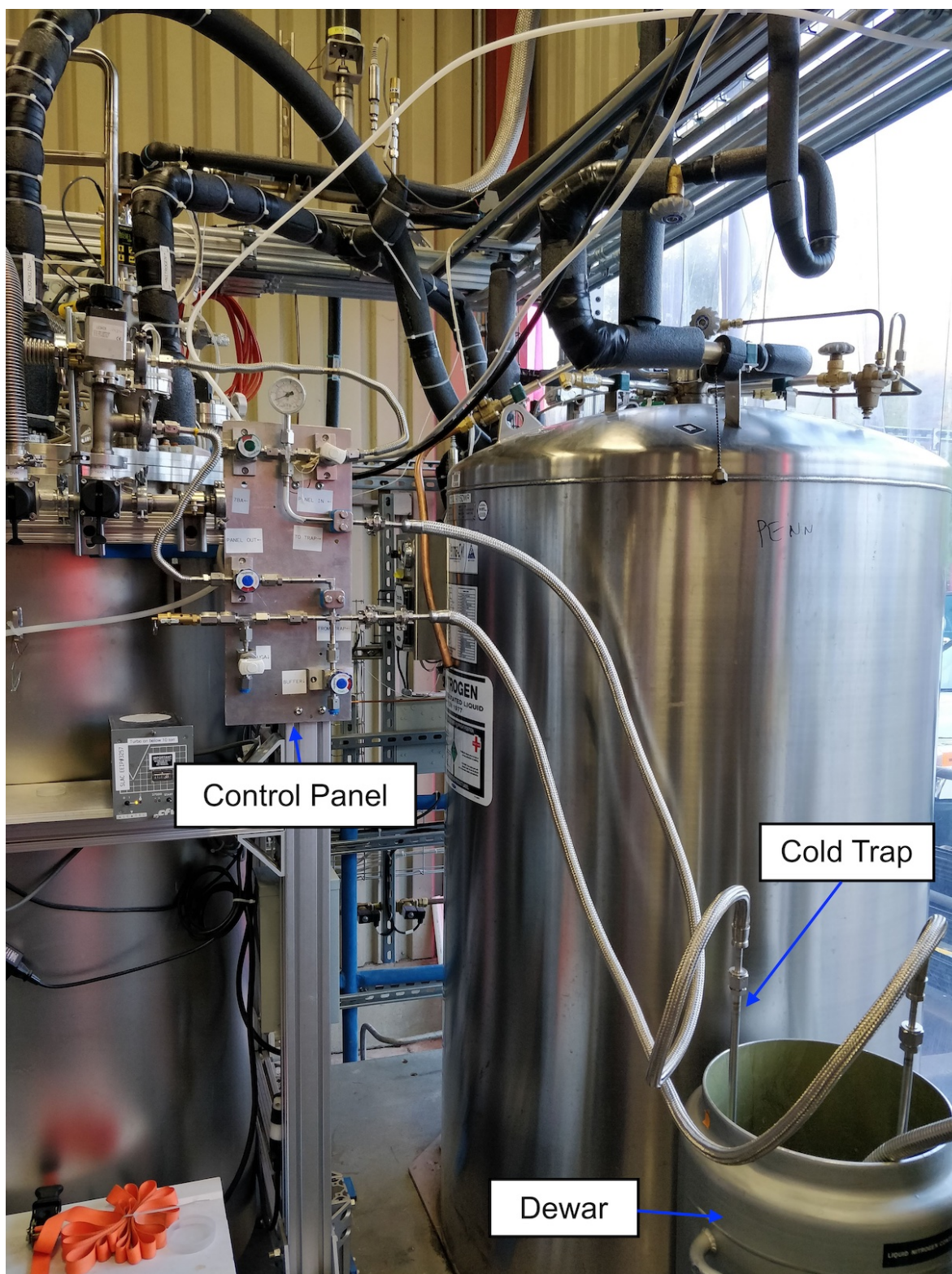


Figure 3.6: Xenon recovery cold trap system. The control panel (left) is connected to the krypton removal system and the steel U-shaped pipe located in a dewar (right). Photograph taken by Andrew Naylor (University of Sheffield, UK).



Figure 3.7: The control panel for the xenon recovery cold trap system. Each valve on the panel has been labelled with the destination and gas flow direction. Photograph taken by Eric Miller (SLAC National Accelerator Laboratory, USA).



Figure 3.8: The frozen steel U-shaped trap connected to the xenon recovery cold trap system. Photograph taken by Dan Akerib (Stanford University, USA).

California, Berkeley, USA). The plotting tool extracts sensor data between user specified timestamps from the Ignition database where all sensor information is stored. From the extracted data the tool creates a number of plots based on information specified in a configuration file and then saves the plots as image files. Figure 3.9 shows an example plot created by the tool, displaying pressure and flow rate sensor information from the initial phase of run 22.8.

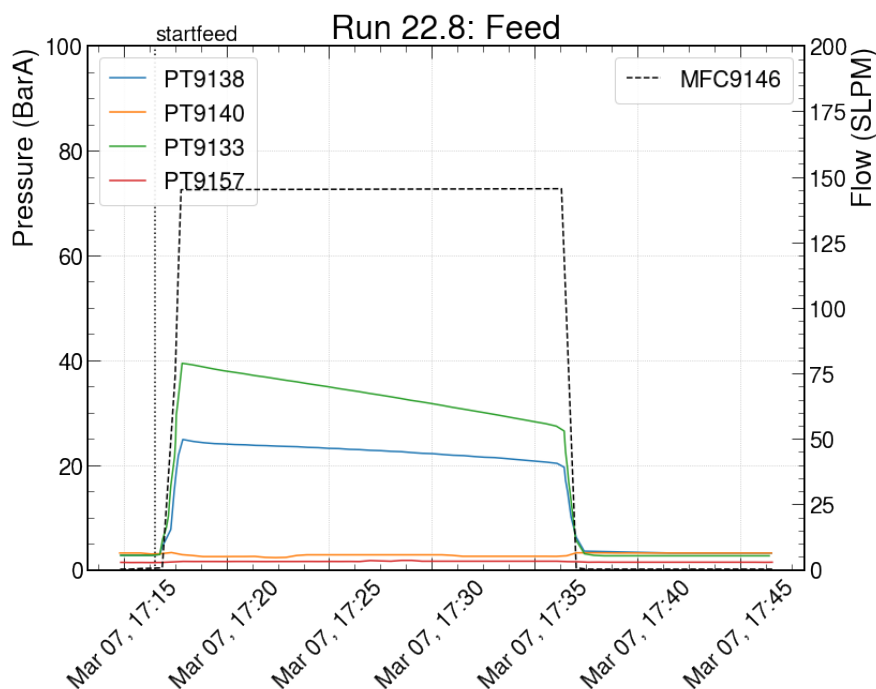


Figure 3.9: A figure produced by the plotting tool about the initial phase of run 22.8 when xenon is injected into the charcoal column. The solid lines are pressure readings from pressure transducers in the system and the dashed line is the xenon flow rate from a mass flow controller (MFC). The beginning of the xenon injection into the helium gas stream is indicated by the dotted line.

To automate the production of sensor data plots, the plotting tool was converted into a Python daemon which runs continually on a machine with access to the Ignition database. The daemon checks for any new krypton removal runs which are logged automatically in the run timestamp MySQL database [119] by the chromatography and recovery Ignition control scripts. Once the daemon finds a new run it executes the plotting tool with the specified run timestamps and produces the sensor data plot images. These images are then accessible on a local website for system operators to view.

The system operators can also interact with the run timestamp MySQL database from the Ignition user interface via an Ignition page I developed. This page, seen in Figure 3.10, allows system operators to view all run entries in the database, edit entries, provides the local website link to the run plots, the status of the plotting daemon and the ability to rerun

the plotting tool on a specific run.

The SLAC LZ krypton research group visit the local sensor data plots website daily to investigate new krypton removal runs and compare them to previous runs. The website speeds up and simplifies analysing chromatography and recovery cycles; thus it helps system operators diagnose any system issues quicker and tune the system for maximum krypton removal efficiency.

3.3 Xenon Cold Trap Sampling System

3.3.1 Method

Detecting and quantifying trace amounts of radioactive impurities in xenon is an important challenge faced by liquid xenon WIMP dark matter experiments. Although some impurities in commercial xenon have small absolute concentrations, they can still produce a significant number of background events for WIMP searches. For the LZ experiment, it is crucial that even very small concentrations of radioactive impurities in the xenon can be observed as it confirms that chromatographic separation was successful when processing the xenon. It also provides information which can constrict the background count rate in the WIMP search due to these radioactive impurities.

Residual gas analysers (RGA) measure the chemical composition of gas, however, they can only detect impurities larger than 1 parts per million which would not be sufficient for the LZ krypton removal system as it has a krypton concentration requirement of 300 ppq set by the LZ experiment. A technique developed by researchers at University of Maryland, utilising a cold trap, is able to increase the impurity sensitivity of an RGA for gaseous xenon [120, 121]. This method, referred to henceforth as “xenon cold trap sampling”, in theory is able to measure krypton concentrations of order 1 ppq in xenon [122].

In xenon cold trap sampling, a gaseous xenon sample flows through a cold trap (for example a U-shaped pipe submerged in a liquid nitrogen bath) via a mass flow controller (MFC) or precision leak valve. The bulk xenon in the sample freezes to the walls of the cold pipes leaving xenon ice vapour and trace impurities, such as krypton, observable at trap output with an RGA (see Figure 3.11 for diagram). The xenon vapours exiting the cold trap are enriched with the impurities, up to a factor of 10^9 .

The enriched impurity partial pressures measured by the RGA are proportional to the absolute impurity concentration in the sample, flow rate of the gas and system impedance. Therefore, if the flow rate and system impedance are fixed a constant of proportionality can be calculated by analysing gaseous xenon samples with known impurity concentrations. This constant, known as the impurity calibration constant, encapsulates the sensitivity of the sampling system to a specific gas species. Once the constant has been determined the concentration of an impurity in a gaseous xenon sample can be calculated.

3.3. Xenon Cold Trap Sampling System

The screenshot displays a web application interface for managing a MySQL database of run timestamps. The main component is a table with the following columns: Run ID, Run Name, Start Chromatogram, Start Feed, End Chromatography, Start Recovery, End Recovery, Column Number, and State. The table lists 25 individual runs, each with a unique ID and corresponding timestamps for various stages of the process. Below the table, there are several interactive elements: a 'Refresh DB View' button, a 'Daemon Status' section with a dropdown menu set to 'Up', and buttons for 'Reset All Rows', 'Reset Selected Row(s)', and 'Delete Selected Row(s)'. Additionally, there are links for 'Link to plots for Selected Row(s)', 'Link to chromatography', 'Link to feed', and 'Link to recovery'. A search bar at the top left contains the number '45', and a 'Submit SQL' button is located at the bottom right.

Run ID	Run Name	Start Chromatogram	Start Feed	End Chromatography	Start Recovery	End Recovery	Column Number	State
4722.8	Mar 7, 2020 5:06 PM	Mar 7, 2020 5:11 PM	Mar 7, 2020 8:41 PM	Mar 7, 2020 11:14 PM	Mar 8, 2020 1:15 AM	2 completed	1	2 completed
4622.7	Mar 7, 2020 1:15 PM	Mar 7, 2020 1:20 PM	Mar 7, 2020 4:19 PM	Mar 7, 2020 4:59 PM	Mar 7, 2020 10:15 PM	1 completed	1	2 completed
4522.6	Mar 7, 2020 9:42 AM	Mar 7, 2020 9:50 AM	Mar 7, 2020 1:06 PM	Mar 7, 2020 1:09 PM	Mar 7, 2020 4:57 PM	2 completed	1	2 completed
4432.5	Mar 5, 2020 3:49 PM	Mar 5, 2020 4:18 PM	Mar 5, 2020 7:07 PM	Mar 5, 2020 8:30 PM	Mar 6, 2020 12:43 AM	2 completed	1	2 completed
4322.4	Mar 5, 2020 12:19 PM	Mar 5, 2020 12:24 PM	Mar 5, 2020 2:45 PM	Mar 5, 2020 3:43 PM	Mar 5, 2020 7:50 PM	1 completed	1	2 completed
4222.3	Mar 5, 2020 9:23 AM	Mar 5, 2020 9:55 AM	Mar 5, 2020 12:05 PM	Mar 5, 2020 12:12 PM	Mar 5, 2020 3:58 PM	2 completed	1	2 completed
4122.2	Mar 4, 2020 3:39 PM	Mar 4, 2020 4:00 PM	Mar 4, 2020 6:39 PM	Mar 4, 2020 6:44 PM	Mar 4, 2020 10:26 PM	2 completed	1	2 completed
4022.1	Mar 3, 2020 1:59 PM	Mar 3, 2020 2:10 PM	Mar 3, 2020 4:49 PM	Mar 3, 2020 5:22 PM	Mar 3, 2020 9:50 PM	2 completed	1	2 completed
3921.1	Feb 10, 2020 4:12 PM	Feb 10, 2020 4:16 PM	Feb 10, 2020 7:02 PM	Feb 10, 2020 7:14 PM	Feb 10, 2020 10:30 PM	2 completed	1	2 completed
3820.1	Feb 7, 2020 3:31 PM	Feb 7, 2020 3:36 PM	Feb 7, 2020 7:18 PM	Feb 7, 2020 7:30 PM	Feb 8, 2020 12:49 AM	2 completed	1	2 completed
3719.1	Feb 3, 2020 2:24 PM	Feb 3, 2020 2:37 PM	Feb 3, 2020 7:07 PM	Feb 3, 2020 7:25 PM	Feb 3, 2020 10:43 PM	2 completed	1	2 completed
3618.1	Jan 27, 2020 11:44 AM	Jan 27, 2020 12:31 PM	Jan 27, 2020 3:31 PM	Jan 27, 2020 3:40 PM	Jan 27, 2020 8:48 PM	2 completed	1	2 completed
3517.1	Jan 24, 2020 1:05 PM	Jan 24, 2020 1:18 PM	Jan 24, 2020 4:45 PM	Jan 24, 2020 5:17 PM	Jan 24, 2020 10:14 PM	2 completed	1	2 completed
3416.1	Jan 22, 2020 11:08 AM	Jan 22, 2020 11:57 AM	Jan 22, 2020 2:46 PM	Jan 22, 2020 3:49 PM	Jan 22, 2020 9:40 PM	2 completed	1	2 completed
3315.1	Jan 20, 2020 10:59 AM	Jan 20, 2020 11:42 AM	Jan 20, 2020 2:17 PM	Jan 20, 2020 3:06 PM	Jan 20, 2020 9:17 PM	2 completed	1	2 completed
3214.1	Jan 16, 2020 3:51 PM	Jan 16, 2020 4:41 PM	Jan 16, 2020 6:31 PM	Jan 16, 2020 6:51 PM	Jan 16, 2020 10:54 PM	2 completed	1	2 completed
3113.1	Jan 14, 2020 12:36 PM	Jan 14, 2020 12:49 PM	Jan 14, 2020 3:13 PM	Jan 14, 2020 5:48 PM	Jan 14, 2020 11:17 PM	1 completed	1	2 completed
3012.1	Jan 10, 2020 1:05 PM	Jan 10, 2020 1:14 PM	Jan 10, 2020 3:06 PM	Jan 10, 2020 3:45 PM	Jan 10, 2020 11:35 PM	2 completed	1	2 completed
2911.2	Jan 2, 2020 10:56 AM	Jan 2, 2020 11:15 AM	Jan 2, 2020 12:51 PM	Jan 2, 2020 1:34 PM	Jan 2, 2020 9:18 PM	2 completed	1	2 completed
2811.1	Jan 1, 2020 4:18 PM	Jan 1, 2020 4:36 PM	Jan 1, 2020 7:39 PM	Jan 1, 2020 7:41 PM	Jan 2, 2020 12:13 AM	2 completed	1	2 completed
2710.2	Dec 30, 2019 1:05 PM	Dec 30, 2019 1:18 PM	Dec 30, 2019 3:06 PM	Dec 30, 2019 3:18 PM	Dec 30, 2019 10:14 PM	2 completed	1	2 completed
2610.1	Dec 28, 2019 1:39 PM	Dec 28, 2019 1:48 PM	Dec 28, 2019 3:33 PM	Dec 28, 2019 4:05 PM	Dec 28, 2019 11:01 PM	2 completed	1	2 completed
259.1	Dec 25, 2019 11:44 ...	Dec 25, 2019 12:15 PM	Dec 25, 2019 1:54 PM	Dec 25, 2019 3:18 PM	Dec 25, 2019 10:47 PM	1 completed	1	2 completed
248.1	Dec 20, 2019 2:42 PM	Dec 20, 2019 3:17 PM	Dec 20, 2019 5:03 PM	Dec 20, 2019 5:10 PM	Dec 20, 2019 10:41 PM	2 completed	1	2 completed
237.7	Nov 25, 2019 2:35 PM	Nov 25, 2019 3:53 PM	Nov 25, 2019 4:38 PM	Nov 25, 2019 4:49 PM	Nov 25, 2019 9:42 PM	2 completed	1	2 completed
227.6	Nov 25, 2019 8:51 AM	Nov 25, 2019 8:57 AM	Nov 25, 2019 10:41 ...	Nov 25, 2019 10:48 AM	Nov 25, 2019 2:15 PM	2 completed	1	2 completed
217.5	Nov 22, 2019 3:36 PM	Nov 22, 2019 3:42 PM	Nov 22, 2019 5:21 PM	Nov 22, 2019 5:24 PM	Nov 22, 2019 11:26 PM	2 completed	1	2 completed
207.4	Nov 21, 2019 11:35 ...	Nov 21, 2019 11:44 AM	Nov 21, 2019 1:23 PM	Nov 21, 2019 1:25 PM	Nov 21, 2019 6:24 PM	2 completed	1	2 completed
197.3	Nov 20, 2019 10:38 ...	Nov 20, 2019 10:47 AM	Nov 20, 2019 12:22 ...	Nov 20, 2019 12:24 PM	Nov 20, 2019 5:51 PM	2 completed	1	2 completed
187.2	Nov 19, 2019 10:41 ...	Nov 19, 2019 10:59 AM	Nov 19, 2019 12:31 ...	Nov 19, 2019 12:40 PM	Nov 19, 2019 6:13 PM	2 completed	1	2 completed
177.1	Nov 14, 2019 2:21 PM	Nov 14, 2019 6:03 PM	Nov 14, 2019 8:28 PM	Nov 15, 2019 0:42 AM	Nov 15, 2019 2:22 PM	2 completed	1	2 completed

Figure 3.10: Run timestamp database Ignition page. System operators can view and edit run entries in the database. It also provides links to the local sensor data plots website and the status of the plotting daemon.

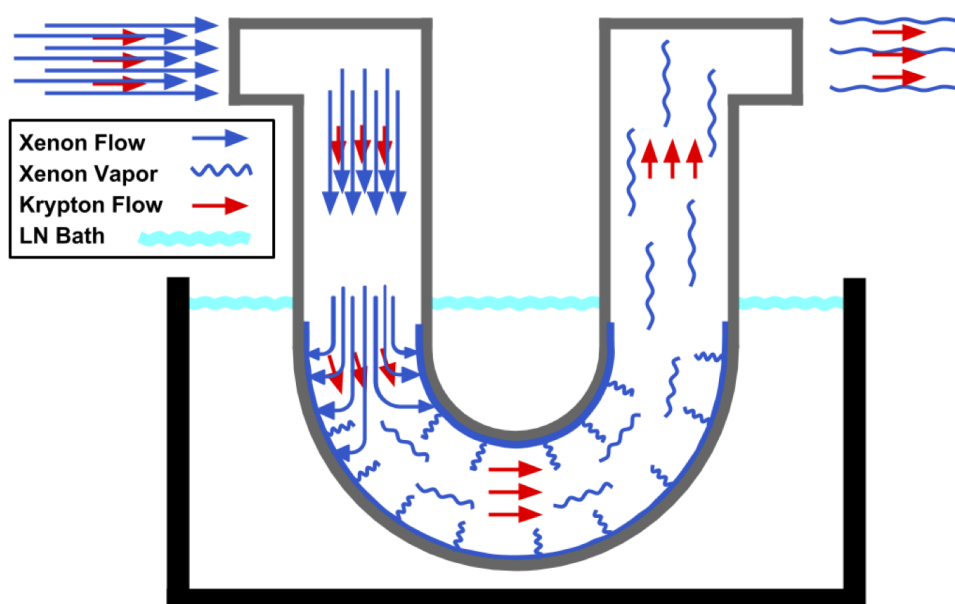


Figure 3.11: Simple diagram of the cold trap in xenon cold trap sampling. Gaseous xenon sample enters on the left and the bulk xenon freezes on the pipe walls. The xenon ice vapour enriched with impurities exits the trap on the right. Figure from Ref. [122].

Increasing the flow rate of the sample through the trap will increase the impurity concentration at the trap output; however, too high a flow rate could overwhelm the cooling power of the cold trap. The system impedance is also maximised to increase the impurity partial pressure at the trap output. These parameters are tuned to achieve high sensitivity.

3.3.2 Sampling in LZ krypton removal system

A dedicated xenon cold trap sampling system was built into the LZ krypton removal system as said system regularly collects gaseous xenon samples to be assayed for krypton and other impurities. Developed by researchers at University of Maryland, USA the LZ krypton removal sampling system (seen in Figure 3.12) consists of source bottles, pressure transducers, MFC, leak valve, cold trap and turbo molecular pumps. The stainless steel cold trap is a stocking shaped pipe that can be submerged in a liquid nitrogen bath by raising a polystyrene dewar. The sampling system is connected directly to the krypton removal system, allowing gaseous xenon in the system to be easily sent to the sampling system for assaying. Calibrations with the sampling system have shown a krypton concentration limit of detection at 25 ppq [116].

Gaseous xenon samples undergo preparation before a high sensitivity krypton measurement to reduce any non-relevant gas species that would saturate the RGA (e.g. helium). To begin the high sensitivity measurement the cold trap is frozen to form a thin

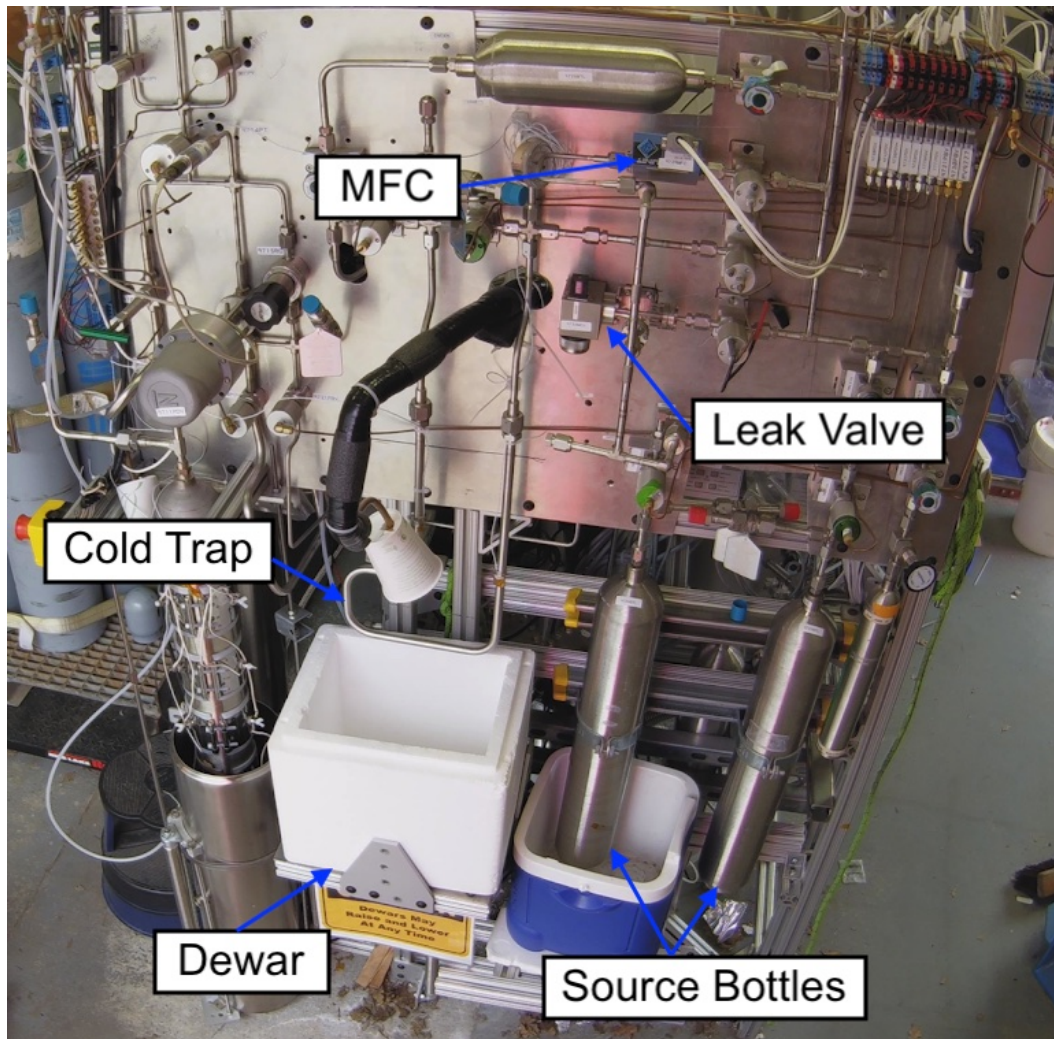


Figure 3.12: Sampling system control panel in the LZ krypton removal system. Photograph taken by Andrew Naylor (University of Sheffield, UK).

xenon ice layer. Once the xenon ice is formed the RGA monitors the cold trap exit vapours for five minutes to determine the krypton background. Subsequently 80 g of the gaseous xenon sample are fed into the cold trap via the MFC over five minutes. The krypton signal is determined by subtracting the average background krypton partial pressure from the integrated krypton flow signal area. Using the krypton calibration constant, determined by calibrations, this krypton signal can be converted into a krypton concentration.

Under the supervision of John Silk (University of Maryland, USA) I regularly performed high sensitivity krypton measurements with the LZ krypton removal sampling system. RGA data of a krypton measurement taken on a xenon sample produced during run 7.4 is visible in Figure 3.13. This gaseous xenon sample was taken from the xenon-helium gas stream exiting the charcoal column immediately after the chromatography phase. The

source xenon used in run 7.4 contained a krypton concentration of 11 ppt. The sampling system measured the krypton concentration of the sample to be 50 ± 28 ppq demonstrating the LZ krypton removal system is able to reduce krypton concentration to below 300 ppq.

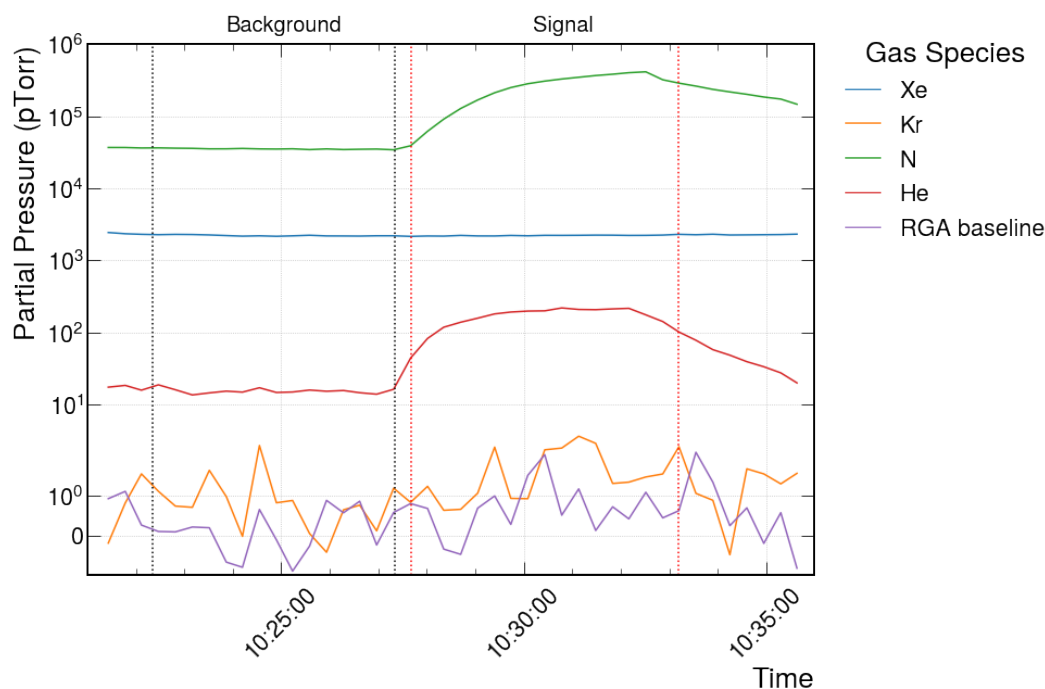


Figure 3.13: RGA partial pressure data from a high sensitivity krypton measurement. The black and red dotted lines indicate the background and signal phases of the measurement respectively. When the background phase ends the xenon sample starts to flow through the cold trap. This run 7.4 xenon sample contains 50 ± 28 ppq of krypton.

The sampling system is also able to clean small batches of xenon to very high purity below the sampling system krypton concentration detection limit. This high purity xenon has many important uses; it can be mixed with helium that has flowed through the krypton traps and then analysed with the sampling system to monitor the traps health. The high purity xenon can also be left in a volume and then measured with the sampling system to determine if there are any leaks or residual impurities in the volume.

One of the most important uses is mixing high purity xenon with known impurities to create xenon samples for calibrating the sampling system. Regular calibrations are undertaken to ensure the validity of the high sensitivity measurements. Figure 3.14 displays RGA data from a high sensitivity krypton measurement of a xenon calibration sample containing 1000 ppq of krypton. The sampling system determined the krypton concentration of the sample to be 1015 ± 86 ppq which confirms the system is still providing accurate results.

As part of the placement I also assisted John Silk (University of Maryland, USA) auto-

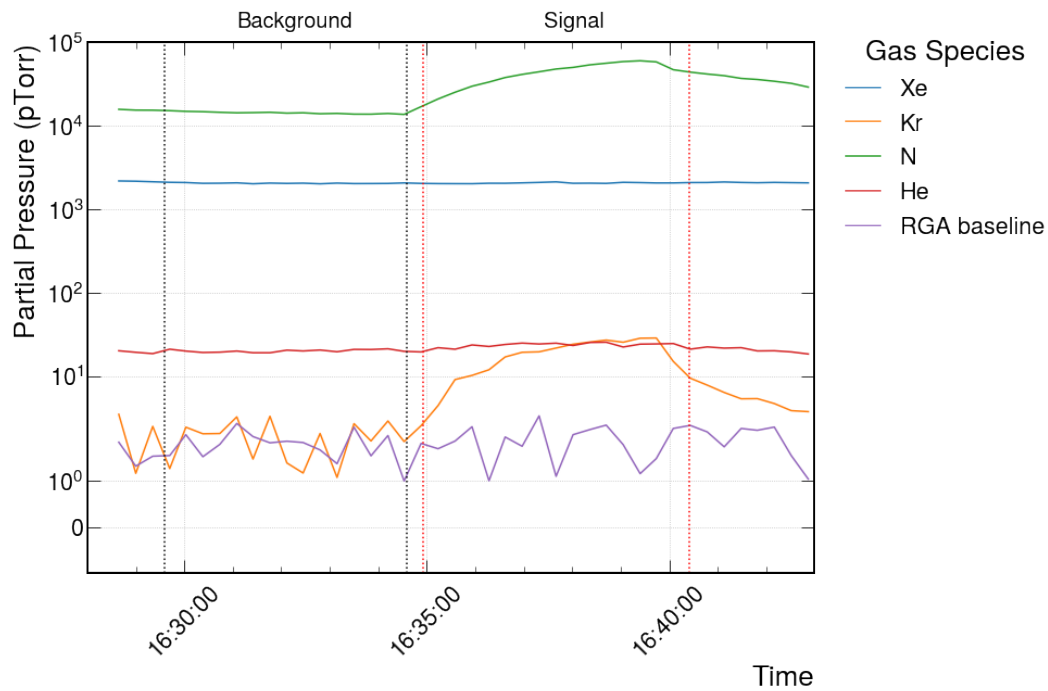


Figure 3.14: High sensitivity krypton measurement RGA partial pressure data. The black and red dotted lines indicate the background and signal phases of the measurement respectively. The 1000 ppq xenon calibration was measured to have 1015 ± 86 ppq of krypton.

mate operations on the LZ krypton removal sampling system. Previously, measurements and xenon cleaning were carried out manually by sampling system operators but Ignition automation scripts were developed to improve consistency between measurements and increase the sampling system operational efficiency.

Chapter 4

Software

4.1 Introduction

Computation plays a vital role in modern particle physics, computers are used to perform computational algebra, execute sophisticated simulations, gather and analyse large datasets, and visualise data. Software designed to accomplish these tasks are important as they allow particle physics experiments, like the LZ experiment, to quickly and easily study massive amounts of complex experimental data along with theories and models of the physical universe.

The LZ experiment has two independent data centres, located in the USA and the UK, which host LZ experiment detector data. They also facilitate data processing and user analysis for the experiment. The USA based data centre is the National Energy Research Scientific Computing Centre (NERSC), a high performance computing user facility operated by the Lawrence Berkeley National Lab. The UK data centre consists of data storage at Imperial College London and computation resources provided by GridPP [123], a collaboration of 19 UK institutions that manage and maintain a distributed computing grid across the UK.

For the LZ experiment I developed a job submission interface (JSI) for PSquared [124], a job submission engine (JSE) used by LZ to perform simulations and data analysis on the supercomputers at NERSC. I also added support for LZap in PSquared and helped test its hyper-threading capabilities.

Furthermore I have created a Python parallel processing analysis framework, called Hyper, in order to simplify and accelerate data analysis within the LZ experiment. Additionally I have also designed LEOPARD, a Python web-based plotting tool which interfaces with the LZ data catalogue.

This chapter covers software I developed for the LZ USA data centre and the other programs I created for the LZ experiment.

4.2 PSquared

4.2.1 Overview of PSquared

The LZ experiment uses the JSE PSquared to enable the creation, monitoring and the provenance of various simulations and analysis tasks executed on the NERSC supercomputer. A JSE is required as the LZ experiment performs large numbers of simulations which should be repeatable and analysis that needs to be easily rerun with different software versions, all whilst keeping track of every task executed.

For example, in order to provide six months of simulated data for the LZ MDC3, it required 8000 simulation tasks a day for three months. Without a JSE it would be unfeasible to create, monitor and record the history of all these tasks. Furthermore, when LZ detector data is produced it is automatically processed at NERSC via PSquared.

PSquared is a java application server. The user interacts with PSquared via a RESTful application programming interface (API) to submit or monitor tasks. It stores the information about submission and execution of tasks in a PostgreSQL database [125]. These tasks are added to a scheduler which then sends the tasks, via RabbitMQ (message-queueing software) [126], to runners that execute the tasks inside jobs running on the supercomputer nodes at NERSC (see Figure 4.1 for overview diagram).

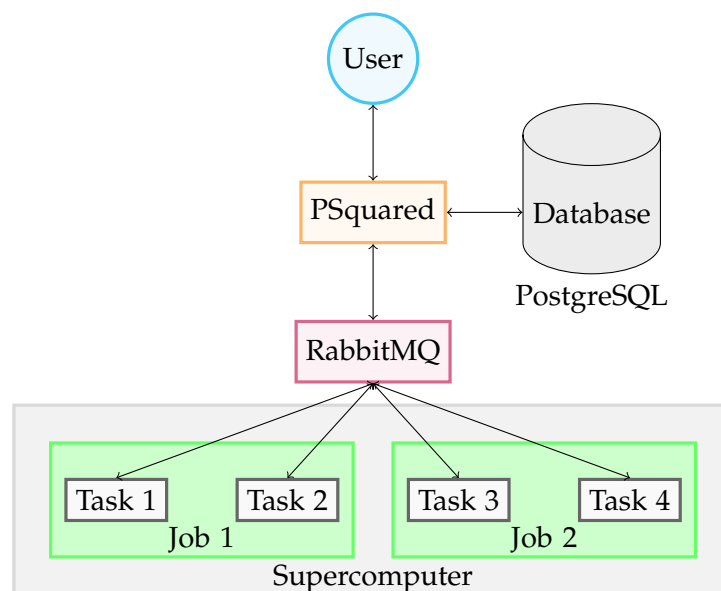


Figure 4.1: Schematic diagram showing the different elements of the LZ job submission system at NERSC. Note PSquared can run large numbers of jobs on the NERSC supercomputers and up to 64 tasks in each job.

4.2.2 Job submission interface

A JSI allows users to create, monitor and control tasks on a JSE; it hides away the complexity of task creation and management on a JSE from the end user. The current JSI to PSquared is via command line interface (CLI). This method requires the user to write long strings to the CLI to submit many jobs which can become cumbersome for the user. As a workaround users wrote their own custom Python script to generate and execute the long strings via CLI. However, this method is not robust or user friendly. Therefore, the solution was to create a graphical user interface (GUI) JSI to PSquared. The JSI has to handle a large number of task submissions but also has to have a user friendly interface to make monitoring and submission of tasks trivial.

It was decided that the JSI should be web-based to allow easy access for a wide range of users. The JSI developed was based on a pre-existing JSI used at the LZ UK data centre [127]. Modern container technology was leveraged to allow for easy development and deployment of the JSI on the web via Spin, a NERSC “Containers-as-a-Service” platform which enables users to deploy and manage applications built from containers [128].

Users are able to access the JSI via a web browser. The JSI container cluster on Spin consists of a CherryPy (an object-oriented Python web framework) web server [129], MySQL database [119] and monitoring/submission daemon as illustrated in Figure 4.2.

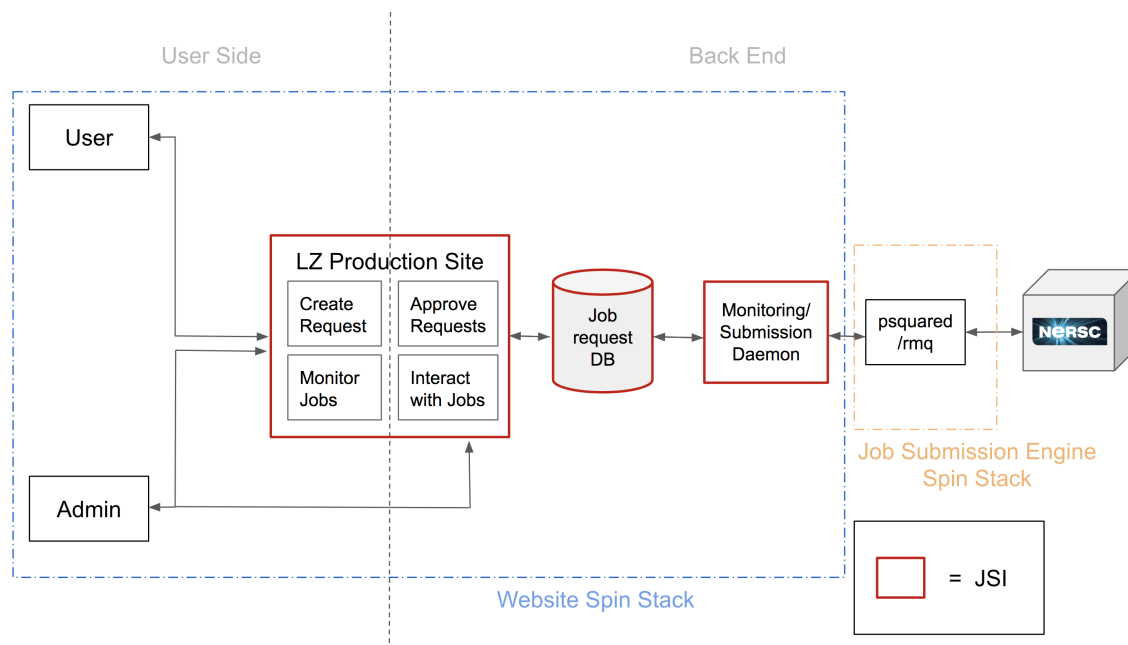


Figure 4.2: Illustration of the JSI running at NERSC interfacing with PSquared to execute simulations and analysis on the NERSC supercomputers where the red outline shows which parts are the JSI.

The CherryPy server creates and monitors job requests from users submissions via the website (as shown in Figures 4.3 & 4.4). Job requests are saved in the database and are then approved by an administrator if they are appropriate and correct. The monitoring/submission daemon periodically checks the job request database which sends any new approved requests to PSquared via the RESTful API. It also updates the status of running jobs which users can view on the website.

The screenshot shows the LZUSDC Production System web interface. The header includes the system name and user information: /test/CN=dummy user/testdn. Below the header are navigation buttons: Submit, Monitor Jobs, and Monitor RMQ. There are also buttons for monitoring different systems: monitoringd UNKNOWN, PSquared UNKNOWN, Cori UNKNOWN, Edison UNKNOWN, and Admins. The main content area shows a table of job requests. The table has columns for ID, Description, Status, Date Requested, and Requester. There is one entry with ID 1, Description 'testing job', Status 'Running', Date Requested '2019-03-22 21:43:09', and Requester 'dummy user'. Below the table is a progress bar for the running job, showing 100% progress. There are also buttons for 'New Request' and 'Export'.

ID	Description	Status	Date Requested	Requester
1	testing job	Running	2019-03-22 21:43:09	dummy user

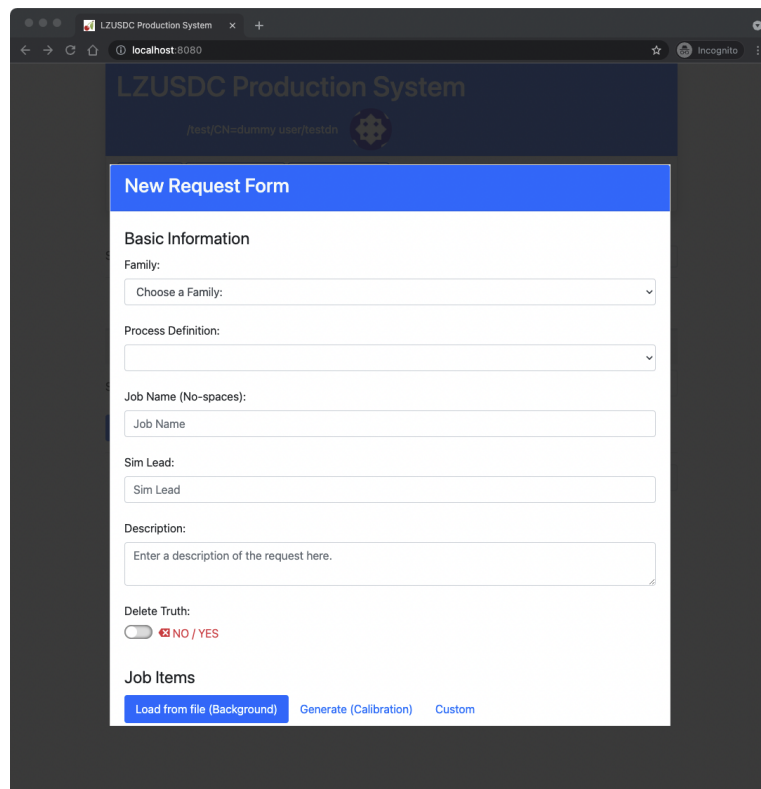
ID	Progress	Status
1.1	100%	Running
1.2	100%	Submitted
1.3	100%	Submitted

Figure 4.3: Screenshot of the JSI web interface running on Spin at NERSC. It is showing an example job request which has 1 task running and 2 other tasks submitted waiting to be executed on the NERSC Cori supercomputer nodes.

The newly developed GUI JSI is ready to be used by LZ for job submission and monitoring at NERSC; It satisfies the requirements of being user friendly and able to handle large numbers of tasks for submission. Initial documentation for users and developers has been provided.

4.2.3 LZap

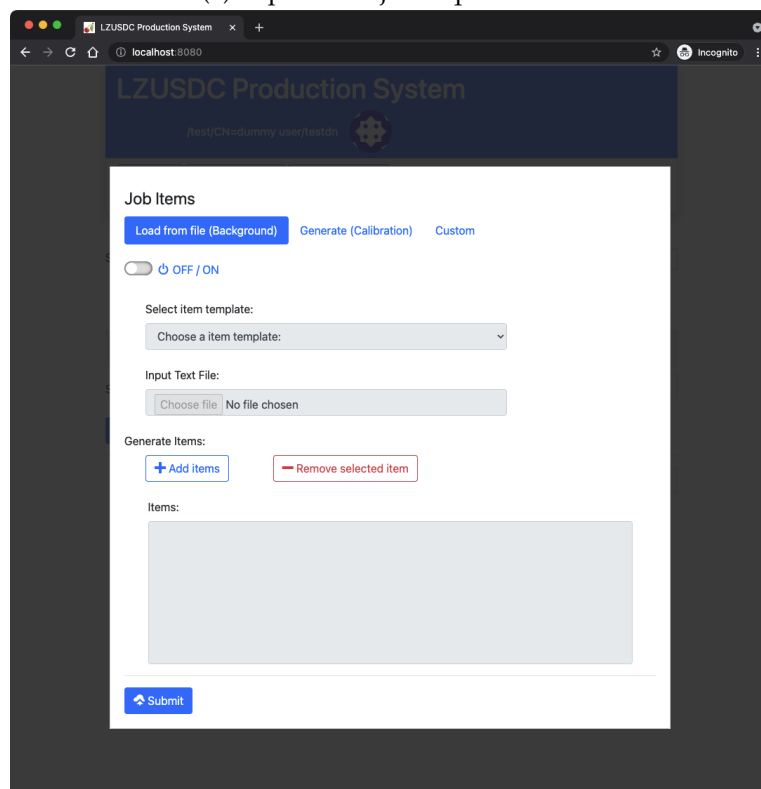
For LZap to operate on PSquared it required the creation and testing of a new job configuration within PSquared. Once LZap support was added, the performance of LZap in PSquared was investigated on the NERSC Cori supercomputer. Testing is not only important to verify that the job configuration works as intended but also to optimise the job configuration as the LZ experiment has limited NERSC computation resource credits



The screenshot shows the top portion of a web form titled "New Request Form" within the "LZUSDC Production System" interface. The form is displayed in a browser window at localhost:8080. The form fields include:

- Family:** A dropdown menu with the text "Choose a Family:".
- Process Definition:** A dropdown menu.
- Job Name (No-spaces):** A text input field with the placeholder "Job Name".
- Sim Lead:** A text input field with the placeholder "Sim Lead".
- Description:** A larger text area with the placeholder "Enter a description of the request here."
- Delete Truth:** A toggle switch currently set to "NO / YES".
- Job Items:** A section containing three buttons: "Load from file (Background)", "Generate (Calibration)", and "Custom".

(a) Top of new job request form.



The screenshot shows the bottom portion of the "New Request Form" web interface. The form fields include:

- Job Items:** A section containing three buttons: "Load from file (Background)", "Generate (Calibration)", and "Custom".
- Toggle:** A toggle switch currently set to "OFF / ON".
- Select item template:** A dropdown menu with the text "Choose a item template:".
- Input Text File:** A file selection area with the text "Choose file" and "No file chosen".
- Generate Items:** Two buttons: "+ Add items" and "- Remove selected item".
- Items:** A large, empty rectangular area for displaying generated items.
- Submit:** A blue button with a white arrow icon and the text "Submit".

(b) Bottom of new job request form.

Figure 4.4: A screen capture of the new job request form on the JSI web interface at NERSC running on the Spin platform. Users fill in the form to create a job request to be approved by an administrator before the jobs are sent to PSquared and executed on the NERSC supercomputers.

(henceforth referred to as NERSC CPU credits). These credits buy computing time on the supercomputers to perform simulations or analysis and different NERSC computational resources have different NERSC CPU credit costs per hour.

There are two Intel CPU architectures Haswell (HSW) and Knights Landing (KNL) available on the Cori supercomputer. The KNL CPU's have more physical CPU cores than HSW CPUs, 68 and 32 respectively. However, the KNL CPU's have a lower clock speed than HSW, 1.4 GHz and 2.3 GHz respectively, and less memory per node, 96 GB and 128 GB respectively.

Both Cori Intel CPU architectures HSW and KNL were tested along with the performance of LZap when using hyper-threading, a process where the physical CPU cores are split into virtual cores allowing for each CPU core to do tasks simultaneously. The benefit of hyper-threading is that it can maximise the usage of each core in a CPU. As the LZap program only utilises a single CPU core, multiple CPU cores will not decrease the processing time per event but will allow for multiple concurrent LZap tasks; thus more events processed per second.

The tests carried out executed LZap version 3.12.0 on data from the LZ MDC2. On HSW 64, 48 and 32 concurrent LZap tasks were tested with hyper-threading enabled to allow for up to 64 concurrent tasks. To compare HSW to KNL 64 concurrent LZap tasks were also tested. KNL was not tested with hyper-threading as there is not enough memory per LZap task when reaching the number of concurrent tasks which would require hyper-threading to be enabled on KNL. The results of the tests are displayed in Table 4.1.

Table 4.1: Results of the LZap PSquared tests with a single NERSC Cori supercomputer node. KNL and HSW are the two Intel CPU architectures tested, Knights Landing and Haswell respectively. HT indicates that hyper-threading was enabled.

CPU architecture	Number of concurrent tasks	Average processing time per event (s)	NERSC CPU credit cost per task
KNL	64	14.99 ± 0.38	0.67
HSW (HT)	64	4.641 ± 0.057	0.55
HSW (HT)	48	3.954 ± 0.046	0.59
HSW	32	2.919 ± 0.037	0.68

As shown in Table 4.1 LZap runs slower on KNL than HSW, this is partly due to KNL's lower clock speed which means it cannot perform as many calculations per second. KNL also has less memory per LZap task, for each of the 64 concurrent LZap tasks there was 1.5 GB of memory on KNL and 2 GB of memory on HSW. Therefore when an LZap task requires more memory than is available it has to wait for memory to be freed to continue; consequently, slowing down the program. A KNL cori node costs less NERSC CPU credits per hour than a HSW cori node, however LZap runs too slowly on KNL to benefit from the

reduction in NERSC CPU credit cost.

Executing only 32 concurrent LZap tasks on HSW resulted in the shortest average processing time per event. This is expected as each LZap task is assigned to a single physical CPU core providing each task with the most processing power and speed. However, this configuration has the highest NERSC CPU credit cost per task whereas the lowest is from 64 concurrent LZap tasks on HSW. Although with hyper-threading on HSW the average processing time per event increases, due to the increased load on the CPU, the time does not scale linearly with the number of concurrent task; thus the optimum solution is to run 64 concurrent LZap tasks on a single HSW node with hyper-threading. This optimised LZap PSquared job configuration is now being used in the LZ experiment.

4.3 Hyper

Analysing simulated and real data is a key part of modern particle physics and the ability to do this swiftly without difficulty is pivotal in the pursuit of scientific discoveries. Although researchers have access to powerful computer systems (e.g. supercomputers, distributed computing, etc.), those system tend to be complex and dealing with large datasets is often nontrivial. Unfortunately sometimes developing analysis code can be challenging and time consuming. It is crucial that analysis code is easy to write, simple to understand, works on multiple computer systems and runs quickly.

The Hyper analysis framework was developed to meet these requirements within the LZ experiment for analysis code using ROOT files, created by the ROOT software toolkit [130]. Hyper is written in Python, the popular programming language widely used in science communities, as Python is designed to be easy to learn and have high readability. The aim of Hyper is to reduce the time researches spend developing analysis code and shorten the runtime of analysis codes in order to maximise efficiency.

Hyper executes a custom user function over ROOT files in parallel via workers and merges the output into a single object (see Figure 4.5 for illustration). The user creates a custom `hyper_obj` Python class in which they write their analysis function. Using this Python class object users input the ROOT file paths, either local or XRootD [131], and can execute their custom analysis function over the data contained within the ROOT files. Users can run their code on a local CPU with multiple CPU cores via the `run_multicore_uproot` function which creates workers using the `concurrent.futures` Python library. They can also run their code on many different types of computer systems via the `dask` Python library [132] with the `run_dask_uproot` function instead. This function sends the custom analysis function to a Dask cluster, which can contain many computers, that distributes the work to Dask workers which are running on those machines. The workers read the ROOT files with the `uproot` Python library [133] into Python data structures and then perform

the users custom analysis function on the data returning the output data (for example a histogram) to be merged into a single output data object. For an example Hyper analysis code see Appendix A.

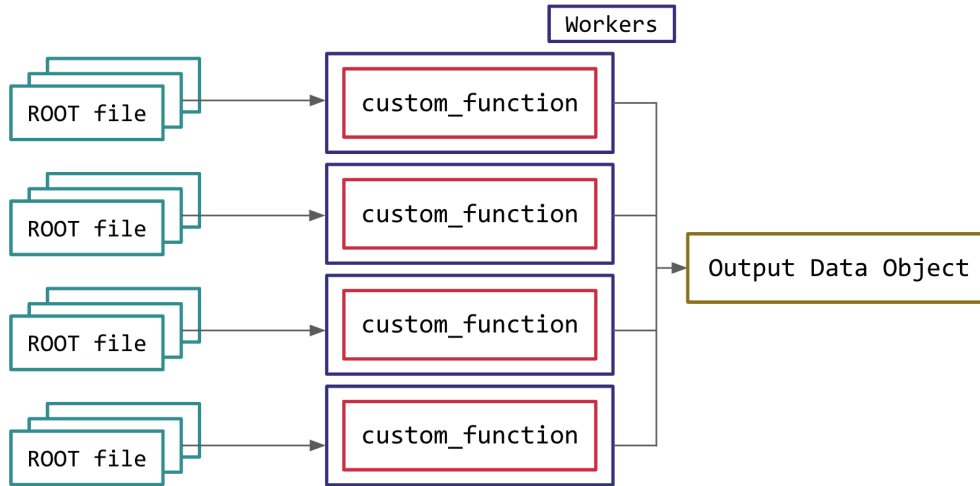


Figure 4.5: Schematic diagram of Hyper framework overview.

A simple analysis code was constructed in both the Hyper framework and a C++ framework, used by LZ, to benchmark the performance of Hyper. The analysis code consists of multiplying different event variables, applying simple cuts and then histogramming the remaining events. The benchmark was carried out on a single NERSC Cori supercomputer node on the same LZ MDC3 ROOT dataset. Figure 4.6 shows the number of events processed per second by the simple analysis code written in the Hyper and C++ frameworks.

It is clear from Figure 4.6 that in every case tested utilising more CPU cores for the analysis increased the number of events that could be processed per second as would be expected. The simple analysis code written with Hyper was able to process more events per second than the analysis code written with the C++ framework; however, once the code was optimised in the C++ framework it was able to process more events per second than the code in Hyper. Although the optimisation increased the analysis code performance it required C++ expertise and time to optimise the code.

The Hyper framework provides users who want to work in Python the option to write fast analysis code. Additionally the framework contains inbuilt tools to allow users to easily execute their analysis code on supercomputers and on distributed computers through dask, whereas no such tools exist in the C++ framework.

The LZ experiment is currently using the Hyper framework is to analyse real LZ detector data. Chapter 7 explores LZ commissioning data with analysis constructed in the Hyper framework. There are future plans to support Hyper running on GPUs which would allow

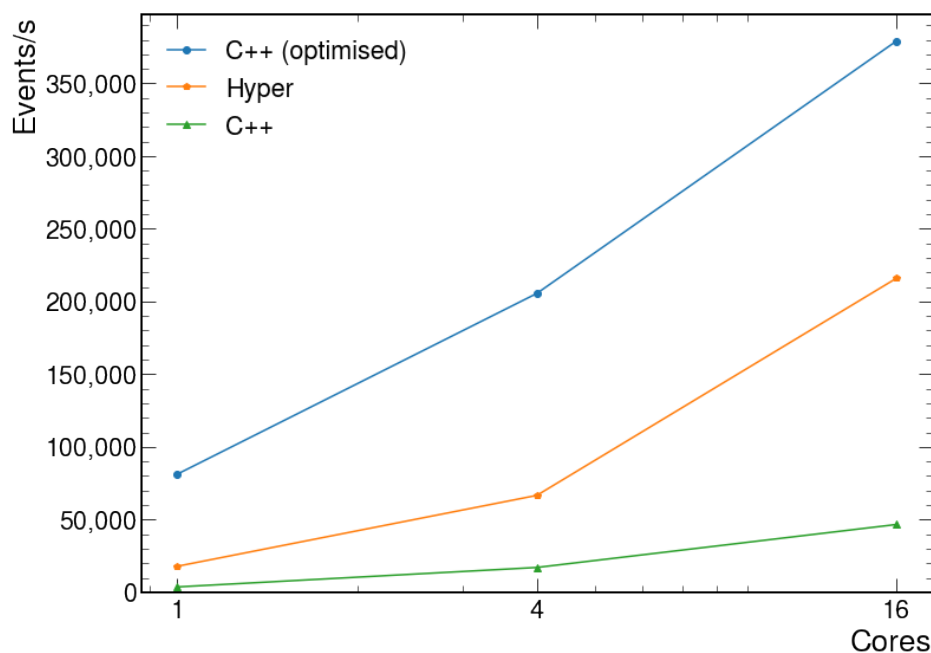


Figure 4.6: Number of events processed per second in a simple analysis code written with Hyper and C++ frameworks.

users to take advantage of GPUs in their analysis significantly increasing the number of events which can be processed per second.

4.4 LEOPARD

Being able to easily and quickly plot data is important for researchers including the LZ experiment. During the commissioning phase of the LZ detector the daily incoming data needs to be explored and understood in order to tune and validate the LZ detector settings. LEOPARD (Lz Exploring Online PAcKage Root Data), a Python web-based plotting tool, was developed to assist in this data exploration.

The LEOPARD Python tool is a website where users can plot LZap ROOT data in 1D and 2D histograms with cuts applied. Users can plot data located on either the USA or UK data centres; LEOPARD will then execute the cuts on the data and return the histograms requested.

Using the dash Python library [134] a prototype website was constructed. On the website users specify the input data, any cuts to apply and what to plot in 1D and 2D histograms (as displayed in Figure 4.7). The input data can either be a list of LZap ROOT file paths or an LZ data catalogue request written in YAML (e.g. specifying files created on a certain day). The LZ experiment has a software documentation website where users

can find information on all the different event variables in an LZap ROOT file. Using this information users construct analysis cuts with mathematical expressions and determine exactly what variables to plot. The user also decides the number of bins and the range of the histogram.

When the green "GENERATE" button is pressed the Hyper framework, as discussed in Section 4.3, runs very quickly in the background executing cuts and filling histograms with variables or expressions specified by the user. The histograms, created by the boost-histogram Python library [135], are then plotted with mplhep, a Python plotting library for high energy physics [136], and displayed to the user in the browser (as seen in Figure 4.8).

The screenshot shows a web browser window with the URL `localhost:8252`. The page title is "LEOPARD (Lz Exploring Online PAcKage Root Data) Quickly and easily plot LZap Data from the LZ data catalog with Hyper". The page features logos for LEOPARD and Hyper on the left, and a stylized 'LZ' logo on the right. The main content area is a form titled "Inputs" and "Hyper Job".

Inputs

Data Catalog Request

```
production_version: 'MDC3'
usecase: 'SimRQ'
software_versions: 'lzap-4.7.0'
```

OR

File Path List

Enter list of file paths

Hyper Job

Aliases

```
aliases:
- name: 'radius_cm'
var: ...
```

Cuts

```
cuts:
- name: 'single_scatters'
var: ...
```

Histograms

```
hists:
- name: 's1-s2-hist-ss'
var: ...
```

A green "GENERATE" button is located at the bottom center of the form. A blue circular button with "<>" is located at the bottom right of the form.

Figure 4.7: A screenshot of the prototype LEOPARD Python website user input form. Users can input data catalogue requests with specified cuts and histograms for LEOPARD to execute and return the histograms.

The prototype website demonstrates the ease and speed at which researchers can explore LZ detector data. As LEOPARD is a website it requires no installation or setup for

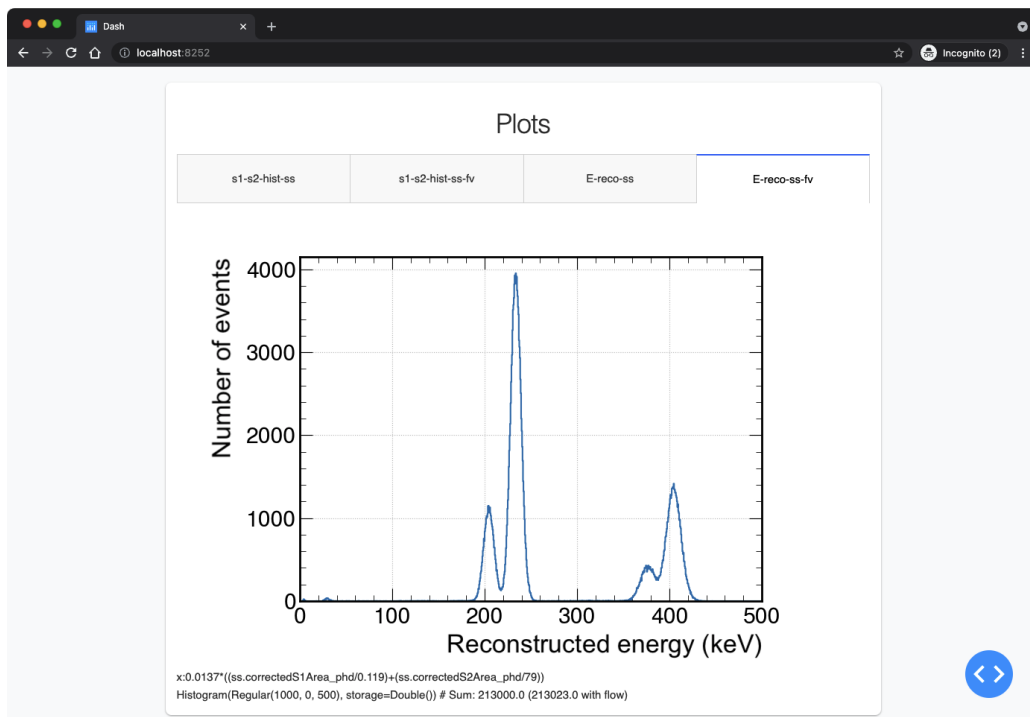


Figure 4.8: Screen capture of plots produced by a user request on the prototype LEOPARD Python website. Users can browser the different plots generated by the request.

the user and it is quick to produce plots with Hyper processing the data in the background. The LEOPARD website could be hosted on the Spin platform to provide access for NERSC LZ users and at Imperial College London for the UK LZ users. Further development time is required to transition the prototype website into a live website as LZ user authentication protocols would need to be implemented and graphical issues would need to be fixed.

Chapter 5

Cavern wall gamma rays

5.1 Motivation

As discussed in Chapter 2, LUX and LZ have many schemes in place which tackle the multitudes of backgrounds. It is critical that backgrounds are well understood and mitigated in order to obtain the high sensitivity required for WIMP detection.

The source of background outside the water tank arises from the Davis cavern rock surrounding the detector. High energy gamma rays and neutrons are produced in the cavern rock from either the naturally occurring uranium, thorium and potassium or induced by atmospheric muons. Both the LUX and LZ detectors were placed inside a large water tank to significantly attenuate the γ -flux in the detector. A low-radioactivity steel pyramid located below the detector in the cavern floor also provided further shielding. Any remaining background from these gamma rays should be suppressed with event selection cuts.

It is salient to check the γ -flux is substantially reduced by these schemes and also characterise this background. Cavern wall gamma rays produce electron recoils (ER) contributing to the WIMP search background in LUX and LZ, as well as other physics studies such as neutrinoless double beta decay ($0\nu\beta\beta$). Although ER rejection in LZ is assumed to be 99.5% efficient (based on LUX measurements and extrapolation to LZ), it is not perfect, therefore it is still very important to understand the ER background.

Due to the high suppression factor, to fully understand this background $\mathcal{O}(10^{16})$ initial decays in the rock need to be simulated. This is computationally impractical to perform using standard GEANT4 simulations. Instead it requires the simulation to be broken up into several stages employing an event biasing method, described in the following section.

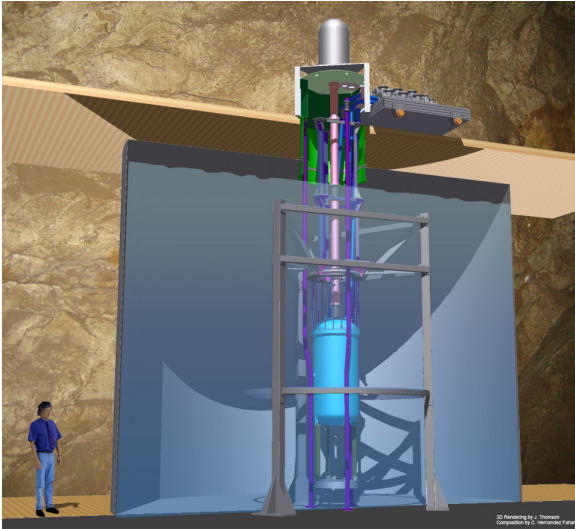
This chapter will explore the event biasing cavern wall gamma ray simulations undertaken to determine the background to the WIMP search for LUX and LZ. Results of this study have been published in Ref. [110]. Also covered are the cavern wall gamma ray background simulations for the LZ $0\nu\beta\beta$ search and the RockGammas BACCARAT generator created to simplify simulating this background.

5.2 Event biasing simulations

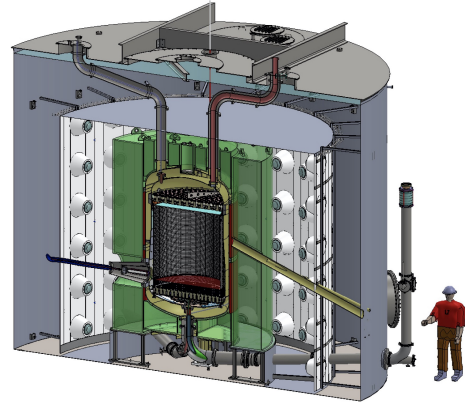
The water tank, shown in Figure 5.1, and the steel pyramid provides significant shielding for the LUX and LZ detectors; therefore, many decays need to be simulated in order to produce events in the liquid xenon (LXe) after standard background cuts are applied. The number of simulated decays (N_{decay}) of a radioactive isotope required to produce a desired number of events in the TPC (N_{TPC}) can be estimate with the following equation:

$$N_{decay} = \frac{M_s[\text{kg}] \cdot A_s[\text{Bq kg}^{-1}] \cdot N_{TPC}}{B[\text{s}^{-1}]} \quad (5.1)$$

where A_s is activity, M_s is mass of component where the γ -ray sources are located and B is an estimate of the background contribution in the detector per second.



(a) LUX detector in the water tank.



(b) Cutaway of the LZ detector in the water tank.

Figure 5.1: 3D renderings of the LUX and LZ detectors in the water tank ($h \times d = 592.8 \text{ cm} \times 762 \text{ cm}$) in the Davis cavern. Inverted steel pyramid under water tank not shown. Figures (a) & (b) from Ref. [97] & [60] respectively.

For example, to produce ~ 100 events in the LZ TPC after standard background cuts are applied from ^{232}Th decays in the cavern wall requires 1.75×10^{16} simulated decays, calculated using a previous estimate of the background rate ($B \sim 8.6 \times 10^{-8}$ [137]). To simulate this with standard GEANT4 simulations would be computationally impractical. Therefore, in order to achieve high statistics event biasing simulations are necessary.

Event biasing accelerates the simulation of desired events. The simulation of the particle transport through cavern is divided into multiple consecutive stages. The gamma rays which successfully traverse the stage are saved and then re-propagated numerous times in the next stage, as illustrated by Figure 5.2.

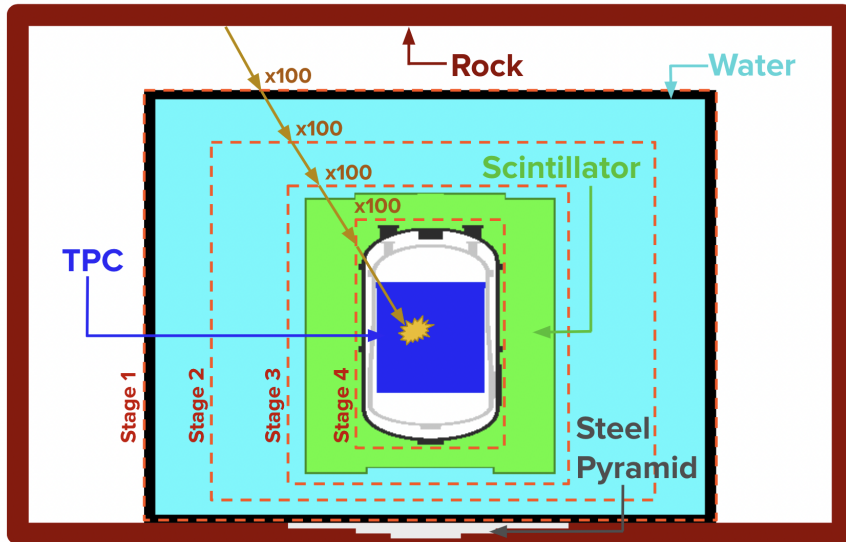


Figure 5.2: Illustration of the event biasing method implemented into BACCARAT and LUXSim allowing effective simulation of large number of decays. The red-dashed lines represent the stage boundaries. Note there is a scintillator in the LZ detector only. Relative dimensions in the Figure not to scale. Figure published in Ref. [110].

In the initial stage, the decay of radioactive isotopes in the cavern walls are simulated with `GEANT4` using data libraries from the Evaluated Nuclear Structure Data File [138] and the Livermore Evaluated Atomic Data Library [139]. The path of gamma rays produced from these decays are simulated and any that reach the surface of a cylinder just outside the water tank are saved to a file.

In the subsequent stages, the gamma rays are re-propagated numerous times with the same initial position and momentum and are then transported to the stage boundary, with the surviving gamma rays undergoing re-propagation in the next stage. These boundaries, shown as the red-dashed lines in Figure 5.2, are defined as concentric cylinders in the simulation geometry. This re-propagation method effectively increases the initial number of decays by a factor of $f = \prod_{i=1}^n m_i$, where m_i is the stage multiplication factor and n is the number of stage boundaries. In the final stage, interactions within the LXe (and scintillator for LZ) are recorded for further analysis.

Both LUXSim and BACCARAT have been modified, for LUX and LZ respectively, in order to split particle transport into several user definable stages. David Woodward (University of Sheffield, UK) carried out the original modification to LUXSim and Sally Shaw (University of California, Santa Barbara, USA) ported the modification across to BACCARAT. The modification allowed particles to be terminated depending on which user defined volume they were located in. As physical volumes within the simulation geometry are not allowed to overlap an innovative solution was required. Parallel worlds, a

GEANT4 feature which allows the creation of volumes in a parallel world permitting overlapping volumes, was employed to enable user defined stage boundaries. LUXSim and BACCARAT are now able to terminate the transport of a particle once it crosses into a parallel volume defined by the user. These particles can be saved and later re-propagated in another stage.

The daughter decays from ^{232}Th , ^{238}U and ^{40}K dominate the cavern wall gamma rays. Therefore, event biasing simulations of the full decay chains were undertaken with LUXSim and BACCARAT assuming secular equilibrium for the LUX and LZ detectors respectively.

Using this event biasing method, a batch of 100 simulations each with 10^7 initial primary decays was simulated through additional 4 separate stages with a stage multiplication factor of 100. This resulted in 10^{17} effective number of primary decays. For ^{40}K only the final stage multiplication factor was increased to 1000 to boost statistics yielding 10^{18} effective number of primary decays.

In the simulation geometry a 30 cm shell of rock was constructed as the source volume for these decays, as this thickness of rock was determined to contribute substantially to the γ -flux [104]. Additionally a cylindrical section of rock was added below the steel pyramid beneath the water tank. The positions of the stage boundaries in the geometry was chosen in order to ensure that the gamma rays travel through comparable amounts of shielding in every stage on all sides, rough approximations of the boundaries are given in Figure 5.2. The amount of shielding in each stage is also important as too much in one stage could incorrectly bias the simulation if only a small number of gamma rays survive.

There could be potential biasing of the results as the surviving cavern wall gamma rays undergo re-propagation several times. Although this dominates the systematic uncertainty of the simulations it has been concluded from previous testing of multiple event biasing simulations that the results are consistent within 20%.

5.3 Analysis

The LUX and LZ experiments use similar approaches to determine WIMP-like events from simulated data. The energy depositions produced in the simulation are converted to prompt and secondary scintillation light pulse areas, S1 & S2 respectively, via the background analysis chains developed for each experiment. Both sets of analysis software utilise the NEST (Noble Element Simulation Technique) [112] package with parameterisations of the detector response. After this conversion, standard background analysis cuts are applied to select WIMP-like events from the simulated data.

The analysis methods employed by the LUX and LZ experiments are very alike. In both experiments the standard background analysis cuts, defined in Section 2.6, reject events with multiple scatters, mis-reconstructed wall events near the edge of the time projection

chamber (TPC) and those outside of the WIMP search region of interest (ROI). Although only the LZ experiment has active veto detectors (xenon skin & outer detector (OD)) allowing it to reject TPC events with time-coincident signals detected in either of its veto detectors.

In the LUX analysis to boost statistics energy depositions up to 100 keV were considered as the initial simulation analysis revealed this background was flat below 100 keV. This allows more WIMP-like events to be included which can then be scaled down later to the WIMP ROI, approximately 1.5–6.5 keV_{ee} for ERs and 6–30 keV_{nr} for nuclear recoils (NR).

For the LZ analysis it is important to note that energy depositions within the OD were only saved in the final simulation stage in order to reduce the disk space required to store the simulation output. Therefore, some γ -ray OD triggers could have been missed suggesting that the LZ results are conservative.

Following the analysis cuts normalisation is applied to determined the equivalent run time corresponding to the number of simulated decays:

$$t = \frac{N_{decay}}{M_s[\text{kg}] \cdot A_s[\text{Bq kg}^{-1}] \cdot 86400[\text{s day}^{-1}]} \quad (5.2)$$

where t is run time (days) and M_s is mass of component where the γ -ray sources are located (30 cm shell of rock = 1.19×10^6 kg). The following activities were used to normalise the simulations ^{232}Th - 13 Bq/kg, ^{238}U - 29 Bq/kg and ^{40}K - 220 Bq/kg, determined from γ -ray spectra measurements taken in the Davis cavern [140].

5.4 Results

5.4.1 Attenuation of gamma rays in water

The simulations confirm the significant attenuation of the γ -flux the water tank provides as can be seen in Figure 5.3, that shows the γ -ray energy spectra at the end of each stage (except the final stage) for all simulated decay chains in BACCARAT. As Figure 5.3 shows there is a substantial difference in the γ -flux between the end of stage 1 and the end of stage 4, where the gamma rays have been considerably attenuated by the water as they reach the outer cryostat vessel. It is clear from Figure 5.3a that the largest contributor to the overall flux at the end of stage 4 is the 2.6 MeV line from ^{208}Tl .

The majority of gamma rays which reach the TPC are from the top due to less shielding, see the ER energy deposition positions in Figure 5.4. Due to the large steel pyramid beneath the water tank there are very few gamma rays which reach the TPC from underneath. Figure 5.4 also displays the effectiveness of the standard background analysis cuts to remove these γ -ray ERs.

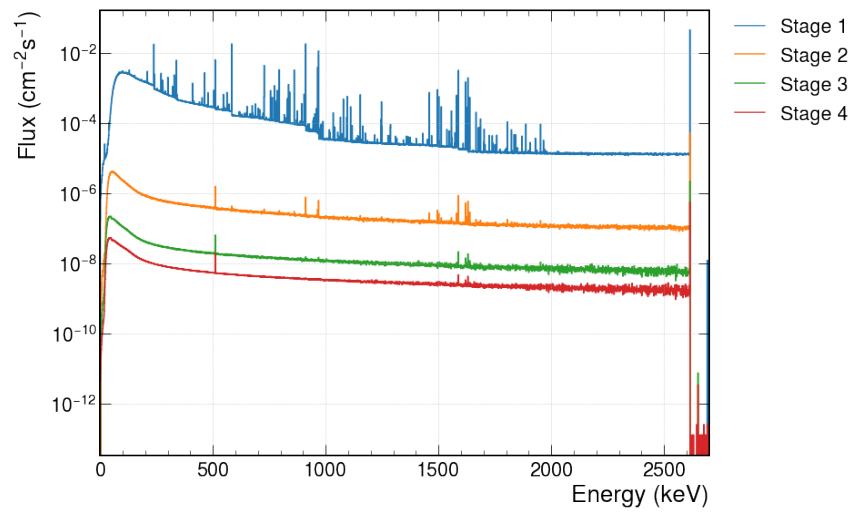
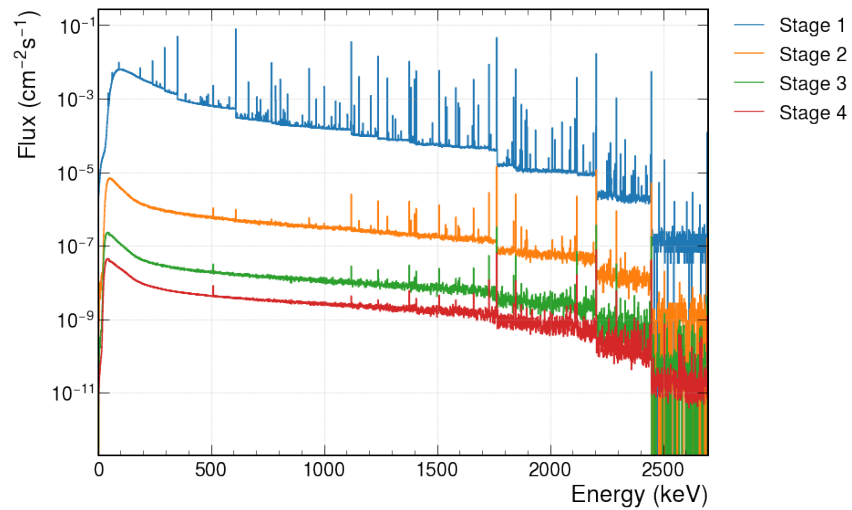
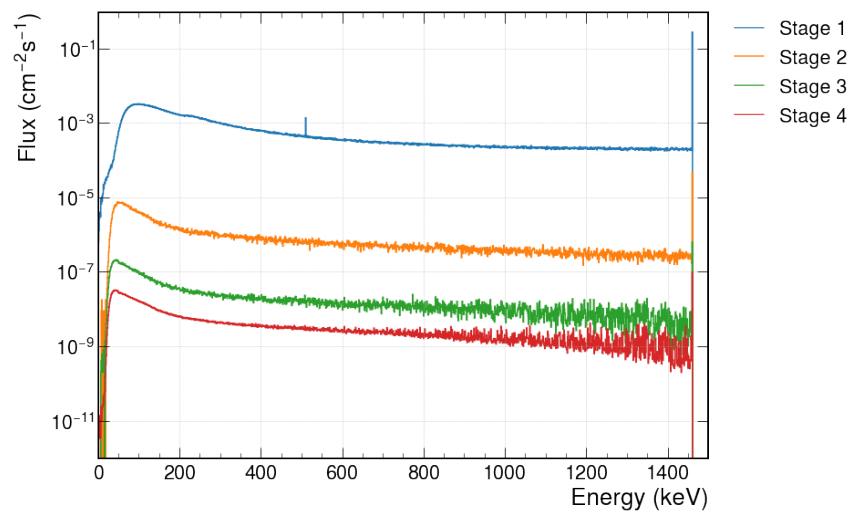
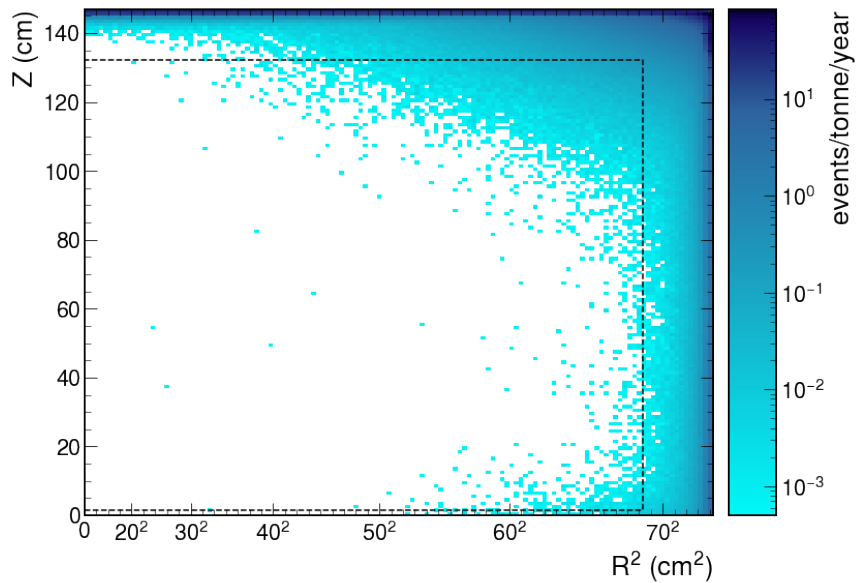
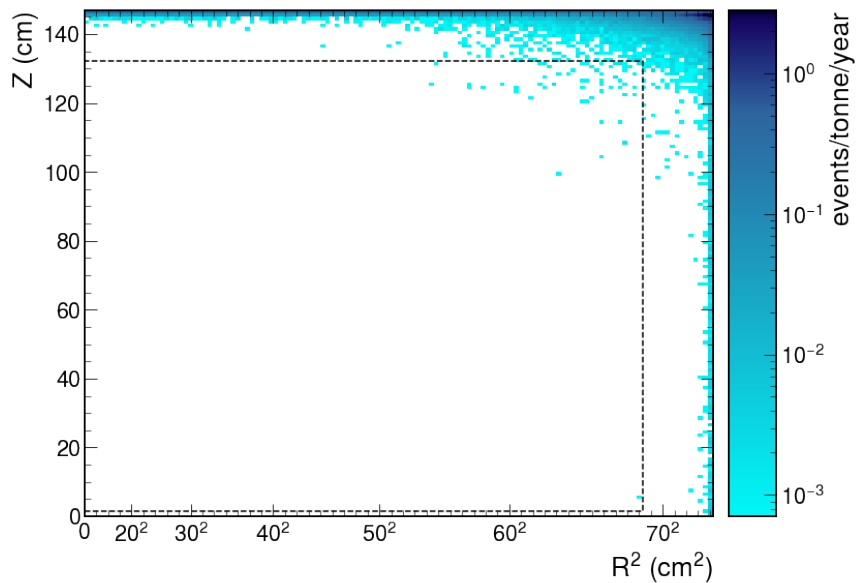
(a) ^{232}Th .(b) ^{238}U .(c) ^{40}K .

Figure 5.3: γ -ray energy spectrum at the end of each simulation stage (except the final stage) produced in BACCARAT for LZ by ^{232}Th , ^{238}U and ^{40}K decay chains.



(a) No cuts applied.



(b) Standard background cuts applied (except fiducial volume).

Figure 5.4: Z position (along the drift field) vs radius squared R^2 for ER energy depositions up to 100 keV from ^{232}Th BACCARAT simulations. The black dashed line represents the 5.6 tonne fiducial volume with the cathode located at $z = 0$ cm. No cuts were applied in (a). The standard background cuts (except for fiducial volume) have been applied in (b), highlighting the effectiveness of the single scatter, outer detector, xenon skin and WIMP ROI cut.

5.4.2 LUX results

The energy spectra of ERs from the cavern wall gamma rays produced by ^{232}Th , ^{238}U and ^{40}K decay chains simulated in the LUX detector with LUXSim are shown in Figure 5.5. The shielding around the LUX detector has considerably diminished the γ -flux detected inside the TPC. Analysis cuts used in conjunction with the shielding also drastically minimise the cavern wall γ -ray background for the WIMP search, as can be seen in Figure 5.5.

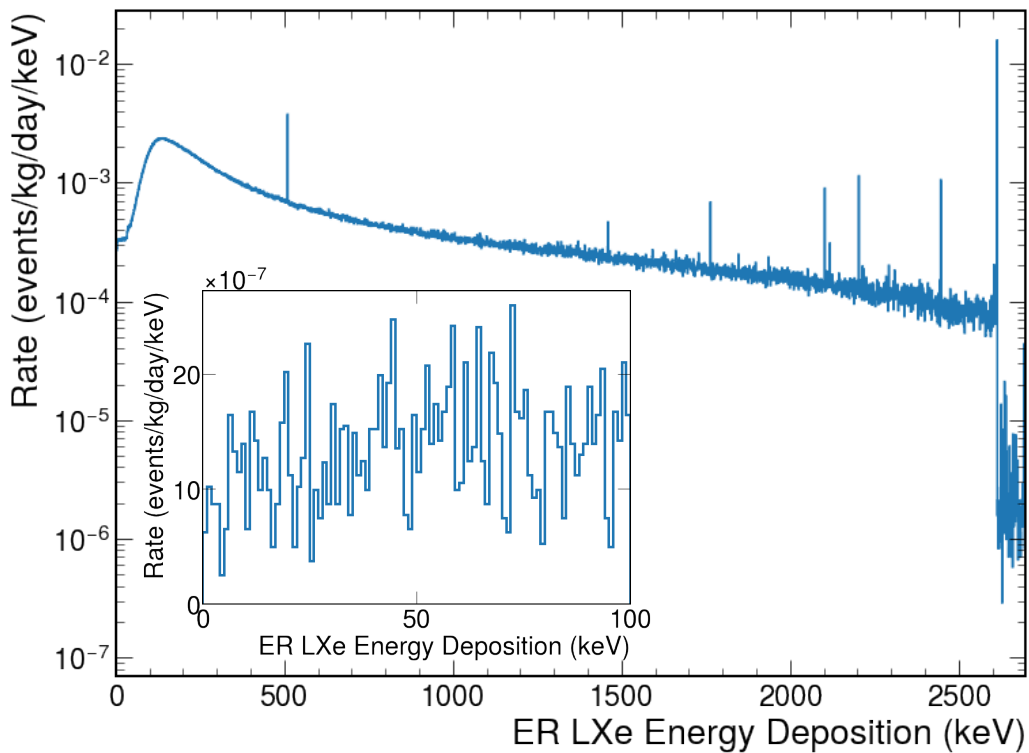


Figure 5.5: Energy spectra of simulated ERs from cavern wall gamma rays produced by LUXSim. These gamma rays are located within the TPC and no standard background cuts have been applied. The insert presents the energy spectra at low energies after standard cuts are applied.

The results of the event biasing simulations undertaken with LUXSim are given in Table 5.1. The cavern wall γ -ray background up to 100 keV in a 300 day WIMP search (LUX Run4 was 332 days) for the LUX detector would be 4.31 ± 0.15 events. The LUX total observed background rate, $(3.6 \pm 0.4) \times 10^{-3}$ events/kg/day/keV [99], is much higher than the total rate of the cavern wall gamma rays, displayed in Table 5.1, showing it is a sub-dominant background.

Table 5.1: Results from LUXSim cavern wall γ -ray event biasing simulations. Calculations consider energy depositions up to 100 keV and use a 105.4 kg fiducial volume. No ER/NR discrimination cut applied. Errors quoted are standard error.

Isotope	Simulated run time (days)	WIMP-like events	Background events in 300 days after cuts	Rate (10^{-6} events/kg/day/keV)
^{232}Th	7.51×10^4	853	3.41 ± 0.12	1.08 ± 0.04
^{238}U	3.37×10^4	97	0.86 ± 0.09	0.27 ± 0.03
^{40}K	4.44×10^4	6	0.04 ± 0.02	0.013 ± 0.005
Total			4.31 ± 0.15	1.36 ± 0.05

5.4.3 LZ results

The energy spectra produced by BACCARAT of the ERs from cavern wall gamma rays in the LZ detector is displayed in Figure 5.6. As with the LUX TPC, the γ -flux inside the LZ TPC has been heavily suppressed due to the shielding and the standard background cuts applied are highly effective at significantly reducing the background for the WIMP search.

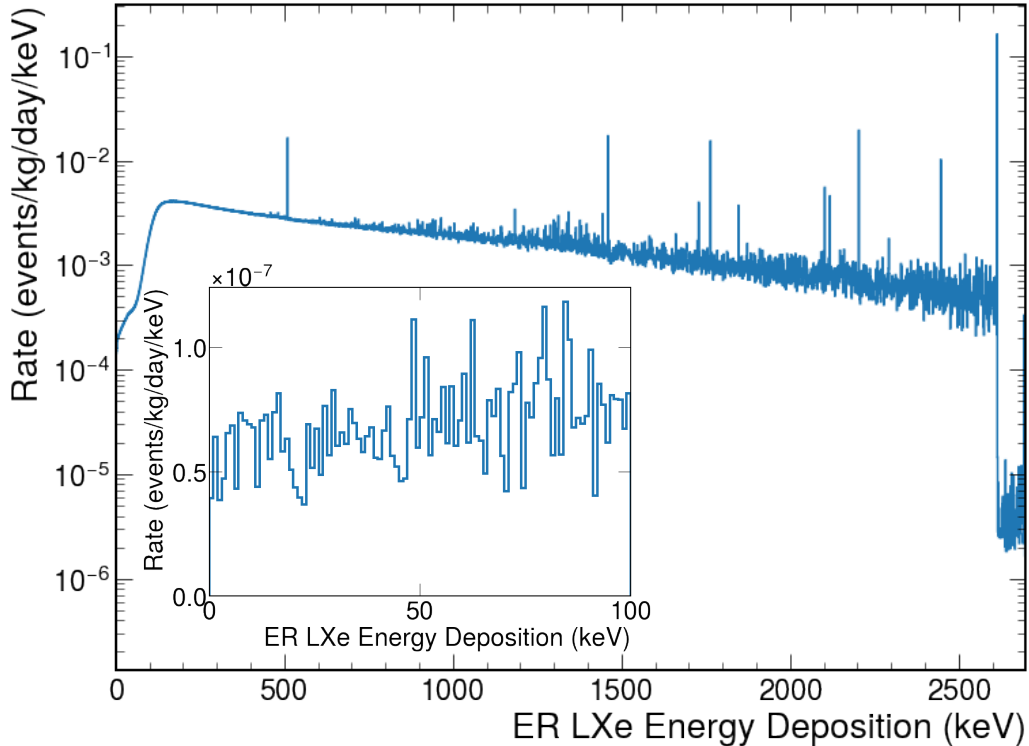


Figure 5.6: The cavern wall gamma rays ER energy spectra produced by BACCARAT simulations. These gamma rays are located within the TPC and no standard background cuts have been applied. The insert presents the energy spectra at low energies after standard cuts are applied.

Table 5.2 provides the results of the BACCARAT event biasing cavern wall γ -ray simulations. After standard background cuts are applied in a 1000 day WIMP exposure only 1.81 ± 0.19 events would remain. This is close to a previous rough estimation of the background which suggested ~ 7 events would be detected after all cuts [137]. Again the cavern wall γ -ray background is a sub-dominant background to the LZ WIMP search. This is due to the cavern wall gamma rays making minimal contribution to the background in comparison to many other ER background sources in LZ, such as xenon contaminants and physics background sources which contribute 819 and 258 background events in 1000 day WIMP search after cuts respectively [60]. The total rate of cavern wall gamma rays observed in the LZ detector, $(0.065 \pm 0.007) \times 10^{-6}$ events/kg/day/keV, is considerably lower than the rate observe in the LUX detector, $(1.36 \pm 0.05) \times 10^{-6}$ events/kg/day/keV, highlighting the success of the new background reduction methods deployed in LZ.

Table 5.2: BACCARAT cavern wall γ -ray event biasing simulation results. Calculations apply no ER/NR discrimination and use a 5.6 tonne fiducial volume. Errors quoted are standard error.

Isotope	Simulated run time (days)	WIMP-like events	Background events in 1000 days after cuts	Rate (10^{-6} event/kg/day/keV)
^{232}Th	7.50×10^4	78	1.04 ± 0.12	0.037 ± 0.004
^{238}U	3.37×10^4	17	0.50 ± 0.12	0.018 ± 0.004
^{40}K	4.44×10^4	12	0.27 ± 0.08	0.010 ± 0.003
Total			1.81 ± 0.19	0.065 ± 0.007

5.5 Gamma background from cavern walls for neutrinoless double beta decay

Although the cavern wall γ -ray background is sub-dominant for the LZ WIMP search the high energy gamma rays produced by the ^{232}Th and ^{238}U decay chains in the cavern rock contribute substantially to the LZ $0\nu\beta\beta$ search background.

Two-neutrino double beta decay ($2\nu\beta\beta$), where a nucleus emits two electrons and two antineutrinos, has already been observed in ^{136}Xe [141]. If neutrinos are their own antiparticles (known as Majorana particle) then $0\nu\beta\beta$, where a nucleus only emits two electrons, should be possible. In $0\nu\beta\beta$ the two resulting electrons carry almost all of the total energy produced by the double beta decays, therefore, in the beta spectrum there should be a mono-energetic peak at the double beta decay Q-value, $Q_{\beta\beta}$. However, to date there have been no clear observations of $0\nu\beta\beta$.

LZ aims to search for $0\nu\beta\beta$ with ^{136}Xe which at natural abundance is ~ 600 kg of the

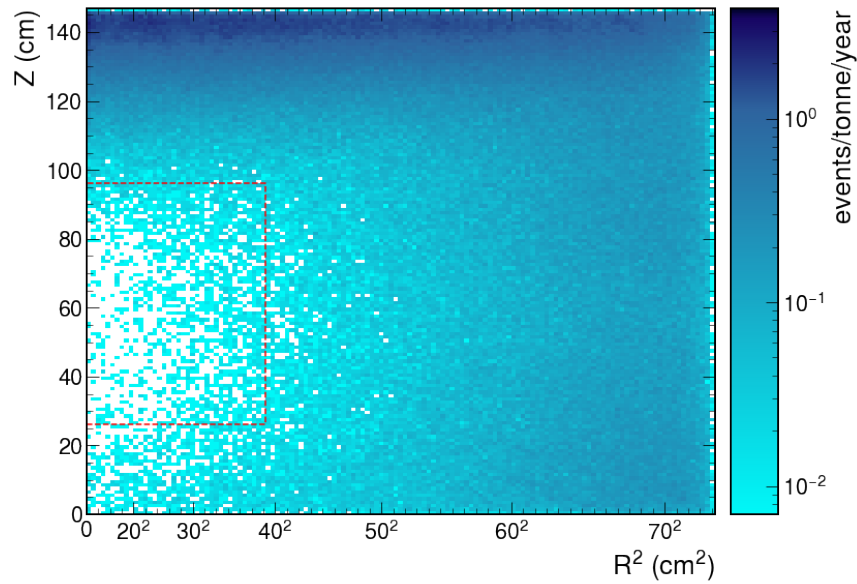
7 tonne active LXe mass of the TPC. From the analysis of the cavern wall gamma ray simulations it was determined that extra shielding above the water tank was required for the $0\nu\beta\beta$ search to reduce the incoming γ -flux from above. To provide extra shielding an additional square steel plate (2.7 m \times 2.7 m) with 8 cm thickness was laid directly on top of the water tank.

This extra shielding was added to the simulation geometry in BACCARAT and new cavern wall gamma ray simulations were undertaken. For these simulations the event biasing method in BACCARAT was modified slightly as ^{136}Xe $2\nu\beta\beta$ has a high Q-value, $Q_{\beta\beta} = 2457.83 \pm 0.37$ keV [142], therefore gamma rays with energies below 2 MeV can be ignored. BACCARAT was modified to save only gamma rays with energies above 2 MeV in order to produce higher statistics with less CPU time and to reduce the disk space required to store the simulation output.

The cavern wall gamma ray event biasing simulations performed have 10^{16} and 10^{17} effective number of primary decays for ^{232}Th and ^{238}U decay chains respectively. The approach to analysing these simulations is similar to that of the WIMP search; events are rejected using single scatter, fiducial volume, active veto detectors and energy ROI cuts. However, the analysis cuts used to determine the $0\nu\beta\beta$ search background differ [143]. Single scatters are defined as events with $\Delta_Z < 0.3$ cm, where Δ_Z is the vertical separation between multiple vertices. The redefined fiducial volume, $26 < Z < 96$ cm and $R < 39$ cm, encompasses less LXe (967 kg). The time-coincident signal windows for the xenon skin and OD active veto detectors are reduced to 1 μs and triggered for energy depositions larger than 100 keV. The energy ROI is $Q_{\beta\beta} \pm 1\sigma$ ($2433.3 < E < 2482.4$ keV) as an energy resolution (σ/E) of 1% is considered.

Figure 5.7 confirms that the additional top steel plate provides the necessary shielding to substantially reduce the γ -flux in the TPC coming from above the water tank. There is a significant difference in the fiducial volume size between the WIMP and $0\nu\beta\beta$ search, as can be seen in Figure 5.7. This is due to the high energy cavern wall gamma rays travelling further into the TPC.

The energy spectra of the BACCARAT cavern wall gamma rays simulation is displayed in Figure 5.8. As seen in both Figure 5.7b & 5.8b the $0\nu\beta\beta$ background cuts considerably reduce the cavern wall γ -ray background. However, the high energy γ -rays are still a major contributor to the $0\nu\beta\beta$ search background. Results of these simulations were included in Ref. [143].



(a) No cuts applied.

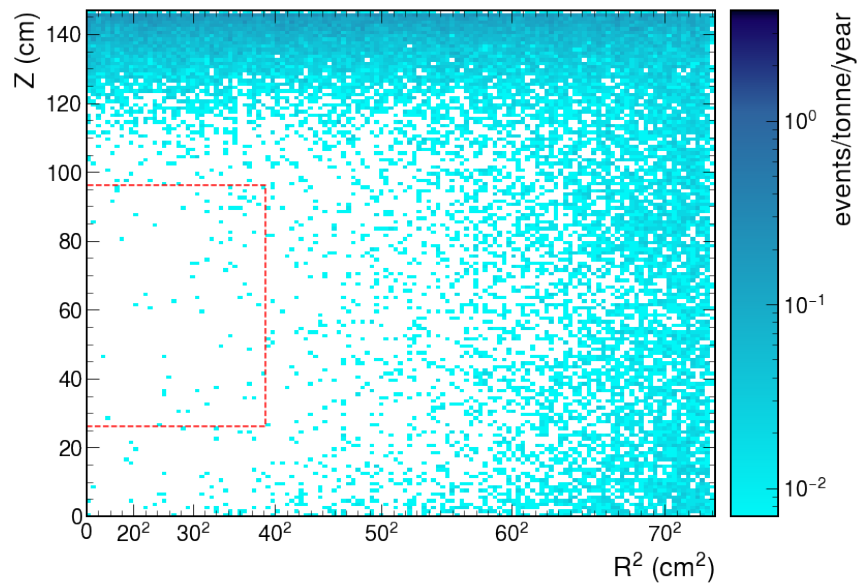
(b) $0\nu\beta\beta$ background cuts applied (except fiducial volume).

Figure 5.7: Z position (along the drift field) vs radius squared R^2 for ER energy depositions in the energy ROI, $Q_{\beta\beta} \pm 1\sigma$, from ^{232}Th BACCARAT simulations. The red dashed line represents the 967 kg fiducial volume with the cathode located at $z = 0$ cm. No cuts were applied in (a). $0\nu\beta\beta$ background analysis cuts (except for fiducial volume) were applied in (b), displaying the significant reduction to the $0\nu\beta\beta$ search background.

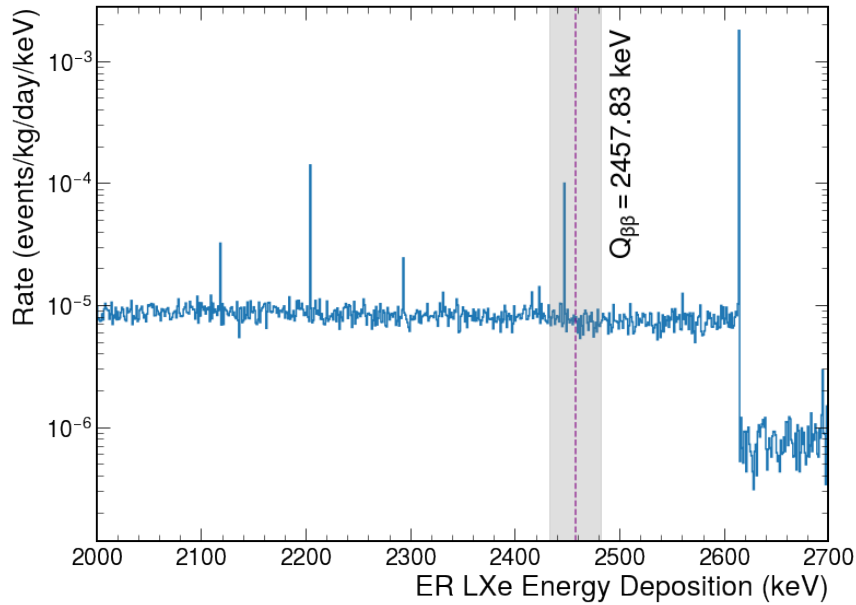
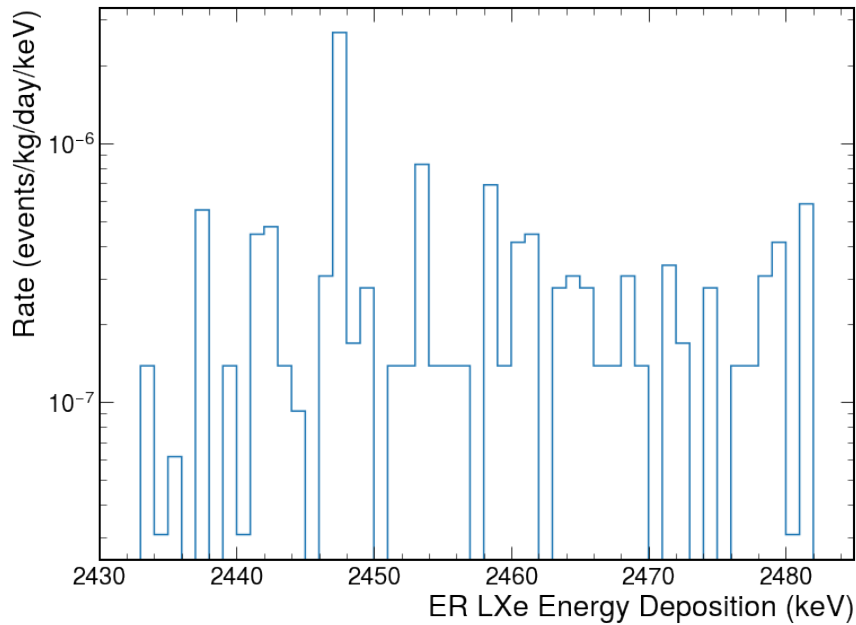
(a) $0\nu\beta\beta$ fiducial volume cut applied.(b) All $0\nu\beta\beta$ background cuts applied.

Figure 5.8: BACCARAT simulation energy spectra of ERs from the cavern wall gamma rays. These gamma rays are located within the inner 967 kg LXe fiducial volume. Around the $Q_{\beta\beta}$, dashed purple, is a grey band representing the energy ROI, $Q_{\beta\beta} \pm 1\sigma$, in (a). All $0\nu\beta\beta$ background cuts were in applied in (b).

5.6 RockGammas BACCARAT generator

Although the event biasing method deployed in LUXSim and BACCARAT has greatly decreased the CPU time required for cavern wall gamma rays simulations the effort and time needed to simulate is still sizeable. Additional cavern wall gamma ray simulations could be performed in order to increase statistics and include all OD energy depositions from gamma rays reaching the TPC. Therefore, a new BACCARAT generator was created to provide a quick and simple way to simulate the cavern wall gamma rays in the LZ TPC.

Working in partnership with Sally Shaw (University of California, Santa Barbara, USA) we developed a BACCARAT generator, called RockGammas, that uses information about cavern wall gamma rays from a previous simulation to create representative gamma rays outside the LZ TPC to be simulated. The final position, direction and energy of the gamma rays in stage 3, just outside the OD (see Figure 5.2), from a previous event biasing simulation was saved into a 7D THnSparse histogram. The generator samples the histogrammed distribution to obtain a random initial position, direction and energy for the γ -ray before simulating its transport through the LZ detector. This method reduces the complexity and time needed to simulate cavern wall gamma rays as the initial stages of event biasing simulations can be skipped.

Cavern wall gamma rays from ^{232}Th and ^{238}U decay chain event biasing BACCARAT simulations have been stored in this generator. In MDC3 the RockGammas generator was deployed as part of a number of ER background simulations for the LZ WIMP search.

5.7 Conclusion

High statistics simulations of the cavern wall gamma rays in both the LUX and LZ detectors were carried out using an event biasing method with LUXSim and BACCARAT respectively.

As expected the simulations confirmed significant attenuation to the γ -flux inside the LUX and LZ detectors with most of the gamma rays coming from the top where there is less shielding. Analysis of the simulations showed that the cavern wall γ -ray background is a sub-dominant background in both detectors and does not provide an issue for WIMP searches, see Tables 5.1 & 5.2. The success of the new background reduction methods deployed in LZ can also be seen when comparing the total cavern wall γ -ray rate observed in both detectors; $(1.36 \pm 0.05) \times 10^{-6}$ events/kg/day/keV and $(0.065 \pm 0.007) \times 10^{-6}$ events/kg/day/keV, in LUX and LZ respectively.

Modified BACCARAT simulations were performed to understand the impact of the high energy cavern wall gamma rays on the $0\nu\beta\beta$ search with extra steel plating.

Additionally a new BACCARAT generator has been created to speed up and simplify simulating cavern wall gamma rays.

Chapter 6

Xenon activation in the LZ detector

6.1 Activation processes

Calibrating the LZ detector with neutron sources is an important part of understanding the detector response. However, neutron radiation can induce radioactivity in materials. Radioactive isotopes can be produced either via thermal neutron capture or fast neutron inelastic scattering. Radioactive isotopes produced in neutron calibrations create additional background events which could potentially impact some of the physics studies in LZ.

Thermal neutron capture is possible as neutrons can thermalise in detector materials. Neutron inelastic scattering on nuclei is dependent on its neutron cross-section and the neutron energy. When the neutron scatters inelastically off a nucleus it often excites the nucleus, sometimes putting it into a metastable state, which will then emit some radiation to return the nucleus back to the ground state. Neutron capture happens predominantly for thermal neutrons whereas inelastic scattering does not occur below a certain threshold incident energy (as displayed in Figure 6.1).

Cosmic rays can also activate materials. The flux of cosmic ray hadrons is heavily suppressed by a few meters of rock and the cosmic ray muon flux is attenuated with kilometres of rock; consequently, compared to the surface, cosmogenic activation of materials underground is highly reduced [145]. To minimise exposure to cosmic rays, once the xenon was purified, it was transported straight to the Sanford Underground Research Facility (SURF) and stored underground. No additional shielding from activation is required for xenon storage underground [105].

The two main LZ neutron calibration sources are deuterium-deuterium (DD) and AmLi. The DD neutron source is critical for calibrating the LZ detector as it creates neutrons with known high energy. The AmLi neutron source is significant as it provides neutron recoils which span the energy range of the WIMP search region of interest (ROI).

This chapter explores the impact on LZ physics studies from xenon activation produced by the DD and AmLi neutron calibration sources.

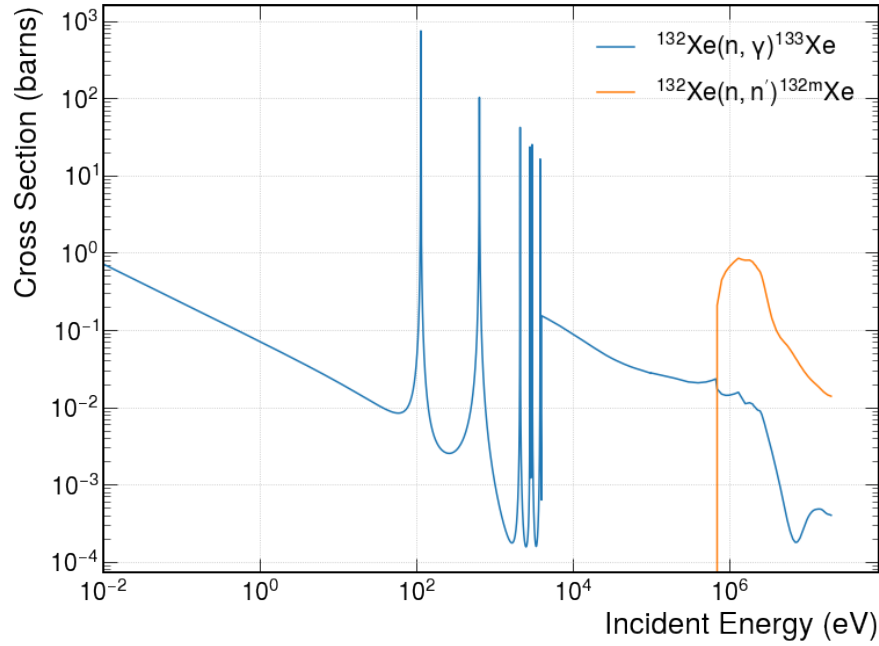


Figure 6.1: Example xenon neutron cross-sections. Neutron radiative capture (blue line) and neutron inelastic (orange line) cross-sections on ^{132}Xe . Cross-section data taken from ENDF/B-VIII.0 evaluated nuclear reaction data library [144].

6.2 Activation from neutron calibration

6.2.1 Description of sources

Probably the main source of activation from detector calibrations will come from the DD neutron calibration. The deuterium-deuterium fusion source generates mono-energetic 2.45 MeV neutrons. The neutrons are emitted isotropically from the source; a collimator (tube) is used to direct neutrons through the water tank and OD into the TPC.

The scattering angle between two neutron interactions in the time projection chamber (TPC) can determine the nuclear recoil energy which is why DD neutron calibrations are very useful [146]. This angle is calculated using event position reconstruction and the direction of the neutron calibration beam. As the initial neutron energy is known, the scattering angle provides a measurement of the recoil energy at the scattering vertex.

Before science runs the calibration is expected to run continuously for two days with a total flux of 8.6×10^{11} neutrons [147]. This translates to ~ 23 neutrons per second at the end of the conduit (as seen in Figures 6.2 & 6.3). For further information on the DD neutron calibration see [87].

Another source of activation is the AmLi neutron calibration. AmLi is an (α, n) neutron source. The main neutron production channel is $\alpha + {}^7\text{Li} \rightarrow {}^{10}\text{B} + n$ (α comes from ${}^{241}\text{Am}$). The source gives a maximum neutron energy of 1.5 MeV (as seen in AmLi neutron energy

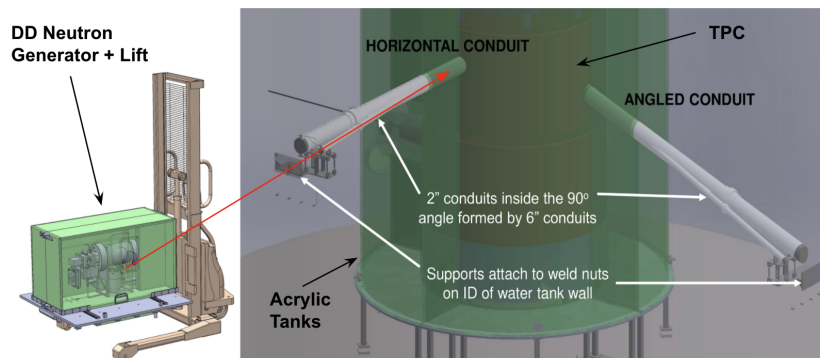


Figure 6.2: Drawing of the DD neutron generator (light green) positioned outside the water tank to fire neutrons into the LZ TPC located inside the water tank. The DD neutron generator is mounted on a lift which can be moved to emit a neutron beam either through the horizontal or angled conduit (light grey). The red line is an example neutron beam path that the DD neutron generator will use to fire neutrons into the LZ TPC. The acrylic tanks (dark green), part of the OD include cutouts for the two conduits to allow the neutron beam to travel through the tanks to the LZ TPC which is encased in a titanium cryostat. Figure not to scale. Figure from Ref. [148].

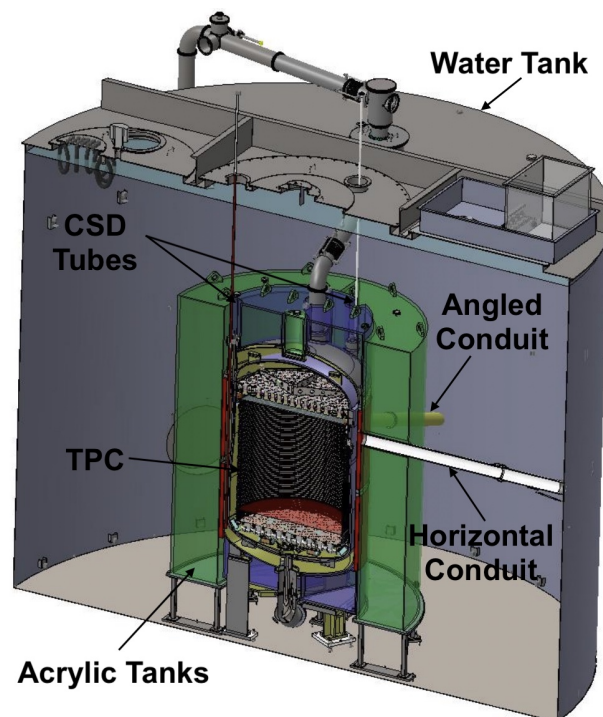


Figure 6.3: Cutaway drawing of LZ detector in the water tank without the OD PMTs. The horizontal and angled conduits are used with the DD neutron generator for calibrations. Also labelled are the two visible calibration source deployment (CSD) tubes in which a radioactive source can be lowered into the space between the OCV and ICV for calibrations. Figure not to scale. Figure from Ref. [148].

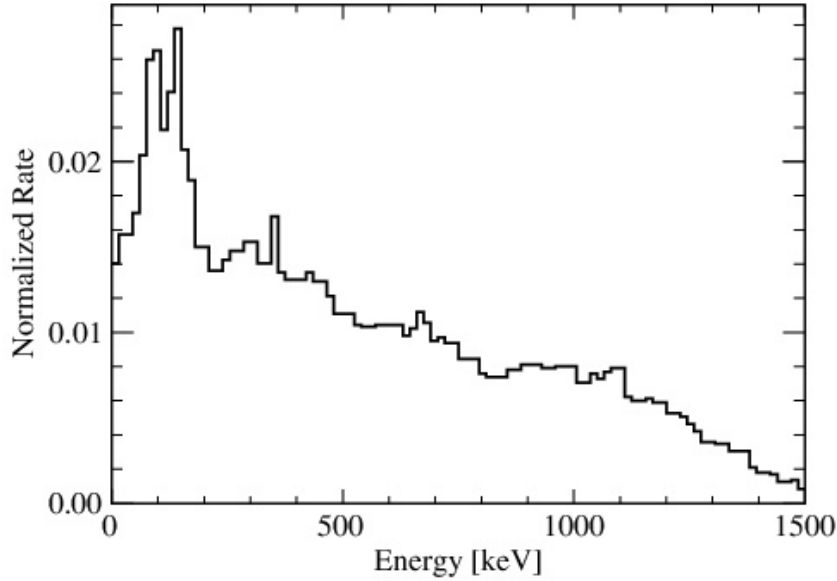


Figure 6.4: Measured neutron energy spectrum of a prototype AmLi source for the LZ experiment. Figure from Ref. [110].

spectrum shown in Figure 6.4), which produces Xe nuclear recoils with energies up to $\sim 40 \text{ keV}_{\text{nr}}$ ($7 \text{ keV}_{\text{ee}}$) [87]. These Xe nuclear recoils span the energy range of the WIMP search ROI ($1.5\text{-}6.5 \text{ keV}_{\text{ee}}$). Additionally the measurement of the maximum Xe nuclear recoil energy acts as energy calibration point. These factors make AmLi an advantageous neutron calibration source.

The AmLi source is lowered into the detector by the calibration source deployment (CSD) system, seen in Figure 6.5, via the CSD tubes (also visible in Figure 6.3) into the space between the ICV and OCV. This calibration will run for ~ 9 hours and produce 58 neutrons per second overall [149]. For information about the AmLi neutron source see [87].

Both of these neutron calibration sources also have a low inherent gamma to neutron production ratio which means the vast majority of events from the sources will be in the nuclear recoil (NR) band and very few events in the electron recoil (ER) band. This is important as it help provide a clear demarcation between the ER and NR bands that ultimately helps reject background events.

The DD and AmLi generators in BACCARAT [110] have been used to simulate both of these neutron calibration sources and the LZ detector response to said source. However, currently excited nuclear states from neutron interaction are not tracked in BACCARAT due to a GEANT4 [108] issue so instead $^{129\text{m}}\text{Xe}$ and $^{131\text{m}}\text{Xe}$ were simulated separately using G4GeneralParticleSource in BACCARAT. To read more about these metastable simulations and results see Section 6.3.

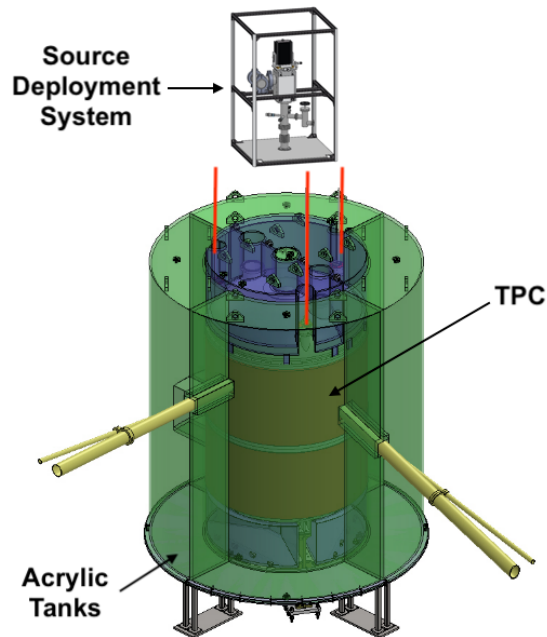


Figure 6.5: Drawing of the CSD system (top of the figure) inside the water tank. The CSD system will lower the AmLi neutron calibration source into the three tubes (highlighted by the red lines) located in between the outer and inner titanium cryostat vessels, OCV and ICV respectively. The OCV is surrounded by the acrylic tanks that make up the OD and the ICV houses the LZ TPC. Figure not to scale. Figure from Ref. [148].

6.2.2 Background analysis chain

Simulations of the DD and AmLi neutron calibration were performed by MPhys and MSc students at the University of Sheffield with my close supervision (academic supervisor Prof. Kudryavtsev) using the DD and AmLi neutron generators in BACCARAT version 4.3.8 and 5.2.6, respectively. Both BACCARAT versions are built on GEANT4 10.03.p02. In the case of the DD neutron calibration simulations neutrons were only fired down the horizontal conduit shown in Figure 6.2. For the DD and AmLi neutron calibration simulations a total of 4.59×10^8 and 1.01×10^8 events were generated in BACCARAT, respectively. These numbers of events are equivalent to 32 and 11 days of DD and AmLi neutron calibrations, respectively. Calculation of the equivalent run time will be given below.

Although the real DD neutron generator produces neutrons isotropically, the BACCARAT DD neutron generator does not simulate the full 4π solid angle. Instead the initial neutron momenta projections are constricted to a square pyramid (see Figure 6.6) as it is computationally expensive to generate neutrons isotropically when only a small fraction of them will travel down the conduit (seen in Figure 6.2) towards the LZ TPC.

The solid angle of the BACCARAT DD neutron generator, determined by Eq. 6.1, was calculated to be 3.6×10^{-3} sr as $-0.03 < \phi < 0.03$ rad and $\frac{\pi}{2} - 0.03 < \theta < \frac{\pi}{2} + 0.03$ rad

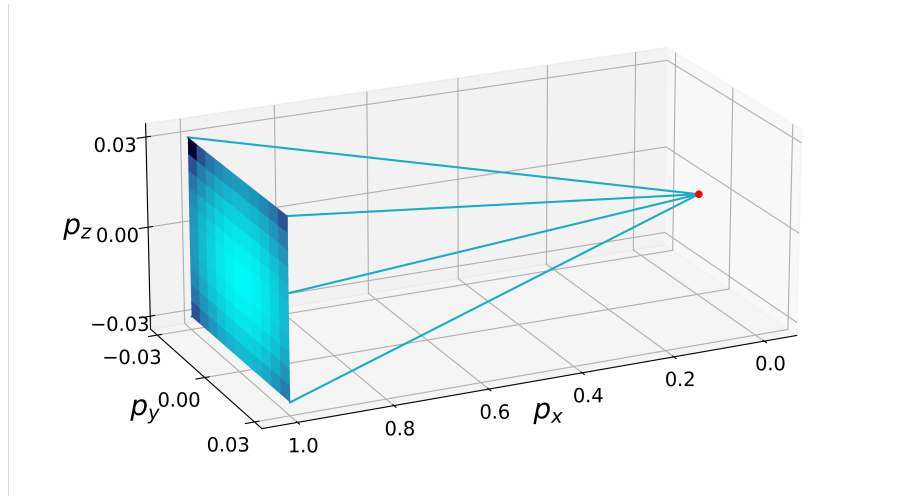


Figure 6.6: Initial particle momenta projections (direction cosines) (p_x , p_y & p_z) generated by the BACCARAT DD neutron generator. The particle momenta projections are without units and lie on the bottom surface of a rounded square pyramid. As the bottom face has a small curvature the value of p_x was expressed via colour; the lighter blue colour signifies larger p_x and the darker smaller p_x . The red dot is (0, 0, 0). Note the different axes scales with p_x from 0 to 1 and p_y & p_z from -0.03 to 0.03.

where ϕ is azimuth angle and θ is polar angle in spherical coordinates.

$$\Omega = (\phi_{max} - \phi_{min})(\cos \theta_{min} - \cos \theta_{max}) \quad (6.1)$$

where Ω is the solid angle and ϕ & θ are the minimum and maximum angles in the spherical co-ordinate system.

To determine the equivalent number of days of DD neutron calibrations from the number of events simulated, the number of neutrons per second in the solid angle 3.6×10^{-3} sr should be calculated. The average flux of the DD neutron generator is 4.98×10^6 neutrons per seconds as the expected total number of neutrons is 8.6×10^{11} from the two days of DD neutron calibrations. Therefore in a solid angle of 3.6×10^{-3} sr there are 1.43×10^3 neutrons per second.

The number of events simulated, 4.59×10^8 , combined with the number of neutrons per second in a solid angle of 3.6×10^{-3} sr converts into 3.7 days of DD neutron calibrations. However, an early version of the detector geometry was used in the BACCARAT simulation in which the conduit area was 8.6 times larger than the real conduit used during the calibration. Thus leading to 8.6 times more neutrons per second entering the TPC in the BACCARAT simulation than expected for the same DD neutron generator flux. To correct for this, the number of events simulated is scaled by 8.6 times which translates to 32 days of DD neutron calibrations.

To calculate the equivalent number of hours of AmLi calibrations from the simulations

requires the number of neutrons produced per second from the AmLi sources which is assumed to be 58 altogether [149]. The three AmLi sources will take place simultaneously in three different positions for three hours in each position. This results in the production of 1.88×10^6 neutrons. The number of events simulated, 1.01×10^8 , translates to 11 days worth of AmLi calibrations simulated.

These activation simulations have been studied using a modified version of the background analysis chain, previously developed to process the LZ TDR and WIMP sensitivity paper simulations [60, 87]. The full model simulation chain, which uses DER and LZAP, could not be used to analyse these activation simulations as it cannot split events into sub-events. Thus it does not allow separation of the neutron scattering event from the decay of the activated isotope. In addition simulating large statistics in a reasonable time frame with the full model simulation chain is computationally unfeasible.

The background analysis chain converts energy depositions to primary scintillation photons and ionisation electrons. It is achieved by combining the NEST (Noble Element Simulation Technique) [112] package with a parameterisation of the LZ detector response. However, the background analysis chain available at the time of this study requires modification because it removes timing information to reduce the amount of data stored on the disk. All the hits in the TPC have the same time as the first energy deposition. Therefore all energy depositions of radioisotopes produced by activation will appear to happen at the same time as the activation itself. This leads to all the hits getting added together and energy deposition being summed which is not what the detector would observe. The modified background analysis chain finds the maximum time step in the event, then counts all hits within $800 \mu\text{s}$ around this time in TPC, xenon skin and OD. Therefore only the last decays are recorded, isolating the activation decays if they are present in an event.

To determine WIMP-like events standard background cuts have been applied, previously defined in Section 2.6. There are four standard background cuts; single scatter, fiducial volume, outer detector, xenon skin. As WIMPs will scatter only once in the LZ detector any non single scatter events can be removed. To remove mis-reconstructed wall events, found near the edges of the TPC, only events within a fiducial volume are chosen. Events in the TPC can be removed if they have a time correlated signal in either of the veto detectors, outer detector or xenon skin.

Once these standard background cuts are applied the WIMP ROI is examined. An extended WIMP ROI is also explored in this analysis. This is different from the WIMP ROI as defined in the LZ TDR which is $3 < S1_c < 20$ phd and $S2 > 350$ phd which approximately translates to ER (NR) energy depositions between 1.5-6.5 keV_{ee} (6-30 keV_{nr}) [87]. The extended WIMP ROI is defined as $3 < S1_c < 80$ phd and $S2 > 415$ phd which approximately correlates to ER (NR) energy depositions between 1.5-15 keV_{ee} (4-60 keV_{nr}) [60]. In this analysis both WIMP ROI's were used to produce different estimates and

they are referred to as WIMP TDR ROI and WIMP PLR ROI, respectively. In addition LZ is also exploring independent effective field theory (EFT) operators to characterise WIMP-nucleon interactions. Therefore a LUX-like EFT ROI cut has been added which is 1.5-70 keV reconstructed energy [150].

This study examines the decays of activated nuclei for a data taking period of 60 days (live time). We assume that the science data taking starts a week after the end of the neutron calibration to allow for short-lived isotopes to decay.

6.2.3 DD neutron calibration simulation results

Figure 6.7 shows the total number of radioisotopes produced in the TPC, xenon skin and OD from the DD neutron simulations without applying the 60 day data taking time window. It shows that ^{133}Xe and ^{125}Xe have the highest number of events as expected since their parent isotopes (^{132}Xe and ^{124}Xe respectively) abundance times neutron capture cross-section are higher at lower neutron incident energies and have higher peaks than other stable xenon isotopes, see Figure 6.8. In addition the abundance times neutron capture cross-section of ^{132}Xe , seen in Figure 6.8, is higher around 1 MeV than for other stable xenon isotopes. This also explains why ^{133}Xe has the highest number of events out of the radioisotopes in the DD neutron calibration simulation.

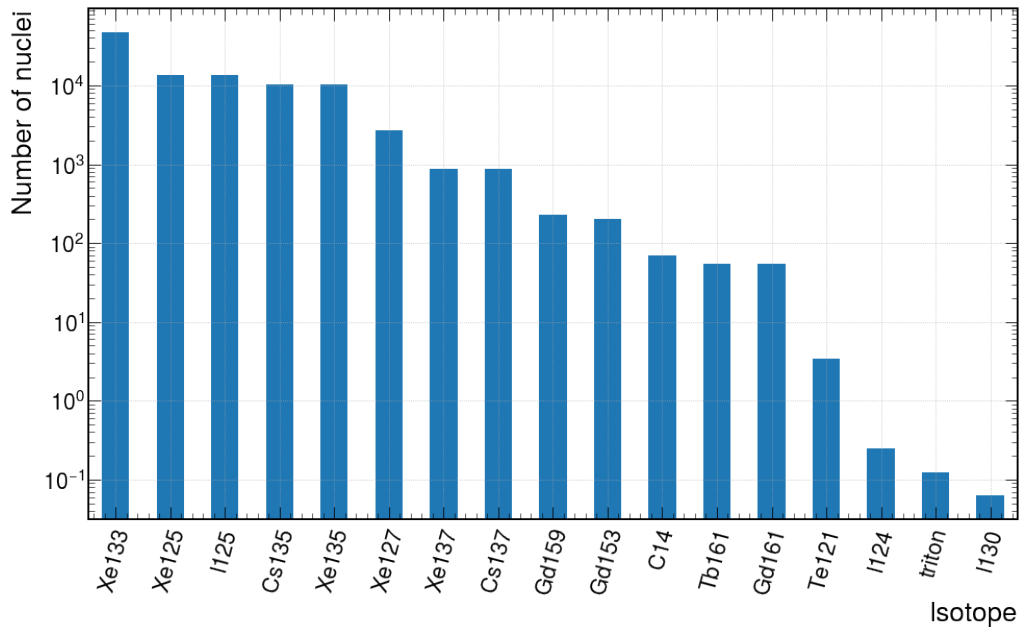


Figure 6.7: The number of radioactive nuclei produced in the DD neutron calibration simulations in the TPC, xenon skin and OD. The number of events has been normalised to 2 days of DD neutron calibrations.

Of the 4.59×10^8 DD neutrons simulated, about 277,000 events had an energy deposi-

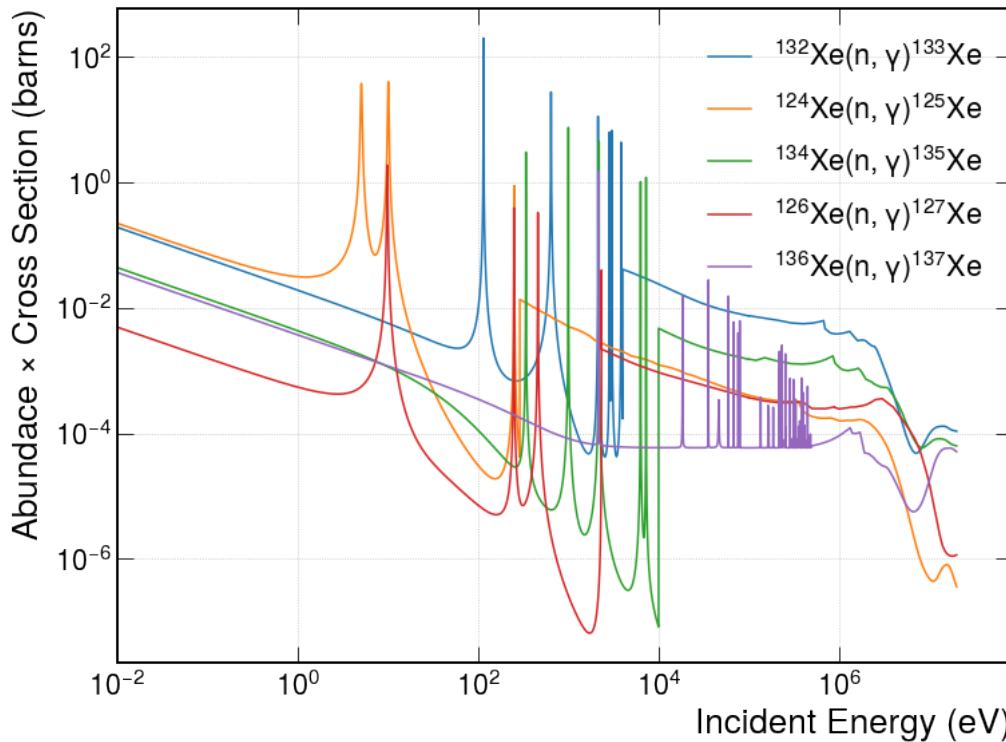
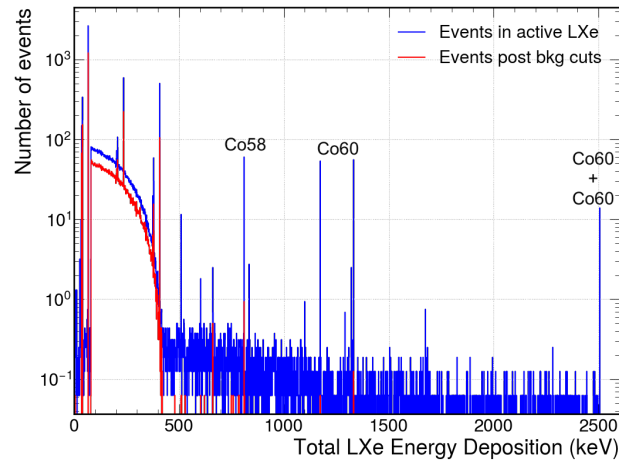


Figure 6.8: Neutron radiative capture cross-sections of a few stable xenon isotopes multiplied by their natural abundance against neutron incident energy. Cross-section data from ENDF/B-VIII.0 evaluated nuclear reaction data library [144].

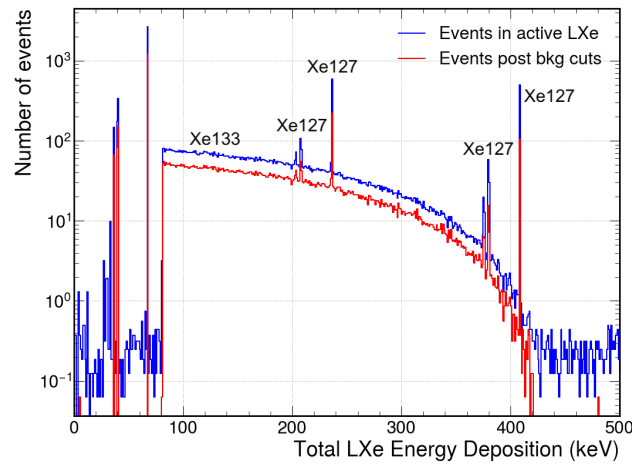
tion which took place within the 60 day data run inside the 7 tonne active liquid xenon (LXe) mass of the TPC. The total simulated energy depositions of these events, normalised to 2 days of DD neutron calibrations, are plotted in Figure 6.9, highlighting the efficacy of the standard background cuts and the accuracy of the BACCARAT simulation.

Decay lines for ^{60}Co , in Figure 6.9a, are visible at 1173, 1332 and 2505 keV (with the latter being the sum of the former two). This is expected as the end of the horizontal neutron beam pipe is close to the top photomultiplier tube (PMT) array and part of the PMTs are made of a Kovar alloy, containing ^{59}Co which can undergo neutron capture. The neutron activation product ^{60}Co has a half-life of 5.27 yrs and decays via beta decay to ^{60}Ni . ^{58}Co decay line at 810 keV is visible as ^{58}Ni is also present in the Kovar alloy used in the PMTs. ^{58}Ni can undergo a (n, p) reaction to produce ^{58}Co which has a half-life of 70.86 days and decays via electron capture to ^{58}Fe .

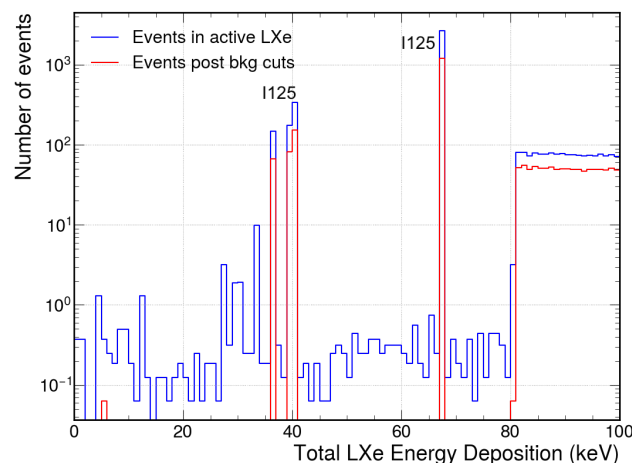
Other prominent isotope decay lines, expected as xenon undergoes activation, can be seen in Figure 6.9b. One such isotope is ^{127}Xe with decay lines at 203, 207, 236, 379 and 408 keV. Neutron capture on ^{126}Xe will produce ^{127}Xe which has a half-life of 36.35 days and decays via electron capture to ^{127}I . ^{132}Xe also undergoes neutron capture to produce ^{133}Xe which has a half-life of 5.28 days and decays via beta decay to ^{133}Cs . The beginning



(a) 0 to 2500 keV.



(b) 0 to 500 keV.



(c) 0 to 100 keV.

Figure 6.9: Total simulated energy deposition in the DD neutron calibration simulations in active LXe for events taking place during a 60 day data run. The number of events has been normalised to 2 days of DD neutron calibrations. The blue histogram is all events which took place in the active LXe and the red histogram is only those events in the active LXe which passed the standard background cuts. Notable isotope decay lines have been labeled.

of the ^{133}Xe beta decay spectrum, seen in Figure 6.9c, starts at 81 keV as predicted from the 81 keV gamma ray emitted due to the de-excitation of ^{133}Cs .

Another isotope undergoing neutron capture is ^{124}Xe . The activation product of this neutron capture is ^{125}Xe which has a half-life of 16.9 hours and decays via electron capture to ^{125}I . ^{125}I is also unstable, half-life 59.49 days, and decays via electron capture to ^{125}Te . Although the ^{125}Te de-excitation only produces a 35 keV gamma ray, electron capture returns an X-ray or Auger electron. The combination of the two results in the three ^{125}I decays lines seen in Figure 6.9c, the first two lines at 36 and 40 keV contain an L-shell Auger electron and the last line at 67 keV contains a K-shell X-ray. Figure 6.9c also displays the power of the standard background cuts to remove lots of low energy deposition background events.

One thing to note is that this analysis does not take into account xenon purification cycles. The current assumption is that most of the ^{125}I will be removed by the getter over a period of a week, the exact amount and time frame was not known at the time of this analysis.

Examining the positions of events which passed standard background cuts shows that the bulk of the energy depositions are at the top and towards the walls of the fiducial volume cylinder inside the TPC, as seen in Figure 6.10. Although the initial positions of the activated isotopes will be close to the end of the neutron beam pipe, located below the top PMT array at the walls of the inner detector vessel, xenon will constantly be circulated and over time the activated isotopes will spread throughout the LXe.

Activated isotopes in detector components surrounding the TPC, for example ^{60}Co produced in the PMTs, will not mix with the LXe. These isotopes do not pose a threat to a 60 day WIMP search or EFT study as energy depositions from their decays are well outside of any of the ROIs.

6.2.4 DD neutron simulation with uniform distribution of decays

As a result of the lack of mixing in the original DD neutron calibration simulations, a separate set of BACCARAT simulations, using version 5.2.6, was undertaken. This new set of BACCARAT simulations used the BACCARAT generator DecayChain to simulate the decay of specific xenon activated isotopes that would be produced in LXe from DD neutron calibration.

The DecayChain BACCARAT generator uses the GEANT4 G4RadioactiveDecay library to simulate time-ordered decays from a user specified radioactive decay chain. DecayChain simulates each step in the decay chain until a stable isotope is reached. It distributes the decays, and the daughter decays, randomly throughout specified detector geometries. This important feature allows for the decays of the isotope to be distributed randomly throughout the TPC volume which is more representative of the mixing of these isotopes throughout the LXe over time.

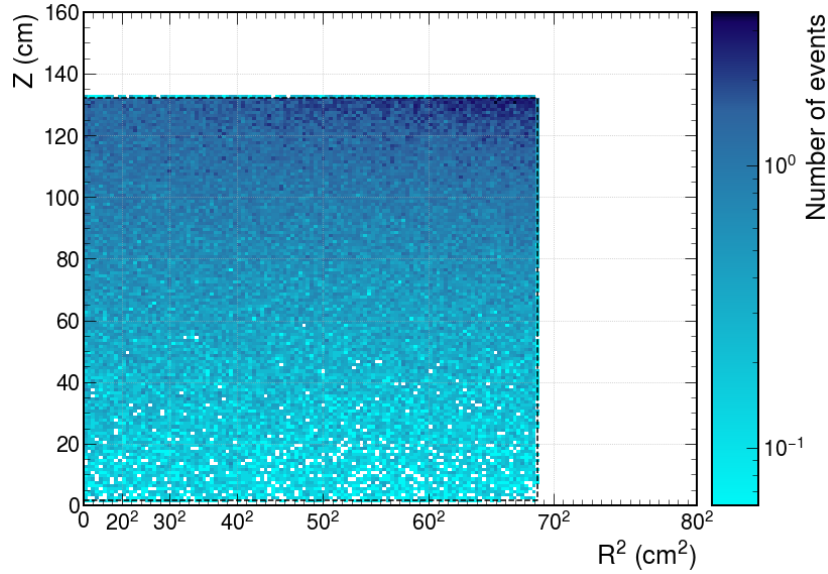


Figure 6.10: Z position (along the drift field) vs radius squared R^2 for events induced by the decays of activated isotopes from the DD neutron calibration simulations for events taking place during a 60 day data run in active LXe. The analysis assumed that the radioisotope decayed at the same position as they were produced. Events shown survived standard background cuts. The number of events has been normalised to 2 days of DD neutron calibrations. The black dotted line is the edge of the fiducial volume.

Figure 6.7 shows that these radioisotopes; ^{137}Xe , ^{135}Xe , ^{133}Xe , ^{127}Xe and ^{125}Xe were all produced in large quantities from 2 days of DD neutron calibrations and their decay products can produce background events which is why they were chosen to be simulated in BACCARAT with the DecayChain generator.

In total $\sim 6.84 \times 10^5$ xenon isotope decays were simulated with the DecayChain generator along with their decay products, see Table 6.1 for a breakdown of the number of decays for each simulated xenon isotope and Figure 6.11 for their decay chains.

Table 6.1: The number of xenon isotope decays simulated in the active LXe with BACCARAT using the DecayChain generator.

Isotope	Number of simulated decays
^{137}Xe	4.54×10^3
^{135}Xe	5.00×10^4
^{133}Xe	5.00×10^5
^{127}Xe	3.00×10^4
^{125}Xe	1.00×10^5

These simulations were studied with the standard background analysis chain, previously developed to process the LZ TDR and WIMP sensitivity paper simulations [60, 87],

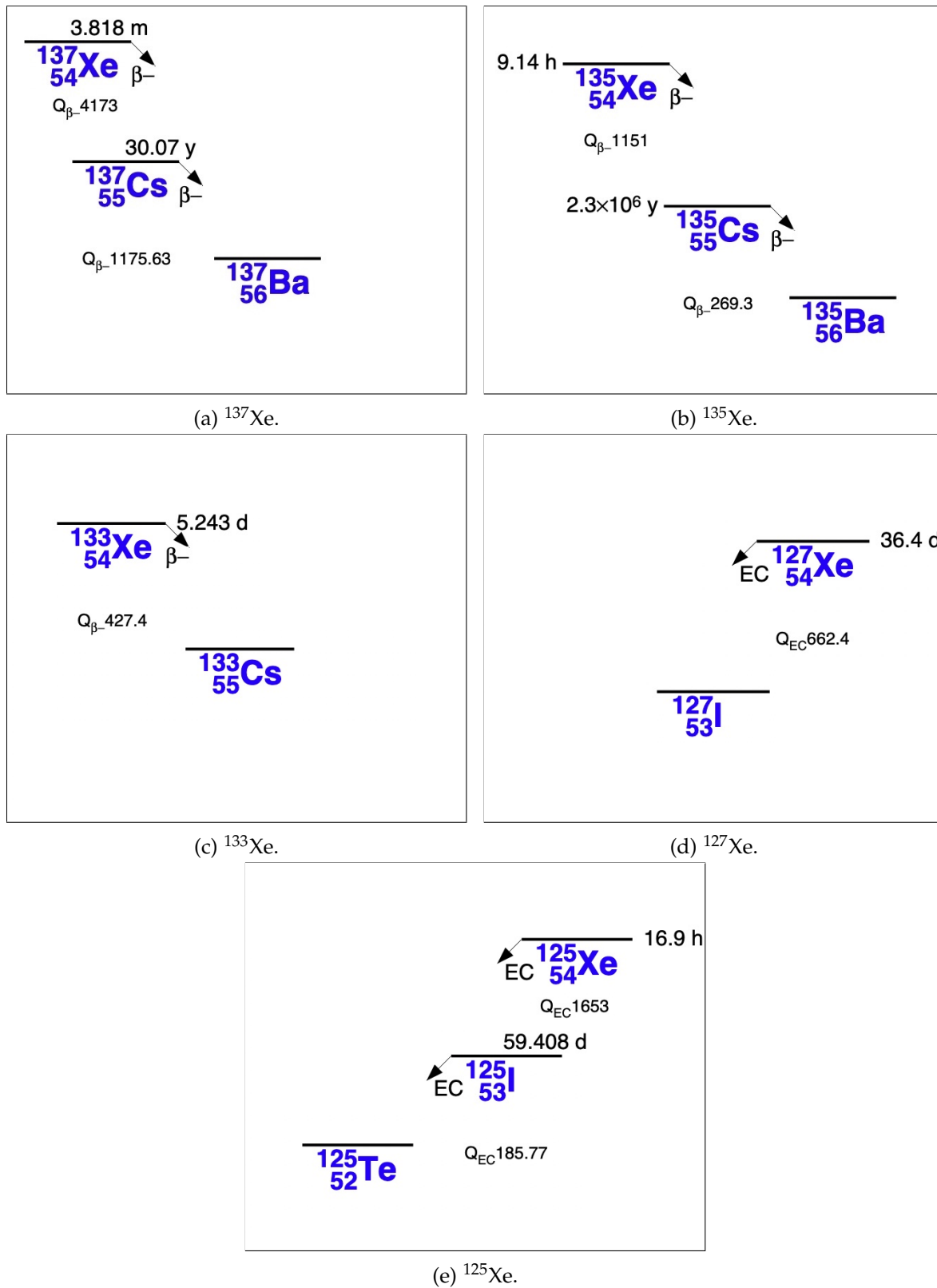


Figure 6.11: Decay chains of xenon isotopes which were simulated with the BACCARAT DecayChain generator. Half-life of the isotopes and their decay modes are given. Q values displayed are in keV. Decay chains taken from Ref. [151].

as only the activated isotope decays were simulated thus removing the need to separate the activation by neutrons from the decay of the activated isotopes.

Analysing these DecayChain simulations reveals the energy depositions in the LXe are uniformly distributed as shown by the position of events passing standard background cuts presented in Figure 6.12. In the simulations there are prominent decay lines from ^{127}Xe and ^{125}I along with the ^{133}Xe beta decay spectrum visible in Figure 6.13. There is good agreement between the decay lines seen in the DecayChain simulations and those described in DD neutron calibration simulations as would be expected.

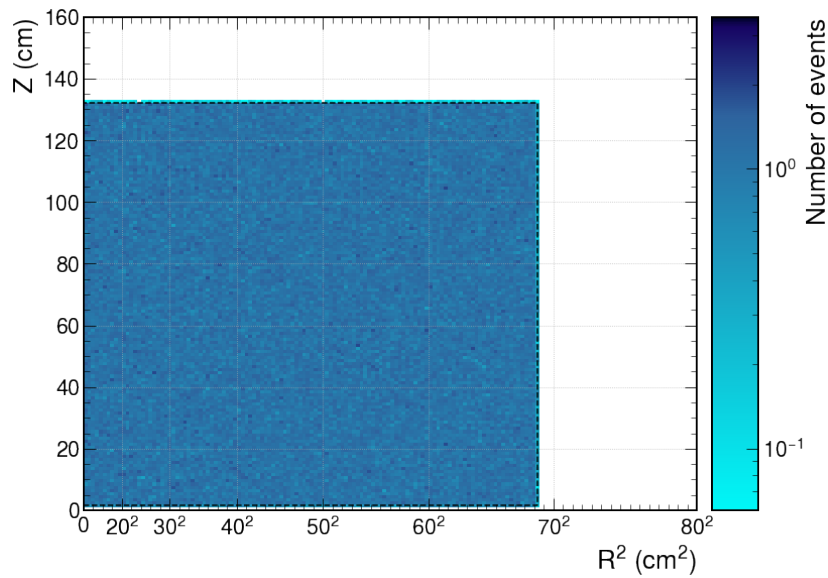
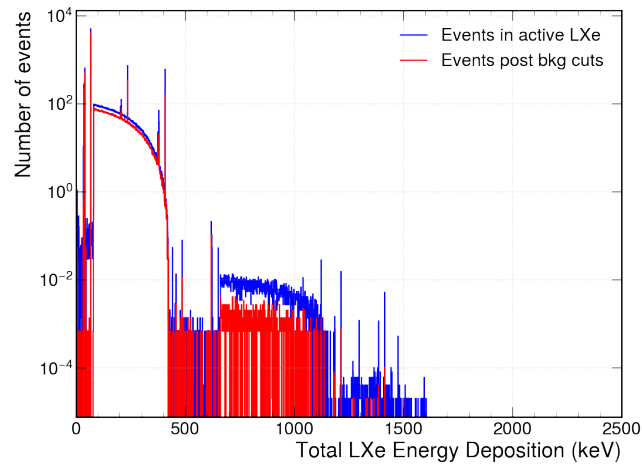


Figure 6.12: Z position (along the drift field) vs radius squared R^2 for events from the DecayChain BACCARAT simulations for events in active LXe taking place during SR1. Events shown survived all background cuts. The number of events has been normalised to 2 days of DD neutron calibrations. The black dotted line is the edge of the fiducial volume.

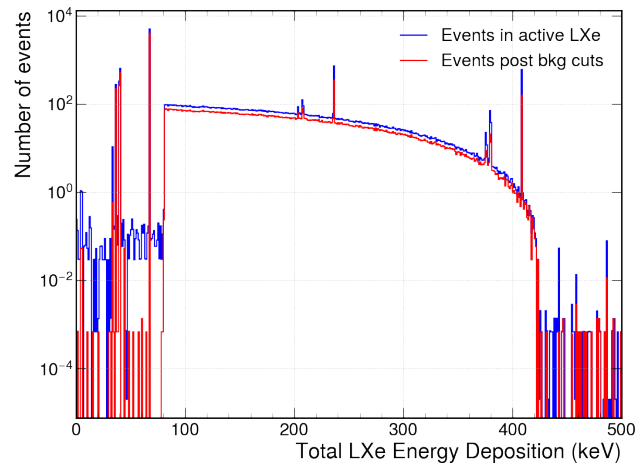
In the LZ detector, sometimes event energy depositions cannot be determined directly from data. However, they can be reconstructed using the event corrected primary and secondary scintillation pulse areas, $S1_c$ and $S2_c$ respectively, using Eq. 2.5. The scintillation pulse areas are corrected for the fluctuations in light collection efficiency throughout the detector. In this simulation the primary (g_1) and secondary (g_2) scintillation channel gains were set to 0.075 phd per photon and 60.306 phd per liquid electron respectively.

Figure 6.14 shows the expected reconstructed energy depositions from the $S1$ and $S2$ signals inside active LXe for a 60 day data run from the 2 days of DD neutron calibrations. When comparing Figures 6.13 & 6.14 the decay lines broaden as the scintillation pulse area measurements also depend on the light collection efficiency and electron attenuation which vary throughout the detector.

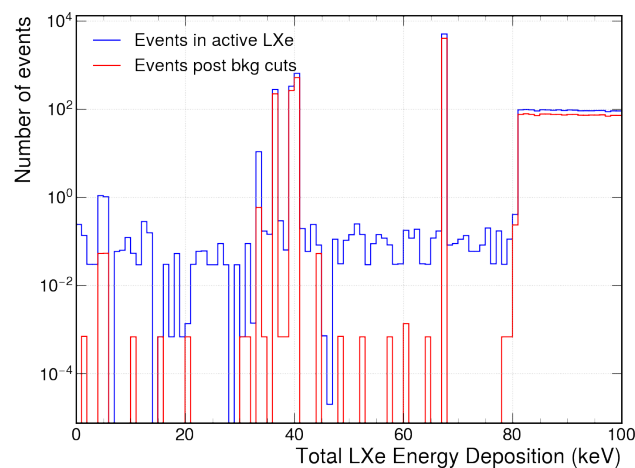
The majority of events in $S1$ - $S2$ space (displayed in Figure 6.15) lie along the ER band



(a) 0 to 2500 keV.

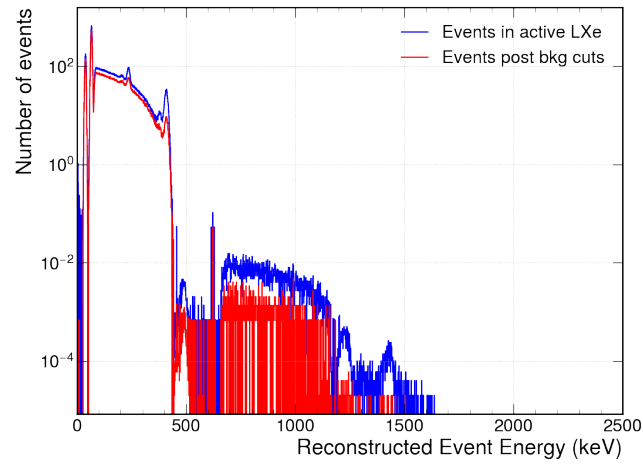


(b) 0 to 500 keV.

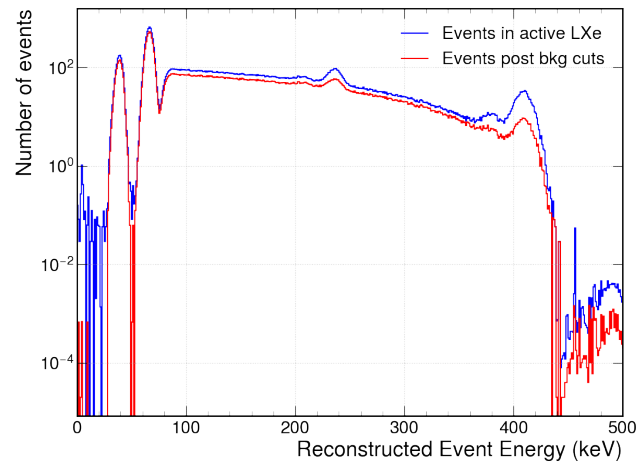


(c) 0 to 100 keV.

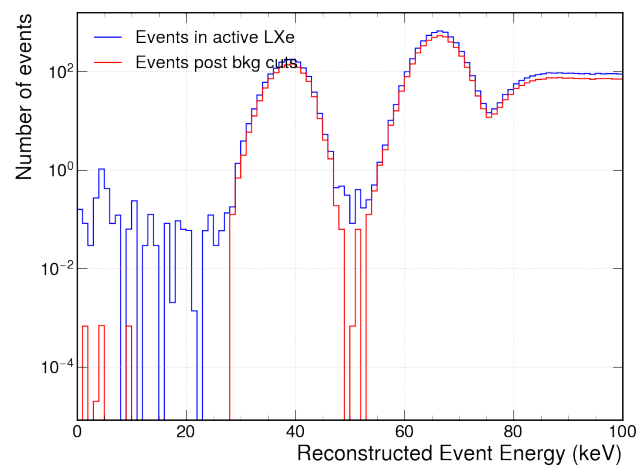
Figure 6.13: Total simulated uniformly distributed energy depositions in the DecayChain simulations in active LXe for events taking place during 60 day data run. The number of events has been normalised to 2 days of DD neutron calibrations. The blue histogram includes all events that took place in the active LXe whereas the red histogram is only includes those events in the active LXe that passed all standard background cuts.



(a) 0 to 2500 keV.



(b) 0 to 500 keV.



(c) 0 to 100 keV.

Figure 6.14: Total reconstructed energy deposition from generated $S1$ and $S2$ signals in the DecayChain simulations in active LXe for events taking place during 60 day data run. The number of events has been normalised to 2 days of DD neutron calibrations. All events which took place in the active LXe are included in the blue histogram and only those events in the active LXe which passed the standard background cuts are in the red histogram.

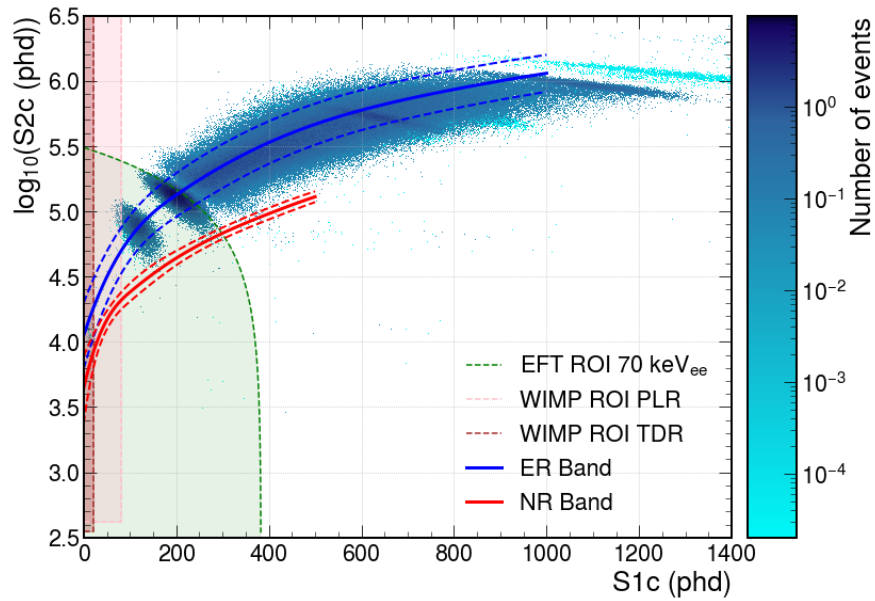
and outside WIMP ROI's as would be predicted. Of these events some inside the EFT ROI pass the standard background cuts, shown in Figure 6.16a. The bulk of these events are from ^{125}I decays. This is anticipated as below 70 keV the only prominent decay lines are from ^{125}I , see Figure 6.13c. The two clusters of events inside the EFT ROI correspond to the two ^{125}I decay peaks seen in Figure 6.14c.

Once all events from ^{125}I decays are removed, shown in Figure 6.16b, only a few events from the DecayChain simulations remain inside the EFT ROI and WIMP ROIs. These remaining events are from other decays which will not be removed by purification cycles, however once normalised to 2 days of DD neutron calibrations there are $0.000712^{+0.146}_{-0.000075}$ events in the WIMP TDR ROI, $0.00138^{+0.146}_{-0.00036}$ events in the WIMP PLR ROI and $0.12^{+0.28}_{-0.04}$ events in the EFT ROI.

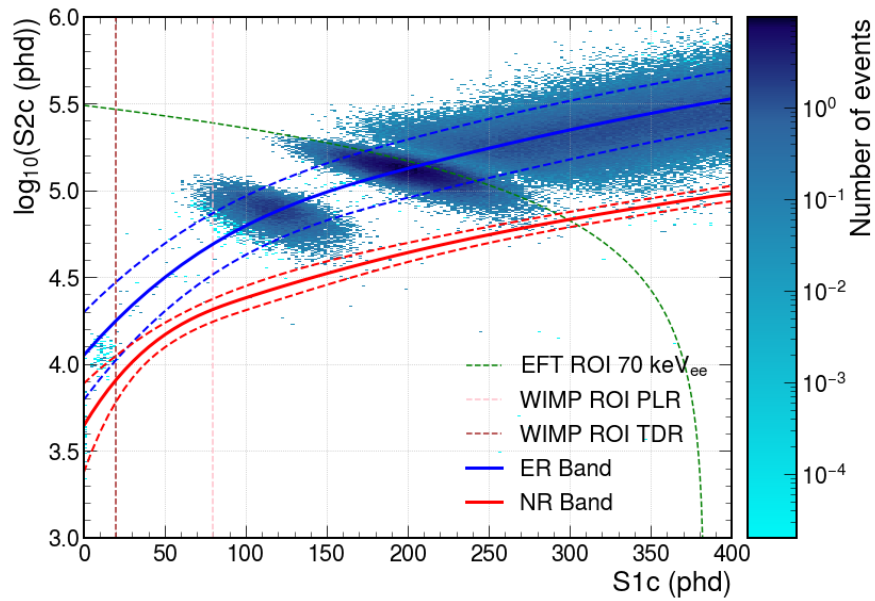
Table 6.2 shows the number of events from the DecayChain simulations within a 60 day data taking period with standard background cuts and various different ROI applied. The numbers of events in the table has been normalised to 2 days of DD neutron calibrations. The standard background cuts are effective as they remove 20% of events within the 60 day data run and once ^{125}I decays are removed there are significantly fewer events in all ROIs. The events in the WIMP and EFT ROIs, that pass all standard background cuts, are above the NR band and thus the DD neutron calibrations should not be an issue for WIMP searches or EFT studies from a 60 day data run.

Table 6.2: For the DecayChain simulations the number of events after different cuts are applied normalised to 2 days of DD neutron calibrations. BKG cuts are the standard background cuts defined earlier in Section 6.2.2. No ER/NR discrimination cut applied. Numbers in brackets are determined using the MC truth energies instead of reconstructed energies. Errors quoted are 90% C.L. intervals (for large statistics standard error and for small statistics from Feldman-Cousins [152]).

Cuts	Number of events (normalised to 2 days of DD neutron calibrations)
Events within 60 day data run	22333 ± 245
BKG cuts	17063 ± 43
BKG cuts in WIMP TDR ROI	$0.000712^{+0.211}_{-0.000075}$
BKG cuts in WIMP PLR ROI	$12.5^{+1.5}_{-1.4}$
BKG cuts in EFT ROI	4505 ± 27 (4944 ± 29)
BKG cuts (^{125}I removed)	12119 ± 31
BKG cuts in WIMP TDR ROI (^{125}I removed)	$0.000712^{+0.146}_{-0.000075}$
BKG cuts in WIMP PLR ROI (^{125}I removed)	$0.00138^{+0.146}_{-0.00036}$
BKG cuts in EFT ROI (^{125}I removed)	$0.12^{+0.28}_{-0.04}$ ($0.74^{+1.13}_{-0.44}$)



(a) All events.



(b) Zoom in on WIMP and EFT ROI's.

Figure 6.15: $\log_{10}(S2_c)$ vs $S1_c$ for events in active LXe during 60 days of data taking from the DecayChain simulations. The number of events plotted in the figures has been normalised to 2 days of DD neutron calibrations. The blue and red bands are the electron and nuclear recoil bands respectively (solid: mean; dashed: $\pm 1.28\sigma$ contours). The different shaded areas and corresponding dotted lines represent different ROI's; the green is the EFT ROI, the pink is the WIMP PLR ROI and the brown is the WIMP TDR ROI.

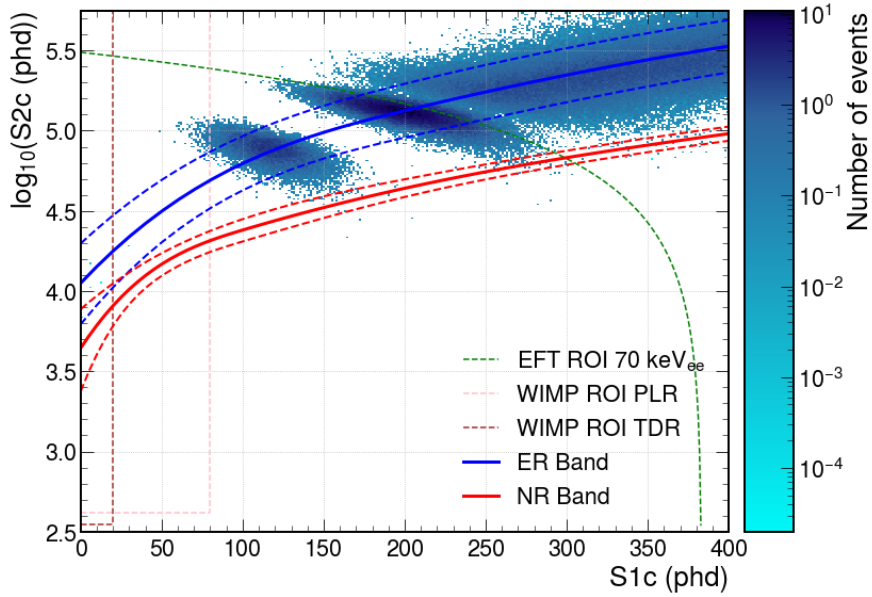
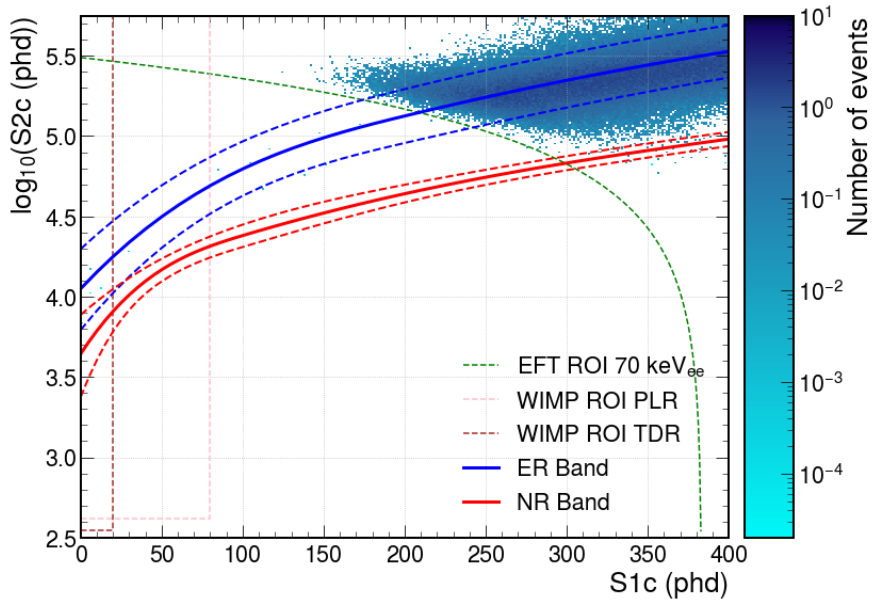
(a) With ^{125}I .(b) Without ^{125}I decays.

Figure 6.16: $\log_{10}(S2_c)$ vs $S1_c$ for events from the DecayChain simulations which were in active LXe during 60 days of data taking. In the figures the number of events plotted has been normalised to 2 days of DD neutron calibrations. Figure (a) shows all events which survived standard background cuts and Figure (b) displays the same events minus any events generated from ^{125}I decays. The different ROIs are represented by dotted lines in the figure; the green is the EFT ROI, the pink is the WIMP PLR ROI and the brown is the WIMP TDR ROI. The blue and red lines shows the boundary for the electron and nuclear recoil bands respectively (solid: mean; dashed: $\pm 1.28\sigma$ contours).

6.2.5 AmLi neutron calibration simulation results

Counting the total number of radioisotopes produced in the TPC, xenon skin and OD for AmLi neutron simulations, seen in Figure 6.17, reveals that the top two isotopes produced are ^{133}Xe and ^{125}Xe as in the DD neutron calibration simulations and would be predicted from xenon neutron capture cross-sections shown in Figure 6.8.

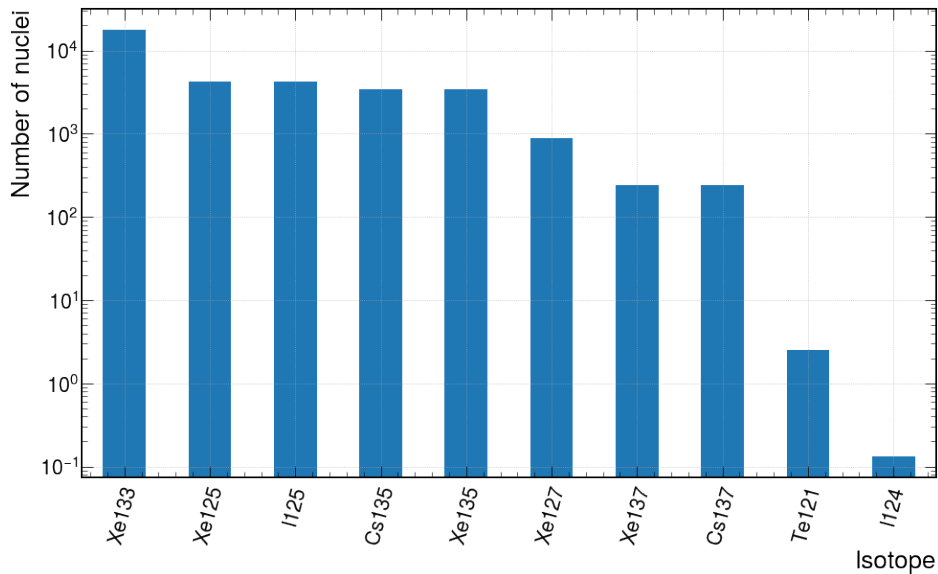
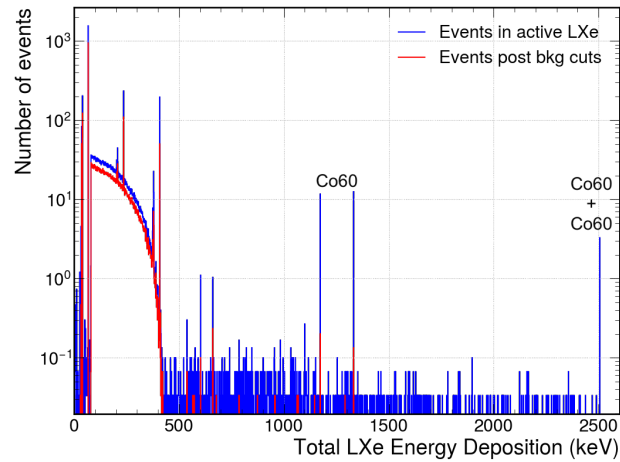


Figure 6.17: The number of radioactive nuclei produced in the TPC, xenon skin and OD in the AmLi neutron calibration simulations. The number of events has been normalised to 9 hours of AmLi neutron calibrations.

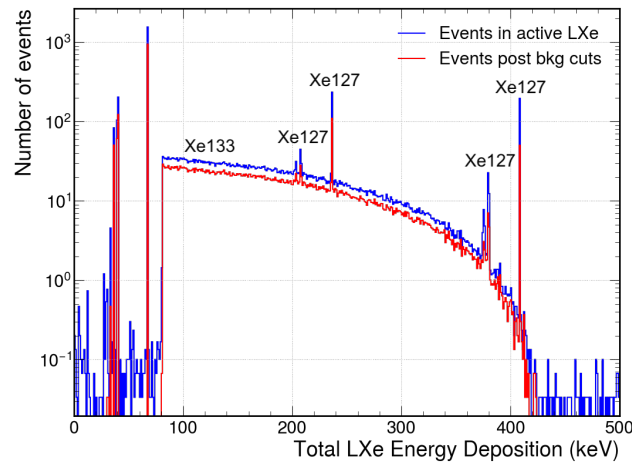
About 238,000 events, of the $\sim 1.01 \times 10^8$ simulated AmLi neutrons, had an energy deposition that would take place during a 60 day data run inside the active LXe. In Figure 6.18 the total simulated energy depositions of these events has been plotted and normalised to 9 hours of AmLi neutron calibrations. This figure demonstrates the power of the standard background cuts which remove many events.

Prominent decay lines from ^{60}Co , ^{133}Xe , ^{127}Xe and ^{125}I are seen in the energy deposition spectra as was seen in the DD neutron calibration simulations. However there is no decay line from ^{58}Co as neutron cross-sections are energy dependent and AmLi neutrons have a lower maximum neutron energy than DD neutrons.

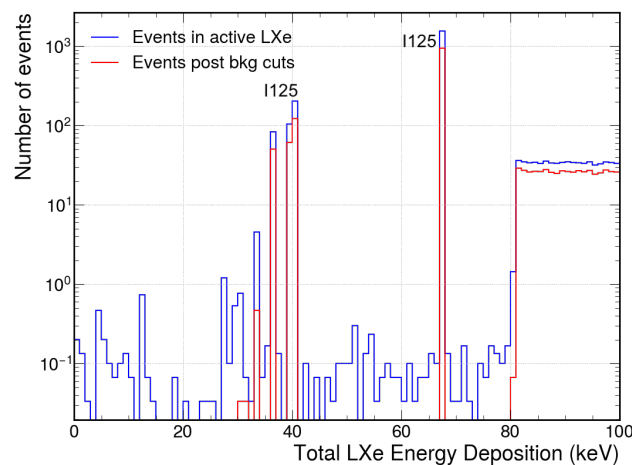
The majority of the energy depositions that pass standard background cuts (Figure 6.19) were at the edge of the fiducial volume in the centre of the TPC. Initially activated isotopes would be located close to the edge of the fiducial volume, however, over time the activated isotopes would disperse throughout the LXe as the xenon is constantly circulating.



(a) 0 to 2500 keV.



(b) 0 to 500 keV.



(c) 0 to 100 keV.

Figure 6.18: Total simulated energy deposition in the AmLi neutron calibration simulations for events taking place during a 60 day data run in active LXe. The number of events has been normalised to 9 hours of AmLi neutron calibrations. The blue histogram displays all events in the active LXe and the red histogram includes only events in the active LXe that passed the standard background cuts. Notable isotope decay lines have been labeled.

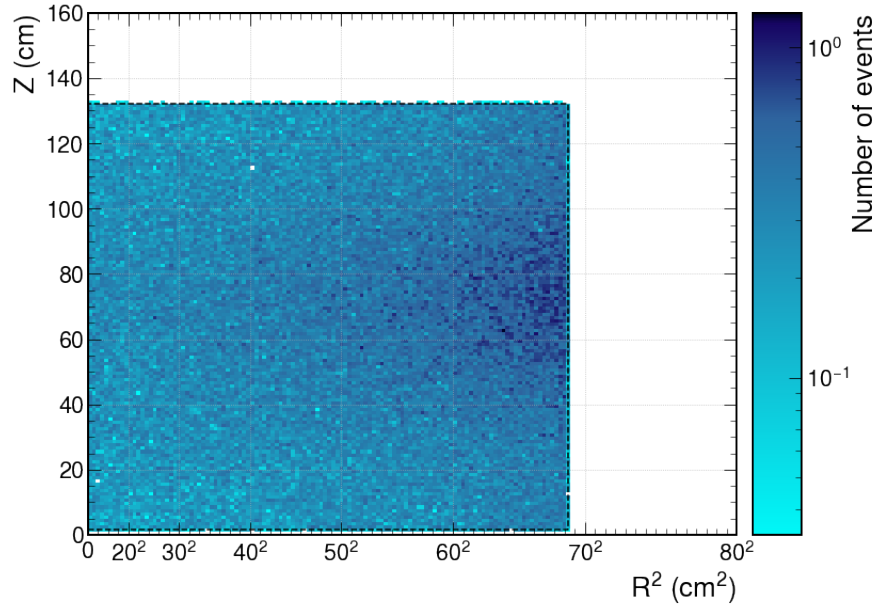


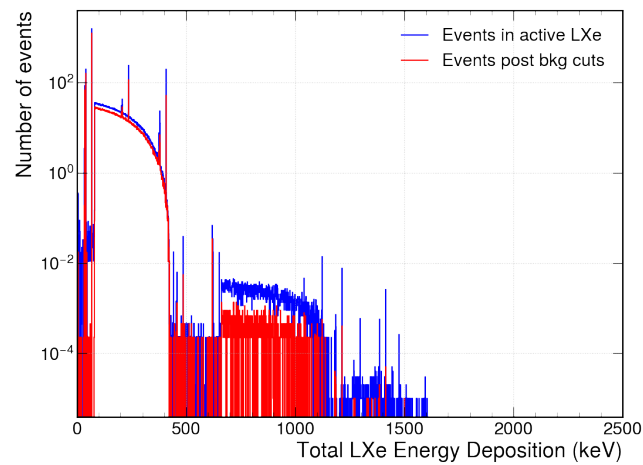
Figure 6.19: Z position (along the drift field) vs radius squared R^2 for events induced by the decays of the activated isotopes during a 60 day data run in active LXe from the AmLi neutron calibration simulations. The analysis assumed that the radioisotope decayed at the same position as they were produced. Events displayed passed all background cuts. The number of events has been normalised to 9 hours of AmLi neutron calibrations. The black dotted line is the edge of the fiducial volume.

6.2.6 AmLi neutron simulation with uniform distribution of decays

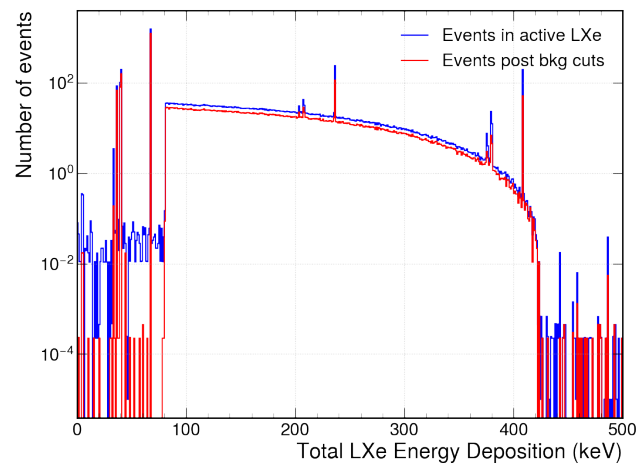
Due to the absence of mixing in the original AmLi neutron calibration simulations, the DecayChain simulations (discussed in Section 6.2.4) were used to simulate the decay of specific activated xenon isotopes that would be produced in LXe from AmLi neutron calibration. As with the DD neutron calibration sims, these radioisotopes were all produced in significant quantities in the AmLi neutron calibration simulations (normalised to 9 hours of AmLi neutron calibrations); ^{137}Xe , ^{135}Xe , ^{133}Xe , ^{127}Xe and ^{125}Xe .

As discussed previously the energy depositions in the DecayChain simulations are uniformly distributed in the LXe. The energy deposition and the expected reconstructed energy deposition spectrum of the DecayChain simulations, shown in Figure 6.20 & 6.21 respectively, has been normalised to 9 hours of AmLi neutron calibrations. These figures show there is good agreement between the AmLi neutron calibration simulations and the DecayChain simulations.

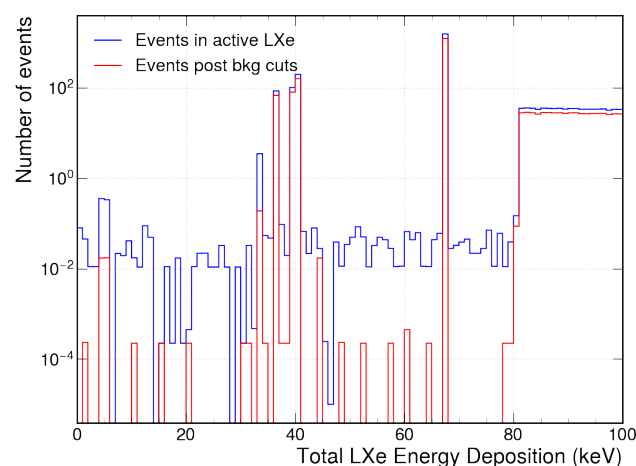
Figure 6.22 shows these events in S1-S2 space normalised to 9 hours of AmLi neutron calibrations. This figure shows that the bulk of events lie along the ER band and outside WIMP ROIs which is expected. The majority of these events in the ROIs which pass all standard background cuts are from ^{125}I decays as illustrated by Figure 6.23. Most of these



(a) 0 to 2500 keV.

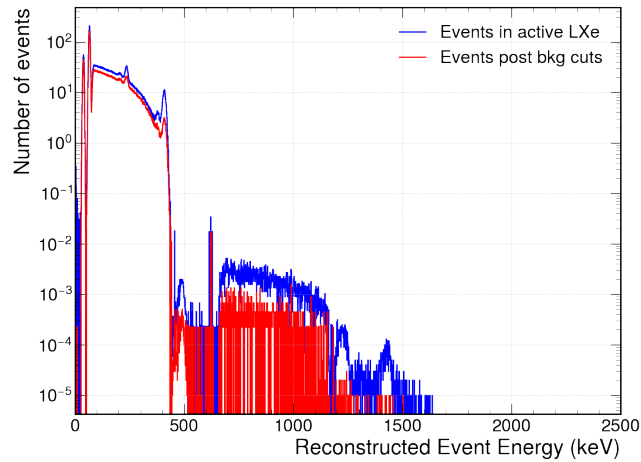


(b) 0 to 500 keV.

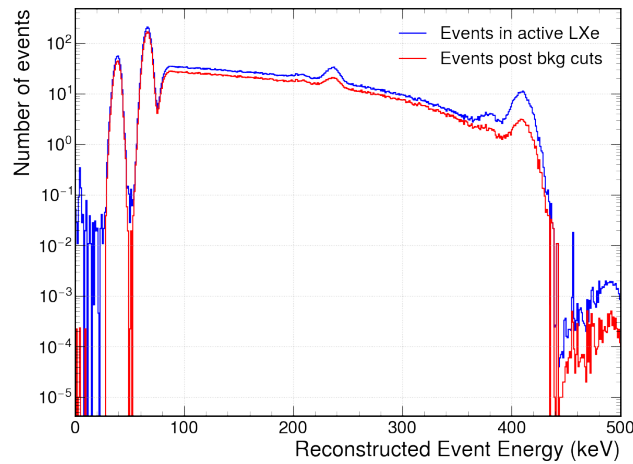


(c) 0 to 100 keV.

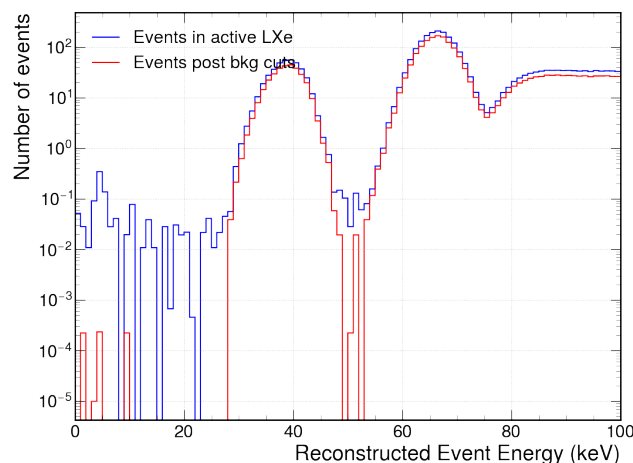
Figure 6.20: Total simulated uniformly distributed energy deposition in the DecayChain simulations in active LXe for events taking place during 60 day data run. The number of events has been normalised to 9 hours of AmLi neutron calibrations. The blue histogram includes all events that took place in the active LXe whereas the red histogram is only includes those events in the active LXe that passed all standard background cuts.



(a) 0 to 2500 keV.



(b) 0 to 500 keV.



(c) 0 to 100 keV.

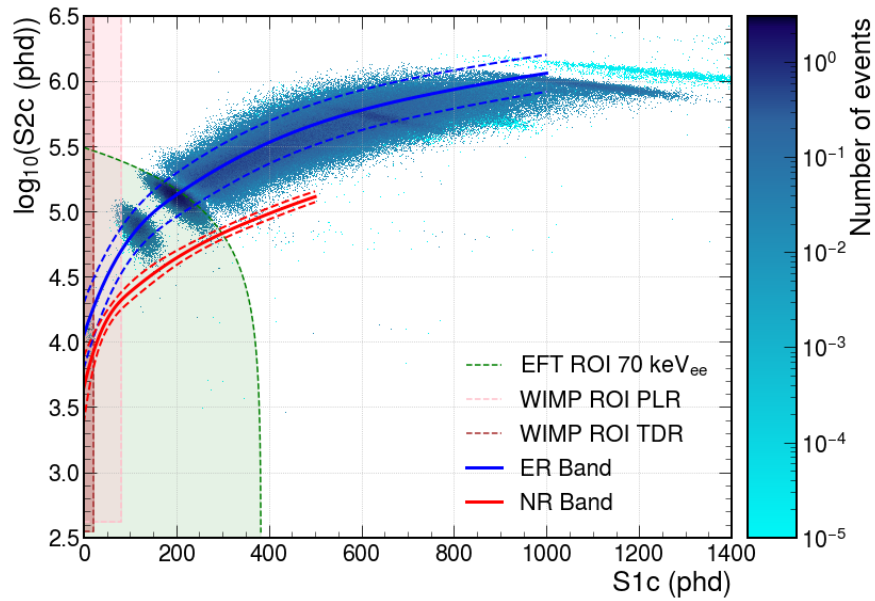
Figure 6.21: Total reconstructed energy deposition from generated $S1$ and $S2$ signals in the DecayChain simulations in active LXe for events taking place during 60 days of data taking. The number of events has been normalised to 9 hours of AmLi neutron calibrations. All events which took place in the active LXe are included in the blue histogram and only those events in the active LXe which passed the standard background cuts are in the red histogram.

Table 6.3: For the DecayChain simulations the number of events after various cuts are applied. The numbers of events has been normalised to 9 hours of AmLi neutron calibrations. BKG cuts are the standard background cuts defined earlier in Section 6.2.2. No ER/NR discrimination cut applied. Numbers in brackets are determined using the MC truth energies instead of reconstructed energies. Errors quoted are 90% C.L. intervals (for large statistics standard error and for small statistics from Feldman-Cousins [152]).

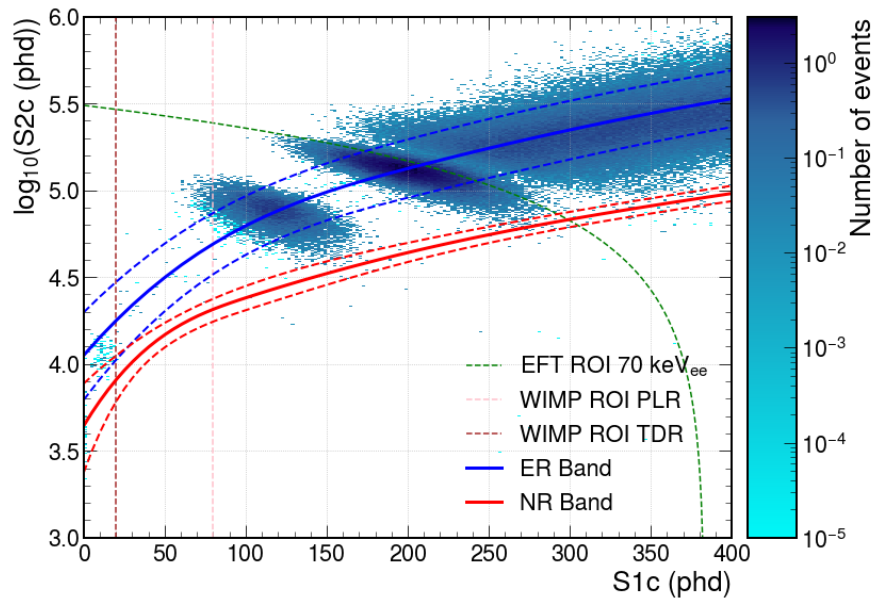
Cuts	Number of events (normalised to 9 hours of AmLi neutron calibrations)
Events within 60 day data run	7846 ± 145
BKG cuts	6010 ± 15
BKG cuts in WIMP TDR ROI	$0.000244^{+0.0682}_{-0.000025}$
BKG cuts in WIMP PLR ROI	$3.88^{+0.45}_{-0.45}$
BKG cuts in EFT ROI	1398 ± 9 (1534 ± 9)
BKG cuts (^{125}I removed)	4476 ± 12
BKG cuts in WIMP TDR ROI (^{125}I removed)	$0.000244^{+0.0493}_{-0.000025}$
BKG cuts in WIMP PLR ROI (^{125}I removed)	$0.00047^{+0.0493}_{-0.00012}$
BKG cuts in EFT ROI (^{125}I removed)	$0.046^{+0.102}_{-0.016}$ ($0.24^{+0.37}_{-0.15}$)

events will be removed by the getter. There are very few events from other decays in the ROIs which the purification cycles will not remove, although when normalised to 9 hours of AmLi neutron calibrations there are $0.000244^{+0.0493}_{-0.000025}$ events in the WIMP TDR ROI, $0.00047^{+0.0493}_{-0.00012}$ events in the WIMP PLR ROI and $0.046^{+0.102}_{-0.016}$ events in the EFT ROI.

In Table 6.3 the number of events within a 60 day data run from the DecayChain simulations are shown with background cuts and several different ROI applied normalised to 9 hours of AmLi neutron calibrations. As the table shows within the 60 day time window the background cuts remove lots of events and there are much fewer events in all ROIs once ^{125}I decays have been removed. These events in the WIMP and EFT ROIs are above the NR band and therefore should not be an issue for either WIMP searches or the EFT studies in a 60 day data run.



(a) All events.



(b) Zoom in on WIMP and EFT ROI's.

Figure 6.22: $\log_{10}(S2_c)$ vs $S1_c$ for events in active LXe during 60 days of data taking from the DecayChain simulations. The number of events plotted in the figures has been normalised to 9 hours of AmLi neutron calibrations. The blue and red bands are the electron and nuclear recoil bands respectively (solid: mean; dashed: $\pm 1.28\sigma$ contours). The different shaded areas and corresponding dotted lines represent different ROI's; the green is the EFT ROI, the pink is the WIMP PLR ROI and the brown is the WIMP TDR ROI.

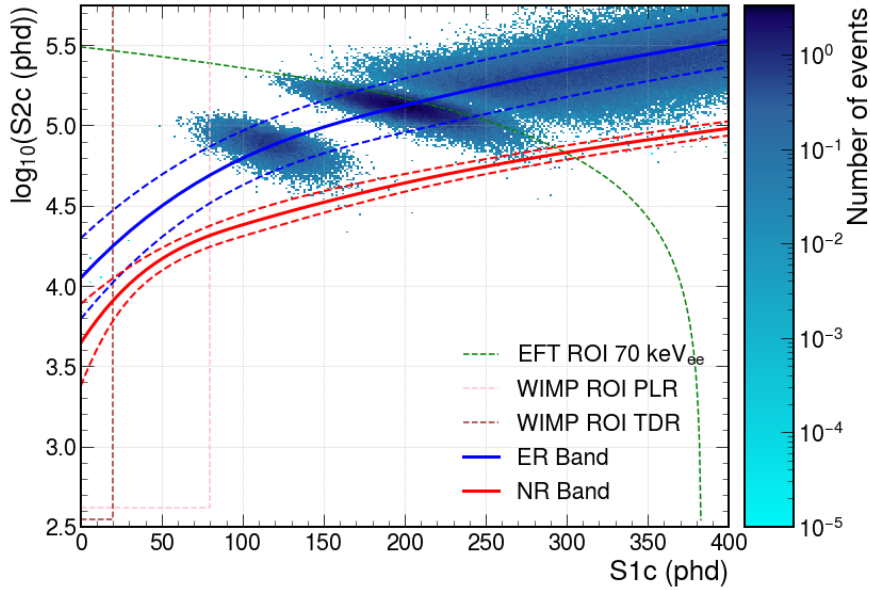
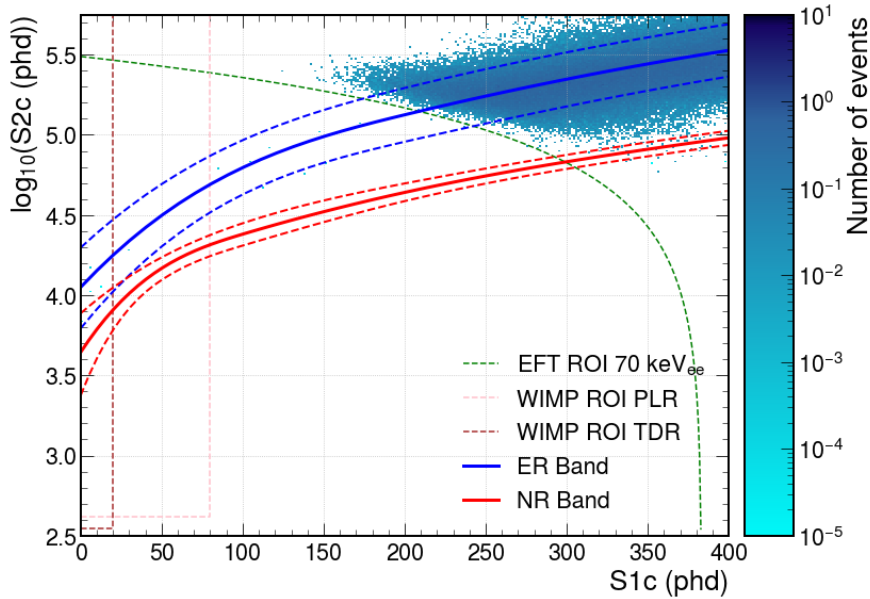
(a) With ^{125}I .(b) Without ^{125}I decays.

Figure 6.23: $\log_{10}(S2c)$ vs $S1c$ for events from the DecayChain simulations which were in active LXe during 60 day data run. In the figures the number of events plotted has been normalised to 9 hours of AmLi neutron calibrations. Figure (a) shows all events which survived standard background cuts and Figure (b) displays the same events minus any events generated from ^{125}I decays. The different ROIs are represented by dotted lines in the figure; the green is the EFT ROI, the pink is the WIMP PLR ROI and the brown is the WIMP TDR ROI. The blue and red lines shows the boundary for the electron and nuclear recoil bands respectively (solid: mean; dashed: $\pm 1.28\sigma$ contours).

6.3 $^{129\text{m}}\text{Xe}$ & $^{131\text{m}}\text{Xe}$

Calibration neutron sources activate xenon in the TPC which results in metastable isotopes of xenon. Metastable isotopes can be simulated in BACCARAT as `G4UAtomicDeexcitation` is enabled allowing for the simulation of atomic de-excitation. However, `GEANT4` is unable to track the production of metastable isotopes from neutron physics if the high precision neutron physics library (`G4HadronPhysicsQGSP_BIC_HP_Gd`) is used. Unfortunately `G4HadronPhysicsQGSP_BIC_HP_Gd` is required as it is the only neutron physics library that produces reliable results. Therefore metastable isotopes cannot be analysed in current neutron calibration simulations as they are not tracked. Nonetheless metastable isotopes can be simulated and analysed by separately generating the isotopes in BACCARAT using `G4GeneralParticleSource` and tracking their decay products.

A BACCARAT generator, called `GPSIon` [153], has been developed to allow the creation of ions, via `G4GeneralParticleSource`, in any LZ detector volumes with any Z , A and excitation energy the user defines at runtime. Metastable isotopes and their decay products can be created and tracked with this generator. The generator uses the Evaluated Nuclear Structure Data File [138] library to determine the features of the metastable decay, such as the half-life time, to enable the simulation of the decay.

6.3.1 Validation

To validate that this new BACCARAT generator is correctly simulating metastable decays, 10^8 decays from two metastable isotopes, $^{129\text{m}}\text{Xe}$ and $^{131\text{m}}\text{Xe}$ (their decay schemes shown in Figure 6.24) were simulated and analysed, no cuts applied. These simulations were performed in BACCARAT version 5.2.5 with the `GPSIon` generator. The isotope was uniformly distributed in the active LXe in each of the two metastable isotope simulations.

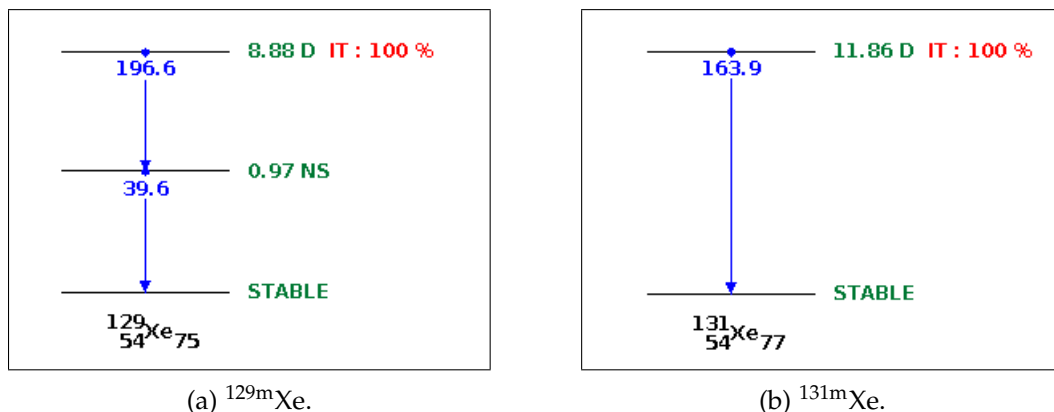


Figure 6.24: Metastable decay schemes taken from NuDat 2.8 [154]. The red text is the decay mode and branching ratio in percent. The green text is the half-life of that energy level and the blue text is the energy of the gamma in keV.

The sum of electron and photon energies was inspected for each decay which should consistently equal the excitation energy of the isotope. As shown by Figures 6.25 & 6.26, in all simulated decays the sum of the electron energies and the sum of the photon energies lie along the red line which denotes the excitation energy; 236.14 keV and 163.93 keV for $^{129\text{m}}\text{Xe}$ and $^{131\text{m}}\text{Xe}$ respectively.

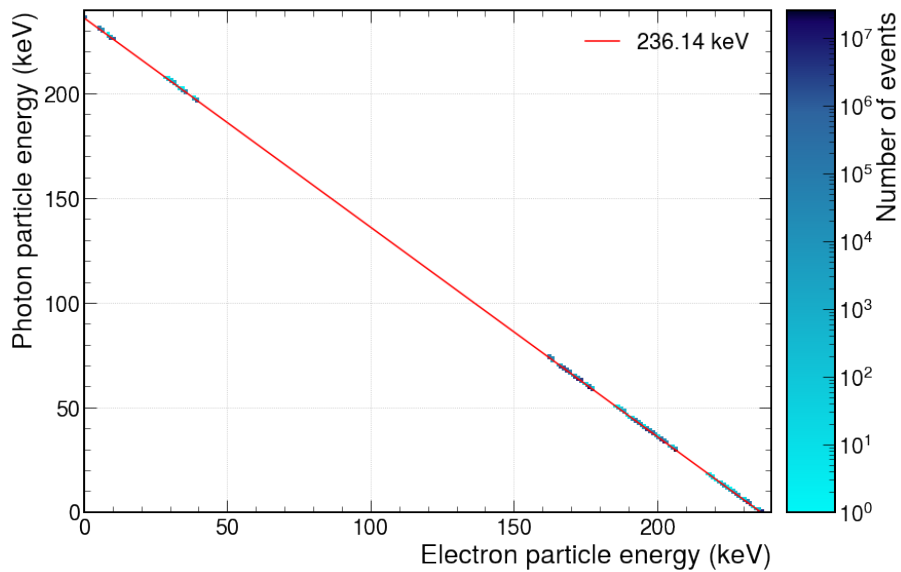


Figure 6.25: The sum of electron vs the sum of photon energies for $^{129\text{m}}\text{Xe}$ decays. The red line denotes the excitation energy for $^{129\text{m}}\text{Xe}$ (236.14 keV).

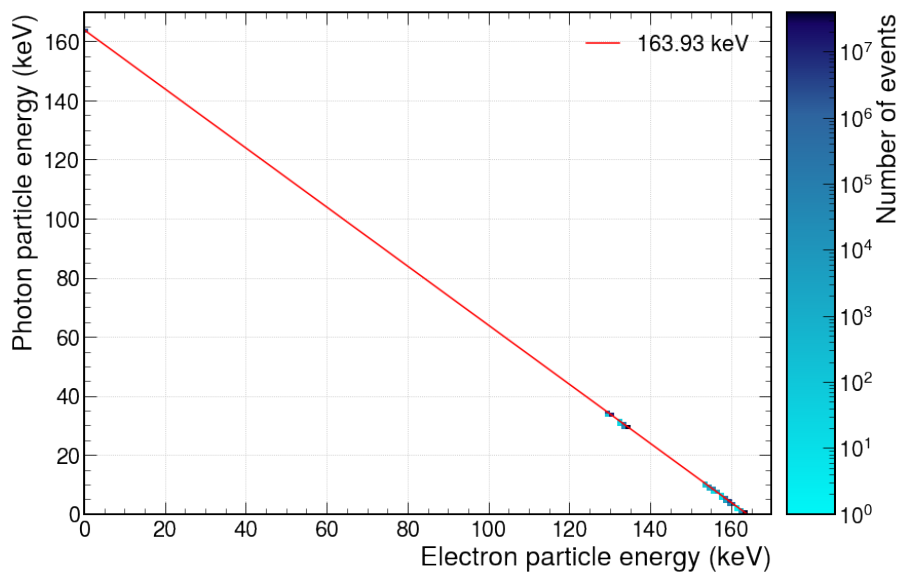
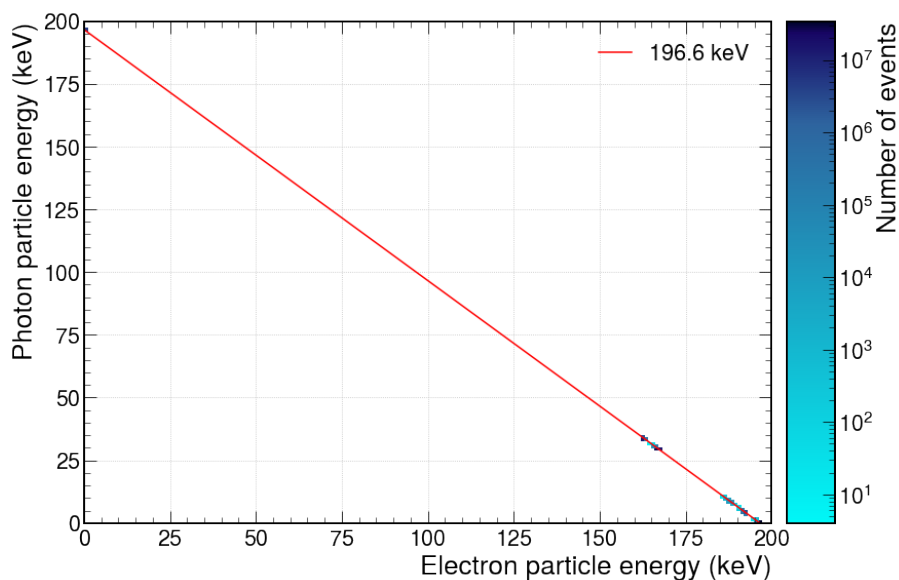
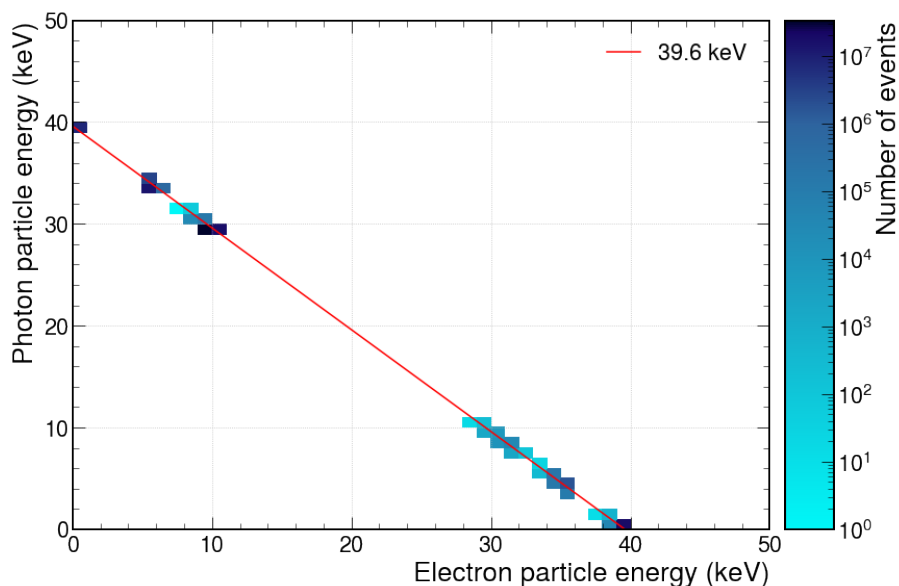


Figure 6.26: The sum of electron vs the sum of photon energies for $^{131\text{m}}\text{Xe}$ decays. The excitation energy for $^{131\text{m}}\text{Xe}$ (163.93 keV) is indicated by the red line.

In both parts of the $^{129\text{m}}\text{Xe}$ decay scheme (seen in Figure 6.24a), it is expected that the sum of electron and photon energies for every decay is equal to the difference in energy between the nuclear states. The sum of electron energies and the sum of the photon energies should total in the first part of the decay 196.6 keV and in the second part of the decay 39.6 keV. Figure 6.27 shows that this is the case for all the simulated $^{129\text{m}}\text{Xe}$ decays.



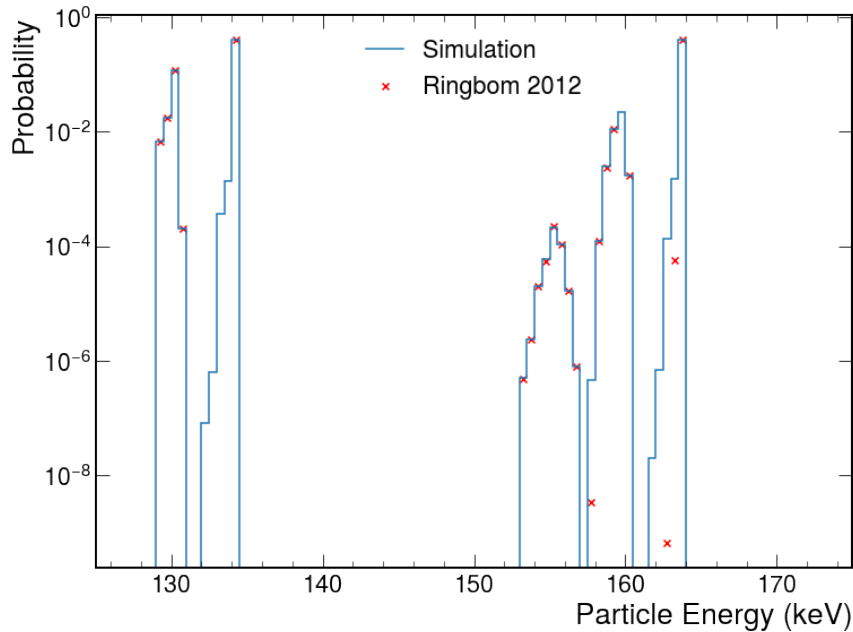
(a) First part of the decay.



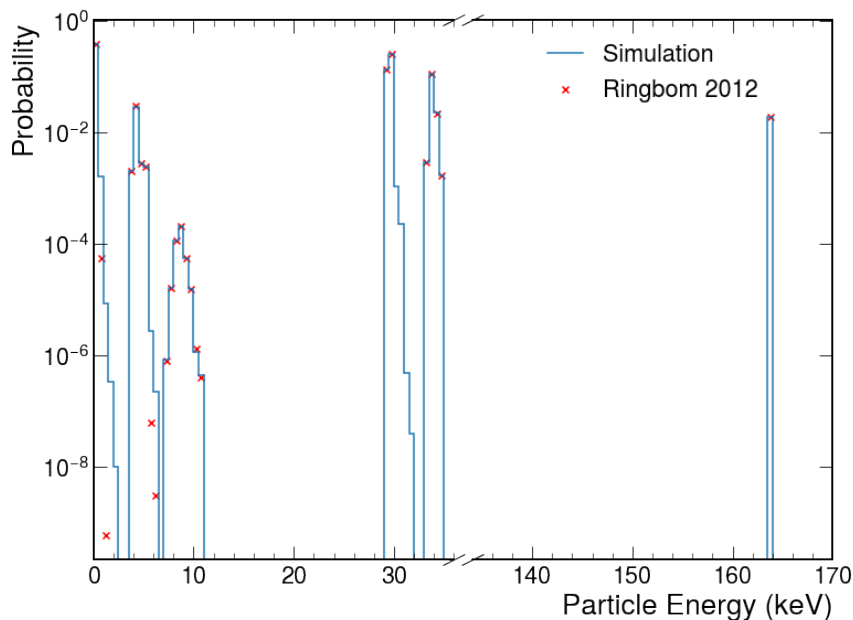
(b) Second part of the decay.

Figure 6.27: The sum of electron vs the sum of photon energies for both part of $^{129\text{m}}\text{Xe}$ decay scheme. The red line indicates the energy difference between nuclear states, 196.6 keV and 39.6 keV for the first and second parts of the decay respectively.

Furthermore the individual electron and photon energies of each decay ^{131m}Xe decay has been inspected. The two histograms in Figure 6.28 show that the simulated ^{131m}Xe electrons and photons probabilities and particle energies agree very well with previously calculated values [155].



(a) Electron energy.



(b) Photon energy.

Figure 6.28: The individual electron and photon energies for the simulated ^{131m}Xe decays as compared to a calculation with an accurate atomic model (red crosses) [155].

As shown above, the GPSIon BACCARAT generator produces metastable isotope decay events with the correct half-lives and the correct photon and electron probabilities and energies. This BACCARAT generator is able to correctly simulate the decays of $^{129\text{m}}\text{Xe}$ and $^{131\text{m}}\text{Xe}$ in the LZ detector which will enable LZ to better understand background events from activation.

6.3.2 Method

Simulations of uniformly distributed $^{129\text{m}}\text{Xe}$ and $^{131\text{m}}\text{Xe}$ decays in active LXe have been performed with the GPSIon generator in BACCARAT version 5.2.5. The number of decays simulated in BACCARAT was 10^8 for $^{129\text{m}}\text{Xe}$ and $^{131\text{m}}\text{Xe}$ which is substantially more than expected number of decays ($102,728$ $^{129\text{m}}\text{Xe}$ and $75,727$ $^{131\text{m}}\text{Xe}$) from 2 days of DD neutron calibrations. Calculation of the expected number of decays will be given below.

To make a conservative estimate of the number of expected decays the assumption was made that all the neutrons in the TPC interact with xenon nuclei. From simulations it was determined that only 13.84% of the 1.43×10^3 neutrons per second generated by the BACCARAT DD neutron generator (within a solid angle of 3.6×10^{-3} sr) enter the TPC. Therefore, once scaled down by 8.6 due to the incorrect conduit area, approximately 23 neutrons per second enter the TPC from the DD neutron calibration beam pipe. The xenon activation cross-section calculation undertaken by Will Taylor (Brown University, USA) [147] determine that only 0.20% of xenon captures will result in $^{129\text{m}}\text{Xe}$. These calculations only take into account neutron capture and does not consider neutron inelastic scattering. Therefore from 2 days of DD neutron calibrations 7.93×10^3 $^{129\text{m}}\text{Xe}$ decays are expected to be produced from neutron capture (see Eq. 6.2).

$$N_d = tn_s f_c \quad (6.2)$$

where N_d is number of expected decays, t is time in seconds, n_s is neutrons per second and f_c is fraction of xenon captures resulting in a specific isotope.

If we apply the same equation for $^{131\text{m}}\text{Xe}$, taking that only 0.50% of xenon captures will result in $^{131\text{m}}\text{Xe}$ (determined by Will Taylor (Brown University, USA) [147]), then 1.98×10^4 $^{131\text{m}}\text{Xe}$ decays produced by neutron capture are expected from 2 days of DD neutron calibrations.

The production rate (R) of $^{129\text{m}}\text{Xe}$ and $^{131\text{m}}\text{Xe}$ from neutron inelastic scattering was estimated using the following equation:

$$R = \phi_n \left(1 - \exp \left(\frac{-\sigma_{ins} N_A L f}{A} \right) \right) \quad (6.3)$$

where ϕ_n is the neutron flux, σ_{ins} is the inelastic neutron scattering cross-section, N_A is

the Avogadro constant, L is the mean track length of a neutron in the TPC, f is the target isotope fractional abundance in natural xenon and A is the atom weight of the target isotope. The neutron spectra at the end of the neutron conduit from the BACCARAT DD neutron calibration simulation was combined with $^{129\text{m}}\text{Xe}$ and $^{131\text{m}}\text{Xe}$ inelastic scattering cross-sections from ENDF/B-VIII.0 evaluated nuclear reaction data library [144] to produce the expected rate. The predicted rate is 0.549 and 0.381 s^{-1} for the production of $^{129\text{m}}\text{Xe}$ and $^{131\text{m}}\text{Xe}$ nuclei respectively from neutron inelastic scattering. This results in the production of 9.48×10^4 $^{129\text{m}}\text{Xe}$ and 6.59×10^4 $^{131\text{m}}\text{Xe}$ decays from 2 days of DD neutron calibrations.

Combining the production of $^{129\text{m}}\text{Xe}$ and $^{131\text{m}}\text{Xe}$ from neutron capture and inelastic scattering, it is expected that 1.03×10^5 $^{129\text{m}}\text{Xe}$ and 7.57×10^4 $^{131\text{m}}\text{Xe}$ decays will be produced from the 2 days of DD neutron calibrations.

As these metastable isotope simulations only contain the decay of the activated isotope the simulations were analysed using the standard, unmodified, background analysis chain referenced earlier, see Section 6.2.2. The standard background cuts to determine WIMP-like events and ROI's, that were defined previously see Section 6.2.2, have been used.

Two types of events have been studied which can mimic WIMP-like signal, making background event removal more challenging. One such type of event is partial energy depositions (PEDs) and the other is multiple scatter single ionisation (MSSI).

In a PED event not all of the energy from the isotope decay is deposited into the active LXe. This can happen when some of the decay products of the isotope escape the LXe. These events are precarious as only a fraction of their energy is measure in the TPC and hence the event can appear in the WIMP ROI.

For this set of analyses PED events were selected by choosing which events had a total Monte Carlo energy deposition in LXe of less than 163 keV and 236 keV , the decay energy of the metastable isotope $^{131\text{m}}\text{Xe}$ and $^{129\text{m}}\text{Xe}$ respectively.

MSSI events are categorised as multiple-vertex events where at least one vertex contributes to the $S1$ signal of the event but not the $S2$ signal. Thus altering event reconstruction in potentially problematic ways. It alters the $S2/S1$ ratio, possibly shifting the event lower from the ER band to the NR band, leading to the danger of it being misclassified.

MSSI events occurs when an event has energy depositions on both sides of the cathode, in the forward and reverse field regions. For example, an isotope decay could deposit some of its decay energy in the forward field region, where the $S2$ signal is unaffected. Then the rest of its decay energy could be transported across the cathode via a photon to deposit its energy in the reverse field region. Any electrons generated in the reverse field region would not be able to drift up to the anode contributing to the $S2$ signal but instead drift downwards from the cathode, thus affecting the $S2$ signal.

To select MSSI events for this analysis, events were chosen that had at least one energy deposition in both the forward field region and in the MC truth reverse field region. Then

events were removed which could easily be identified as either $^{129\text{m}}\text{Xe}$ or $^{131\text{m}}\text{Xe}$ from their reconstructed energy depositions.

Figure 6.29 shows $^{129\text{m}}\text{Xe}$ and $^{131\text{m}}\text{Xe}$ reconstructed event energy depositions from generated S1 and S2 signals. Events with energies above the red dotted line in Figure 6.29 can be identified as from either $^{129\text{m}}\text{Xe}$ or $^{131\text{m}}\text{Xe}$ decays.

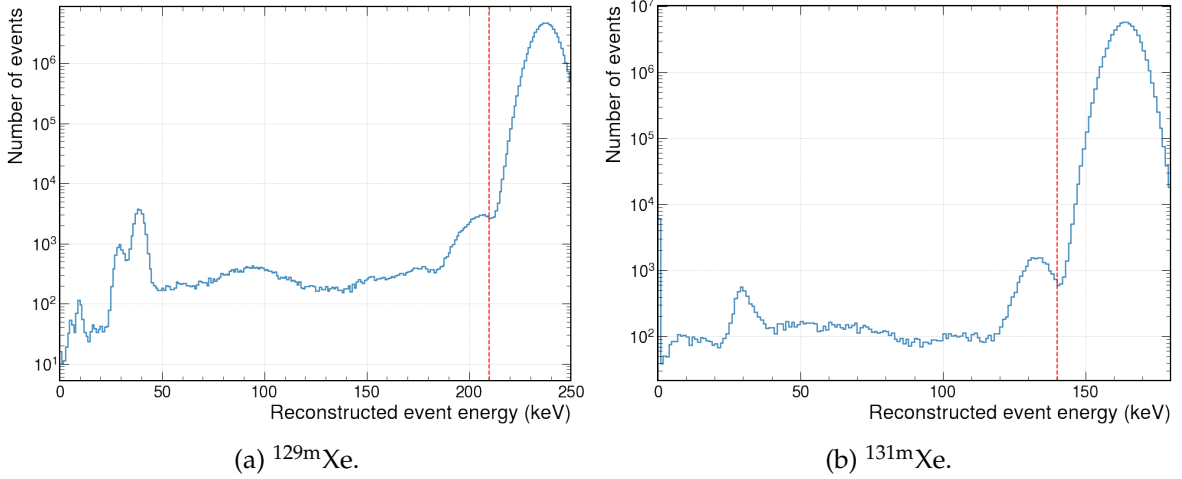


Figure 6.29: Total reconstructed energy depositions from generated S1 and S2 signals where the red line is the minimum reconstructed energy associated with either $^{129\text{m}}\text{Xe}$ or $^{131\text{m}}\text{Xe}$ decays, 210 and 150 keV respectively.

6.3.3 Results

6.3.3.1 $^{129\text{m}}\text{Xe}$ decays

Of the 1×10^8 simulated $^{129\text{m}}\text{Xe}$ decays, within the 60 day data taking time window $\sim 3.5 \times 10^7$ events had an energy deposition which took place inside the active LXe. About 22% of those events are removed once standard background cuts are applied and none of the remaining events lie within the WIMP ROI's, shown in Table 6.4. However, there are events within the EFT ROI and the number of events in the ROI are significantly different depending on how the ROI is defined either using Monte Carlo truth energy or reconstructed energy. As seen in Figure 6.30 some of the energy depositions, around 50 keV, are incorrectly reconstructed and appear to have a higher energy leading to less events in the EFT ROI for the reconstructed energy versus the Monte Carlo truth energy, these discrepancies are explained subsequently.

The events in the EFT ROI are from $^{129\text{m}}\text{Xe}$ decays which have not deposited all of their energy into the active LXe. From examining the $^{129\text{m}}\text{Xe}$ PED events in S1-S2 space (see Figure 6.31), it is clear that these events are separate from the bulk of the events in the 60 day time window and are not part of the oval-shaped area that arises from the detector

Table 6.4: The number of events in the $^{129\text{m}}\text{Xe}$ simulation after different cuts are applied. These numbers have been normalised to 2 days of DD neutron calibrations. BKG cuts are the standard background cuts defined earlier in Section 6.2.2. No ER/NR discrimination cut applied. Numbers in brackets are determined using the Monte Carlo truth energies instead of reconstructed energies. Errors quoted are 90% C.L. intervals (for large statistics standard error and for small statistics from Feldman-Cousins [152]).

Cuts	Number of events	Number of events (normalised to 2 days of DD neutron calibra- tions)
Events within 60 day data run	$3.50 \times 10^7 \pm 9.70 \times 10^3$	35959 ± 10
BKG cuts	$2.73 \times 10^7 \pm 8.57 \times 10^3$	28020 ± 9
BKG cuts in WIMP TDR ROI	$0_{-0}^{+2.44}$	$0_{-0}^{+0.0025}$
BKG cuts in WIMP PLR ROI	$0_{-0}^{+2.44}$	$0_{-0}^{+0.0025}$
BKG cuts in EFT ROI	$11_{-5.91}^{+17.81} (261 \pm 26)$	$0.011_{-0.006}^{+0.018} (0.27 \pm 0.03)$

capturing the full decay energy in the LXe. The position of these PED events are at the edge of the radius and bottom of the fiducial volume, seen in Figure 6.32. This is expected due to the short photon mean free path in LXe, 1.8 mm for 100 keV photon in LXe of density 2.88 g cm^{-3} (calculated using attenuation data from [156]). Photons that escape detection travel outside of the TPC but they cannot travel far from the point of origin, thus the origin of the events are at the edge of the TPC already close to the insensitive regions.

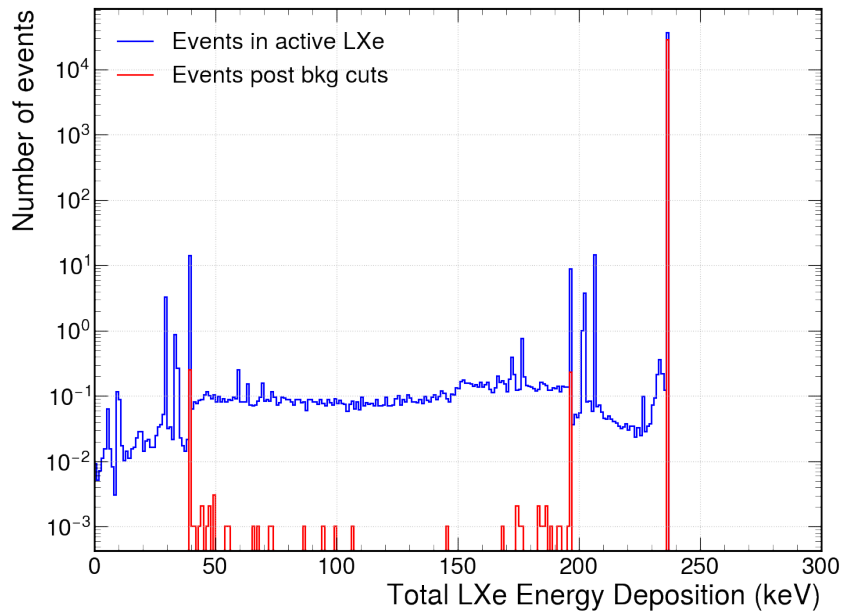
The majority of these PED events in the $^{129\text{m}}\text{Xe}$ simulation are MSSI events, where at least one vertex contributes to the S1 signal of the event but not the S2 signal. These MSSI events explain the discrepancies between the number of events in the Monte Carlo truth and reconstructed energy EFT ROI's. As expected all of these MSSI events take place at the very bottom of the fiducial volume in the TPC near the cathode (see Figure 6.33). In S1-S2 space there are only a few MSSI events within the EFT ROI (see purple crosses in Figure 6.34), yet when defining the EFT ROI with the Monte Carlo truth energy it captures many more $^{129\text{m}}\text{Xe}$ MSSI events, see Table 6.5. The event energy is incorrectly reconstructed because some of the energy deposition occurs below the cathode where energy depositions only contribute to the S1 signal as electrons produced, S2 signal, drift downward away from the cathode. Thus making it appear as if the event has deposited more energy in the TPC than it actually has. Examining the MSSI event Monte Carlo total energy depositions, shown in Figure 6.35, clearly shows two gamma decays of $^{129\text{m}}\text{Xe}$, see Figure 6.24a.

The number of events from $^{129\text{m}}\text{Xe}$ decays in the EFT ROI when normalised to 2 days

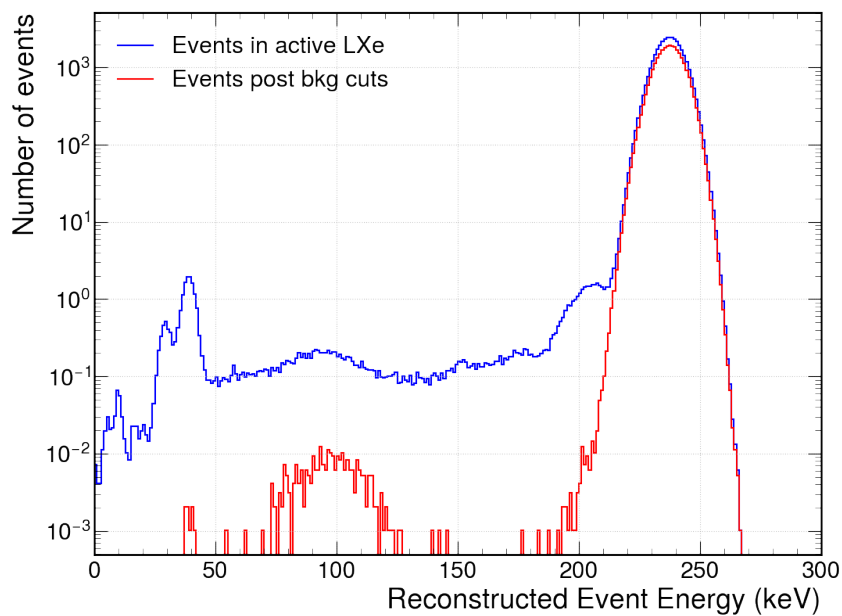
Table 6.5: The number of MSSSI events in $^{129\text{m}}\text{Xe}$ simulations after various cuts have been applied. These numbers have been normalised to 2 days of DD neutron calibrations. BKG cuts are the standard background cuts defined earlier in Section 6.2.2. No ER/NR discrimination cut applied. Numbers in brackets are determined using the Monte Carlo truth energies instead of reconstructed energies. Errors quoted are 90% C.L. intervals (for large statistics standard error and for small statistics from Feldman-Cousins [152]).

Cuts	Number of events	Number of events (normalised to 2 days of DD neutron calibra- tions)
MSSSI Events in 60 day data run	6568 ± 133	6.7 ± 0.1
MSSSI + BKG cuts	373 ± 32	0.38 ± 0.03
MSSSI + BKG cuts in WIMP TDR ROI	$0^{+2.44}_{-0}$	$0^{+0.0025}_{-0}$
MSSSI + BKG cuts in WIMP PLR ROI	$0^{+2.44}_{-0}$	$0^{+0.0025}_{-0}$
MSSSI + BKG cuts in EFT ROI	$2^{+5.91}_{-0.53} (252 \pm 26)$	$0.00206^{+0.00607}_{-0.00054}$ (0.26 ± 0.03)

of DD neutron calibrations is $0.011^{+0.018}_{-0.006}$ events in the EFT ROI, see Table 6.4. Nonetheless, there were no events in the WIMP ROIs and the PED events in the EFT ROI which did survive standard background cuts are above the NR band and so should not cause problems for EFT studies.

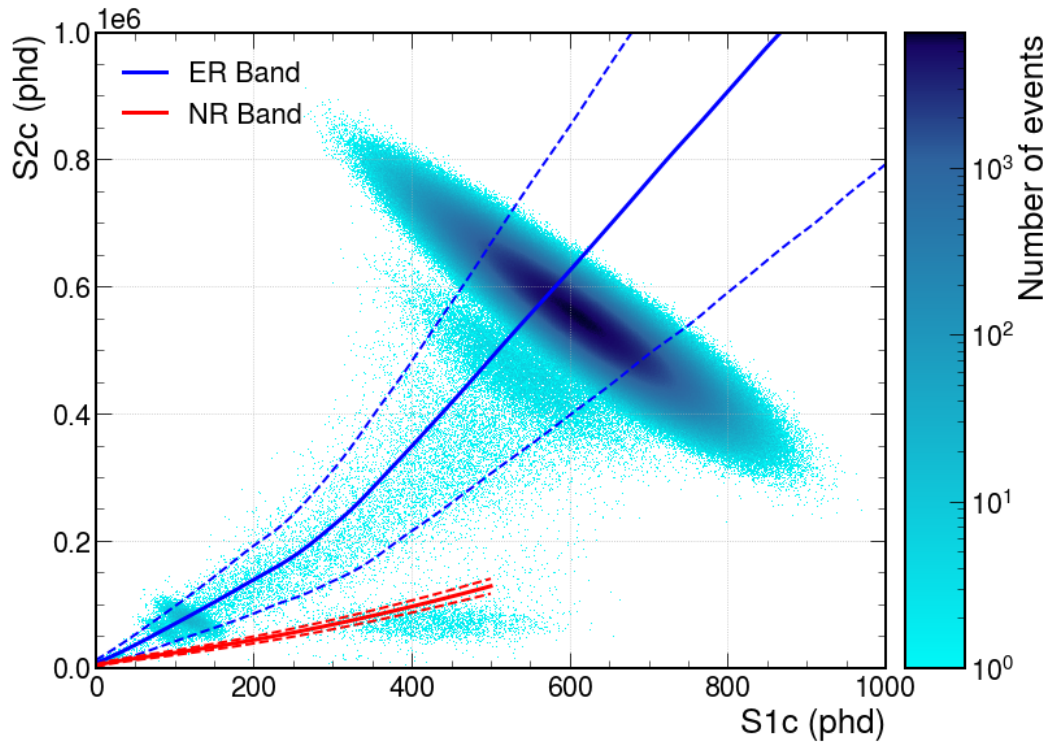


(a) Monte Carlo truth energy deposition.

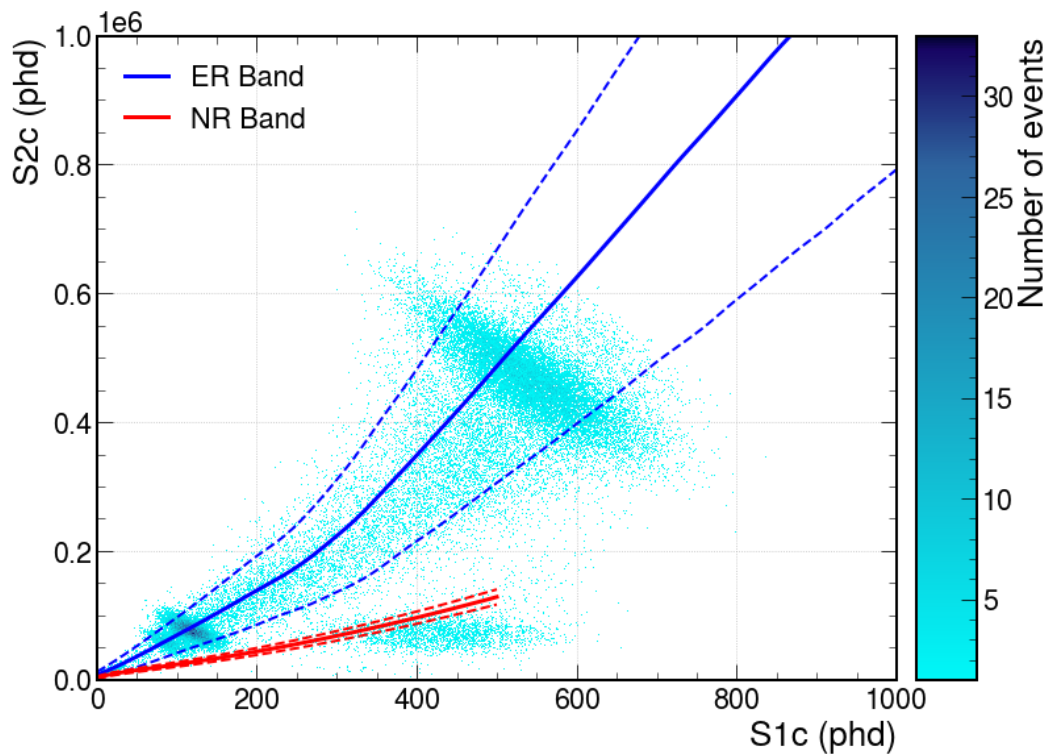


(b) Total reconstructed energy deposition.

Figure 6.30: Energy deposition in the ^{129m}Xe simulation for events taking place during a 60 day data run in active LXe. The number of events has been normalised to 2 days of DD neutron calibrations. The blue histogram is all events which took place in the active LXe and the red histogram is only those events in the active LXe which passed the standard background cuts.



(a) All events.



(b) PED events.

Figure 6.31: $S2_c$ vs $S1_c$ for all events in the ^{129m}Xe simulation. The blue and red lines are the electron and nuclear recoil bands respectively (solid: mean; dashed: $\pm 1.28\sigma$ contours). Note linear scale on the y -axis for $S2_c$.

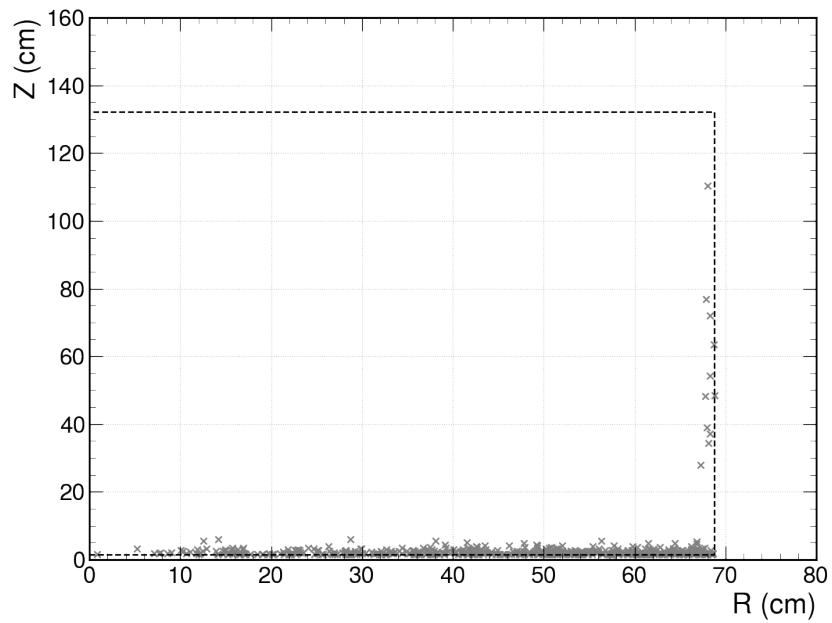


Figure 6.32: Z vs R for all $^{129\text{m}}\text{Xe}$ PED events after standard background cuts applied except for energy range cuts.

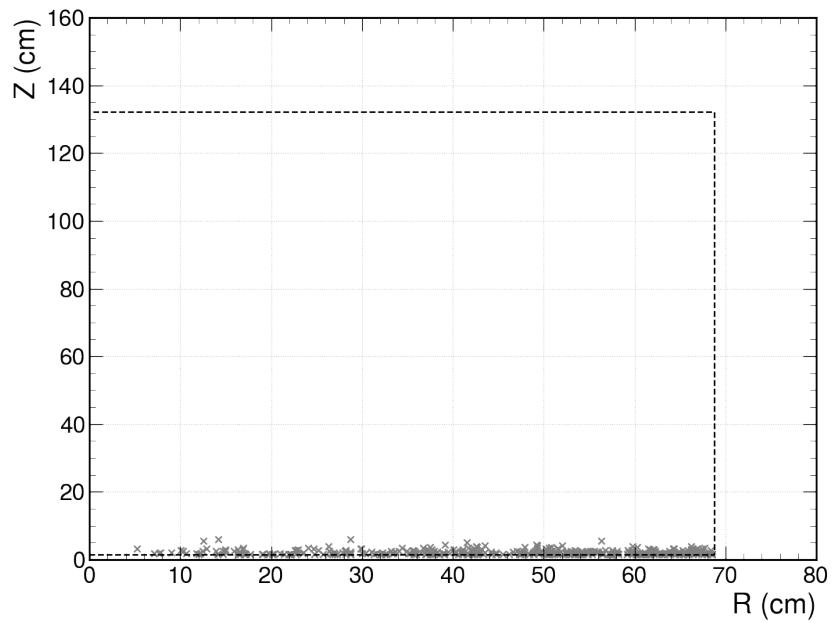


Figure 6.33: Z vs R for all $^{129\text{m}}\text{Xe}$ MSSl events after standard background cuts applied except for energy range cuts.

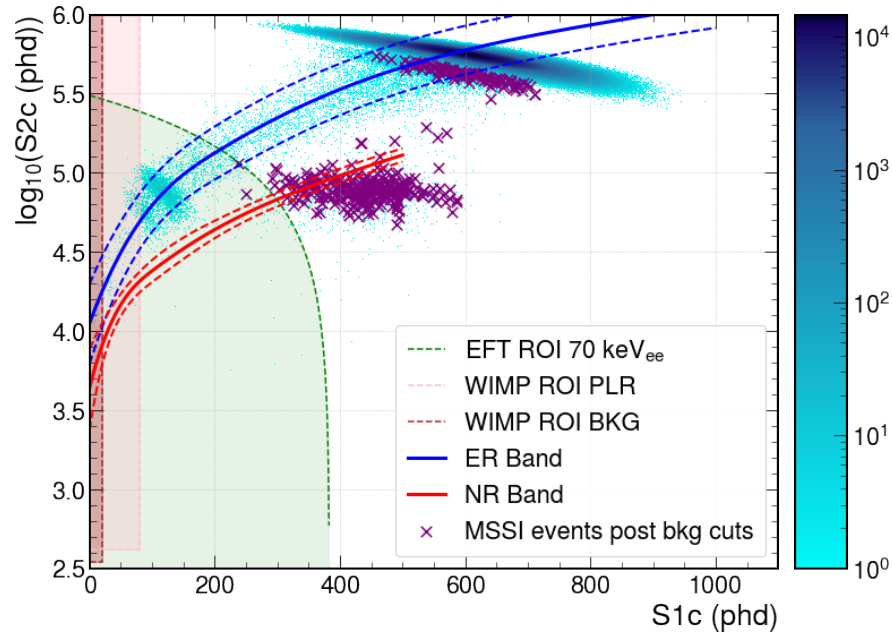


Figure 6.34: $\log_{10}(S2_c)$ vs $S1_c$ for all $^{129\text{m}}\text{Xe}$ events in a 60 day data run, no cuts applied. The purple crosses are $^{129\text{m}}\text{Xe}$ MSSI events with standard background cuts except for energy range cuts. The different ROIs are represented by the shaded areas and corresponding dotted lines in the figure; the brown is the WIMP ROI TDR, the pink is the WIMP ROI PLR and the green is the LUX-like EFT ROI. The blue and red bands are the electron and nuclear recoil bands respectively (solid: mean; dashed: $\pm 1.28\sigma$ contours).

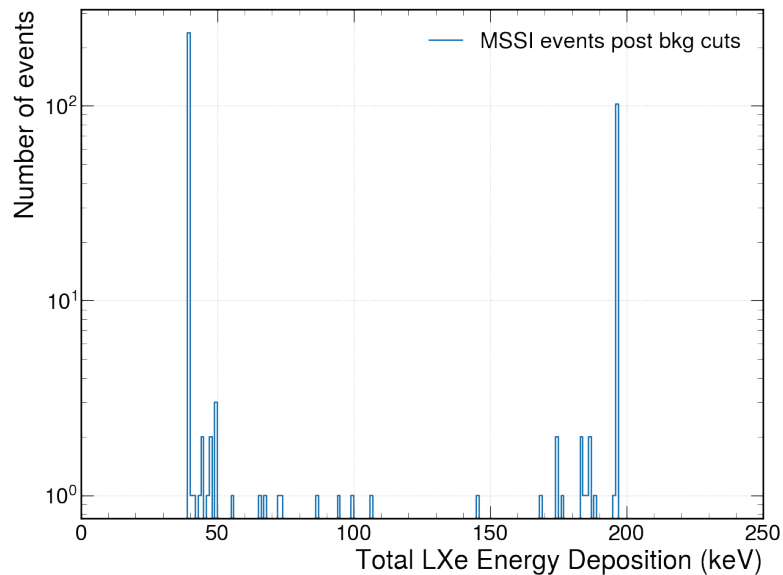


Figure 6.35: Total Monte Carlo truth energy deposition in active LXe for $^{129\text{m}}\text{Xe}$ MSSI events after standard background cuts applied except ROI.

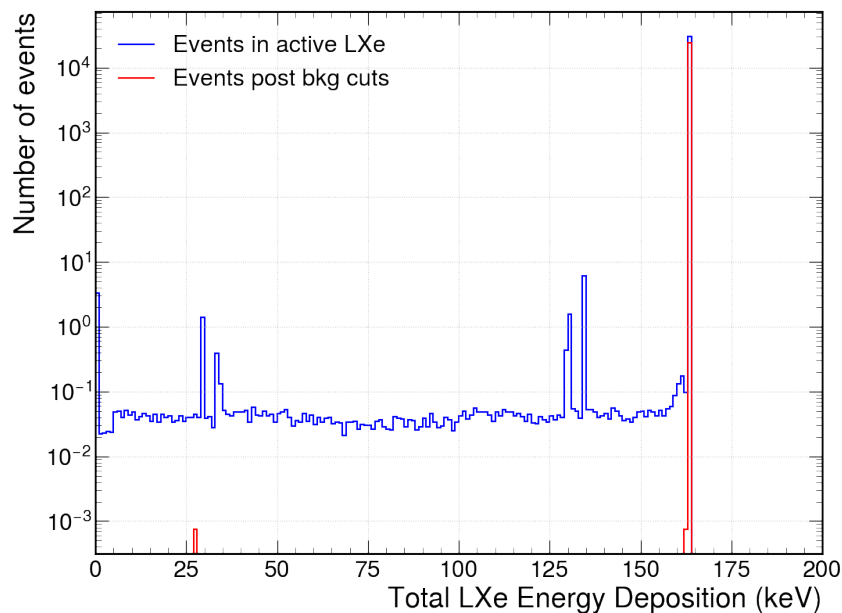
6.3.3.2 $^{131\text{m}}\text{Xe}$ decays

For $^{131\text{m}}\text{Xe}$, $\sim 4 \times 10^7$ decays, of the 1×10^8 simulated, had energy deposition which took place inside the active LXe within 60 day data taking time window. Similarly to $^{129\text{m}}\text{Xe}$, $\sim 20\%$ of events were removed once standard background cuts were applied and none of the remaining events were within the WIMP ROI's, shown in Table 6.6. In the EFT ROI there are no events, however, when using the EFT Monte Carlo truth energy ROI there is one event after standard background cuts are applied. Like with the $^{129\text{m}}\text{Xe}$ simulation, the reconstructed energy of this event is higher than the Monte Carlo truth energy, displayed in Figure 6.36. This is an MSSI event which is on the perimeter of the EFT ROI in S1-S2 space (see purple cross in Figure 6.37).

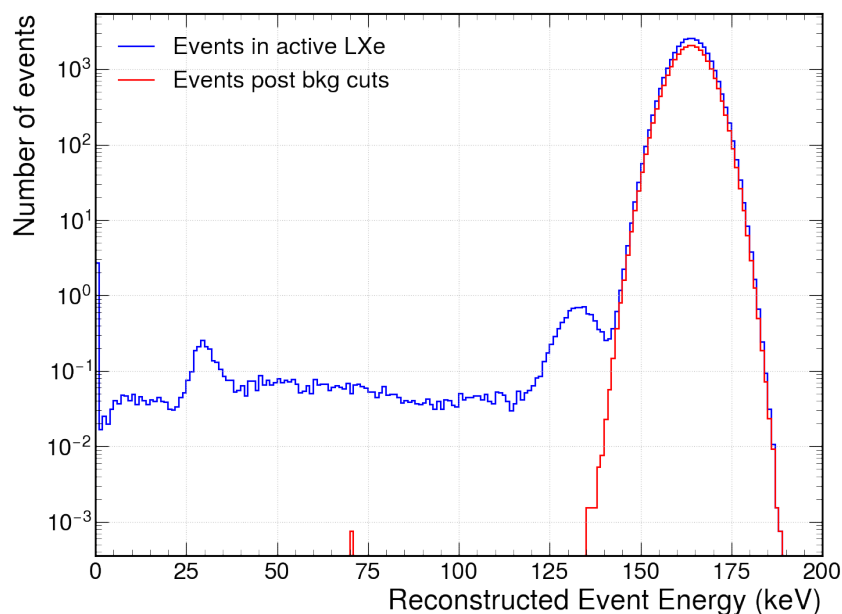
Table 6.6: The number of events in the $^{131\text{m}}\text{Xe}$ simulation after different cuts are applied. These numbers have been normalised to 2 days of DD neutron calibrations. BKG cuts are the standard background cuts defined earlier in Section 6.2.2. No ER/NR discrimination cut applied. Numbers in brackets are determined using the Monte Carlo truth energies instead of reconstructed energies. Errors quoted are 90% C.L. intervals (for large statistics standard error and for small statistics from Feldman-Cousins [152]).

Cuts	Number of events	Number of events (normalised to 2 days of DD neutron calibra- tions)
Events within 60 day data run	$4.04 \times 10^7 \pm 1.04 \times 10^4$	30586 ± 8
BKG cuts	$3.21 \times 10^7 \pm 9.29 \times 10^3$	24297 ± 7
BKG cuts in WIMP TDR ROI	$0_{-0}^{+2.44}$	$0_{-0}^{+0.0018}$
BKG cuts in WIMP PLR ROI	$0_{-0}^{+2.44}$	$0_{-0}^{+0.0018}$
BKG cuts in EFT ROI	$0_{-0}^{+2.44} (1_{-0.11}^{+4.36})$	$0_{-0}^{+0.0018}$ ($0.000757_{-0.000083}^{+0.00331}$)

The $^{131\text{m}}\text{Xe}$ decays should not cause concern as there were no events in either WIMP ROI and there was a very low rate in the EFT ROI. When normalised to 2 days of DD neutron calibrations there are no events in the EFT ROI (using reconstructed energies) but $0.000757_{-0.000083}^{+0.00331}$ events in the ROI if using Monte Carlo truth energies, see Table 6.6.



(a) Monte Carlo truth energy deposition.



(b) Total reconstructed energy deposition.

Figure 6.36: Energy deposition in the $^{131\text{m}}\text{Xe}$ simulation for events taking place during a 60 day data run in active LXe. The number of events has been normalised to 2 days of DD neutron calibrations. The blue histogram is all events in the active LXe and the red histogram is only those events that passed all standard background cuts in the active LXe.

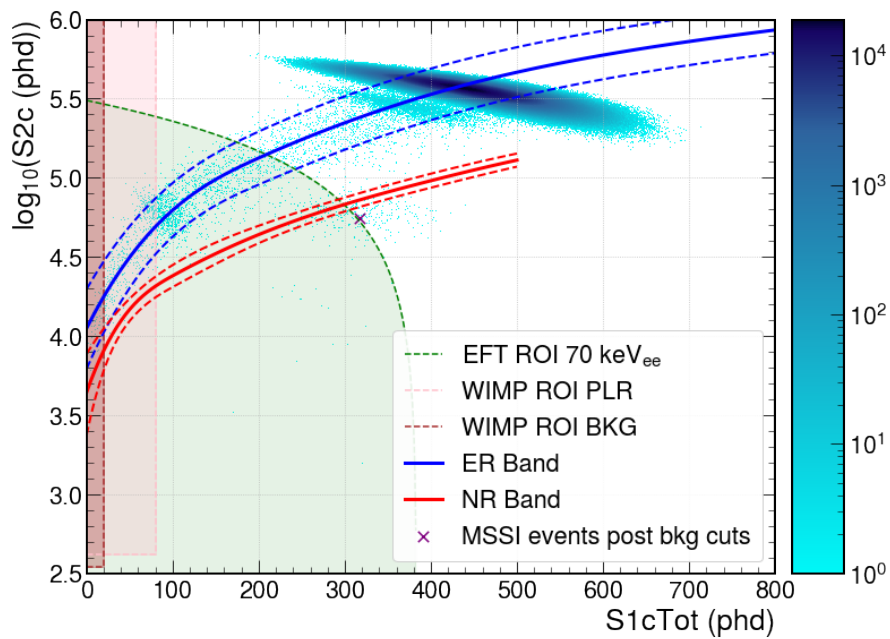


Figure 6.37: $\log_{10}(S2_c)$ vs $S1_c$ for all ^{131m}Xe events in a 60 day data run, no cuts applied. The purple cross is the only ^{131m}Xe MSSSI event which passed standard background cuts except energy range cuts. The different ROIs are represented by the shaded areas and corresponding dotted lines in the figure; the brown and the pink are the WIMP ROI TDR and PLR, respectively, and the green is the LUX-like EFT ROI. The blue and red lines show the boundary of the electron and nuclear recoil bands respectively (solid: mean; dashed: $\pm 1.28\sigma$ contours).

6.4 Conclusion

Simulations of DD and AmLi neutron calibrations in the LZ detector have been performed using the DecayChain BACCARAT generator and analysed. From the simulated events that passed standard WIMP background cuts in the 60 day data taking time window, once ^{125}I was removed, there was $0.000712^{+0.146}_{-0.000075}$ ($0.000244^{+0.0493}_{-0.000025}$) events in the WIMP TDR ROI, $0.00138^{+0.146}_{-0.00036}$ ($0.00047^{+0.0493}_{-0.00012}$) events in the WIMP PLR ROI and $0.12^{+0.28}_{-0.04}$ ($0.05^{+0.10}_{-0.02}$) events in the EFT ROI from DD (AmLi) neutron calibrations once normalised to 2 days (9 hours) of calibrations.

Likewise simulations of $^{129\text{m}}\text{Xe}$ and $^{131\text{m}}\text{Xe}$ decays in the LZ detector have been undertaken with the new validated BACCARAT GPSIon generator. Analysis found no events which passed all standard WIMP background cuts in either WIMP ROIs in a 60 day data run for both isotopes. In the EFT ROI there was $0.011^{+0.018}_{-0.006}$ (using reconstructed energies) events from $^{129\text{m}}\text{Xe}$ once normalised, to 2 days of DD neutron calibrations and no events from $^{131\text{m}}\text{Xe}$ simulations.

The events found in the WIMP and EFT ROIs are above the NR band and hence, should not be an issue for WIMP searches or EFT studies in a 60 day data run.

Chapter 7

LZ commissioning data

A key part of the LZ detector commissioning phase is exploring and understanding the data taken during this period. As was discussed in Chapter 5 high energy γ rays and neutrons from the Davis cavern rock are a source of background outside the water tank. Part of the commissioning phase is to verify that the current shielding, from the water tank and steel pyramid, adequately attenuates γ -flux in the detector. The data can also be used to validate simulations of the background.

This chapter examines data taken during the cold xenon gas (GXe) phase of commissioning before and after detector shielding was in place (tank filled with water and OD filled with scintillator). Also explored is the comparison of that data to previous backgrounds simulations.

7.1 Background acquisitions

A number of background data acquisitions were taken during the detector commissioning phase when there was cold GXe in the LZ time projection chamber (TPC). Although the detector signals produced from particle interactions in GXe differ from those in liquid xenon (LXe) the shielding attenuation can still be measured. The resulting scintillation pulses from an energy deposition in the gas have a longer duration than the equivalent in liquid [157]. Due to the low density recoiling particles travel further and create less dense tracks. In addition, as no voltage was applied to the grids during these acquisitions there is no secondary scintillation light (S_2) as electroluminescence requires a strong electric field.

Two groups of acquisitions were taken BKG-1 & BKG-2, before and after the water tank and outer detector (OD) tank were filled, respectively. The conditions of the GXe in the TPC were similar in both datasets; GXe temperature 187 K (179 K) and pressure 1.87 bar (1.81 bar) in BKG-1 (BKG-2). Although the GXe condensing phase began before the BKG-2 acquisitions the liquid level of the xenon in the TPC was below the bottom photomultiplier tube (PMT) faces during the acquisitions.

The BKG-1 acquisitions were conducted non-consecutively over a three week period. During this period short calibration runs were also undertaken in between the background acquisitions, although these are not expected to affect the background measurements. Conversely the BKG-2 acquisitions were performed successively over 2 days.

In all acquisitions the LZ PMT DAQ was triggered randomly with a specified frequency. Some acquisitions also included an S1 trigger as well, which activates when large pulses are detected. For each random trigger the DAQ saved the PMT data 2 ms before and after the trigger. A random trigger rate of ~ 20 Hz was used in the BKG-1 acquisitions. As the system was more stable by the BKG-2 acquisitions they used a higher random trigger rate ~ 45 Hz for most of the acquisitions with the rate increased to ~ 90 Hz in the final 12 hours. The DAQ runtime and live time, which is the duration of the saved data, for both groups of acquisitions is visible in Table 7.1.

Table 7.1: Information about the background acquisition datasets. The DAQ runtime and live time is provided with the number of biased PMTs active during data taking. Also indicated is whether the OD and water tank were filled during those acquisition.

Dataset	Runtime (h)	Live time (h)	Biased PMTs			OD & water tank
			Top	Bottom	Total	
BKG-1	170.69	13.28	228	217	445	empty
BKG-2	38.14	10.00	143	212	355	full

Ideally all PMT channels should be available, however, some PMTs in the commissioning phase displayed erratic rate behaviour or had power issues and thus were unbiased (switched off) in acquisitions whilst undergoing diagnosis and resolution. Table 7.1 shows the number of biased PMTs used in both groups of background acquisitions. As the biased PMTs were not the same throughout all acquisitions, a combined biased PMT map was created in order to compare both datasets, shown in Figure 7.1. In the combined PMT map there are a total of 349 biased PMTs, 141 on the top array and 208 on the bottom array.

7.2 Analysis

In dual-phase TPC analysis the scintillation signals produced are corrected with light collection efficiency maps. These corrected signals are then used to reconstruct the event position and recoil energy, relying upon previous simulations and calibrations. However, during the LZ TPC GXe period the extensive simulations and calibrations required in order to map the scintillation signals to recoil energies and produce the light collection efficiency maps were not available. Additionally event position reconstruction in the TPC is poor

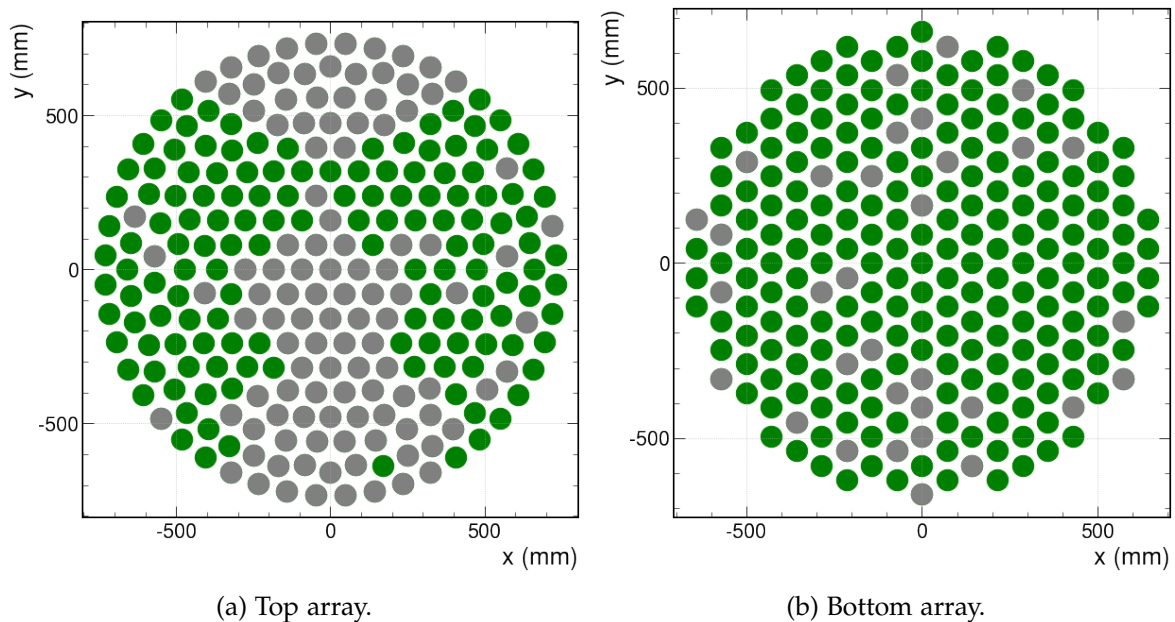


Figure 7.1: The combined biased PMT map for the top (Figure (a)) and bottom (Figure (b)) PMT arrays for all background acquisitions. The green and grey represent the biased and unbiased PMTs, respectively. The PMT $x - y$ positions are accurate but their size is not to scale.

due to the absence of the $S2$ signal. Therefore, this study of the background GXe data only analysed the pulse areas measured by the biased PMTs. The PMT channel pulse areas provide a good indicator of the recoil energies produced in the TPC and can be used to measure the shielding attenuation.

Unfortunately, the pulse rates before the random DAQ trigger were smaller than those after the trigger during some of these background acquisitions and thus only post random trigger pulses were analysed, halving the live time of the datasets explored. This was due to an issue with the $S1$ trigger and random trigger employed in the acquisitions. Pulses undergo sparsification, trigger decision stage, and if large pulses are detected then the $S1$ trigger is activated. However, the random trigger was only activated if there were no large pulses in the 2 ms pre-trigger window, as this would have activated the $S1$ trigger instead. This led to a collection bias in the pre-trigger window for the random triggered events.

As mentioned in the previous section in order to compare both groups of background acquisitions a combined PMT map with a total of 349 biased PMTs was used when analysing the data, visible in Figure 7.1. In these datasets only the post-trigger pulses from the randomly triggered events were considered. For each of these pulses the individual pulse areas detected by each PMT in the combined bias PMT map was summed. The total pulse areas were histogrammed and then divided by the livetime of dataset to produce the observed pulse rate against pulse area.

A comparison between the BKG-1 acquisitions and a previous set of BACCARAT GXe background simulations has also been undertaken. These energy deposition simulations, performed by Sally Shaw (University of California, Santa Barbara, USA), aimed to determine the background in the LZ GXe TPC produced by the cavern wall gamma rays when there was no shielding from the full water tank or scintillator. These simulations, using Eq. 5.2, have been normalised with the following activities calculated from Davis cavern γ -ray spectra measurements ^{232}Th - 13 ± 3 Bq/kg, ^{238}U - 29 ± 15 Bq/kg and ^{40}K - 220 ± 60 Bq/kg [140]. In this comparison the post-trigger random pulses from the BKG-1 acquisitions using all 445 biased PMTs were examined.

The NEST (Noble Element Simulation Technique) [112] package was utilised, by Greg Rischbieter (State University of New York at Albany, USA), to convert energy depositions in the BACCARAT simulation to pulse area in order to directly compare with the real data. Unfortunately, the NEST package is unable to simulate zero electric field and thus it was set to its minimum electric field of 1 V cm^{-1} . The gain from primary scintillation channel (g_1) was determined by fitting the photon yield peak to the backscatter peak in the BKG-1 acquisitions. The NEST gamma model was used with the BKG-1 detector conditions and g_1 to produce the scintillation pulse areas.

This analysis study was carried out on both the UK and USA LZ data centres using analysis code constructed with the Hyper framework, discussed in Chapter 4.

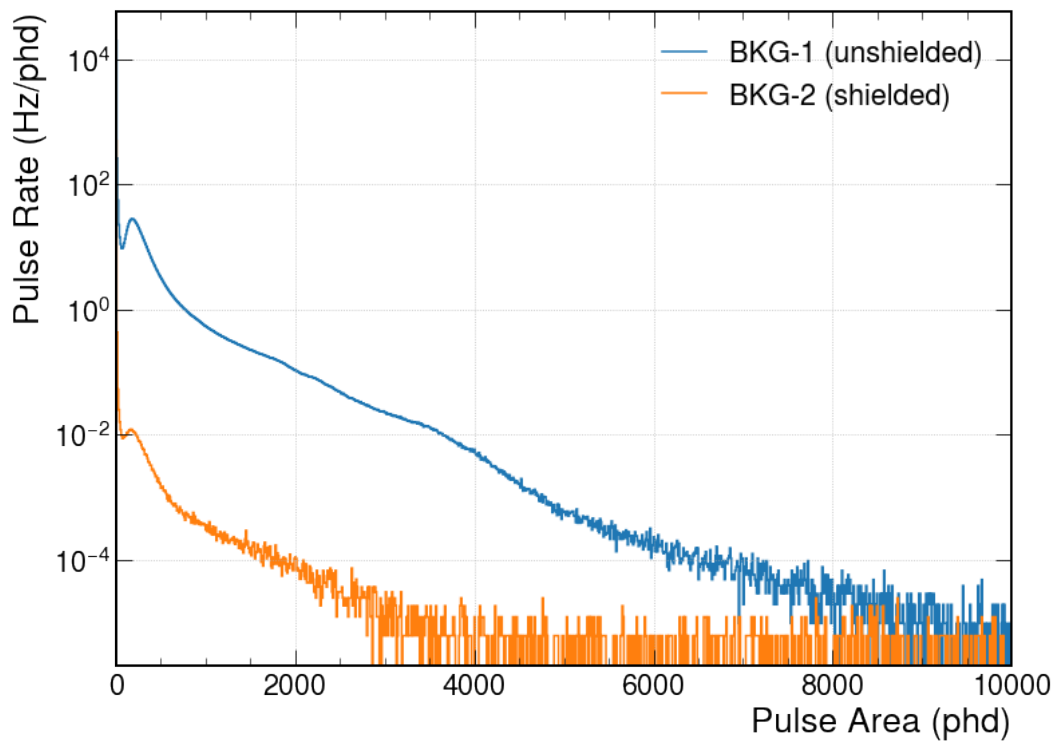
7.3 Results

As can be seen in Figure 7.2 the full OD and water tank provide substantial shielding for the LZ TPC from the cavern wall gamma rays. The overall pulse rate drops significantly between the two groups of background acquisitions, displayed in Table 7.2.

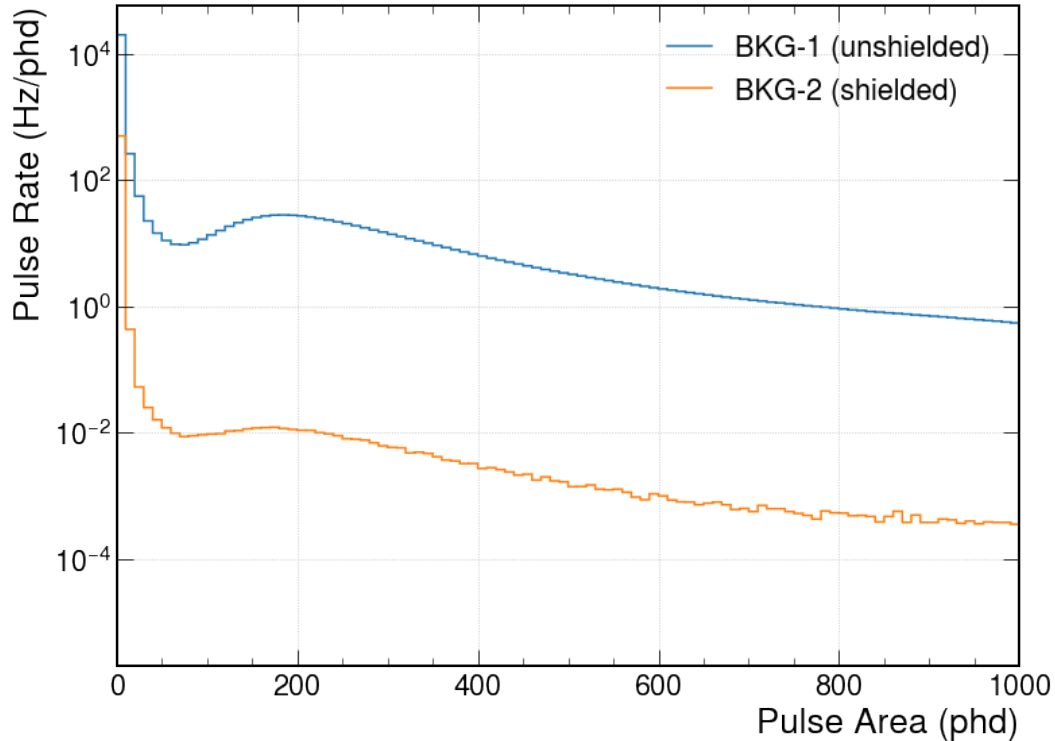
Table 7.2: Post-trigger pulse rate for the BKG-1 and BKG-2 acquisitions using the combined PMT map. The OD and water tank were empty in during BKG-1 and filled by the BKG-2 acquisitions.

Dataset	Total pulse rate (kHz)	Pulse rate (Pulse area > 10 phd) (Hz)	Pulse rate (Pulse area > 50 phd) (Hz)
BKG-1	210.74	10951.51	7398.21
BKG-2	5.02	9.07	3.77

The large spike in pulse rate below 50 phd in all acquisitions, visible in Figure 7.2b, was initially puzzling as this was not expected. However, after investigation the likely cause of this large spike was due to electroluminescence, the process where scintillation photons are produced as a result of collisions between gas atoms and ionised electron



(a) 0 to 10000 phd.



(b) 0 to 1000 phd.

Figure 7.2: The rate of post-trigger pulses versus pulse area in the BKG-1 (blue) and BKG-2 (orange) background acquisitions using the combined PMT map. The OD and water tank were empty during BKG-1 and filled by the BKG-2 acquisitions.

accelerated in an external electric field. Although none of the grids were active it has been suggested that the electric field was strong enough for electroluminescence in small regions between the bottom PMT array and the bottom grid, as PMTs are biased and the field lines around the grid wires or PMTs could possibly be non-uniform. Impurities from the bottom grid produce free electrons which resulted in electroluminescence causing the large spike in pulse rate at low pulse area. Once the LZ TPC transitioned to the LXe phase and the grid settings were altered the rate of the low pulse area electroluminescence reduced considerably.

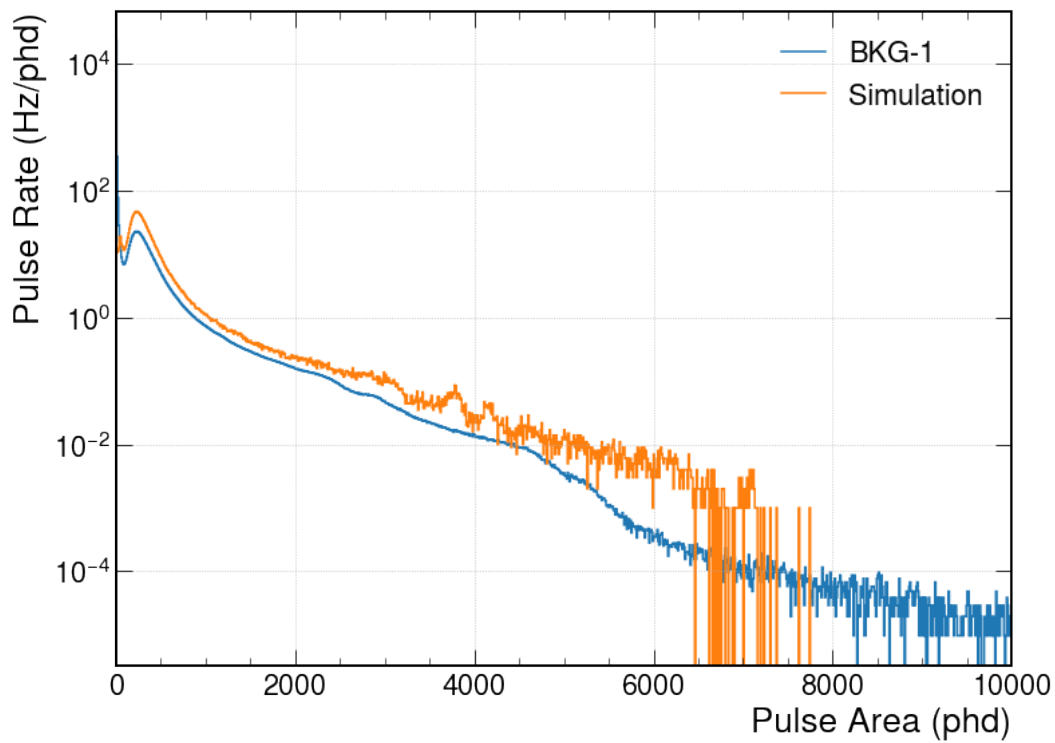
In order to better compare the two groups of background acquisitions Table 7.2 contains the pulse rate for pulse areas larger than 50 phd, thus omitting the low pulse area electroluminescence peak. The OD and water tank full reduces the event rate by a factor of ~ 2000 and no additional background suppression methods were used (e.g. veto detector rejection, fiducialisation, etc.). It is important to note that although this may appear to be a small suppression factor there was already some shielding in place during BKG-1 acquisitions. The frame of the water tank, the square plate on top of the tank and the pyramid beneath the tank, all made of steel, reduced the cavern wall gamma ray background in the BKG-1 acquisitions. In addition, the residual background in the TPC in BKG-2 acquisitions comes from the detector components, which is not reduced by shielding. The detector shielding from the cavern wall gamma rays in conjunction with event selection cuts will greatly suppress the cavern wall background in the LZ TPC.

The cavern wall gamma ray BACCARAT GXe simulations approximately concurs with the BKG-1 background acquisitions. The simulated pulse area rate spectra conforms to a similar shape as the real data (see Figure 7.3), however, the total pulse rate is ~ 2 times larger, when comparing above pulse areas of 50 phd (see Table 7.3).

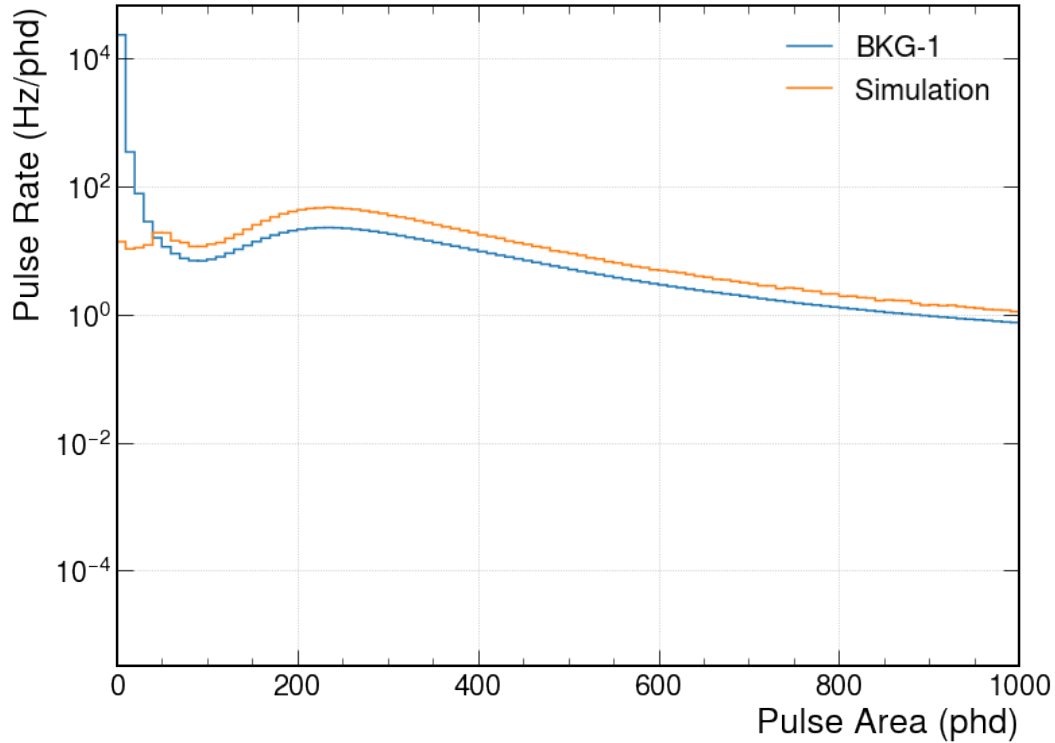
This is likely due to slight inaccuracies of the light collection efficiency estimates and the uncertainties in the activities used to normalise the GXe LZ TPC simulations. These background acquisitions will help inform future simulations and will improve the light collection efficiency estimates.

Table 7.3: Pulse rate for the BKG-1 acquisitions and BACCARAT background GXe simulations.

Dataset	Total pulse rate (kHz)	Pulse rate (Pulse area > 10 phd) (kHz)	Pulse rate (Pulse area > 50 phd) (kHz)
BKG-1	247.73	12.24	7.52
Simulation	14.63	14.49	13.96



(a) 0 to 10000 phd.



(b) 0 to 1000 phd.

Figure 7.3: The rate of pulses versus pulse area in the BKG-1 (blue) background acquisitions compared to the BACCARAT background GXe simulations (orange). The simulations were processed with NEST using $g1 = 0.0665$ and $E = 1 \text{ V cm}^{-1}$.

7.4 Summary

In conclusion LZ TPC GXe background acquisitions taken during the LZ detector commissioning phase were explored using the Hyper framework. The acquisitions analysed were taken before and after the OD and water tank was filled.

The shielding provided by the OD and water tank reduce the pulse rate, for pulse areas greater than 50 phd, by a factor of ~ 2000 significantly reducing the cavern wall γ -ray background in the TPC. In conjunction with event selection cuts this background should not be an issue for WIMP searches.

BACCARAT GXe simulations of the cavern wall gamma ray approximately concur with the background acquisitions. The discrepancy in event rate between the two will inform future simulations and improve light collection efficiency estimates.

Chapter 8

Conclusion

Dark matter has intrigued the scientific community for many years, however, its constituents still remain a mystery. There is a great deal of evidence of this non-luminous matter and a few promising dark matter particle candidates, explored in Chapter 1. Many experiments are searching for the favoured dark matter candidate (WIMPs) using a variety of different methods, also described in Chapter 1. The LZ dark matter experiment aims to have significantly greater sensitivity to WIMPs than its predecessor LUX. An overview of the LUX and LZ experiments along with dual-phase xenon TPC technology was covered in Chapter 2. This thesis presents the authors' contributions towards background characterisation and suppression in the LUX and LZ experiments.

A key background reduction strategy employed in both the LUX and LZ experiments is xenon purification prior to detector installation. Overviews of the LZ gas charcoal chromatography system, used to remove problematic noble radioactive impurities (mainly ^{85}Kr) in xenon, and the sampling system are detailed in Chapter 3. Impurity measurements taken with the LZ krypton removal sampling system confirm that the system is able to reduce the krypton concentration in xenon to below 300 ppq. Additionally, work undertaken to construct the xenon recovery cold trap and automate the plotting of important LZ krypton removal system information is also presented in Chapter 3.

A JSI software has been created to enable LZ users to perform simulations and data analysis on the LZ USA data centre (NERSC) via the JSE PSquared. Furthermore, Hyper (parallel processing Python analysis framework) was developed in order to simplify and accelerate data analysis within the LZ experiment. A prototype Python website tool, called LEOPARD, was also constructed to allow users to easily produce 1D and 2D histograms of real LZ detector data with simple analysis cuts applied. These software programs developed for LZ are described in Chapter 4.

High statistics simulations characterising the cavern wall γ -ray background in the LUX and LZ WIMP searches are presented in Chapter 5. The shielding provided by the water tank, inverted steel pyramid and background rejection analysis cuts substantially sup-

press this background in the TPC. The total cavern wall γ -ray rate observed in the LUX and LZ detectors was $(1.36 \pm 0.05) \times 10^{-6}$ events/kg/day/keV and $(0.065 \pm 0.007) \times 10^{-6}$ events/kg/day/keV respectively. This reduction in rate between the LUX and LZ detectors highlights the success of the new background reduction methods deployed in LZ. In both cases this background is sub-dominant and does not cause any issues for WIMP searches. Also covered in Chapter 5 are the cavern wall γ -ray simulations carried out for the LZ $0\nu\beta\beta$ search and the RockGammas BACCARAT generator.

Neutron calibration sources can activate xenon and its surroundings in the LZ detector potentially creating additional background events in the TPC. Simulations of the DD and AmLi neutron calibrations were performed using the DecayChain BACCARAT generator. As BACCARAT was unable to track ^{129m}Xe & ^{131m}Xe production in the neutron calibration simulations a new BACCARAT generator, called GPSIon, was developed to simulate metastable isotopes. A separate set of ^{129m}Xe & ^{131m}Xe simulations were carried out using the GPSIon BACCARAT generator. These simulations and their analysis are described in Chapter 6. Analysis of the simulations determined that in a 60 day run there were no background events after standard background cuts in the NR band or below in either the WIMP or EFT ROI and hence these calibration should not be an issue in a 60 day data run.

Finally, LZ detector commissioning data has also been explored, detailed in Chapter 7. The substantial difference between the background event rate in the LZ GXe TPC before and after the water tank and OD were filled demonstrates high efficiency of shielding against gamma rays coming from the cavern walls.

The work outlined in this thesis, characterising and mitigating several key sources of background events in the LZ experiment, played a key role in enabling the LZ detector to achieve the desired sensitivity to WIMPs, greatly surpassing the LUX detector. Exciting times are ahead as LZ is now taking science data enabling it to probe unexplored WIMP parameter space. Current and future LZ science campaigns will elucidate WIMP dark matter.

Appendix A

Hyper example code

```
1 import boost_histogram as bh
2 import numpy as np
3 from hyper import get_files_from_list, hyper_obj
4
5 class fill_histogram(hyper_obj):
6     """Custom Hyper job class"""
7     def __init__(self, tree, data_obj):
8         super().__init__(tree, data_obj)
9         self.func = self.single_scatters_slc_s2c
10
11     def single_scatters_slc_s2c(self, uproot_tree, cfg_dict, local_data_obj):
12         """Extract single scatters and fill histogram with slc and log10(s2c)"""
13         #Get data from root file
14         variables = ['ss.nSingleScatters', 'ss.correctedS1Area_phd', 'ss.
15 correctedS2Area_phd']
16         arrays = uproot_tree.arrays(variables)
17
18         #Get all single scatters
19         ss_mask = (arrays['ss.nSingleScatters'] == 1)
20
21         #Fill histogram with slc and log10(s2c)
22         local_data_obj.fill(
23             arrays['ss.correctedS1Area_phd'][ss_mask],
24             np.log10(arrays['ss.correctedS2Area_phd'][ss_mask])
25         )
26
27         #return histogram as job output
28         return local_data_obj
29
30 #Load in list of ROOT file paths (either local or xrootd)
31 root_file_paths = get_files_from_list('ROOT_file_paths.txt')
32
33 #Create histogram to fill
34 xbins, xmin, xmax = 1100, 0., 2200.
35 ybins, ymin, ymax = 1000, 3.5, 6.5
36 slc_log10_s2c_hist = bh.Histogram(
37     bh.axis.Regular(xbins, xmin, xmax),
38     bh.axis.Regular(ybins, ymin, ymax),
39 )
40
41 #Create Hyper job
42 slc_log10_s2c_job = fill_histogram('Scatters', slc_log10_s2c_hist)
43
44 #Execute Hyper job with 64 local CPU cores
45 slc_log10_s2c_job.run_multicore_uproot(root_file_paths, 64)
46
47 #Save histogram to file
48 slc_log10_s2c_job.save('slc_log10_s2c_histogram.root')
```

Program A.1: Example Python analysis code written with the Hyper framework.

Bibliography

- [1] F. Zwicky, "Die Rotverschiebung von extragalaktischen Nebeln," *Helv. Phys. Acta* **6**, 110–127 (1933).
- [2] J. C. Kapteyn, "First Attempt at a Theory of the Arrangement and Motion of the Sidereal System," *Astrophys. J.* **55**, 302 (1922).
- [3] J. H. Oort, "The force exerted by the stellar system in the direction perpendicular to the galactic plane and some related problems," *Bull. Astron. Inst. Neth.* **6**, 249 (1932).
- [4] J. H. Jeans, "The Motions of Stars in a Kapteyn Universe," *Mon. Not. R. Astron. Soc.* **82**, 122–132 (1922).
- [5] V. C. Rubin and J. Ford, W. Kent, "Rotation of the Andromeda Nebula from a Spectroscopic Survey of Emission Regions," *Astrophys. J.* **159**, 379 (1970).
- [6] K. G. Begeman, A. H. Broeils, and R. H. Sanders, "Extended rotation curves of spiral galaxies : dark haloes and modified dynamics." *Mon. Not. R. Astron. Soc.* **249**, 523 (1991).
- [7] M. Milgrom, "A modification of the Newtonian dynamics - Implications for galaxies." *Astrophys. J.* **270**, 371–383 (1983).
- [8] R. Nemiroff and J. Bonnell, "Astronomy Picture of the Day," <https://apod.nasa.gov/apod/ap111221.html> (2011), [Online; accessed 27-Jan-2022].
- [9] D. Walsh, R. F. Carswell, and R. J. Weymann, "0957+561 A, B: twin quasistellar objects or gravitational lens?" *Nature* **279**, 381–384 (1979).
- [10] A. Einstein, "Lens-Like Action of a Star by the Deviation of Light in the Gravitational Field," *Science* **84**, 506–507 (1936).
- [11] H. Hoekstra, M. Bartelmann, H. Dahle, H. Israel, *et al.*, "Masses of galaxy clusters from gravitational lensing," *Space Sci. Rev.* **177**, 75–118 (2013), arXiv:1303.3274 [astro-ph.CO] .

- [12] D. Clowe, M. Bradač, A. H. Gonzalez, M. Markevitch, *et al.*, “A direct empirical proof of the existence of dark matter,” *Astrophys. J. Lett.* **648**, L109–L113 (2006), arXiv:astro-ph/0608407 .
- [13] G. Bertone and D. Hooper, “History of dark matter,” *Rev. Mod. Phys.* **90**, 045002 (2018), arXiv:1605.04909 [astro-ph.CO] .
- [14] A. A. Penzias and R. W. Wilson, “A Measurement of Excess Antenna Temperature at 4080 Mc/s.” *Astrophys. J.* **142**, 419–421 (1965).
- [15] N. Aghanim, Y. Akrami, F. Arroja, M. Ashdown, *et al.* (Planck), “Planck 2018 results. I. Overview and the cosmological legacy of Planck,” *Astron. Astrophys.* **641**, A1 (2020), arXiv:1807.06205 [astro-ph.CO] .
- [16] P. A. R. Ade, N. Aghanim, M. I. R. Alves, C. Armitage-Caplan, *et al.* (Planck), “Planck 2013 results. I. Overview of products and scientific results,” *Astron. Astrophys.* **571**, A1 (2014), arXiv:1303.5062 [astro-ph.CO] .
- [17] R. J. Cooke, M. Pettini, K. M. Nollett, and R. Jorgenson, “The primordial deuterium abundance of the most metal-poor damped Ly α system,” *Astrophys. J.* **830**, 148 (2016), arXiv:1607.03900 [astro-ph.CO] .
- [18] V. Springel, S. D. M. White, A. Jenkins, C. S. Frenk, *et al.*, “Simulating the joint evolution of quasars, galaxies and their large-scale distribution,” *Nature* **435**, 629–636 (2005), arXiv:astro-ph/0504097 .
- [19] M. Vogelsberger, S. Genel, V. Springel, P. Torrey, *et al.*, “Introducing the Illustris Project: Simulating the coevolution of dark and visible matter in the Universe,” *Mon. Not. Roy. Astron. Soc.* **444**, 1518–1547 (2014), arXiv:1405.2921 [astro-ph.CO] .
- [20] J. Schaye, R. A. Crain, R. G. Bower, M. Furlong, *et al.*, “The EAGLE project: Simulating the evolution and assembly of galaxies and their environments,” *Mon. Not. Roy. Astron. Soc.* **446**, 521–554 (2015), arXiv:1407.7040 [astro-ph.GA] .
- [21] P. A. Zyla, R. M. Barnett, J. Beringer, O. Dahl, *et al.* (Particle Data Group), “Review of Particle Physics,” *Prog. Theor. Exp. Phys.* **2020**, 083C01 (2020).
- [22] B. Carr, F. Kuhnel, and M. Sandstad, “Primordial Black Holes as Dark Matter,” *Phys. Rev. D* **94**, 083504 (2016), arXiv:1607.06077 [astro-ph.CO] .
- [23] H. Niikura, M. Takada, N. Yasuda, R. H. Lupton, *et al.*, “Microlensing constraints on primordial black holes with Subaru/HSC Andromeda observations,” *Nature Astron.* **3**, 524–534 (2019), arXiv:1701.02151 [astro-ph.CO] .

- [24] P. Tisserand, L. Le Guillou, C. Afonso, J. N. Albert, *et al.* (EROS-2), “Limits on the Macho Content of the Galactic Halo from the EROS-2 Survey of the Magellanic Clouds,” *Astron. Astrophys.* **469**, 387–404 (2007), arXiv:astro-ph/0607207 .
- [25] S. D. M. White, C. S. Frenk, and M. Davis, “Clustering in a Neutrino Dominated Universe,” *Astrophys. J. Lett.* **274**, L1–L5 (1983).
- [26] S. Dodelson and L. M. Widrow, “Sterile-neutrinos as dark matter,” *Phys. Rev. Lett.* **72**, 17–20 (1994), arXiv:hep-ph/9303287 .
- [27] R. Adhikari, M. Agostini, N. A. Ky, T. Araki, *et al.*, “A White Paper on keV Sterile Neutrino Dark Matter,” *JCAP* **01**, 025 (2017), arXiv:1602.04816 [hep-ph] .
- [28] C. A. Argüelles, I. Esteban, M. Hostert, K. J. Kelly, *et al.*, “MicroBooNE and the ν_e Interpretation of the MiniBooNE Low-Energy Excess,” *Phys. Rev. Lett.* **128**, 241802 (2022), arXiv:2111.10359 [hep-ph] .
- [29] A. Aguilar, L. B. Auerbach, R. L. Burman, D. O. Caldwell, , *et al.* (LSND), “Evidence for neutrino oscillations from the observation of $\bar{\nu}_e$ appearance in a $\bar{\nu}_\mu$ beam,” *Phys. Rev. D* **64**, 112007 (2001), arXiv:hep-ex/0104049 .
- [30] A. A. Aguilar-Arevalo, B. C. Brown, J. M. Conrad, R. Dharmapalan, *et al.* (Mini-BooNE), “Updated MiniBooNE neutrino oscillation results with increased data and new background studies,” *Phys. Rev. D* **103**, 052002 (2021), arXiv:2006.16883 [hep-ex] .
- [31] K. C. Y. Ng, B. M. Roach, K. Perez, J. F. Beacom, *et al.*, “New Constraints on Sterile Neutrino Dark Matter from *NuSTAR* M31 Observations,” *Phys. Rev. D* **99**, 083005 (2019), arXiv:1901.01262 [astro-ph.HE] .
- [32] L. Roszkowski, E. M. Sessolo, and S. Trojanowski, “WIMP dark matter candidates and searches—current status and future prospects,” *Rept. Prog. Phys.* **81**, 066201 (2018), arXiv:1707.06277 [hep-ph] .
- [33] P. S. Bhupal Dev, A. Mazumdar, and S. Qutub, “Constraining Non-thermal and Thermal properties of Dark Matter,” *Front. in Phys.* **2**, 26 (2014), arXiv:1311.5297 [hep-ph] .
- [34] S. P. Martin, “A Supersymmetry primer,” *Adv. Ser. Direct. High Energy Phys.* **18**, 1–98 (1998), arXiv:hep-ph/9709356 .
- [35] J. M. Yang, “SUSY Dark Matter In Light Of CDMS/XENON Limits,” *Int. J. Mod. Phys. D* **20**, 1383–1388 (2011), arXiv:1102.4942 [hep-ph] .

- [36] A. Canepa, “Searches for Supersymmetry at the Large Hadron Collider,” *Rev. Phys.* **4**, 100033 (2019).
- [37] T. Flacke, D. W. Kang, K. Kong, G. Mohlabeng, *et al.*, “Electroweak Kaluza-Klein Dark Matter,” *JHEP* **04**, 041 (2017), arXiv:1702.02949 [hep-ph] .
- [38] E. W. Kolb, D. J. H. Chung, and A. Riotto, “WIMPzillas!” *AIP Conf. Proc.* **484**, 91–105 (1999), arXiv:hep-ph/9810361 .
- [39] R. D. Peccei and H. R. Quinn, “CP Conservation in the Presence of Instantons,” *Phys. Rev. Lett.* **38**, 1440–1443 (1977).
- [40] R. D. Peccei and H. R. Quinn, “Constraints Imposed by CP Conservation in the Presence of Instantons,” *Phys. Rev. D* **16**, 1791–1797 (1977).
- [41] J. H. Christenson, J. W. Cronin, V. L. Fitch, and R. Turlay, “Evidence for the 2π Decay of the K_2^0 Meson,” *Phys. Rev. Lett.* **13**, 138–140 (1964).
- [42] C. Abel, S. Afach, N. J. Ayres, C. A. Baker, *et al.*, “Measurement of the Permanent Electric Dipole Moment of the Neutron,” *Phys. Rev. Lett.* **124**, 081803 (2020), arXiv:2001.11966 [hep-ex] .
- [43] R. D. Peccei and H. R. Quinn, “CP Conservation in the Presence of Instantons,” *Phys. Rev. Lett.* **38**, 1440–1443 (1977).
- [44] R. D. Peccei and H. R. Quinn, “Constraints Imposed by CP Conservation in the Presence of Instantons,” *Phys. Rev. D* **16**, 1791–1797 (1977).
- [45] L. D. Duffy and K. van Bibber, “Axions as Dark Matter Particles,” *New J. Phys.* **11**, 105008 (2009), arXiv:0904.3346 [hep-ph] .
- [46] H. Primakoff, “Photoproduction of neutral mesons in nuclear electric fields and the mean life of the neutral meson,” *Phys. Rev.* **81**, 899 (1951).
- [47] P. Sikivie, “Experimental Tests of the Invisible Axion,” *Phys. Rev. Lett.* **51**, 1415–1417 (1983), [Erratum: *Phys.Rev.Lett.* **52**, 695 (1984)].
- [48] D. G. Cerdeño and A. M. Green, “Direct detection of WIMPs,” in *Particle Dark Matter: Observations, Models and Searches*, edited by G. Bertone (Cambridge Univ. Press, Cambridge, 2010) Chap. 17.
- [49] J. I. Read, “The Local Dark Matter Density,” *J. Phys. G* **41**, 063101 (2014), arXiv:1404.1938 [astro-ph.GA] .
- [50] F. J. Kerr and D. Lynden-Bell, “Review of galactic constants,” *Mon. Not. Roy. Astron. Soc.* **221**, 1023 (1986).

- [51] M. C. Smith, G. R. Ruchti, A. Helmi, R. F. G. Wyse, *et al.*, “The RAVE Survey: Constraining the Local Galactic Escape Speed,” *Mon. Not. Roy. Astron. Soc.* **379**, 755–772 (2007), arXiv:astro-ph/0611671 .
- [52] Y. Nagashima, *Beyond the standard model of elementary particle physics* (Wiley-VCH, Weinheim, USA, 2014).
- [53] J. D. Lewin and P. F. Smith, “Review of mathematics, numerical factors, and corrections for dark matter experiments based on elastic nuclear recoil,” *Astropart. Phys.* **6**, 87–112 (1996).
- [54] I. Olcina Samblas, *A statistical framework for the characterisation of WIMP dark matter with the LUX-ZEPLIN experiment*, Ph.D. thesis, Imperial Coll., London (2019).
- [55] E. Aprile, J. Aalbers, F. Agostini, M. Alfonsi, *et al.* (XENON), “Dark Matter Search Results from a One Ton-Year Exposure of XENON1T,” *Phys. Rev. Lett.* **121**, 111302 (2018), arXiv:1805.12562 [astro-ph.CO] .
- [56] M. Schumann, “Direct Detection of WIMP Dark Matter: Concepts and Status,” *J. Phys. G* **46**, 103003 (2019), arXiv:1903.03026 [astro-ph.CO] .
- [57] G. J. Alner, H. M. Araújo, A. Bewick, C. Bungau, *et al.*, “First limits on WIMP nuclear recoil signals in ZEPLIN-II: A two phase xenon detector for dark matter detection,” *Astropart. Phys.* **28**, 287–302 (2007), arXiv:astro-ph/0701858 .
- [58] J. Angle, E. Aprile, F. Arneodo, L. Baudis, *et al.* (XENON), “First Results from the XENON10 Dark Matter Experiment at the Gran Sasso National Laboratory,” *Phys. Rev. Lett.* **100**, 021303 (2008), arXiv:0706.0039 [astro-ph] .
- [59] D. S. Akerib, H. M. Araújo, X. Bai, A. J. Bailey, *et al.* (LUX), “First results from the LUX dark matter experiment at the Sanford Underground Research Facility,” *Phys. Rev. Lett.* **112**, 091303 (2014), arXiv:1310.8214 [astro-ph.CO] .
- [60] D. S. Akerib, C. W. Akerlof, S. K. Alsum, H. M. Araújo, *et al.* (LUX-ZEPLIN), “Projected WIMP sensitivity of the LUX-ZEPLIN dark matter experiment,” *Phys. Rev. D* **101**, 052002 (2020), arXiv:1802.06039 [astro-ph.IM] .
- [61] X. Cui, A. Abdukerim, W. Chen, X. Chen, *et al.* (PandaX-II), “Dark Matter Results From 54-Ton-Day Exposure of PandaX-II Experiment,” *Phys. Rev. Lett.* **119**, 181302 (2017), arXiv:1708.06917 [astro-ph.CO] .
- [62] P. Agnes, I. F. M. Albuquerque, T. Alexander, A. K. Alton, *et al.* (DarkSide), “DarkSide-50 532-day Dark Matter Search with Low-Radioactivity Argon,” *Phys. Rev. D* **98**, 102006 (2018), arXiv:1802.07198 [astro-ph.CO] .

- [63] P. Agnes, T. Alexander, A. Alton, K. Arisaka, *et al.* (DarkSide), “First Results from the DarkSide-50 Dark Matter Experiment at Laboratori Nazionali del Gran Sasso,” *Phys. Lett. B* **743**, 456–466 (2015), arXiv:1410.0653 [astro-ph.CO] .
- [64] K. Abe, K. Hiraide, K. Ichimura, Y. Kishimoto, *et al.* (XMASS), “A direct dark matter search in XMASS-I,” *Phys. Lett. B* **789**, 45–53 (2019), arXiv:1804.02180 [astro-ph.CO] .
- [65] R. Ajaj, P. A. Amaudruz, G. R. Araujo, M. Baldwin, *et al.* (DEAP), “Search for dark matter with a 231-day exposure of liquid argon using DEAP-3600 at SNOLAB,” *Phys. Rev. D* **100**, 022004 (2019), arXiv:1902.04048 [astro-ph.CO] .
- [66] B. S. Neganov and V. N. Trofimov, “Colorimetric method measuring ionizing radiation,” *Otkryt. Izobret.* **146**, 215 (1985).
- [67] P. N. Luke, “Voltage-assisted calorimetric ionization detector,” *J. Appl. Phys.* **64**, 6858–6860 (1988).
- [68] E. Armengaud, Q. Arnaud, C. Augier, A. Benoît, *et al.* (EDELWEISS), “Performance of the EDELWEISS-III experiment for direct dark matter searches,” *JINST* **12**, P08010 (2017), arXiv:1706.01070 [physics.ins-det] .
- [69] R. Agnese, T. Aramaki, I. J. Arnquist, W. Baker, *et al.* (SuperCDMS), “Results from the Super Cryogenic Dark Matter Search Experiment at Soudan,” *Phys. Rev. Lett.* **120**, 061802 (2018), arXiv:1708.08869 [hep-ex] .
- [70] A. H. Abdelhameed, G. Angloher, P. Bauer, A. Bento, *et al.* (CRESST), “First results from the CRESST-III low-mass dark matter program,” *Phys. Rev. D* **100**, 102002 (2019), arXiv:1904.00498 [astro-ph.CO] .
- [71] R. Bernabei, P. Belli, A. Bussolotti, F. Cappella, *et al.*, “First model independent results from DAMA/LIBRA-phase2,” *Nucl. Phys. Atom. Energy* **19**, 307–325 (2018), arXiv:1805.10486 [hep-ex] .
- [72] G. Adhikari, E. B. de Souza, N. Carlin, J. J. Choi, *et al.* (COSINE-100), “Strong constraints from COSINE-100 on the DAMA dark matter results using the same sodium iodide target,” *Sci. Adv.* **7**, abk2699 (2021), arXiv:2104.03537 [hep-ex] .
- [73] J. Amaré, S. Cebrián, D. Cintas, I. Coarasa, *et al.*, “Annual Modulation Results from Three Years Exposure of ANAIS-112,” *Phys. Rev. D* **103**, 102005 (2021), arXiv:2103.01175 [astro-ph.IM] .
- [74] J. Aalbers, F. Agostini, M. Alfonsi, F. D. Amaro, *et al.* (DARWIN), “DARWIN: towards the ultimate dark matter detector,” *JCAP* **11**, 017 (2016), arXiv:1606.07001 [astro-ph.IM] .

- [75] C. Pérez de los Heros, “Status, Challenges and Directions in Indirect Dark Matter Searches,” *Symmetry* **12**, 1648 (2020), arXiv:2008.11561 [astro-ph.HE] .
- [76] H. Abdallah, A. Abramowski, F. Aharonian, F. Ait Benkhali, *et al.* (HESS), “Search for γ -Ray Line Signals from Dark Matter Annihilations in the Inner Galactic Halo from 10 Years of Observations with H.E.S.S.” *Phys. Rev. Lett.* **120**, 201101 (2018), arXiv:1805.05741 [astro-ph.HE] .
- [77] M. Aguilar, G. Alberti, B. Alpat, A. Alvino, *et al.* (AMS), “First Result from the Alpha Magnetic Spectrometer on the International Space Station: Precision Measurement of the Positron Fraction in Primary Cosmic Rays of 0.5-350 GeV,” *Phys. Rev. Lett.* **110**, 141102 (2013).
- [78] W. B. Atwood, A. A. Abdo, M. Ackermann, W. Althouse, *et al.*, “The Large Area Telescope on the Fermi Gamma-Ray Space Telescope Mission,” *Astrophys. J.* **697**, 1071–1102 (2009), arXiv:0902.1089 [astro-ph.IM] .
- [79] M. Ackermann, A. Albert, B. Anderson, W. B. Atwood, *et al.* (Fermi-LAT), “Searching for Dark Matter Annihilation from Milky Way Dwarf Spheroidal Galaxies with Six Years of Fermi Large Area Telescope Data,” *Phys. Rev. Lett.* **115**, 231301 (2015), arXiv:1503.02641 [astro-ph.HE] .
- [80] K. Choi, K. Abe, Y. Haga, Y. Hayato, *et al.* (Super-Kamiokande), “Search for neutrinos from annihilation of captured low-mass dark matter particles in the Sun by Super-Kamiokande,” *Phys. Rev. Lett.* **114**, 141301 (2015), arXiv:1503.04858 [hep-ex] .
- [81] M. G. Aartsen, K. Abraham, M. Ackermann, J. Adams, *et al.* (IceCube), “Improved limits on dark matter annihilation in the Sun with the 79-string IceCube detector and implications for supersymmetry,” *JCAP* **04**, 022 (2016), arXiv:1601.00653 [hep-ph] .
- [82] S. Adrián-Martínez, A. Albert, M. André, G. Anton, *et al.* (ANTARES), “Limits on Dark Matter Annihilation in the Sun using the ANTARES Neutrino Telescope,” *Phys. Lett. B* **759**, 69–74 (2016), arXiv:1603.02228 [astro-ph.HE] .
- [83] C. A. Argüelles, A. Diaz, A. Kheirandish, A. Olivares-Del-Campo, *et al.*, “Dark matter annihilation to neutrinos,” *Rev. Mod. Phys.* **93**, 035007 (2021), arXiv:1912.09486 [hep-ph] .
- [84] S. Giagu, “WIMP Dark Matter Searches With the ATLAS Detector at the LHC,” *Front. in Phys.* **7**, 75 (2019).
- [85] D. Vannerom (CMS), “Dark Matter searches with CMS,” *PoS DIS2019*, 111 (2019).

- [86] H. Baer, V. Barger, S. Salam, D. Sengupta, *et al.*, “Status of weak scale supersymmetry after LHC Run 2 and ton-scale noble liquid WIMP searches,” *Eur. Phys. J. ST* **229**, 3085–3141 (2020), arXiv:2002.03013 [hep-ph] .
- [87] B. J. Mount, S. Hans, R. Rosero, M. Yeh, *et al.* (LUX-ZEPLIN), “LUX-ZEPLIN (LZ) Technical Design Report,” (2017), LBNL-1007256, FERMILAB-TM-2653-AE-E-PPD, arXiv:1703.09144 [physics.ins-det] .
- [88] V. Chepel and H. Araujo, “Liquid noble gas detectors for low energy particle physics,” *JINST* **8**, R04001 (2013), arXiv:1207.2292 [physics.ins-det] .
- [89] E. Hogenbirk, J. Aalbers, P. A. Breur, M. P. Decowski, *et al.*, “Precision measurements of the scintillation pulse shape for low-energy recoils in liquid xenon,” *JINST* **13**, P05016 (2018), arXiv:1803.07935 [physics.ins-det] .
- [90] J. Jortner, L. Meyer, S. A. Rice, and E. G. Wilson, “Localized Excitations in Condensed Ne, Ar, Kr, and Xe,” *J. Chem. Phys.* **42**, 4250–4253 (1965).
- [91] D. S. Akerib, S. Alsum, H. M. Araújo, X. Bai, *et al.* (LUX), “Liquid xenon scintillation measurements and pulse shape discrimination in the LUX dark matter detector,” *Phys. Rev. D* **97**, 112002 (2018), arXiv:1802.06162 [physics.ins-det] .
- [92] P. Adhikari, R. Ajaj, G. R. Araujo, M. Batygov, *et al.* (DEAP), “The liquid-argon scintillation pulshape in DEAP-3600,” *Eur. Phys. J. C* **80**, 303 (2020), arXiv:2001.09855 [physics.ins-det] .
- [93] C. E. Dahl, *The physics of background discrimination in liquid xenon, and first results from Xenon10 in the hunt for WIMP dark matter*, Ph.D. thesis, Princeton U. (2009).
- [94] J. Lindhard, V. Nielsen, M. Scharff, and P. V. Thomsen, “Integral equations governing radiation effects. (notes on atomic collisions, iii),” *Kgl. Danske Videnskab., Selskab. Mat. Fys. Medd.* **33** (1963).
- [95] T. Takahashi, S. Konno, T. Hamada, M. Miyajima, *et al.*, “Average energy expended per ion pair in liquid xenon,” *Phys. Rev. A* **12**, 1771–1775 (1975).
- [96] P. Sorensen and C. E. Dahl, “Nuclear recoil energy scale in liquid xenon with application to the direct detection of dark matter,” *Phys. Rev. D* **83**, 063501 (2011), arXiv:1101.6080 [astro-ph.IM] .
- [97] D. S. Akerib, X. Bai, S. Bedikian, E. Bernard, *et al.* (LUX), “The Large Underground Xenon (LUX) Experiment,” *Nucl. Instrum. Meth. A* **704**, 111–126 (2013), arXiv:1211.3788 [physics.ins-det] .

- [98] D. S. Akerib, H. M. Araújo, X. Bai, A. J. Bailey, *et al.* (LUX), “Chromatographic separation of radioactive noble gases from xenon,” *Astropart. Phys.* **97**, 80–87 (2018), arXiv:1605.03844 [physics.ins-det] .
- [99] D. S. Akerib, H. M. Araújo, X. Bai, A. J. Bailey, *et al.*, “Radiogenic and Muon-Induced Backgrounds in the LUX Dark Matter Detector,” *Astropart. Phys.* **62**, 33–46 (2015), arXiv:1403.1299 [astro-ph.IM] .
- [100] D. S. Akerib, C. W. Akerlof, D. Y. Akimov, S. K. Alsum, *et al.* (LUX-ZEPLIN), “LUX-ZEPLIN (LZ) Conceptual Design Report,” (2015), LBNL-190005, FERMILAB-TM-2621-AE-E-PPD, arXiv:1509.02910 [physics.ins-det] .
- [101] D. S. Akerib, C. W. Akerlof, D. Y. Akimov, A. Alquahtani, *et al.* (LUX-ZEPLIN), “The LUX-ZEPLIN (LZ) Experiment,” *Nucl. Instrum. Meth. A* **953**, 163047 (2020), arXiv:1910.09124 [physics.ins-det] .
- [102] M. Mastromarco, A. Manna, O. Aberle, J. Andrzejewski, *et al.* (n_TOF), “Cross section measurements of $^{155,157}\text{Gd}(n, \gamma)$ induced by thermal and epithermal neutrons,” *Eur. Phys. J. A* **55**, 9 (2019), [Erratum: *Eur.Phys.J.A* 55, 45 (2019)], arXiv:1805.04149 [nucl-ex] .
- [103] “Environmental pollutants | radon,” in *Encyclopedia of Respiratory Medicine*, edited by G. J. Laurent and S. D. Shapiro (Academic Press, Oxford, 2006) pp. 120–125.
- [104] V. Tomasello, M. Robinson, and V. A. Kudryavtsev, “Radioactive background in a cryogenic dark matter experiment,” *Astropart. Phys.* **34**, 70–79 (2010).
- [105] V. Kudryavtsev, P. Beltrame, J. Buzenitz, C. Ghag, *et al.*, “Preliminary Estimate of Cosmic Ray- and Rock Neutron- Activation of Xe,” LZ Note: LzDB00000030 (2014).
- [106] J. Billard, L. E. Strigari, and E. Figueroa-Feliciano, “Solar neutrino physics with low-threshold dark matter detectors,” *Phys. Rev. D* **91**, 095023 (2015), arXiv:1409.0050 [astro-ph.CO] .
- [107] D. Akimov, J. B. Albert, P. An, C. Awe, *et al.* (COHERENT), “Observation of Coherent Elastic Neutrino-Nucleus Scattering,” *Science* **357**, 1123–1126 (2017), arXiv:1708.01294 [nucl-ex] .
- [108] S. Agostinelli, J. Allison, K. Amako, J. Apostolakis, *et al.* (GEANT4), “GEANT4—a simulation toolkit,” *Nucl. Instrum. Meth. A* **506**, 250–303 (2003).
- [109] D. S. Akerib, X. Bai, S. Bedikian, E. Bernard, *et al.*, “LUXSim: A Component-Centric Approach to Low-Background Simulations,” *Nucl. Instrum. Meth. A* **675**, 63–77 (2012), arXiv:1111.2074 [physics.data-an] .

- [110] D. S. Akerib, C. W. Akerlof, A. Alqahtani, S. K. Alsum, *et al.* (LUX-ZEPLIN), “Simulations of Events for the LUX-ZEPLIN (LZ) Dark Matter Experiment,” *Astropart. Phys.* **125**, 102480 (2021), arXiv:2001.09363 [physics.ins-det] .
- [111] M. Szydagis, N. Barry, K. Kazkaz, J. Mock, *et al.*, “NEST: a comprehensive model for scintillation yield in liquid xenon,” *JINST* **6**, P10002–P10002 (2011).
- [112] M. Szydagis, S. Andaloro, J. Balajthy, G. A. Block, *et al.*, “Noble Element Simulation Technique,” <https://doi.org/10.5281/zenodo.4569211> (2021).
- [113] C. F. P. da Silva (LUX), “Dark Matter Searches with LUX,” in *52nd Rencontres de Moriond on Very High Energy Phenomena in the Universe* (2017) pp. 199–209, arXiv:1710.03572 [hep-ex] .
- [114] H. H. Loosli, B. E. Lehmann, and W. M. Smethie, “Noble Gas Radioisotopes: ^{37}Ar , ^{85}Kr , ^{39}Ar , ^{81}Kr ,” in *Environmental Tracers in Subsurface Hydrology*, edited by P. G. Cook and A. L. Herczeg (Springer US, Boston, MA, 2000) pp. 379–396.
- [115] X. Mougeot, “BetaShape: A new code for improved analytical calculations of beta spectra,” *EPJ Web Conf.* **146**, 12015 (2017).
- [116] J. Silk, “Xenon Purity Monitoring for the LUX-ZEPLIN Krypton Removal Campaign,” LZ Note: AnalysisDocDB000083 (2021).
- [117] A. Bolozdynya, P. Brusov, T. Shutt, C. Dahl, *et al.*, “A chromatographic system for removal of radioactive ^{85}Kr from xenon,” *Nucl. Instrum. Methods Phys. Res. A* **579**, 50–53 (2007), Proceedings of the 11th Symposium on Radiation Measurements and Applications.
- [118] Inductive Automation, “Ignition v7.9,” <https://inductiveautomation.com/ignition/>.
- [119] Oracle Corporation, “MySQL,” <https://www.mysql.com/>.
- [120] D. S. Leonard, A. Dobi, C. Hall, L. J. Kaufman, *et al.*, “A simple high-sensitivity technique for purity analysis of xenon gas,” *Nucl. Instrum. Methods Phys. Res. A* **621**, 678–684 (2010), arXiv:1002.2742 [physics.ins-det] .
- [121] A. Dobi, C. Davis, C. Hall, T. Langford, *et al.*, “Detection of krypton in xenon for dark matter applications,” *Nucl. Instrum. Methods Phys. Res. A* **665**, 1–6 (2011), arXiv:1103.2714 [astro-ph.IM] .
- [122] J. Balajthy, *Purity Monitoring Techniques and Electronic Energy Deposition Properties in Liquid Xenon Time Projection Chambers*, Ph.D. thesis, Maryland U. (2018).

- [123] P. J. W. Faulkner, L. S. Lowe, C. L. A. Tan, P. M. Watkins, *et al.* (GridPP), “GridPP: development of the UK computing grid for particle physics,” *J. Phys. G* **32**, N1–N20 (2005).
- [124] S. Patton, “PSquared: v1.1.0,” <http://nest.lbl.gov/projects/psquared/>.
- [125] PostgreSQL Global Development Group and Regents of the University of California, “PostgreSQL,” <https://www.postgresql.org/>.
- [126] Pivotal Software, “RabbitMQ,” <https://www.rabbitmq.com/>.
- [127] D. Bauer, D. Colling, S. Fayer, E. Korolkova, *et al.*, “The LZ UK Data Centre,” *EPJ Web of Conf.* **214**, 03046 (2019).
- [128] NERSC, “Spin,” <https://www.nersc.gov/systems/spin/>.
- [129] CherryPy Team, “CherryPy,” <https://cherrypy.org/>.
- [130] R. Brun and F. Rademakers, “ROOT: An object oriented data analysis framework,” *Nucl. Instrum. Meth. A* **389**, 81–86 (1997).
- [131] A. Dorigo, P. Elmer, F. Furano, and A. Hanushevsky, “XROOTD - A highly scalable architecture for data access,” *WSEAS Transactions on Computers* **1**, 348–353 (2005).
- [132] Dask Development Team, “Dask: Library for dynamic task scheduling,” <https://dask.org>.
- [133] J. Pivarski, H. Schreiner, N. Smith, C. Burr, *et al.*, “scikit-hep/uproot4: 4.1.3,” <https://doi.org/10.5281/zenodo.5539722> (2021).
- [134] Plotly Technologies Inc., “Dash,” <https://plotly.com/dash/>.
- [135] H. Schreiner, H. Dembinski, A. Goel, J. Eschle, *et al.*, “scikit-hep/boost-histogram: Version 1.2.1,” <https://doi.org/10.5281/zenodo.5548612> (2021).
- [136] A. Novak, M. Feickert, H. Schreiner, J. Eschle, *et al.*, “scikit-hep/mplhep: v.0.2.17rc,” <https://doi.org/10.5281/zenodo.4540424> (2021).
- [137] D. Woodward, *Simulations of cosmic muons and background radiations for muon tomography and underground experiments*, Ph.D. thesis, Sheffield U. (2017).
- [138] J. Tuli, “Evaluated nuclear structure data file,” *Nucl. Instrum. and Meth. in Phys. Res. A* **369**, 506–510 (1996).
- [139] S. T. Perkins, D. E. Cullen, and S. M. Seltzer, “Tables and graphs of electron interaction cross-sections from 10-eV to 100-GeV derived from the LLNL evaluated electron data library (EEDL), $Z = 1 - 100$,” *Tech. rep.* (1991), 10.2172/5691165.

- [140] D. S. Akerib, C. W. Akerlof, S. K. Alsum, N. Angelides, *et al.* (LUX-ZEPLIN), “Measurement of the gamma ray background in the Davis cavern at the Sanford Underground Research Facility,” *Astropart. Phys.* **116**, 102391 (2020), arXiv:1904.02112 [physics.ins-det] .
- [141] N. Ackerman, B. Aharmim, M. Auger, D. J. Auty, *et al.* (EXO-200), “Observation of Two-Neutrino Double-Beta Decay in ^{136}Xe with EXO-200,” *Phys. Rev. Lett.* **107**, 212501 (2011), arXiv:1108.4193 [nucl-ex] .
- [142] M. Redshaw, E. Wingfield, J. McDaniel, and E. G. Myers, “Mass and double-beta-decay Q value of Xe-136,” *Phys. Rev. Lett.* **98**, 053003 (2007).
- [143] D. S. Akerib, C. W. Akerlof, A. Alqahtani, S. K. Alsum, *et al.* (LUX-ZEPLIN), “Projected sensitivity of the LUX-ZEPLIN experiment to the $0\nu\beta\beta$ decay of ^{136}Xe ,” *Phys. Rev. C* **102**, 014602 (2020), arXiv:1912.04248 [nucl-ex] .
- [144] D. Brown, M. Chadwick, R. Capote, A. Kahler, *et al.*, “ENDF/B-VIII.0: The 8th Major Release of the Nuclear Reaction Data Library with CIELO-project Cross Sections, New Standards and Thermal Scattering Data,” *Nucl. Data Sheets* **148**, 1–142 (2018).
- [145] V. A. Kudryavtsev, “Cosmogenic activation: Recent results,” *AIP Conf. Proc.* **1921**, 090004 (2018).
- [146] J. R. Verbus, C. A. Rhyne, D. C. Malling, M. Genecov, *et al.*, “Proposed low-energy absolute calibration of nuclear recoils in a dual-phase noble element TPC using D-D neutron scattering kinematics,” *Nucl. Instrum. Meth. A* **851**, 68–81 (2017), arXiv:1608.05309 [physics.ins-det] .
- [147] W. Taylor, Private Communication (2021).
- [148] A. Kamaha, “LZ Calibrations Operations,” (2020), Presentation at LZ Collaboration Meeting, Rutherford Appleton Laboratory, UK.
- [149] R. Sazzad, Private Communication (2021).
- [150] D. S. Akerib, S. Alsum, H. M. Araújo, X. Bai, *et al.* (LUX), “Effective field theory analysis of the first LUX dark matter search,” *Phys. Rev. D* **103**, 122005 (2021), arXiv:2003.11141 [astro-ph.CO] .
- [151] R. B. Firestone, *Table of Isotopes*, 8th ed., edited by C. M. Baglin and S. Y. F. Chu (John Wiley & Sons, New York, NY, 1996) and CD Update (1998).
- [152] G. J. Feldman and R. D. Cousins, “A Unified approach to the classical statistical analysis of small signals,” *Phys. Rev. D* **57**, 3873–3889 (1998), arXiv:physics/9711021 .

- [153] A. Naylor, "GPSIon BACCARAT Generator Validation," (2021), Presentation at LZ Weekly Background Meeting.
- [154] R. R. Kinsey, C. L. Dunford, J. K. Tuli, and T. W. Burrows, "The NUDAT program for nuclear data," <https://www.nndc.bnl.gov/nudat2> (1996).
- [155] A. Ringbom, "Calculation of electron–photon coincidence decay of ^{131m}Xe and ^{133m}Xe including atomic relaxation," *Appl. Radiat. Isot* **70**, 1499–1508 (2012).
- [156] M. J. Berger, J. H. Hubbell, S. M. Seltzer, J. Chang, *et al.*, "XCOM: Photon Cross Section Database (version 1.5)," <http://physics.nist.gov/xcom> (2010).
- [157] M. Mimura, S. Kobayashi, N. Masuyama, M. Miyajima, *et al.*, "Average numbers of scintillation photons and electrons produced by an alpha particle in high-density xenon gas," *Jpn. J. Appl. Phys.* **48**, 076501 (2009).